In depth Raman analysis of the ferroelectrics $KTiOPO_4$ and $LiNbO_3$

Role of domain boundaries and defects

Michael Rüsing

Supervisor: Prof. Dr. Artur Zrenner

Department Physik
Universität Paderborn

Der Fakultät für Naturwissenschaften vorgelegte Dissertation zur Erlangung des akademischen Grades eines
Dr. rer. nat.

January 2018

Declaration

I hereby declare that I prepared this thesis entirely on my own and have not used outside sources without declaration in the text. Any concepts or quotations applicable to these sources are clearly attributed to them. This thesis has not been submitted in the same or substantially similar version, not even in part, to any other authority for grading and has not been published elsewhere.

Michael Rüsing
January 2018

Abstract

In the context of ferroelectrics spatially resolved Raman spectroscopy is a powerful tool to investigate stoichiometry, defects or the ferroelectric properties, as well as to visualize domain structures or waveguides. Using Raman spectroscopy for investigations requires a throughout understanding of the spectra and underlying mechanisms. For example, in the context of the common nonlinear materials, lithium niobate and potassium titanyl phosphate, no comprehensive understanding of the Raman spectra of the bulk materials is available, while the underlying mechanism of the domain wall contrast in Raman spectroscopy is not well understood.

In this work, questions like these have been addressed in terms of systematic experimental investigations in close cooperation with density functional theory. In particular, it was possible to present a complete assignment of all phonons in the lithium niobate system, which serves as the basis for the understanding of the domain wall spectrum. Here, the domain wall spectrum can be explained with regard to microscopic structural effects, such as strains and electric fields, as well as a macroscopic change of selections rules. Both mechanisms are likewise present in the domain wall spectrum, while being present at different length scales. In the context of potassium titanyl phosphate the first throughout Raman investigations of domain structure, waveguides and periodically poled waveguides are presented. In the context of Rb-exchanged waveguides the change in stoichiometry, but also effects of strain are detected. Here, the Raman analysis provides a method to evaluate these effects.

Table of contents

Chapter 1

Introduction

The term *Integrated Optics* was first coined by Stewart E. Miller and his colleagues in four articles in the Bell System Technical Journal, where they envisioned integrated optical circuitry in analogy to integrated electronics and microwave circuitry [1–4]. Integrated optical devices offer much smaller footprints, are compatible for mass production, provide improved thermal and mechanical stability and the absence of coupling losses. These advantages make integrated optical approaches in particular attractive for nonlinear and quantum optical applications, which require on the one hand high power densities and on the other hand are restrained by losses.

A major class of nonlinear materials with applications in quantum optics are ferroelectric crystals. Due to the lack of an inversion center these materials provide a second order nonlinearity with large nonlinear coefficients. Nonlinear optical frequency conversions have first been investigated in the early sixties shortly after the invention of the first lasers [5–8]. Among the first materials used for nonlinear experiments were potassium dihydrogen phosphate (KDP) and ammonium dihydrogen phosphate (ADP) crystals. More durable alternatives such as lithium niobate were investigated early [9–11]. Soon the problem of phase matching in nonlinear processes was recognized, as pump, signal and idler beams are subject to dispersion. Dispersion leads to a constant dephasing of the interacting beams. This limits the power if not correctly accounted for. Early solutions were phase matching by exploiting the birefringence or material structuring, i.e. periodic poling to achieve quasi-phase matching as shown in Fig. 1.1b).

Nowadays, nonlinear processes, such as parametric down conversion (PDC), are one of the primary sources for light with quantum mechanical light properties, e.g. entangled photons or squeezed light. Ferroelectric materials, however, are not only employed for their intrinsic nonlinearities. These materials offer the possibility to employ the quasi-phase matching technique in periodically inverted, ferroelectric domain structures. The quasi phase matching enables high conversion efficiencies and can in principal be employed over a large frequency range, as the phase matching spectrum can be adjusted via the period length of the ferroelectric domain grid. Here, the technological challenge is to create high quality domain grids with the appropriate period length over a long crystal. The second component for integrated nonlinear optics are wave-guiding structures. In the context of nonlinear effects waveguides enables to reach the necessary high power densities with much lower absolute powers. Waveguides are typically formed by doping or ion exchange, which both induces external defects, or by deliberately creating internal defects, e.g. by ion bombardment or laser damage. Fabricating a periodic domain grid, a waveguide or subsequently periodically poled waveguides requires a fundamental knowledge of the material properties, the formation mechanisms and interactions. Recent developments aim at the fabrication of sub-micron period domain structures, which will allow frequency conversion processes in the optical regime, as well as completely new schemes, such as counter-propagating parametric down

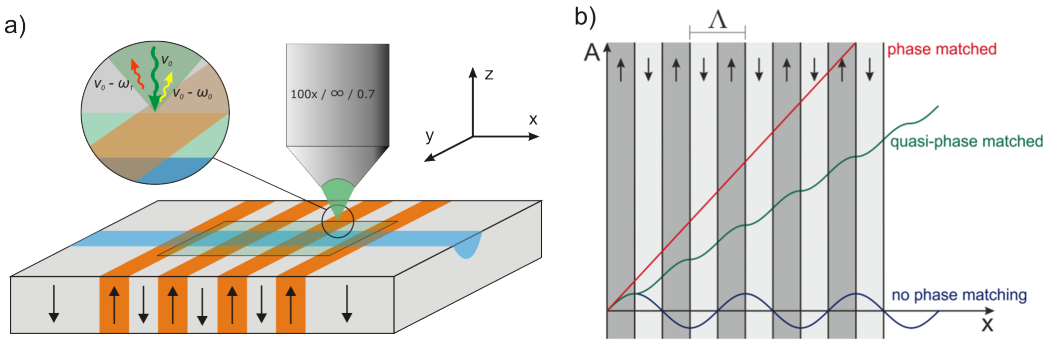

Fig. 1.1 a) Sketch of a periodically poled waveguide [17]. b) Amplitude increase of second harmonic generation for a phase matched, quasi-phase matched and non-phase matched scheme [17].

conversion. Counter propagation PDC offers a more narrow spectrum, as well as intrinsic separation of the created photons [12–16]. Efficient devices, however, will require periodically poled waveguides with ultra-short poling periods and low losses. In this context, a throughout understanding of the fabrication mechanism and underlying physical properties is inevitable, to assess the limits and possibilities of the fabrication processes and technologies. This requires methods to thoroughly investigate material properties. Experimentally confocal Raman spectroscopy presents a method to assess this properties in a noninvasive way.

The Raman effect was discovered in the 1920s, but due to the lack of appropriate light sources in the early years it was superseded by infrared spectroscopy [18]. The breakthrough of Raman spectroscopy as a standard characterization tool came with the invention of the laser in the early 1960s, which eventually resulted in the the first commercially available systems. In a simple picture the Raman effect is the inelastic scattering of light with low energy excitations in molecules or solid state systems. These low energy excitations range from phonons in crystal lattices, quantized rotational and vibrational states in molecules, to magnons or plasmons. As phonons and vibrations are very sensitive to structural changes, Raman spectroscopy enables the investigations of a very wide range of material properties with a single method. The possibilities range from stoichiometry, structure and composition [19–21], defects [22], (nano-)particle sizes [23, 24], to phase transitions [25], strain and stresses [26–30], to magnetic [31–35] and dielectric properties [36, 37] or charge-carrier-densities [38–40]. Raman spectroscopy usually uses optical or near infrared sources for excitation, while the signals are in the same frequency range. In contrast to IR spectroscopy, which often uses wavelength up to tens of microns, this allows to combine Raman spectroscopy with optical microscopy using conventional optical components, such as microscopy objective lenses and polarizers. This enables to perform Raman spectroscopy with diffraction limited resolution on the sub-micron scale, which is sometimes referred to as μ-Raman spectroscopy. A typical Raman experiment on periodically poled waveguides is depicted in Fig. 1.1a). In confocal application even three-dimensional resolutions are achievable. Super-resolution approaches, like tip-enhanced Raman spectroscopy, even can reach nanometer resolution [41–43]. This versatility makes (confocal) Raman microscopy one of the primary methods for analysis in solid state physics and chemistry.

In this work Raman spectroscopy is employed to extensively investigate the common nonlinear materials lithium niobate (LN, $LiNbO_3$), lithium tantalate ($LiTaO_3$) and potassium titanyl phosphate (KTP, $KTiOPO_4$). In the context of those materials Raman spectroscopy has been used to address variety of questions. Fundamental spectra have been studied, the influence of doping and defects and many other properties [44, 22]. Within the last decade confocal Raman imaging was used to visualize and analyze waveguide structures [45] and ferroelectric domain grids [46]. Despite the frequent use and numerous available papers, there are still a lot

of open questions in particular in the interpretation of results. One big issue is the assignment of all phonons to their respective symmetry groups and displacement patterns. Although lithium niobate has been studied for more than five decades [44], the phonon spectrum is not entirely understood [47]. This issue is even more pressing in the $KTiOPO_4$ material family. The complexity of the single KTP spectra prohibited so far a complete assignment and most works relegated to the analysis of qualitative features.

The correct assignment is important for multiple reasons. The Raman spectrum is connected to various physical properties, such as the dielectric functions [36] or the electro-optic properties [48]. A correct assignment is even more pressing for the subsequent interpretation of spectroscopic analysis. Here, the correct phonon assignments will allow to better understand the role of defects, their location in the crystal lattice or involved atoms. Alike, the three-dimensional analysis of changes in spectra in confocal Raman spectroscopy requires a fundamental knowledge of the Raman spectra. To address this issues not only Raman analysis is necessary, but needs to be combined with a fundamental theoretical analysis. This can be provided in close cooperation with atomistic simulations based on density functional theory (DFT). DFT allows to calculate the ground energy state of a crystal lattice based on a minimal set of input parameters. This results form the basis for the calculation of any material parameter, e.g. Raman scattering efficiencies and frequencies. A rigorous comparison of experiment and theory will subsequently lead to a deep understanding of material properties and the influence of certain parameters. The understanding of the properties of the bulk material will form the basis to investigate and understand the properties of more advanced structures, such as periodically poled lithium niobate thin films [49] or Rb-exhanged waveguides in KTP.

While spatially resolved Raman spectroscopy is used for the imaging of ferroelectric domain structures, the underlying mechanism is not well understood. This limits the use of this method to mere imaging in many works. In the past the domain walls in lithium niobate have been found to be accompanied with a huge number of secondary effects like electric fields [50], large strain fields ($> 10\ \mu$m) [51], birefringence and refractive index contrast [52], non-ising and chiral domain walls [53] or complex defect-domain wall interaction [54]. It is unclear how all these effects manifest themselves in Raman spectra of domain walls. This is a particular interesting issue, because Raman spectroscopy allows in a single measurement run to non-invasively investigate domains walls and waveguides with three-dimensional resolution. Such a full view is inevitable, if Raman spectroscopy is used to judge and analyze periodically poled waveguides. In the light of ultra-short domain periods it will be necessary to understand the underlying boundaries and physical mechanisms to ultimately achieve small domain periods in reproducible fabrication runs.

The immediate goals of this work are therefore to provide an improved understanding of the physical properties of the mentioned crystals. This includes a better understanding of the underlying mechanisms, which influence the Raman spectra of bulk crystals as well as domain structures or waveguides. Here, the long term vision are improved and novel devices based on a broad understanding of the materials properties.

Structure of this thesis

This thesis is divided in four main parts. Chapter 2 discusses the basic properties of the materials systems investigated in this work, the $LiNbO_3$/$LiTaO_3$ family and the $KTiOPO_4$ family. A broad background on the material properties, fabrication methods and defects is an important prerequisite for interpretation of any experimental results.

Chapter 3 focuses on the background regarding the methods used in this work. Here, first the theoretical background of the Raman effect is reviewed in the classical, as well as the quantum mechanical picture including an introduction of the applications of group theory in the context of selection rules. After the theoretical background, the experimental instrumentation of the confocal Raman setup and the principal execution of an experiment is discussed. In support of the Raman microscopy, confocal nonlinear microscopy is performed. Here, an overview of the setup is given in the subsequent section. For both methods several examples for applications are discussed based on measured results outside of the main context of this work. In a major part of this work dry, confocal microscopy in highly refracting materials, e.g. $LiNbO_3$, is performed. Here, refraction leads to a deviation of the nominal focus position, from the actual focus position. In this context, a correction method is investigated experimentally, which closes this chapter.

The driving questions in this work can be distinguished into a purely spectroscopic part (Chapter 4), and a spatially resolved microscopy part (Chapter 5). In this context, Chapter 4 addresses the basic vibrational properties of both material families and discusses the questions of phonon assignment and identification in terms of an in depth spectroscopic analysis of $LiNbO_3$, $LiTaO_3$ and mixed crystals, as well as $KTiOPO_4$ and related compounds. The analysis of the $LiNbO_3$/$LiTaO_3$ is supported by density functional analysis. The subsequent Chapter 5 is divided in two main parts. First, the problem of the domain wall contrast is discussed based on extensive analysis of the spectra of periodically poled $LiNbO_3$, $LiTaO_3$ and $KTiOPO_4$. The second part discusses the strength of Raman spectroscopy in the context of (periodically poled) Rb-exchanged waveguide in $KTiOPO_4$. Each chapter closes with specific concluding remarks, while a general summary and conclusion is given in Chapter 6.

Chapter 2

Material systems

In the following pages, the general background and properties of the material systems analyzed in this work will be be reviewed. The goal is to provide the reader with the background and context of research in these materials systems and to provide a good starting point for more in-depth research about any specific material related questions.

2.1 $LiNbO_3$ and $LiTaO_3$

Lithium niobate ($LiNbO_3$, LN) and the isostructural lithium tantalate ($LiTaO_3$, LT) are widely used materials in academics and industry due to their outstanding combination of physical properties, like mechanical and chemical stability, piezo-electricity, pyroelectricity, large nonlinear optical, electro-optical or elasto-optical constants [55, 56]. The applications of these materials range from RF filters in electronics via surface acoustic wave devices [57] to integrated linear and nonlinear optical devices [58, 59], holographic storage [60–62], over micro-electro-mechanical systems [63], photovoltaic patterning and general photovoltaics [64–67] to pyro-electrically driven fusion [68]. This leads to a wide availability of $LiNbO_3$ and $LiTaO_3$, where the annual production can be estimated in the range of several hundred tons[1]. In particular, in integrated nonlinear optics lithium niobate is widely applied, because its ferroelectric properties allows to employ the quasi-phase matching technique in periodically inverted domain grids.

2.1.1 Crystal structure and crystal growth

In this section, the properties of $LiNbO_3$ will now be reviewed briefly. As mentioned, lithium niobate and lithium tantalate are isostructural crystals. Here, Nb and Ta can be substituted over the complete compositional range for each other forming $LiNb_{(1-x)}Ta_xO_3$ lithium niobate tantalate mixed crystals [69]. The properties of both materials are very similar and in this chapter $LiNbO_3$ and $LiTaO_3$ may be used synonymously, if not stated otherwise.

Probably one of the first works mentioning lithium niobate was the famous Norwegian mineralogist William Zachariasen in 1928, who investigated and identified the crystallographic structure of many ABO_3 compounds in his PhD thesis [71]. However, it was only in 1949 when the ferroelectricity of $LiNbO_3$ and $LiTaO_3$ was discovered [72, 73]. Its nonlinear properties were probably first discussed and analyzed in 1964 by Boyd *et.*

[1] Crystal technology, Inc alone states an annual production of 60 tons $LiNbO_3$ as of 2011 business report.

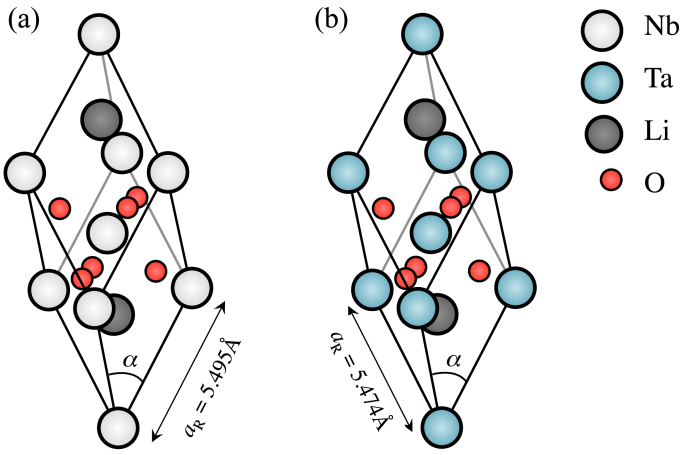

Fig. 2.1 Rhombohedral unit cells of lithium niobate and lithium tantalate with lattice parameter as calculated in DFT [70].

al. as a superior alternative to the then mostly used potassium dihydrongen phosphate (KDP) and ammonium dihydrogen phosphate (ADP) crystals [9, 10], which both are nonlinear and piezoelectric, but soluble in water, which is a major drawback.

In their ferroelectric phase $LiNbO_3$ and $LiTaO_3$ belong the the C_{3v} point group and space group R3c. Their unit cell is either described in the rhombohedral unit cell as shown in Fig. 2.1. It is the primitive unit cell and contains two formula units. The small number of atoms per unit cell make it often applied in DFT calculations [70]. Its character as a primitive cell also does not reproduce extra phonons at the Γ-point. As a rhombohedral cell, it does however not conserve the full symmetry of the crystal. Therefore and for demonstrative purposes it is useful to take a look at the hexagonal unit cell in Fig. 2.2. Here, it can be seen lithium niobate is build up by hexagonal layers of oxygen atoms, which are oriented orthogonally to the optical axis *c*. Viewed from the side the oxygen layers form octahedrons, where two opposing sides are part of the oxygen layers. This forms octahedral-coordinated interstitials along the *c*-axis. In this interstitials the Nb^{5+} and Li^{+} ions reside. In the ferroelectric phase, the ions are stacked in these vacancies in the following way: after a Nb-ion follows a vacancy followed by a Li atom. The spontaneous polarization in ferroelectric lithium niobate originates from slight displacements of the Nb^{5+} and Li^{+} ions with respect to their symmetric positions in the O^{2-}-layers as shown in Fig. 2.2. This leads to an effective dipole moment along the c-direction. At the ferroelectric-paraelectric phase transition, the crystal structure changes to the $R\bar{3}c$. Here, the Nb^{5+} ion moves to the symmetrical center of an octahedron, whereas the Li^{+} moves to the (at least on average) center of an oxygen plane as shown in Fig. 2.2. During ferroelectric polarity reversion, it is generally believed, that the Nb^{5+} ion moves inside the octahedron, while the Li^{+} ion is pushed through the oxygen plane. This seems reasonable due to the much smaller ionic radius of the Li^{+} ion compared to Nb^{5+}. As seen in Fig. 2.3 the hexagonal crystals structure features three equivalent x-axes and three equivalent y-axes, which represent planes of symmetry.

The commonly accepted hexagonal lattice parameters for congruent $LiNbO_3$ and $LiTaO_3$ [76–79, 69] are given by $a_{LT} = 5.1543$ Å, $c_{LT} = 13.7835$ Å, $a_{LN} = 5.1483$ Å and $c_{LN} = 13.8631$ Å.

$LiNbO_3$ and $LiTaO_3$ can be grown by the standard Czochralski method from melts of Li_2O and Nb_2O_5 or Nb_2O_5, respectively. The phase diagram for the case of Li_2O-Nb_2O_5 melt is given in Fig. 2.4. The diagram shows the lithium stoichiometry in the melt versus the melt temperature. Here, it can be seen that $LiNbO_3$ crystals can be only obtained in a narrow range of LiO_2 concentration given in mol% ($[Li_2O]/[Li_2O+Nb_2O_5]$)

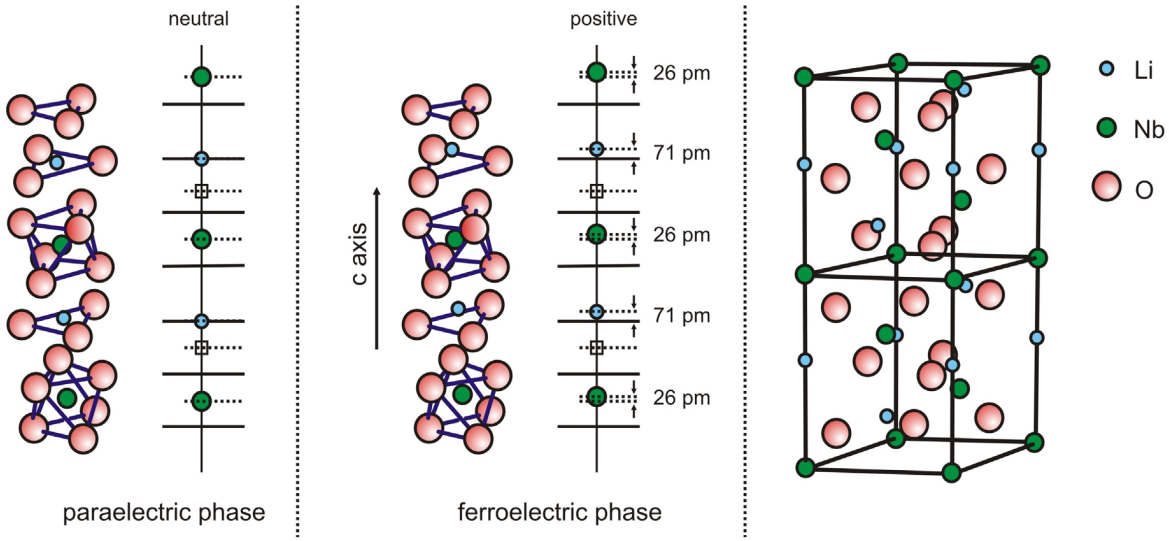

Fig. 2.2 From left to right: ionic positions in lithium niobate in the paralectric, ferroelectric phase and hexagonal unit cell [74, 75].

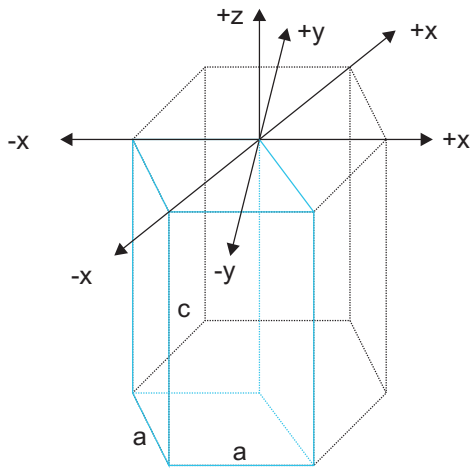

Fig. 2.3 Symmetry axis and planes of a general hexagonal unit cell. Here, three equivalent x and y-axes can be identified, respectively.

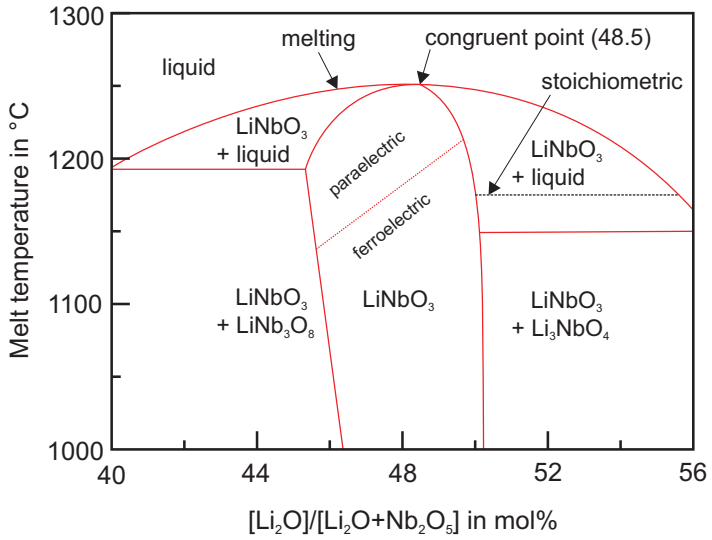

Fig. 2.4 Phase diagram of Li_2O-Nb_2O_5 melt system [56, 81].

between approximately 46 mol% and 50.5 mol%. For lithium rich melt concentrations $>$ 50.5 mol% a phase separation to $LiNbO_3$ and Li_3NbO_4 crystals takes place, while for Li poor melts, mixed phases of $LiNbO_3$ and $LiNb_3O_8$ appear. Most crystal growth in the $LiNbO_3$ system is performed at the congruent point, where the melt composition (liquid phase) matches the crystal composition. This enables to grow large boules with a homogeneous composition over the complete crystal, as crystal pulling does not change the composition in the melt. Here, commercially grown wafers in optical quality between 3 to 6 inch are available[2]. However, the congruent growth comes with a major drawback, because the crystals are not stoichiometric $LiNbO_3$, but suffer from a lithium deficiency. For lithium niobate the congruent point is at approximately 48.5 mol% or lithium, while being slightly better in $LiTaO_3$, where values up to 49 mol% are reported [80–82]. In principle, stoichiometric crystals can be grown from a melt, as indicated by the dashed line on the Li rich side in Fig. 2.4. This however comes with different Li composition in the crystal and the melt. Therefore, during growth, the composition in the melt will slowly vary leading to a variable composition along the growth axis of a crystal.

To obtain stoichiometric and near-stoichiometric crystals, several method have been invented [56]. The first is called Vapor Transport Equilibration (VTE). Here, conventionally grown, i.e. congruent, crystal wafers of 1 to 3 mm thickness are placed together with Li containing powder in a Pt crucible and heated above 1000°C for several days. Here, the Li vapor will diffuse into the crystal leading to more stoichiometric crystals [83–85]. The growth of stoichiometric crystals directly from the melt is possible with two methods. The first method uses melts with the addition of more than 10 mol% of K_2O, which improves the Li stoichiometry of lithium niobate by changing the growth conditions and phase diagram, while potassium itself is not found to be included in the crystals itself in any large quantity [86, 87]. The second method is the a double crucible Czochralski (DCCZ) technique developed by Kitamura *et. al*. Here, the crystals are grown from Li rich melt in an inner crucible, which is connected to an outer crucible, which is constantly and slowly supplied by Li_2O powder. This enables a constant resupply of the growing Li deficiency in the inner crucible, enabling the growth of near stoichiometric crystals with no significant composition variation over the boule [88]. More recently, epitaxial growth, usual liquid phase epitaxy, of lithium niobate thin films plays an increasingly important role, not only in RF electronics [89], but also for optical applications [57].

[2]Precision Micro-Optics Inc., MA, USA

2.1.2 Intrinsic and extrinsic defects in $LiNbO_3$ and $LiTaO_3$

Due to the easy growth conditions and therefore lower price, the majority of supplied $LiNbO_3$ and $LiTaO_3$ is congruent material. In this context, in particular the lithium deficiency is the source behind most intrinsic defects in this material system. As these defects are responsible for many of the (unusual) properties of lithium niobate, it is therefore useful to review the properties, mechanisms and influences of these defects. The following pages should give the reader a concise overview about the manifold type of defects in this material class, whereas for a more detailed analysis about the properties, the many specialized reviews and sources should be concerned, e.g. Refs. [54, 90, 91, 22, 92].

As we have seen before, the predominant reason for intrinsic defects in (congruent) $LiNbO_3$ and $LiTaO_3$ is the lithium deficiency, which needs to be compensated. Here, in the literature three models are usually discussed, the *oxygen vacancy model*, the *niobium vacancy model* and the *lithium vacancy model*. In the first and most simple model, the lithium vacancies (V_{Li}^{-1}) are charge compensated by oxygen vacancies (V_O^{+2}). This *oxygen vacancy model* is reasonable, because oxygen vacancies are a typical observation for many complex oxides [56]. For the case of lithium niobate, this would mean that two V_{Li}^{-1} are compensated by one V_O^{+2}. However, experimental observation shows that oxygen vacancies are almost not present in $LiNbO_3$, which is also confirmed by theory [93–95]. For example it is observed that the density of $LiNbO_3$ even increases with increasing lithium deficiency [96]. This suggest an involvement of the Nb atom, which occupies the lithium sites (Nb_{Li}^{4+}). Indeed, experimental results show Nb antisites to be a predominant intrinsic defect [93–95]. This anti site then itself needs to be charge compensated giving rise to two fundamentally different models. The first is the *Nb-vacancy model*. Here, four Nb_{Li}^{4+} are compensated by five V_{Nb}^{5+}. The second model is the *lithium vacancy model*. Here, one Nb_{Li}^{4+} anti site can compensate for four V_{Li}^{-1}. DFT Analysis of single point defects suggest that the Li vacancy is more stable, than the Nb vancancy [97–99], however more recent analysis suggest that the various defects, Nb V_{Nb}^{5+}, V_{Li}^{-1} and Nb_{Li}^{4+}, do coexist under certain conditions [100]. However, the charge compensation here will result in the formation of defect clusters, which are more energetically favorable than randomly placed, single point defects. And defect clusters have been found to be particular stable for the *lithium vacancy model*, because here the defects can be placed much closer [101]. An example for such a defect complex proposed by Kim *et. al.*[102]. In this context, several theoretical studies were performed to analyze defect complexes [101, 103, 98].

These defect clusters are only formed upon slow cooling of single domain crystal and are virtually stable at room temperature, even in a frustrated state. Here, the main mechanism of building and reorganization is the diffusion of Li^+ atoms and hence the reorganization of Li vacancies, which has activation energies of 0.6-0.7 eV range [104, 105]. An exponential increase in Li mobility is observed above 150°C, where the defect clusters start to be destroyed and randomly oriented point defects start to dominate and no three dimensional correlation is anymore observed.

An idealized picture as proposed by Kim *et. al.* of such an (Nb_{Li}^{4+} - $4\times V_{Li}^{-1}$) and its orientation of polarization with respect to the crystal main axis is displayed in Fig. 2.5b) [102, 54]. Here, Fig. 2.5a) shows parts of a unit cell of an ideal, stoichiometric crystal, while b)-c) shows two possible orientations of the defect polarization before and after domain reversal (Switching of the spontaneous polarization). After annealing the complex in c) will reorient to a state similar to b), where the defect polarization has reoriented parallel to the spontaneous polarization. This picture should only be seen as an idealized version. Real defect clusters may have sizes larger tthan displayed here. X-ray data suggest sizes of ≈ 11.4 Å, which is more than four cation sites. Furthermore, while DFT theory indeed suggests, that a defect cluster is energetically more favorable and hence more stable, than randomly oriented defects, theory also suggest, that the intuitively suggested structure

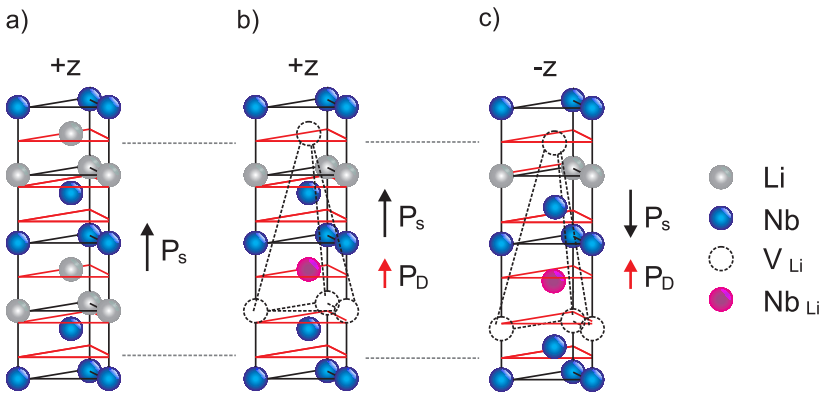

Fig. 2.5 Proposed structure of a defect complex in the niobium vacancy model. a) Stoichiometric crystal structure. b) Defect complex in grown material. c) Defect complex after polarization switching, where the defect polarization has not yet switched (after [102, 54]).

by Kim et al. is *not* the energetically most favorable [103, 101]. Here, for example a positioning of the $V^{-}1_{Li}$ vacancies on nearest neighbors sites to the Nb_{Li}^{4+} antisite appears more favorable [103, 101]. Some of the more stable defect clusters do not preserve the C_3 anymore giving rise to an off axis polarization component [101], which may be of particular importance around domain walls [53].

In contrast to this intrinsic defects, many extrinsic defects are known as well. Among those, the transition-metal-point-defects are almost omnipresent in the $LiNbO_3$ system, i.e. Fe, Mn, Cu, Cr and many more [56, 106]. In this context, the iron defect, appearing as either Fe^{2+} or Fe^{3+}, is one of the most important one, because it is one of the major sources behind the fairly strong photorefraction in the $LiNbO_3$ system [107]. Photorefraction is the name for a multi-step process leading to a change in refractive index and absorption by (high intensity) light illumination. Here, electrons from donor centers are excited via (one or multiple photon absorption) into the conduction band. These, electrons then can freely diffuse until they recombine or are bound at acceptor centers forming polarons. The bound electrons at acceptor sites will lead to absorption lines in the visible and near infrared limiting the performance of devices [92, 108]. If the illumination is inhomogeneous, e.g. light being guided in waveguides, the electrons will be trapped outside of the bright areas leading to a net space charge. This space charge will result in a static electric field in the crystal, which will lead to a change in refractive index via the electro-optical effect. The generated space charge patterns are stable at room temperature and can be erased by annealing [67]. In this context, Fe^{3+} represents a particular strong and stable acceptor leading to the formation of Fe^{2+} bound polarons. In congruent material, the Nb_{Li}^{4+} is also a particular good acceptor, knowing to form Nb_{Li}^{5+} polarons. Consequently, to reduce photorefraction (and the respective power damage thresholds) many research was directed to either improve the stoichiometry directly by growing stoichiometric crystals or finding appropriate dopants. In practical application, the photorefractive effect can be used to create erasable (by temperature), holographic data storages in lithium niobate, or for nanoparticle patterning on surfaces. In this context, iron doped crystals are used to enhance the photorefraction [67, 109].

Waveguides in lithium niobate have been fabricated with many different methods. Here, prominent methods include doping/exchange with foreign atoms, e.g. Ni, Ti or MgO indiffusion or reverse proton exchange [110, 107, 111–113], etching ridge waveguide [114, 115], creating high index barriers by ion irradiation [116, 117] or laser damage [118, 45, 27, 30]. More, recently ion slicing, sometimes referred to as "Smart cut", allows to create thin film lithium niobate on foreign substrates, e.g. SiO_2, so called lithium niobate on insulator with intrinsic waveguiding properties [119–121]. In the context of waveguides fabricated by doping,

in particular Ti in-diffusion is one of the standard methods, because it leads to an increase of the refractive index for both polarizations allowing to fabricate TE and TM guiding waveguides, which is in contrast to other dopants, which often only increase the refractive index for one polarization [110, 107, 111–113]. For Ti-waveguide low losses down to 0.05 db/cm have been achieved in a combined Ti-indiffused ridge waveguide [122]. As many properties also the diffusion is a function of stoichiometry, where the titanium diffusivity decreases with increasing stoichiometry [112], which suggests that the titanium preferentially occupies Li sites (Ti_{Li}^{4+}), which are less populated in congruent material [123]. Recent theoretical work suggests that the actual refractive index increase for both polarizations is not explained by changed electronic properties introduced by the Ti^{4+} ion, but mainly by strain due to the larger size of the Ti ion occupying a Li lattice site [123]. Apart from the titanium atom on a lithium site (Ti_{Li}^{4+}), also the defect of Ti on Nb sites (Ti_{Nb}^{3+}) is known. This defect leads to optical absorption by electronic states within the band gap, but can be prohibited by the appropriate fabrication. Despite the advantageous features, the Ti^{4+} defect also has undesirable side effects. Here, a particular issue is that Ti^{4+} ions have been observed to stabilize the iron defect in the Fe^{2+} state, which is one of the main origins behind the photorefraction in $LiNbO_3$. This leads to a significant decrease in the optical damage resistance inside Ti-indiffused waveguides [124, 125].

The photo-refraction in congruent crystals can be influenced by doping, which is easier to fabricate, than directly growing stoichiometric material. In this context, many doping materials have been studied, such as Mg, Zn, In or Sc [126–131]. Here, the main mechanism leads to an improved stoichiometry, as the integration of external defects improves the stoichiometry by reducing the number of intrinsic defects, i.e. Nb_{Li} antisites and Li_{Vi} vacancies. In this context, MgO is one of the more prominent doping materials. Here, MgO doped congruent LN (MgO:$LiNbO_3$) with typical doping concentrations from 2 to 7 mol% MgO are available from many commercial suppliers. Due to the improved stoichiometry, the coercive field for MgO:$LiNbO_3$ is lower compared to the undoped material and closer to the coercive fields of stoichiometric material [132]. However, doping also influences nonlinear and electro-optical properties, as well as linear optical properties, i.e. refractive index and birefringence, which may be disadvantageous depending on the desired application.

$LiNbO_3$ crystals grown under normal atmosphere suffer from the incorporation of hydroxyl OH^- structures in the crystals. Here, alike to other properties the hydroxyl absorption band in the 3500 cm^{-1} range is known to be heavily influenced by the crystal stoichiometry [133–135]. It is also associated with the origin of internal electric fields by some authors, as this defect heavily depends on the stoichiometry [104].

The Nb_{Li} and Li_{Vi} defects and defect complexes are associated with an internal electric field, additional to the spontaneous polarization. This has two major effects. First, the electric field required for domain inversion depends heavily on stoichiometry. Here, for congruent $LiNbO_3$ coercive fields up to 21 kV/mm are required, while this is reduced to 7 kV/mm in near stoichiometric material [136]. Some sources state even fields down to 0.2 kV/mm for highly stoichiometric crystals [137]. Similar has been observed for $LiTaO_3$, where the electric field strength in congruent material is observed to be in the 20 kV/mm range, while this is reduced to 1.7 kV/mm in near stoichiometric $LiTaO_3$ [138].

While the stated electric fields are enough to reverse the spontaneous polarization of the crystals, this is often not enough to reverse the internal electric fields of the defect complexes leading to frustrated defects. This leads to a shifted hysteresis curve with respect to the electric field [104, 102]. Here, in as-grown (or virgin domains) a higher electrical field is required for reversal, compared to switched domains. This is due to the stable orientation of the defect complexes. In this regard, for example in congruent lithium tantalate a field of $E_f = 20$ kV/mm is required to switch a virgin domain ("forward poling")), while for reverse poling a field of only $E_r = 12$ kV/mm is required [138]. Similar values are observed for congruent $LiNbO_3$ with $E_f = 21$

kV/mm and $E_r = 17$ kV/mm [139]. The difference between E_r and E_f almost vanishes in stoichiometric material [54]. The magnitude of the internal field $E_{Internal}$ is then given by the simple equation

$$E_{Internal} = \frac{E_f - E_r}{2}. \tag{2.1}$$

This suggests, that as-grown domains are more stable, than switched domains. High temperature annealing > 150 °C enhances the mobility of the Li vacancies, which leads to a gradual reversing of the additional defect polarization by the rearranging of the defect complex. This significantly enhances the stability of the domains. Here, the activation energies for the Li vacancy mobility are determined in the 0.6-0.7 eV range [104, 105].

In a completely different context, $LiNbO_3$ and $LiNbO_3$ have been successfully doped with rare earth atoms, e.g. Erbium, for fabrication of (optically pumped) integrated structures, i.e. lasers or amplifiers [140, 58, 141], or quantum memories [142]. For spectroscopic analysis, these rare-earth atoms also can be used as a probe ("designer defect") for internal field strength by the investigation of spectroscopic line shifts [143, 50]. Here, internal fields, which also change towards domain walls, in the order of several kV/mm have been observed. Here, the electric field around a domain wall for an unannealed sample is composed of a short range (4 μm) component of 5 kV/mm and a long range component (22 μm) of up to 11.5 kV/mm difference between poled and grown domains. Part of these fields disappear after annealing, suggesting a connection to the frustrated defects mentioned above [144].

2.2 $KTiOPO_4$-family

An alternative to $LiNbO_3$ in integrated optics is potassium titanyl phosphate $KTiOPO_4$. $KTiOPO_4$ was first introduced as a nonlinear optical material in 1976 by Zumsteg et. al. [145]. This material class offers a large transparency window typically from 0.35 μm up to 4.5 μm for some members of the family [146]. The nonlinear and electro-optical properties are comparable to other materials, such as $LiNbO_3$ [147]. But $KTiOPO_4$ combines this with a generally higher laser damager threshold - up to three orders of magnitude larger than $LiNbO_3$ and four orders compared to KDP [148]. In particular, one of the major drawbacks for the use of lithium niobate in integrated optics is the effect of photorefractivity [128, 149, 129], which is considerably smaller in $KTiOPO_4$ enabling two orders of magnitude larger power densities compared to $LiNbO_3$ [150]. However $KTiOPO_4$ comes with its own technological challenges, which result from is crystal structure and material properties, which will be discussed in this chapter.

$KTiOPO_4$ belongs to a large material family with isomorphic crystal structure and similar properties. The generalized compound formula is given by $MYOXO_4$. Here, M can stand for H, Li, K, Rb, Na, Cs, Tl and/or NH_4, while for Y Ti, Ge, V, Sn, Zr, Fe, Ga, Nb, Mg and/or Mn can be introduced and X can be P, Si, Ge and/or As. Many of these compounds have been synthesized in pure, aswell as in mixed crystal form [151–161]. At room temperature most of these materials belong to the non-centrosymmetric space group $Pna2_1$ and therefore they exhibit piezoelectric and ferroelectric properties. The unit cell of $KTiOPO_4$ contains eight formular units (64 atoms) compared to 10 atoms in the unit cell of $LiNbO_3$. The orthorhombic parameters for a few selected compounds are summarized in Tab. 2.1. Here, the influenced of the growing ionic radii can be directly seen, as $KTiOPO_4$ has the smallest and $KTiOAsO_4$ the largest unit cell.

Curie temperatures are observed over a large temperature range in these compounds. Here, $TlSbOGeO_4$ exhibits the phase transition at 272 K [159], while $KTiOPO_4$ switches to the para-electric phase (space group *Pnna*) around 1218 K [162, 163]. Although even for $KTiOPO_4$ curie temperatures as low as 1156 K have been observed [164], which is shown to be heavily dependent for example on the composition and exact growth

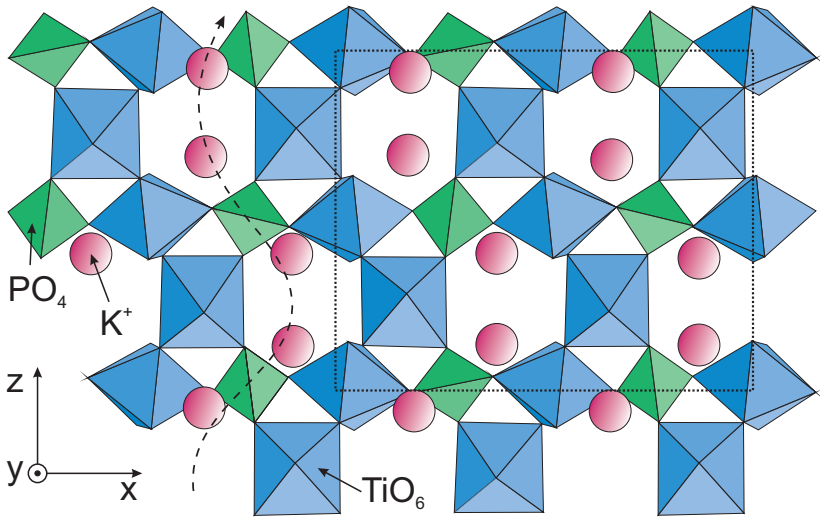

Fig. 2.6 Sketch of the principal crystal of the ferroelectric phase of $KTiOPO_4$. The crystal is built up by chains of TiO_6 octahedrons, which are linked by PO_4 tetrahedrons. In between this lattice of polyhedrons large spacings exists, where the potassium ions K^+ are sited. The potassium ions are weakly bound and can easily be moved in a hopping motion along vacant K^+ sites along the z-axis, which is responsible for the large observed ionic conductivity in z-direction. The dotted box gives an estimate for the size of the unit cell and contains eight formula units.

Table 2.1 Orthorhombic lattice parameters a, b, c of $KTiOPO_4$, $RbTiOPO_4$, $KTiOAsO_4$ grown from a tungstate flux (W), and $KTiOAsO_4$ grown from a arsenate flux (A).

	$KTiOAsO_4$(W)	$KTiOAsO_4$(A)	$RbTiOPO_4$	$KTiOPO_4$	
Source	[157]	[157]	[154]	[159]	[154]
a/ Å	13.138	13.130	12.974	12.814	12.819
b/ Å	6.582	6.581	6.494	6.404	6.399
c/ Å	10.787	10.781	10.564	10616	10.584

conditions [165]. This already hints, that the exact properties of this crystal are very susceptible to defects and slight variations in composition, which is related to the complex crystal structure [166].

The principal crystal structure for the example of $KTiOPO_4$ is sketched in Fig. 2.6. In this simple picture the crystal is built up by chains of TiO_6 octahedrons, which are separated by PO_4 tetrahedrons. One very particular feature of the crystal structure are exceptionally short Ti-O bonds observed along the z-axis. In detail, There are alternating short and long Ti-O bonds reported, which are directly involved in building the chained TiO_6 octahedron. These have length of 1.72–1.74 Åfor the short bond and 2.0–2.1 Åfor the long bond. While the four bonds, which are not involved in building the chains have a medium length of 1.95 to 2.07 Å[159]. The high polarizability of the short Ti-O bond was believed to be one main contributor to the exceptional nonlinear properties [167], although some recent studies show a contribution of the K-O bonds [168], as well as the P tetrahedrons [169]. However, this further depends on the exact composition and hence on the family member [166].

In between the tetrahedrons and octahedrons, the potassium ions K^+ are located in cavities on two high coordination sites, commonly referred as K(1) and K(2). They are coordinated by eight or nine oxygen atoms, respectively. The K^+ ions are only weakly bound to their sites. If K-vacancies are present, which is usually the case, K^+ ions have a high mobility, which is indicated by the dashed line. The movement is understood as

a hopping type of motion from vacancy to vacancy. The activation energy for hopping at room temperature is on the order of 0.3 eV [170]. Therefore, a high ionic conductivity is observed, which is several orders of magnitude larger along the z-axis, than in the x- or y- directions. At low temperature, the ionic conductivity can be suppressed by five orders of magnitude, which may simplify poling processes (10^{-7} Ω^{-1} cm^{-1} at 300 K vs 10^{-12} Ω^{-1} cm^{-1} at 170 K) [171]. From the view point of fabricating periodically poled crystals this ionic conductivity presents a challenge [172], as the successful domain reversal cannot be monitored by the poling current, which usually is several orders of magnitudes smaller than the ionic current and depending on pulse length will not be detectable. Therefore, optical methods have been developed to monitor the successful domain reversal in situ [173, 174]. However, the high mobility of the K^+ ion in z-direction also allows to easily fabricate highly confining waveguides via ion exchange, e.g. by exchanging K^+ for Rb^+, effectively fabricate $Rb_{1-x}K_xTiOPO_4$ mixed crystals embedded in $KTiOPO_4$ [175, 176]. Due to the high ionic conductivity, the exchange mainly is limited to the z-direction, which allows for controllable waveguide fabrication in x-y-direction. In this context, previous work suggest that the larger Rb^+ ions prefer the K(2) site in $Rb_{1-x}K_xTiOPO_4$ mixed crystals [177], because the K(1) site is about 25% smaller compared to K(2) [178].

The type of the phase transition is believed to be of mixed order-disorder and displacive nature [179, 161, 166], somewhat comparable to $LiNbO_3$ [180, 181]. One main contributor to the spontaneous polarization in the ferroelectric phase is the alternating short and long Ti-O bonds along the z-axis. Here, the Ti is continuously displaced from its symmetrical, central position in the octahedron below the Curie temperature [159]. The order-disorder part of the phase transition is presented by the K^+ ion. Below the Curie temperature, it is observed that the K^+ ion can occupy two alternative sites, commonly referred as K(1)s and K(2)s. Depending on the temperature the K^+ ion is distributed between those sites, leading to an order-disorder type transitions. At the ferroelectric-paraelectric phase transition, the four sites K(1), K(2), K(1)s and K(2)s become a group of four sites, two K(1) and two K(2), each [161].

The growth of $KTiOPO_4$ crystals is quite challenging, because these crystal cannot be grown from melt like $LiNbO_3$. The reason for this is that $KTiOPO_4$ decomposes into different components before melting and hence it is not possible to create a congruent melt [160]. Instead this crystals are grown from solutions, which is more demanding in terms. There are two main methods, which are usually employed - the anhydrous flux method and the hydrothermal growth method. In the flux method the crystals are grown from a waterless $KTiOPO_4$/flux solutions made of halides, phosphates, arsenates and/or tungstates in the respective composition at elevated temperatures of 700 to 1000 °C. Growth and crystallization takes place under atmospheric pressure. When the flux is slowly cooled down crystallization begins, which can be spontaneous and by the help of a seed crystal. The process is slow and - depending on the desired crystal size - can take from two weeks to several month. As crystallization happens close to the curie temperature, single domain crystals are not always achieved. The hydrothermal growth happens under high pressure ($2 \cdot 10^8$ Pa) in an inert gold or platinum tube, which can withstand the high pressure and corrosive solvents. Between the tube-ends a temperature gradient is established (typically 550°C on the cold and 600°C on the hot side) and a crystal seed is placed on the colder side, where the crystallization takes place. Typical growth times are also between weeks and several month. Hydrothermal growth in general yields crystals of higher quality with less defects, however the technology and time required makes the growth of large crystals difficult and hence, more expensive.

As certainly in most materials, defects influence and define the material properties, which is also the case for the $KTiOPO_4$-family. In general all members of the $MTiOPO_4$ are never entirely stoichiometric [31, 182] and in particular show a non-stoichiometry of M atoms, which is the main reason behind the high ionic conductivity. This is somewhat similar to the Li vacancies observed in congruent $LiNbO_3$. In this context, in $KTiOPO_4$ K^+

vacancies with concentrations up to 500 to 800 ppm have been estimated from observed ionic conductivities [183]. This stoichiometry can be described by a chemical formula of the form

$$K_{1-x}TiOPO_{4(1-x/8)} + \frac{x}{2}K_2O. \tag{2.2}$$

The K^+ vacancies need to be charge compensated, where two mechanisms are observed. Here, positively charged oxygen vacancies are proposed [183, 184], as well as trapped holes at the oxygen atom bridging two titanium atoms (Ti-O-Ti) [185]. The latter describes a form a bound polaron and is also suspected to be one of the mechanisms behind laser damage in $KTiOPO_4$, usually referred as *gray track formation*.

Chapter 3

Methods

This chapter provides the reader with the necessary background to understand the used methods. The first section deals with the basic theory of the Raman effect in a classical, as well as quantum mechanical picture. Raman spectroscopy is the main method used for investigation in this work and therefore is discussed in detail. The second part provides a basic overview over the experimental setups. The chapter closes with several examples for applications of Raman spectroscopy and second harmonic microscopy. Here, a model for the depth correction in microscopy in highly refracting media is investigated experimentally.

3.1 Introduction to Raman spectroscopy

The Raman effect describes the inelastic scattering of light with low energy excitations in molecules or solids, such as vibrational states. As these vibrational properties are deeply influenced by the material properties, analyzing the scattered light offers a way to probe material properties on a deep level. Raman spectroscopy is one of the foremost and widespread methods to study molecular, as well as solid state systems [186, 187]. The strong sensitivity of the vibrational properties to changes in structure and stoichiometry allows to study a wide range of effects. Examples for the applications of Raman spectroscopy range from the study of defects, over the identification of materials, analysis of phase transitions and magnetic properties to the determination of charge carrier densities.

In a simple picture the Raman effect is the inelastic scattering of a photon with a quasi-particle or low-energy excitation in a molecule or solid, such as a phonon. The photon typically carries an energy two or three order of magnitude larger than the phonon. Optical photons carry energies in the 1 to 4 eV range, while zone-center phonons in most solid states have energies of 10 to 100 meV. A two-level low energy excitation is shown in Fig. 3.1a) labeled as $\langle n_0|$ and $\langle n_1|$. The energy difference between these levels is given by $E_1 - E_0 = \hbar\Omega_n$ and $\langle n_1|$E. This energy levels represents any two energy levels of a quantum mechanical harmonic oscillator. If a photon $\hbar\omega_i$ with an energy larger than the direct transition is incident to this two level system, three processes can happen. The first is elastic scattering. Here, in a simple quantum mechanical picture the phonon or vibration is lifted to a short-lived virtual state $\langle n_V|$ (a vacuum state), from which it almost immediately relaxes to the original state by sending out a photon with the same energy $\hbar\omega_i$. The only thing, which may has changed is the direction. This process is known as Rayleigh scattering. In contrast to this, in the inelastic processes an energy transfer will happen. Again, the incident photon is absorbed, which leads to an excited virtual state, which will quickly decay to $\langle n_0|$ or $\langle n_1|$. Two processes are now possible. In the first process, the low energy excitation

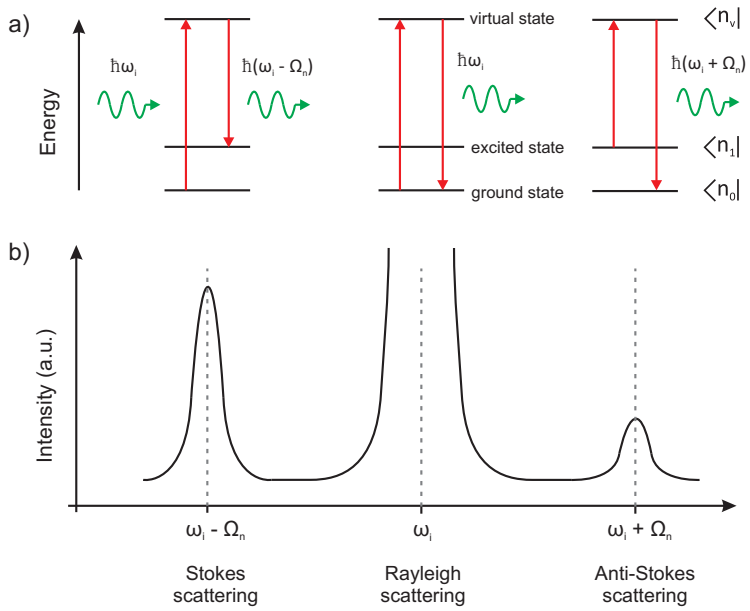

Fig. 3.1 a) Principle sketch showing the excitation paths for the three processes associated with the Raman effect. b) General Raman spectrum showing the position of the Stokes and Anti-Stokes line with respect the Rayleigh line.

can end up in a state higher, then the original process. Then the photon has transferred energy by creating a vibration or phonon. A scattered photon $\hbar(\omega_i - \Omega_n)$ with less energy is emitted. This process is called Stokes scattering. The opposite process can happen, if the vibration or phonon is already in a excited state. Then the vibration is annihilated and a new photon $\hbar(\omega_i + \Omega_n)$ with higher energy is emitted. This is called Anti-Stokes scattering. Stokes and Anti-Stokes scattering form the (spontaneous) Raman effect. The energy of the scattered photon $\hbar\omega_s$ than can be described by

$$\hbar\omega_s = \hbar\omega_i \pm \hbar\Omega \tag{3.1}$$

A typical Raman spectrum is shown in Fig. 3.1b). It consists of a strong elastically scattered Rayleigh peak at the frequency of the incident Radiation with weak, frequency-shifted side bands on both sides of the Rayleigh line. The value of the frequency shift of the side bands is usually independent of the frequency of the incident radiation. The side bands are characteristic for the molecules or solids interacting with the incident radiation and therefore immediately allow an identification of the material via their vibrational fingerprint. One word should be given about the intensity. Compared to the Rayleigh scattering, the Raman effect is a very weak effect. Typically, the intensity of the Stokes and Anti-Stokes peaks are 6 to 10 orders of magnitude weaker than the Rayleigh peak, which immediately explains the necessity of spectral filtering of the Rayleigh signal [188].

Besides energy conservations, also momentum conservation applies. It holds

$$k_s = k_i \pm q, \tag{3.2}$$

where k_s and k_i are the momenta of the photon after and before the process and q is a momentum associated with the vibration. Because phonons have no rest mass, the momentum difference is very small. In the case of

molecule scattering this momentum is believed to be carried by the complete molecule, because the molecular vibrations have no dispersion relations. Momentum conservations, however is very important for crystals, where the scatterers are phonons, magnons or plasmons. Each of these quasi-particle has a distinct dispersion relation. Because the momentum change of the photon is very small, this means that usually only quasi-particles with $q \approx 0$ take part in scattering, i.e. zone center phonons. Scattering with phonons from the rest of the Brillouin zone is usually not possible. That only zone center phonons can take part in scattering also has the interesting consequence that the propagation direction of phonons can be distinguished. For polar crystals this means that longitudinal optical (LO) and transversal optical (TO) phonons can be distinguished based on scattering geometries.

The Raman effect is named for Indian physicist Chandrasekhar Venkata Raman, who is credited with discovering the effect and who also was awarded the Nobel Prize in 1930 for his study of the effect [189]. Although C.V. Raman is credited with discovering the effect, many more scientist have been involved. The history of the Raman effect begins in the 1920s, where a first theoretical description of inelastic light scattering was developed by Adolf Smekal in 1923 [190] and refined by Kramers and Heisenberg in 1925 [191]. Inelastic scattering with optical radiation was discovered by Landsberg and Mandelstam on solid quartz in 1928 [192] independently from Raman, who studied the effect from 1925 on more than 50 different fluids and molecules [189]. C.V. Raman published his results independently from Landsberg and Mandelstam in 1928 [193, 18]. Due to this multi-discovery the effect sometimes was referred to as Smekal-Raman-effect [194], Smekal-Raman-Mandelstam-effect or more neutral "combination scattering", which was also the name C. V. Raman preferred [189]. Nevertheless, due to the Nobel prize and C.V. Raman extensive work on the effect, this physical effect is almost exclusively connected to has name. Already in 1928 more than 16 papers have been published on the topic - most of them by Raman and his colleagues - and a conference was organized in London in 1929 dedicated to this new effect [189]. In the time of its discovery, the Raman effect and the discovery of inelastic scattering was an important experimental puzzle piece towards quantum mechanics [195], because the effect is best explained with quantized photons and other quantized (quasi-)particles and excitations. The Raman effect is a very weak effect, which nowadays can fairly easily be studied due to the availability of highly intense monochromatic light sources in the form of lasers. Only the invention of the first Lasers in the sixties provided the necessary power, which enabled Raman spectroscopy to become one of the standard methods in solid state physics and chemistry. In contrast to this, Raman and his colleagues made use of either with collimated sunlight using a 7 inch telescope [193] or very strong mercury arc lamps [189] in their first attempts to study the effect. Raman often used the adaptability of his naked eye to identify and find the lines, before using photographic film. Nevertheless, often several hour long exposure time on photographic films were necessary to identify the weak side bands [192].

3.1.1 Classical approach

So far, we have discussed the Raman effect in a phenomenological manner. To treat the Raman effect more strictly, i.e. to make predictions of intensities and Raman selection rules, we consider a molecule as depicted in Fig. 3.2 with Q vibrational degrees of freedom. The molecule is irradiated by an electromagnetic wave in the visible or IR wavelength range. Here, we can assume a wavelength much larger than the usual molecule size. Therefore, we can describe the field as a stationary oscillating electric field of the form $E(t) = E_0 \cos(\omega t)$. The oscillating field induces an oscillating dipole moment μ in the molecule depending on the polarizability $\alpha_i j$ of the molecule

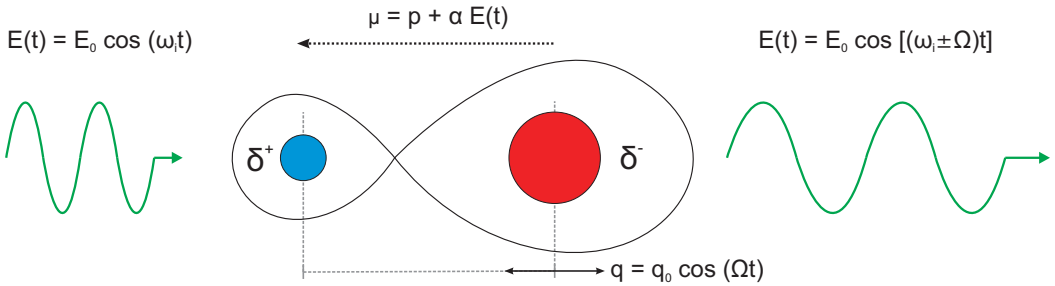

Fig. 3.2 Principle of light scattering by a molecule.

$$\mu = \alpha_{ij} E(t). \tag{3.3}$$

The polarizability $\alpha_i j$ is a second order tensor reflecting the symmetry of the molecule. Further, a molecule may have a permanent dipole moment p, which results in a total dipole moment of

$$\mu = p + \alpha E(t). \tag{3.4}$$

The polarizability and the dipole moment are a function of the nuclei and electronic coordinates. If we assume no electronic resonance at the frequency ω, we can assume the displacements involved to be small. Therefore, we can expand both, the polarizability and dipole moment, in terms of the normal coordinates q_n of the n-th nucleus at its equilibrium position q_0

$$p = p_0 + \sum_n^Q \left(\frac{\partial p}{\partial q_n}\right)_{q=q_0} q + \cdots \tag{3.5}$$

$$\alpha_{ij} = \alpha_{ij,0} + \sum_n^Q \left(\frac{\partial \alpha_{ij}}{\partial q_n}\right)_{q=q_0} q + \cdots \tag{3.6}$$

Here, the sum runs over all normal modes n. As mentioned in the previous chapter, the Raman effect is an inelastic scattering process of photons with molecular vibrations, for example. For small amplitudes a molecular vibration can be described as a harmonic oscillation with the frequency Ω_n of the nucleus around its equilibrium position, which can be written as

$$q = q_0 \cos(\Omega_n t). \tag{3.7}$$

If we now insert Equ. 3.6 and 3.7 in Equ. 3.4 and make use of the trigonometric identity for multiplied cosine functions, we obtain:

$$\begin{aligned} \mu(t) = \quad & p_o + \textstyle\sum_n^Q \left(\frac{\partial p}{\partial q_n}\right)_{q=q_0} q_0 \cos(\Omega_n t) + \alpha_{ij,0} E_0 \cos(\omega t) \\ & + \tfrac{E_0 q_0}{2} \textstyle\sum_n^Q \left(\frac{\partial \alpha_{ij}}{\partial q_n}\right)_{q=q_0} \left[\cos((\omega - \Omega_n)t) + \cos((\omega + \Omega_n)t)\right]. \end{aligned} \tag{3.8}$$

This easily obtained equation now allows us to explain several effects related to molecular scattering [196]. In electrodynamics any oscillating dipole moment $\mu(t)$ will itself emit radiation of the same frequency. The first term p_0 just refers to the permanent dipole moment of the molecule. The second term is associated with IR

activity of a molecule. Here, a molecule can emit or absorb radiation of the vibrational frequency Ω_n, if this vibration is associated with a change in dipole moment $\frac{\partial p}{\partial q_n} \neq 0$. Vibrational modes satisfying this relation will be called infrared-active (IR-active) due to the frequency range of normal vibrational modes, which typically is in the electromagnetic infrared regime. The next term $\alpha_{ij,0} E_0 \cos(\omega t)$ describes the so called Rayleigh scattering (named after Lord Rayleigh). Here, the molecule emits an electromagnetic wave at the incident frequency proportional to the constant polarizability $\alpha_{ij,0}$ of the molecule, i.e. elastic scattering of light. The last term gives an explanation for Raman scattering. If the vibration is connected to a change in polarizability, side bands will be observed at shifted frequencies $\omega \pm \Omega_n$. All vibrational modes, which satisfy $\frac{\partial \alpha_{ij}}{\partial q_n} \neq 0$, are called Raman-active vibrations.

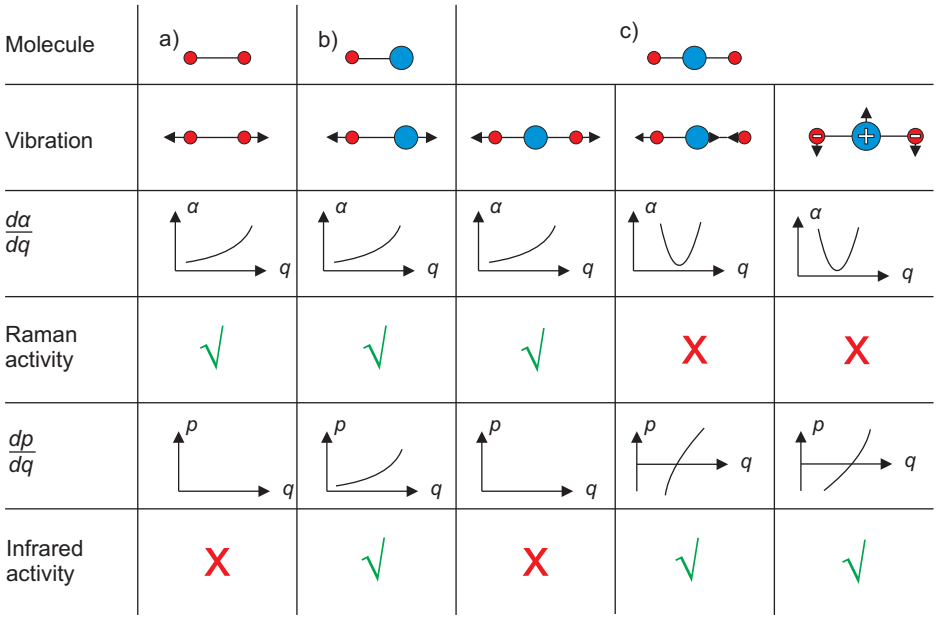

Fig. 3.3 Raman and IR selection rules for a two-atomic and three-atomic molecule (after [197]).

This simple mathematical model now gives an explanation for the typical observed Raman spectrum as shown in Fig. 3.1. Here, a Raman spectrum is comprised of a central Rayleigh line, which represents elastically scattered light, and side bands, which are displaced by the vibrational frequency of the Raman-active, vibrational mode. The principle intensity of the Raman mode is directly proportional to the change in polarizability $\frac{\partial \alpha_{ij}}{\partial q_n}$.

Based on this considerations, we can now discuss the Raman and IR-activity of typical vibrations observed in two and three-atomic molecules. Fig. 3.3 a) shows a symmetric vibration of a two-atomic molecule comprised of two atoms of the same type, e.g. N_2. This vibration leads to a change in polarizability, but due to the symmetry no dipole moment and no change in dipole moment is possible. Hence, one will observe only Raman-activity, but no IR-activity. If this molecule comprises two different atomic species (Fig. 3.3b) and c) the molecule may be observed in IR spectroscopy. In a three-atomic molecule, e.g. CO_2, as displayed in Fig. 3.3c different vibrational modes each with different selection rules will be observed. Again, a symmetric vibration will only be Raman-active, but not IR-active. On the contrary assymetric vibrations will be IR-active due to the change in dipole moment, but not Raman-active due to the symmetric change of polarizability.

A close look onto the different combinations ot Raman and IR activity in Fig. 3.3 hints that the symmetry of the molecule and the vibrations play an important role in predicting the Raman or IR activity of a molecule. In particular in can be seen that only one vibration actually is Raman and IR active at the same time. Indeed,

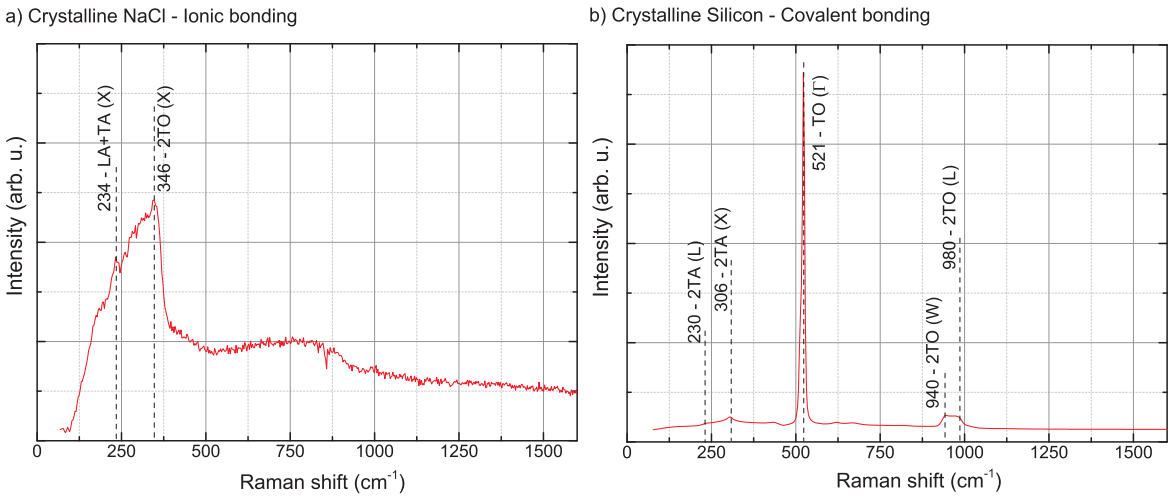

Fig. 3.4 Stokes spectrum of crystalline NaCl (a) versus the Stokes spectrum of crystalline Silicon (b) to illustrate the connection of the Raman effect to the covalent nature of materials. While for the covalent bonded Si a very strong first order TO peak is observed, no first order Raman feature is visible for the ionically bonded rock salt.

according to group theory one vibration can only be Raman and IR active at the same time, if it is lacking a center of symmetry, either Raman or IR activity is possible. This is called *Rule of mutual exclusion*. In this regard, Raman scattering and IR scattering are complementary to each other. The immediate application of this rule allows to determine, if a molecule or solid state material has a symmetry center. For this the IR and Raman spectra can be compared, whether or not vibrations at the same frequencies are detected.

Classical electrodynamics not only allow to predict and understand the Raman or IR activity of molecules, but also can describe the observed intensities. The radiation source is treated as an emitting dipole. In crystal lattice the classical description is very similar. Here, the polarizability is changed for the susceptibility. The polarizability is usually a second rank tensor given by a 3×3 matrix. Therefore, the Raman polarizability change is usually also a second rank tensor, which is called Raman tensor. For practical Raman experiments this means that an excitation with one light polarization (one direction of the incident electric field) can induce a dipole moment along a different axis and hence the Raman scattered light may be detected in a different light polarization. For scattering with liquid or gaseous molecules this is of no concern, because molecules are usually oriented randomly. In solid state materials with defined symmetry axis this may be used to identify and orient the crystal based on the Raman spectrum.

The *Rule of mutual exclusion* can be seen in Fig. 3.4 for solid state materials. Here, the Stokes-Raman spectrum of a crystalline silicon wafer (diamond structure) is compared to the spectrum of powdered rock salt (NaCl). It should be noted that the spectra are not in the same scale. The Raman spectrum of NaCl is significantly weaker, but enlarged in this plot to present the features in more detail. Here, NaCl as a pure ionically bonded material, has no Raman active modes in contrast to silicon, which is purely covalent bond. Here, silicone, in analogy to the molecule in 3.3a) shows Raman activity, but no IR activity (not shown here). However, in NaCl still shows some features in the Raman spectrum. These structures refer to two-phonon process, where a Raman scattering process happens with two phonons. If symmetry allows such processes, this allows to analyze also non-zone-center phonons with Raman spectroscopy [198]. Similarly, in silicone two-phonon peaks can also be identified. In Fig. 3.4 some of these peaks have been labeled [199, 200].

3.1.2 Quantum mechanical description

As seen in the previous chapter the classical description of the Raman effect allows for the explanation of observed intensities and overall Raman activity of certain vibrations by introducing the polarizability change $(\partial \alpha_{ij}/\partial q_n)_{q=q_0}$. However, the classical description fails, when rigorously trying to explain more advanced problems in Raman scattering, such as the intensity ratio of Stokes/Anti-Stokes lines, the rotational Raman effect or resonant Raman techniques, such as CARS ("Coherent anti-Stokes Raman Scattering") or SARS ("Stimulated anti-Stokes Raman scattering"). These problems can be accounted for a more rigorous quantum mechanical description.

In quantum mechanics resonant absorption and emission phenomena are described in terms of transition rates as described in Fermi's golden rule. Here, the transition rate $P_{n\to m}$ in the presence of a small, time dependent perturbation $\hat{H}'$ between two quantum states $|n\rangle$ and $|m\rangle$ and their energy density of states ρ_0 is given by [201]

$$P_{n\to m} = \frac{\pi}{2\hbar^2} |\langle n|\hat{H}'|m\rangle|^2 (E_n - E_m \pm \hbar\omega_i)\rho_0 = \frac{2\pi}{\hbar^2}|H'_{mn}|^2 (E_n - E_m \pm \hbar\omega_i)\rho_0. \tag{3.9}$$

In this notation of Fermi's golden rule only such transitions are efficient and allowed, where the incident photon energy $\hbar\omega_i$ is resonant with the energy difference of the initial and end state $E_n - E_m$. For an incident electromagnetic field the perturbation $\hat{H}'$ is usually represented as an oscillating electrical dipole

$$\hat{H}' = -\hat{\mu} E_0 \cos(\omega_i t), \tag{3.10}$$

where E_0 is the electric field amplitude. Here, $\hat{\mu} = q\hat{x}$ is the dipole moment operator given be the charge q and the position operator $\hat{x}$. In this form Fermi's golden rule is able to describe resonant absorption or emission in a two state system, such as between electronic energy levels in an atom or vibrational states (IR-spectroscopy) in a molecule, but it can not account for the Raman effect. As shown in Fig. 3.1 the spontaneous Raman effect involves at least three levels, where one usually is a short-lived virtual state, and is off-resonant, which means the scattering phonon has a much higher energy than the actual transition between the vibrational levels.

Fermi's golden rule, as discussed above, can be obtained by first order perturbation theory [202, 201]. Here, one main assumption is, that the eigenstates of the system are not altered by the perturbation. This is changed, if we want to account for the Raman effect. In that case, we have to implicitly assume an alteration of the wavefunctions $\Psi_n^{(0)}$ of our system by the perturbation. This alterations will explicitly account for the polarizability, which in classical electrodynamics means nothing more than a changed dipole moment (charge distribution) in the presence of an electric field.

The eigenstates of our system are described by the time-dependent Schrödinger equation [202, 201], which will be the starting point of our analysis.

$$\hat{H}^{(0)}\Psi_n^{(0)} = i\hbar\frac{\partial \Psi_n^{(0)}}{\partial t} \tag{3.11}$$

To account for the alteration of the wavefuntions, we assume that the total wave function Ψ_n can be expanded in a series as follows [203]

$$\Psi_n = \Psi_n^{(0)} + \Psi_n^{(1)} + \cdots. \tag{3.12}$$

In this context $\Psi_n^{(0)}$ is the unperturbed ground state wave functions, while $\Psi_n^{(1)}$ describes the first order perturbation. We insert now the perturbation from Equ. 3.10 and allow the alteration of the eigenstates, we obtain the following equation

$$\left(\hat{H}^{(0)}+\hat{H}'\right)\Psi_n^{(0)}=\left(\hat{H}^{(0)}-\hat{\mu}E_0\cos(\omega_i t)\right)\Psi_n^{(0)}=i\hbar\frac{\partial\Psi_n^{(0)}}{\partial t}. \tag{3.13}$$

Solving this equation allows to formally define a new operator, called the polarizability operator $\hat{\alpha}_{ij}$, which describes the Raman effect. This operator is formally structured in a way, that Raman selections rules and scattering efficiencies can be calculated in analogy to Fermi's golden rule (Equ. 3.9). The derivation can for example be taken from Ref. [203]. The polarizability operator is given by

$$\hat{\alpha}_{ij}=\frac{1}{\hbar}\sum_{n_v}\left(\frac{\hat{\mu}_i\left|r\right\rangle\left\langle r\right|\hat{\mu}_j}{\omega_{rn}-\omega_i}+\frac{\hat{\mu}_j\left|r\right\rangle\left\langle r\right|\hat{\mu}_i}{\omega_{rm}+\omega_i}\right) \tag{3.14}$$

and the transition probability is proportional to

$$P_{n\to m}\propto\left|\left\langle n\right|\hat{\alpha}_{ij}\left|m\right\rangle\right|^2. \tag{3.15}$$

The transition matrix $\langle n|\hat{\alpha}_{ij}|m\rangle$ formally describes first a two part transition from $\langle n|$ to $|r\rangle$ with the transition dipole moment $\hat{\mu}_i$ and from $|r\rangle$ to $\langle m|$ with the dipole moment $\hat{\mu}_j$. This is the first term in Equ. 3.14 and can be identified as the Stokes process, while the second term describes the Anti-Stokes process. Here, $|r\rangle$ is a non-specified intermediate state, which can the previously described vacuum state, but may also coincide with real energy states in molecules or crystals. This second case yields without any preliminary assumptions the above mentioned resonant Raman scattering. The indices of the dipole moments i or j refer to Cartesian coordinates, as a dipole moment may be oriented in x, y or z-directions. Equations 3.14 and 3.15 show, that two dipole moments are associated with Raman spectroscopy. From the view-point of group theory this means that the transition moment transform as $x^2, y^2, z^2, xy, xz, yz$. This is in contrast to the direct transition in IR spectroscopy, where only a single dipole transition transforming as x, y, z. This explains completely different allowed selection rules for Equ. 3.15 (Raman scattering) and Equ. 3.9 (Fermi's golden rule $\rightarrow$ IR transition).

3.2 Experimental Instrumentation

The main experiments in this thesis were performed via three experimental setups. The central part for optical analysis and spectroscopy was given via the confocal Raman Imaging setup. Its construction enables 3D-spatially resolved analysis of a wide range of sample types. Its spectrometer offers a high-throughput combined with adequate spectral resolution for most questions. For higher spectral resolution a low temperature Raman setup was built using a double monochromator. Here, samples can be cooled in cryostat down to liquid helium temperatures leading to a reduction of thermal broadening, which enables the analysis of more subtle effects. The Raman imaging analysis was supported by Second harmonic microscopy, which offers a different contrast mechanism - namely the second order nonlinearity of the material - combined with a fast image acquisition and better optical resolution, in particular in depth. In the following part the characteristics of these setups will be briefly reviewed and some measurement examples will be given.

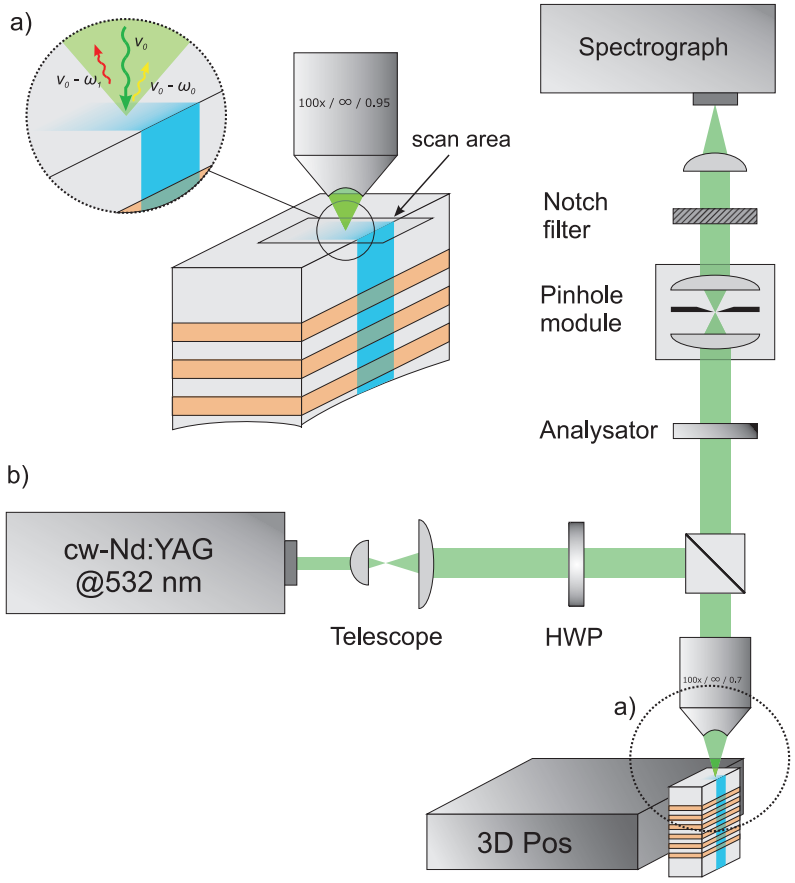

Fig. 3.5 a) Measurement geometry for the analysis of ion-exchanged waveguides as presented in Sec. 5.2.1. The coordinates are given in lab frame of reference. b) Overview of the Confocal μ-Raman setup used for Raman Imaging.

3.2.1 Confocal Raman imaging

The confocal Raman imaging setup and a typical sample geometry are sketched in Fig. 3.5b). For excitation a continuous wave frequency doubled Nd:YAG laser at 532 nm with an output power of up to 50 mW is used. The laser light is focused via an infinity-corrected objective lens onto the sample. The objective lens usually used is a *100x M Plan Apo SL* with a numerical aperture of $NA = 0.7$ and a long working distance. Depending on the task other lenses are available and can be changed. To ensure a complete illumination of the entrance pupil of the respective objective a telescope is added in the excitation path. The scattered light is collected in back-scattering via the same objective lens. The scattered Raman light is split from the Rayleigh light via a dichroic beamsplitter (*Semrock RazorEdgeTM*) with a sharp transmission edge ensuring that Anti-Stokes scattered light with Raman shifts larger than 100 cm^{-1} can pass. For spatial filtering a Confocal pinhole is added, which is mounted to a custom-built positioning unit. Typically a pinhole diameter of 10 μm is chosen, but sizes down to 2 μm are available. A 10 μm pinhole represents a good compromise between signal strength and depth resolution. The spectral analysis is performed in a spectrometer by Kaiser Optical System (Holospec f/1.8i) with an integrated Notch filter an attached CCD camera (Andor Newton BI). The Notch filter attenuates the Rayleigh scattered light by up to six orders of magnitude in $\pm$ 100 cm^{-1} band around the laser frequency.

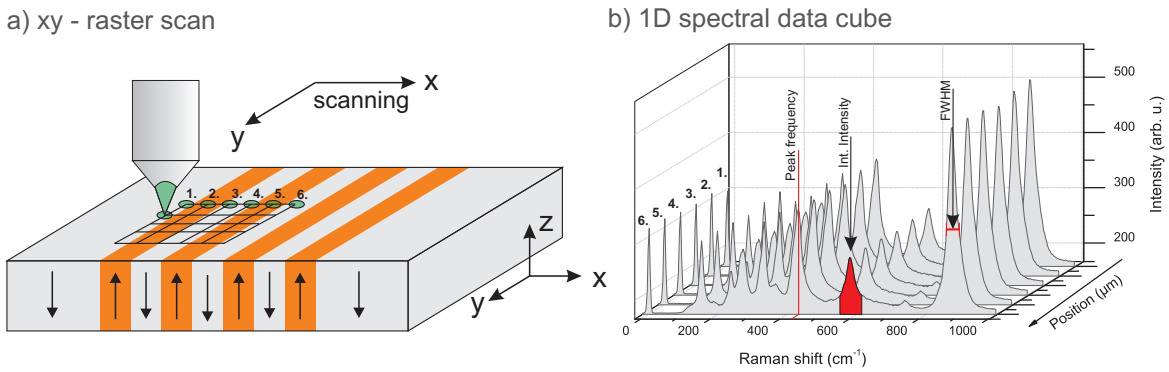

Fig. 3.6 a) Example for a raster scan in x-y direction of a periodically poled samples. At each individual point Raman spectra are recorded and saved with respect to the spatial coordinates, leading to a multidimensional spectral data cube. b) Example for a 1D data cube, showing 6 spectra taken at different positions. For each individual spectra properties such as spectral positions, FWHM or integrated mode intensities can be examined with respect to the data cube coordinates.

For spectral analysis a first order Anti-Stokes holographic grating with spectral coverage of 0 cm^{-1} to 4000 cm^{-1} is applied. The spectrometer offers a spectral resolution of typically 2.3 cm^{-1} with an entrance slit of 25 μm and the specified CCD chip. For polarization dependent analysis a half wave plate (HWP) is added in the excitation path and an analyzer in the detection path. For sample inspection and to identify the relevant scan areas, a simple CCD camera and a LED for illumination can be coupled into the optical path via a flip mirror, which is not sketched in Fig. 3.5b).

The samples are mounted on a two-stage positioning unit. The first stage consist of a lifting actuator (z) and two piezo-actuators of CN110 type. The lifting actuator offers a moving range of 25 mm and a precision of 1 μm and is used to position the relevant sample layers in the focus, while the piezo-driven CN110 actuators offer 35 mm moving range in x- and y- direction with a precision of 50 nm. These are used to reach the relevant scan areas. Scanning is realized via a nanopositioner by Piezosystem Jena (Tritor 200/20 SG). In closed loop it offers a scan area of 180 μm x 180 μm x 20 μm (x, y, z) with a precision of 2 nm. To realize angle-dependent measurements of phonon modes, i.e. the angle dispersion and analysis of mixed LO-TO phonons, the nanopositioner can be replaced with stepper motor, which serves as a goniometer.

All relevant components, the polarizers, the CCD camera and the actuators are computer controlled and enable the realization of scanning routines. During the imaging procedure individual Raman spectra are collected in a coordinate Raster on a sample, as shown in Fig. 3.6a). The data is then saved as a spectral data cube, as shown in Fig. 3.6b). Spectral data cube in this context means, that Raman spectra are saved with respect to their spatial coordinates (x,y,z), as well as with respect to the excitation and detection polarization. Combined with the angle of the sample, this results in an up to six dimensional data cube in our experimental system. The recorded data can then be evaluated post experiment and be used to generate false-color images based on various spectral properties, such as FWHM, peak position or integrated intensities of spectral channels. For accurate spatial resolution, the typical distance between two points in scanning should be less than the spatial resolution as defined by the microscope parameters. In lateral direction (x-y) a resolution of better than $< 350nm$ is achieved, while in depth the focus has a size of 2000 nm. For an accurate reconstruction of any structure the scanning routine should allow a slight overlapping of adjacent points, which results in typical step width in the order of 250 nm.

The scattering geometry in Raman experiments is typically given in Porto's notations (named for Brazilian scientist S.P.S. Porto). This is also used throughout this work. the scattering geometry in Porto's notation is $k_i(e_i,e_s)k_s$. Here k_i and k_s denotes the k-vector of the incoming and scattered photon, while (e_i,e_s) defines the light polarization (vector of the electric field) for (excitation, detection). The vectors are usually given with respect to the crystal coordinate system.

3.2.2 Second-Harmonic Microscopy

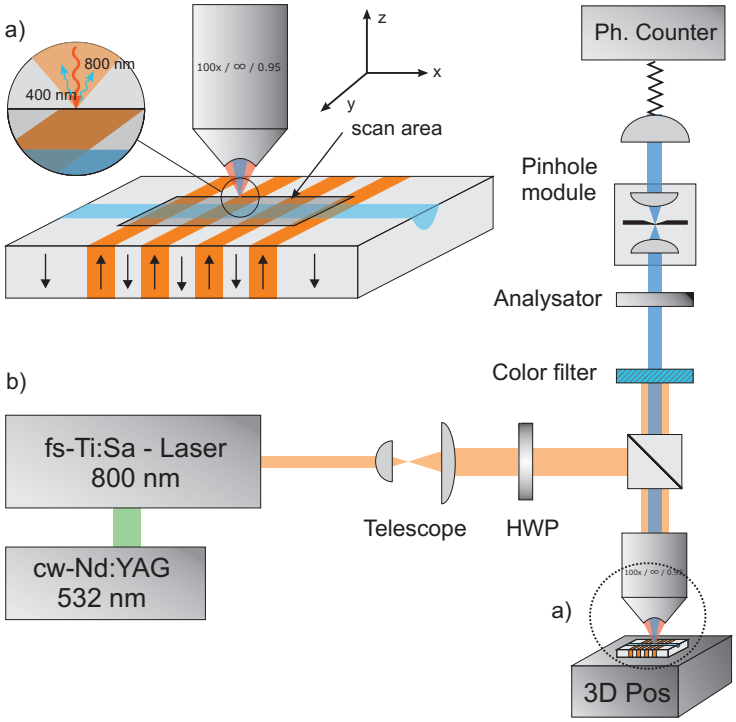

Fig. 3.7 The figure shows b) the sketch of the nonlinear microscopy setup and a) a closeup of a typical sample measurement geometry for the analysis of periodically poled waveguides.

The Raman imaging analysis is supported by second-harmonic microscopy, which has been proven to be a very sensitive method to visualize periodically poled materials [74, 204, 205]. Second harmonic microscopy makes use of the second order nonlinear effect. Here, in the photon picture two photons at frequency ω_{pump} are used to create a new photon at $\omega_{signal} = 2 \times \omega_{pump}$. A second order nonlinearity is only allowed in systems lacking inversion symmetry and is highly sensitive to changes in material symmetry. In contrast, to the spontaneous Raman effect presented above the created light is coherent. In this context, in the vicinity of ferroelectric domain walls the symmetry of the crystal is broken, which will result in a modified SH signal and hence in a contrast for structures, such as domain walls. Because this method is mainly used supportive in this work, for a more detailed background the literature should be concerned. As second harmonic microscopy is a second order nonlinear effect, its intensity scales quadratically with the pump power. This requires a pulsed laser source, which provides the required high power pulses.

The setup sketched in Fig. 3.7 represents a typical nonlinear microscopy setup. Excitation is provided by a pulsed laser system, in this case a femtosecond titanium sapphire laser (Femtosource Compact) pumped

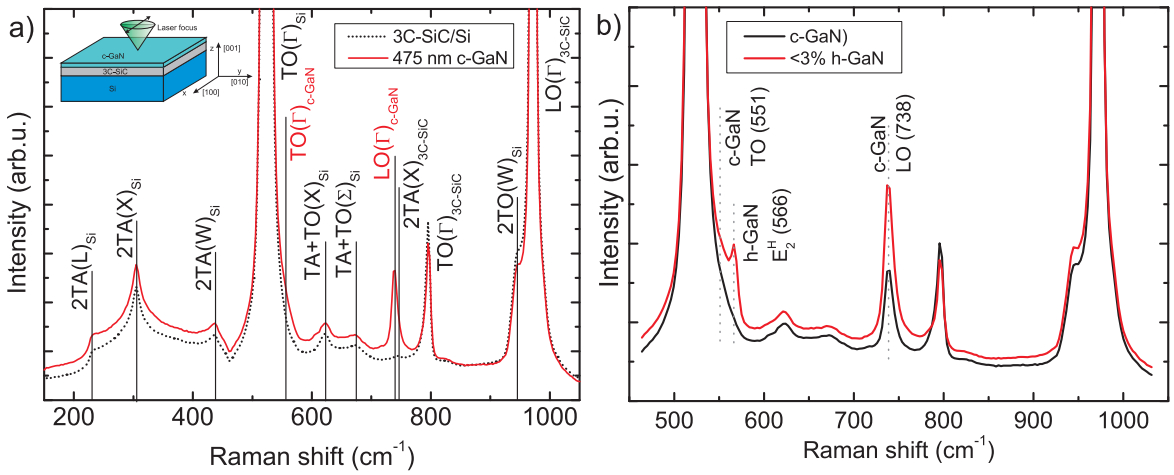

Fig. 3.8 a) Comparison og the spectrum of the substrate and of the spectrum of a 475 nm c-GaN layern grown on the substrate. Only one line and a weak shoulder can be attributed to the cubic GaN spectrum. b) Comparison of the c-GaN sample from a), which has only a very low density of hexagonal phase (< 0.5 %) and a sample with up to 3 % hexagonal inclusions (1000 nm).

by a continuous wave frequency doubled Nd:YAG laser (Coherent Verdi V6) with up to 6 W of pump power. The femtosecond pulses have a pulse length of down to 100 fs at a repetition rate of 80 MHz with wavelength centered at 800 nm. The average excitation power, which is focused on the sample, is in the order of 100 to 200 mW. The excitation pulses are focused via an objective lens onto the sample, which is mounted to a piezo-driven actuator system similar to the Confocal Raman setup. Depending on the experimental question, objective lenses up the $NA = 0.95$ are available. Alike to the Raman setup the SH light is detected in back-scattering geometry. The SH is separated from the pump beam via a dichroic beam splitter reflecting the 800 nm and transmitting the 400 nm wavelength. To further filter the signal in the detection path, color filters are inserted. For confocal operation a pinhole module is included with a diameter of down to 500 nm. Together with the $NA = 0.95$ objective lens, an optical resolutions in lateral direction of < 300nm and < 500 nm in depth is realized. The actual detection is then provided by a photon counting module.

3.3 Selected experimental applications

During the course of this work Raman microscopy and second harmonic microscopy have not only been performed in the context of ferroelectrics, but on other material systems and questions. This chapter gives a brief overview about some selected topics conducted during the course of this thesis. At the same time the examples demonstrate the versatility of the used investigation methods.

3.3.1 Investigation of cubic GaN

Due to their large band gap, nitride semiconductors, i.e. AlN, GaN and InN, form todays basis of optical and UV optoelectronic components. The nitride semiconductors usually crystallize in the hexagonal wurtzite phase. While it is the natural phase of this material class under ambient conditions, it comes with a built-in polarization field, which leads to a bending of the band structure and the quantum-confined Stark-effect. This can limit the performance of devices, e.g. due to decreases mode overlap in quantum wells. One straightforward method

to overcome the issue of the internal fields is to grow the material in the meta-stable zinc-blende phase, also known as the cubic phase. Due to the symmetry no built-in electric fields do exist. The growth of cubic nitrides is typically performed on an appropriate substrate, which offers a cubic symmetry and a low lattice mismatch. Here, the preferred substrate is 3C-SiC grown on silicon, which is also in zinc-blende structure and has a favorably small lattice mismatch for cubic gallium nitride (c-GaN) and cubic aluminum nitride (c-AlN). A typical sample geometry is shown in the inset in Fig. 3.8a). Typical layer thicknesses of c-GaN are between 100 and 1000 nm and for c-AlN less than 200 nm. The cubic GaN and AlN samples for this study were grown in the group of Prof. As and the main collaborators were S. Blumenthal and T. Wecker.

In this context a typical task of Raman spectroscopy is the determination of the quality of grown layers. Depending on the growth conditions, the substrate and many more properties these layers typically can be prone to typical defects. Figure 3.8a) shows a typical spectrum of an approximately 475 nm thick c-GaN layer on the 3C-SiC/Si substrate compared to substrate spectrum without any deposited layer. The spectra have been normalized to the silicon TO peak. Due to the fairly thin films, the diffraction limited depth resolution and the fairly low scattering cross-section of c-GaN compared to the other materials, peaks from silicon, as well as the 3C-SiC are present in the spectrum. The comparison allows to unambiguously identify one peak at ~738 cm^{-1} and a weak shoulder at ~551 cm^{-1} to be c-GaN related peaks [19, 20, 206]. Cubic gallium nitride has only two atoms per unit cell, hence only three optical phonons are expected, which can be distinguished at the zone center into a twofold degenerated TO mode and one LO mode. The higher frequency peak is the LO, as LOs usually have the higher frequency due to the additional restoring force of the long range interaction. The TO appears much weaker in intensity compared to the LO, due to selection rules. In back-scattering geometry scattering with the TO is forbidden in zinc-blende material. The same effect is seen for the TO and LO peaks of the SiC at ~796 cm^{-1} and ~970 cm^{-1}, respectively [207, 208]. The c-GaN and 3C-SiC TO modes are nevertheless present in the spectrum due to defects in the layer relaxing selection rules or by the detection of some forward scattering due to multiple reflections [209, 40]. All other peaks in the spectra can unambiguously be attributed to two-phonon scattering in Si [200, 210]. Two-phonon overtones of the 3C-SiC are also present, but are mostly overlapped by the Si spectrum or are found at higher frequencies (> 1000 cm^{-1}) [207].

Because the cubic phase is only metastable, one of the typical intrinsic defects are inclusions of hexagonal gallium nitride. In this context μ-Raman spectroscopy is a very powerful to detect hexagonal inclusion of very small amounts (1 %), but also to do this on a local scale. The zinc-blende structure (cubic phase) has just two atoms in the unit cell, while the wurtzite phase has four atoms per unit cell. From the perspective of Raman spectroscopy this immediately means, that additional lines will be present in the spectrum due to the larger number of vibrational degrees of freedom. Due to the larger scattering cross sections even smallest contributions can be detected. Figure 3.8b) shows a spectrum of a 1000 nm thick sample with ~3 % hexagonal inclusions, which have been determined previously by x-ray diffractions. In the spectrum an additional line at 566 cm^{-1} is clearly visible, which can be attributed to the E_H^2 peak of wurtzite GaN [211, 212].

Another typical task of Raman spectroscopy in the context of semiconductors is the determination of charge carrier densities. Due to the polar nature of longitudinal optical modes they will couple with free charge carriers and form an new type of quasi-particle called longitudinal optical phonon-plasmon coupled mode often abbreviated as LOPC. In the Raman spectrum this leads to a blue-shift and asymmetric distortion of the LO phonon peak. The expected line shape can be expressed analytically in a semi-classical approach and fitted to determine the plasmon frequency as well as the damping constant. The respective formulas can be taken from literature, e.g Refs. [39, 38, 20]. The plasmon frequency is directly connected to the free charge carrier density, while the plasmon damping constant is a function of the charge carrier mobility. Figure 3.9 shows the enlarged spectral region of the c-GaN LO phonon for three different samples. The spectrum of an undoped sample with

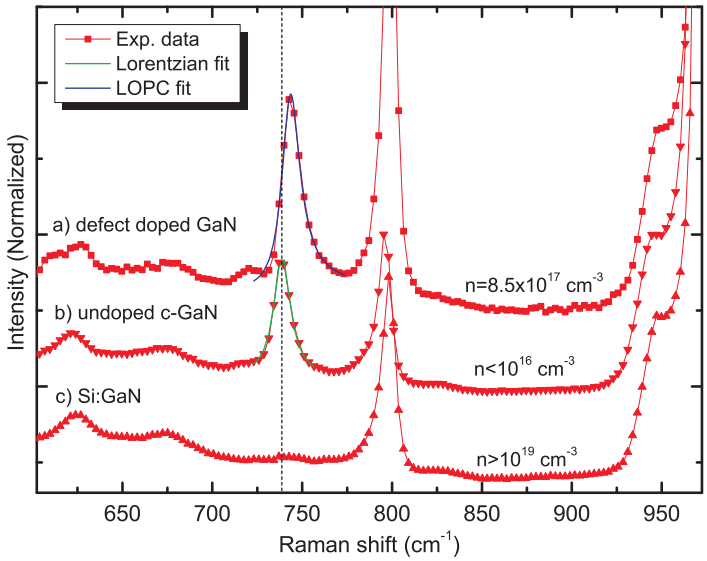

Fig. 3.9 Comparison of the Raman spectra of three samples with different charge carrier densities. Here, a) represents a sample with a slight background doping due to suspected oxygen inclusions, b) represents and undoped sample ($n < 10^{16}$ cm^{-3}) and c) the spectrum of a sample with assumed degenerate doping ($n > 10^{19}$ cm^{-3}).

an almost symmetrical Lorentzian shaped line is shown in b). The spectrum of a) belongs to a sample with a slight background doping due to oxygen defects, which can act as an donator in c-GaN. Here, the peak is clearly shifted to a higher frequency and shows a slight asymmetry. From fitting the analytical LOPC function a plausible doping level of $n \approx 8.5^{17}$ cm^{-3} is determined. In contrast to this Fig. c) shows the spectrum of a highly Si-doped sample. Here, the LO mode has vanished completely due to the almost metal-like electronic properties of the film.

3.3.2 Second harmonic microscopy of c-AlN on 3C-SiC

Recently, photonic crystal resonators with embedded GaN quantum dots in AlN layers have been fabricated [213]. For this the AlN membranes need to be underetched. MBE grown layers are usually strained due to the lattice mismatch to the substrate. Because the AlN layers are lifted from their contact with the substrate layer, a relaxation might occur. To measure this relaxations nonlinear microscopy is perfectly suited, because the nonlinear effect is very sensitive to symmetry changes in the crystal structure. Therefore, such a change in strain should be detectable. In this context a line scan over multiple rows of photonic crystals in c-AlN were performed as shown in the inset in Fig. 3.10. The rows of photonic crystals are approximately 1 μm apart and have a width of 600 nm. This fits well with the periodic signal enhancements between 10 and 25 μm. Each small peak has a width of ~600 nm and correlates to the underetched crystals. This may be understood in terms of a relaxed crystal structure.

However, beside these weak periodic signals also large signal enhancements, which appear to have no apparent connection with any visual or known structure. A subsequent analysis of several samples with c-AlN and c-GaN layers showed also no connection to the deposited layer. Therefore, the origin of theses peaks has to be connected to the substrate. Figure 3.11a) and b) show two scans on a substrate sample. Here, Fig. a) is taken on the optical surface of the 3C-SiC layer. Nonlinear signal enhancements of considerable intensity can

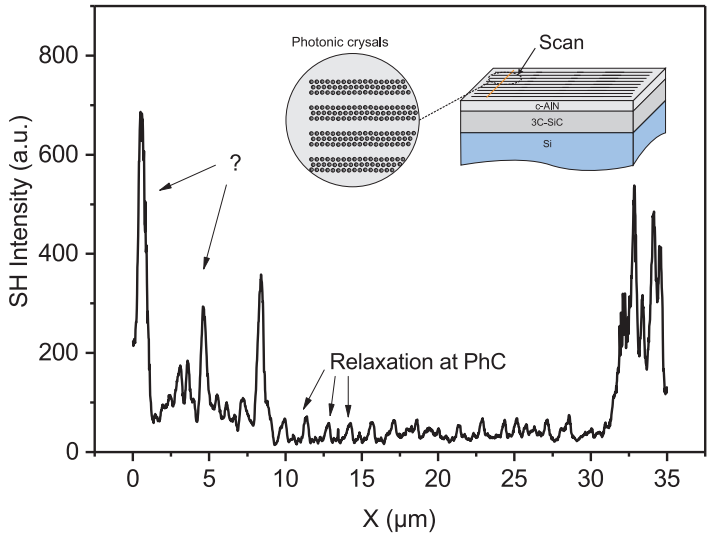

Fig. 3.10 Second harmonic microscopy line scan over a group of underetched photonic crystals in AlN.

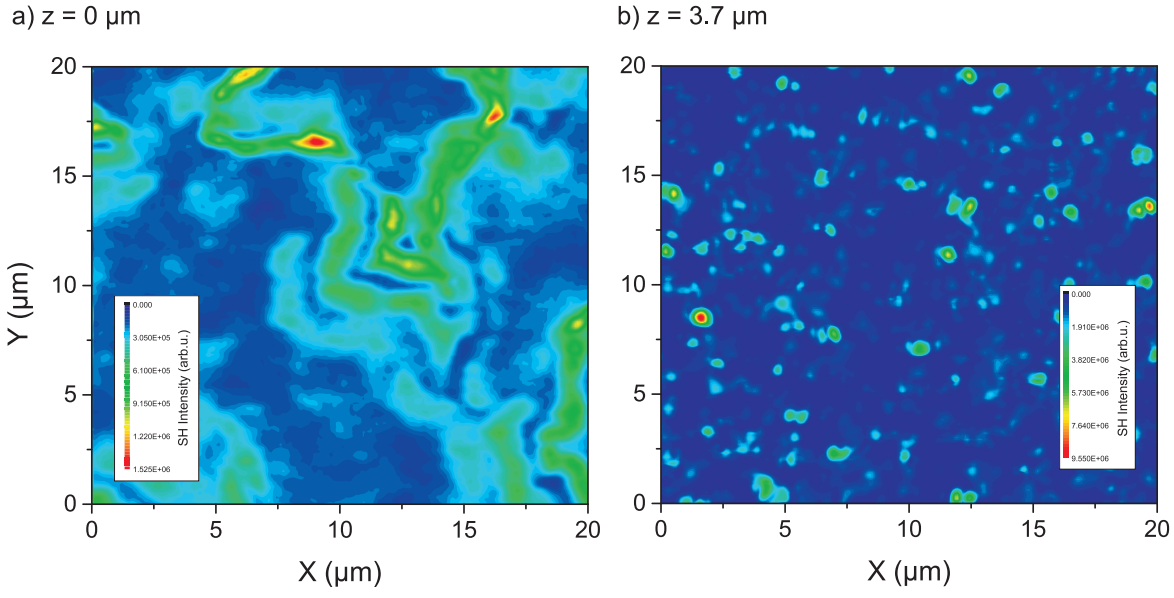

Fig. 3.11 Second harmonic scans of the 3C-SiC substrate used to grow cubic nitrides. Both scans were taken on the same location, but in different depths. Fig. a) was taken with the focus placed on the optical surface, while b) was taken in a depth of 3.7 μm.

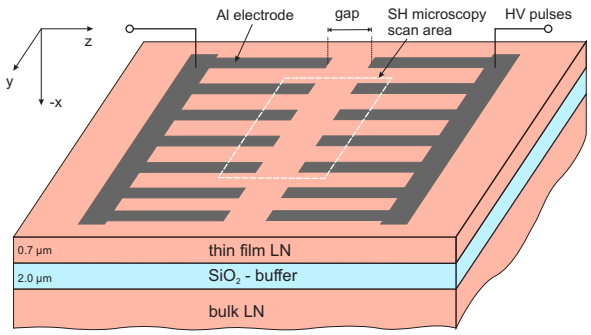

Fig. 3.12 On top of the thin film, an aluminum electrode (40 nm) structured by maskless optical lithography is deposited with gaps along the z-direction. The ferroelectric domain orientation is reversed between the two opposing electrodes by applying multiple HV pulses. The effective domain inversion was verified ex situ by SH microscopy. A typical scan area is highlighted by the dashed rectangle.

be seen arranged along lines. These lines appear to enclose specific regions. One explanation could be that the lines of increased signal represent the borders of so called anti-phase domains. Any zinc-blende material can grow along a [001] direction in two crystallographic distinctly different orientations. In one, the top layer is comprised of a Si layer, while the second is comprised of C on top [214, 215]. These regions are called anti-phase domains. From the viewpoint of crystal symmetry one domain represents a zinc-blende crystal, which is rotated by 90° compared to the other domain type [214]. It seems reasonable that such a domain border will results in an increased SH signal due to the change in crystal symmetry. The second measurement in Fig. 3.11b) was performed at the same location, but the sample was lifted by 3.7 μm along the optical axis. Taking the depth correction from Sec. 3.3.4 into account with a refractive index of $n(SiC) \approx 2.75$ [216] this measurement is taken in a depth of approximately 10 μm close to the surface of the silicon wafer. Here, we detect point-like enhanced nonlinear signals. A possible explanation for this may be two-photon absorption in point defects in the SiC layer. These defects are mainly located at the back-side of the SiC layer. Further spectral and power dependent measurements are indicated to investigate these phenomena further. Nevertheless, this demonstrates the power of second harmonic microscopy and its sensitivity to local changes in symmetry.

3.3.3 Domain imaging in thin film $LiNbO_4$

Thin film lithium niobate is a promising material system for applications in integrated optics. Lithium niobate thin films of thicknesses down to 200 nm are typically bonded to a low index refractive index substrate, such as SiO_2. Therefore, this technology is sometimes referred to as silicon on insulator [119]. This system features inherent wave guiding properties with high optical mode confinements due to the large index contrast [121, 217, 120]. A typical sample structure is depicted in Fig. 3.12. The thin films are fabricated by a process called ion-slicing. Here, a thin film can be ex-foliated from a bulk crystal by creating an amorphous defect layer by ion bombardment [218]. Numerous optical devices have already been demonstrated in this material system, such as waveguides [121, 219], grating couplers [220], photonic crystals [218] or resonators [221, 222]. More recently periodic poling and second harmonic generation was demonstrated. One of the most recent ideas is the combination of silicon photonics with lithium niobate (thin films) leading to hybrid silcon-lithium niobate photonics [223, 224].

One of the most important prerequisites for any nonlinear frequency conversion process in integrated optical structures is phase matching, which in ferroelectrics is usually achieved by the quasi-phase matching technique

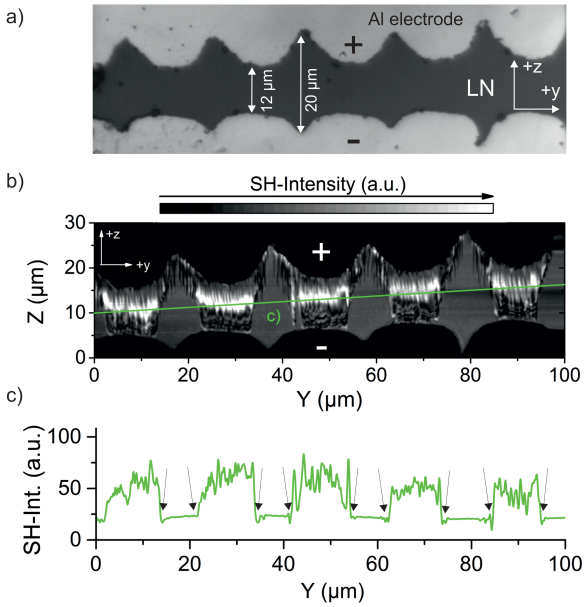

Fig. 3.13 (a) Optical micrograph of the 20lm period electrodes after poling. (b) Confocal SH image of the same area as shown in (a). (c) Cross-section of the SH signal along the solid, green line in (b).

in periodically inverted structures. To demonstrate the fabrication of periodically poled thin films a metal electrode was deposited on top of a x-cut thin film as shown in Fig. 3.12 and HV pulses above the coercive field have been applied [49]. The x-cut geometry is of particular interest for practical applications in integrated optics, as any structuring can be performed on top of the thin film and no removing of back electrodes is required. Poling in x-cut lithium niobate in comparable methods was demonstrated before [225–228, 205], but on x-cut thin films only recently [49, 229, 230].

Important for domain inversion is an examination of the inverted domain structure. In this context nonlinear microscopy offers a high sensitivity for domain inversion. Figure 3.13 shows a result on a typical electrode structure. An optical micrograph with conventional microscopy is shown in the top image. Here, the visual inspection shows no differences of the lithium niobate in the small gaps compared to the large gaps. The situation is different in the second harmonic image. Here, in the gaps the overlapping second harmonic signatures of many domain filaments can be seen. These observations are similar to previous investigations on comparable samples in bulk and ridge structures in x-cut lithium niobate [205, 225, 74]. The filaments appear wider and broader on the + side electrodes, which indicates that domain inversion started here. This is in line with the usually idea of domain inversion in lithium niobate, which is believed to start on the + side [231].

3.3.4 Depth correction in microscopy

In this work, we employ confocal Raman microscopy. During these studies, we not only intend to visualize 2D structures, but aim at the three dimensional visualization of ferroelectric domain structures and waveguides. The three dimensional analysis requires to focus through an interface between refracting media, e.g. from air into lithium niobate, which results in a refracted beam. Here, refraction will lead to a distorted and stretched focus, and to an altered direction of the beam. Usually measurements will be performed orthogonally with respect to the sample surface. Therefore, no deviation on the direction is expected. However, focusing through the interface will lead to an elongated focus and more severe, the focus position in the material will be different,

from the position expected without the interface. The principle situation is sketched in Fig. 3.16. For 3D scanning this means moving the sample an amount x along the optical axis, will lead to excitation and detection at position d. An example from this work is the analysis of periodically poled waveguides, here it is imperative to know how deep the waveguide is with respect to the surface. For this it is necessary to find a quantitative relation of x vs d.

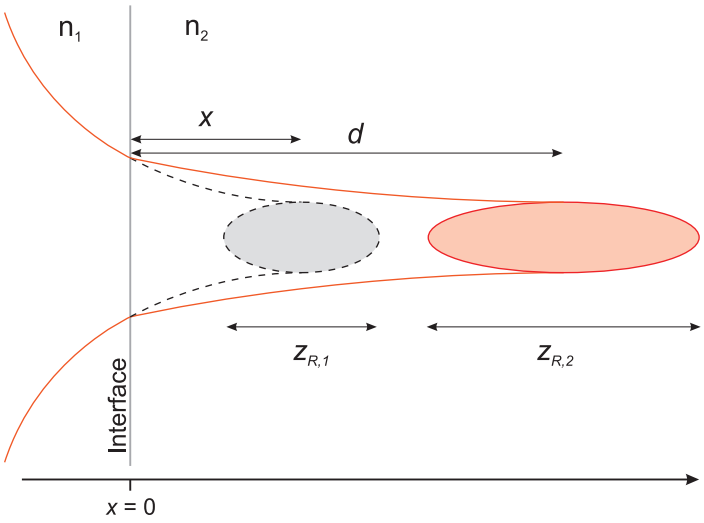

Fig. 3.14 Gaussian focus refracted at an interface between two refracting media. Due to the interface the real focus position d (light red) will differ from the focus position x expected without the interface (light gray). Furthermore, the focus will be elongated, which results in lowered depth resolution determined by the Rayleigh parameters $z_{R,1}$ and $z_{R,2}$.

This problem can be described in a Gaussian beam and ray transfer matrix formalisms [232, 233]. Any Gaussian beam is completely defined by the position and size of its beam waist for any given refractive index [234]. In the ray transfer matrix analysis the beam is described by a two component vector v_r

$$v_r = \begin{pmatrix} r(z) \\ \alpha(z) \end{pmatrix}, \tag{3.16}$$

where $r(z)$ defines the distance of the ray with respect to the optical axis and $\alpha(z)$ the angle between the beam and the optical axis. Based on ray matrices the effect of any optical component or propagation on this vector can be described. The matrix for propagation M_{prop} and refraction M_{ref} is given by [234]

$$M_{prop} = \begin{pmatrix} 1 & x \\ 0 & 1 \end{pmatrix} \text{ and } M_{ref} = \begin{pmatrix} 1 & 0 \\ 0 & \frac{n_1}{n_2} \end{pmatrix}. \tag{3.17}$$

The goal of our calculation is now to find a relationship between the "real" focus position d as shown in Fig. 3.14 and the position of the respective focus in a homogeneous medium x now needs to be determined. For this we assume a beam starting at the interface, which is refracted at the interface and then propagated the distance d, which is described by the matrices

$$\begin{pmatrix} 1 & d \\ 0 & 1 \end{pmatrix} \cdot \begin{pmatrix} 1 & 0 \\ 0 & \frac{n_1}{n_2} \end{pmatrix} = \begin{pmatrix} 1 & d\frac{n_1}{n_2} \\ 0 & \frac{n_1}{n_2} \end{pmatrix}. \tag{3.18}$$

In contrast to this, the beam propagating in a homogeneous medium is not refracted, but only propagated, leading just to the propagation matrix

$$M_{hom} = \begin{pmatrix} 1 & x \\ 0 & 1 \end{pmatrix} \tag{3.19}$$

for this situation. Both beams have at the interface the same properties in terms of their Gaussian beam parameters. This means at the interface $z = 0$ it has to hold

$$\begin{pmatrix} 1 & x \\ 0 & 1 \end{pmatrix} \cdot v_r(0) = \begin{pmatrix} 1 & d\frac{n_1}{n_2} \\ 0 & \frac{n_1}{n_2} \end{pmatrix} \cdot v_r(0). \tag{3.20}$$

Here, one can already see this can only be fulfilled for any given α, if

$$d\frac{n_1}{n_2} = x \Leftrightarrow d = \frac{n_2}{n_1}x, \tag{3.21}$$

which is a reasonable results and can be understood in terms of optical path length conservation. Therefore the difference between the focus position in air, and therefore the movement of the piezostage with respect to the fixed focus, and the "real" focus is determined by the quotient of the refractive indices. To obtain this result for normal incidence and focused beam, the Gaussian beam parameters need to be determined in the ABCD formalism. Here, this more rigorous treatment will as well compute Equ. 3.21. The relation in Equ. 3.21 between the *Actual Focus Position* (AFP) and *Nominal Focus Position* (NFP), as they are called in literature [235], have also been obtained in literature [235–237]. Here, they found that for large aperture, e.g. oil immersion objective with $NA = 1$, deviations of more than 20 % from this relation are observed. However, we detect no such deviation in our experiment discussed below, suggesting that this relation yields good results for $NA \leq 0.7$ as applied in the Raman experiment and may still be accurate enough for most analysis in the second harmonic microscopy experiment.

Furthermore, this allows for the determination of the change in depth resolution as determined by the Rayleigh parameters $z_{R,1}$ and $z_{R,2}$. Here, the calculation yields

$$z_{R,2}\frac{n_1}{n_2} = z_{R,1}, \tag{3.22}$$

where the depth resolution is decreased by the quotient of the refractive indices, which again is explained by optical path length conservation.

The Gaussian beam analysis has revealed a direct connection between the refractive indices of the materials and the "real" focus position. For the experimental investigation of this problem, fused silica (SiO_2) films on silicon substrate have been grown via PECVD with layer thicknesses between 1 μm and 15 μm have been achieved. The layer thickness have been controlled and determined in-situ via the growth rate. Measurements should be performed at the center of the samples, where homogeneous thicknesses are expected, as the growth conditions change towards the sample border. The typical sample geometry is sketched in the inset in Fig. 3.15. This sample know allows to analyze the connection between positioner movement required to see reflected signal at the air/SiO_2 interface and from the SiO_2/Si interfaces. For the experiment axial lines scans orthogonally to the surface of the sample have been performed with the regular Raman imaging setup. For the experiment an objective lens with $NA = 0.7$ and a beam expander was used, to ensure a complete illumination of the entrance pupil. In the experiment Raman spectra have been recorded in steps of 250 nm. Fig. 3.15 shows a typical spectrum. At 0 cm^{-1} Raman shift the reflected laser light ("laserline") is visible as a strong peak, while we

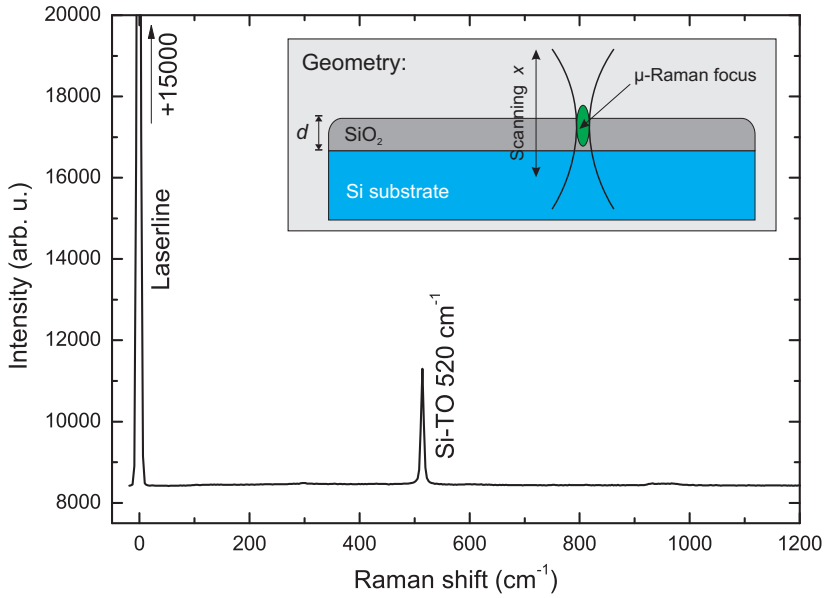

Fig. 3.15 The inset shows the sample geometry for this study with SiO_2 layers of various thickness d deposited on (100) silicon wafer. The Raman spectrum recorded on this samples show two major lines. The strongest signals are the reflected laser light and 0 cm^{-1} Raman shift and the silicon TO at 520 cm^{-1}.

detect the silicon TO at 520 cm^{-1} [199]. Detecting not only the reflected light, but also the silicon line enables the unambiguous identification of the reflection of the SiO_2/Si interfaces, where not only in the laserline a maximum in intensity is expected, but also in the silicon signal.

For the analysis, the intensity of the laserline, as well as the silicon TO is mapped as a function of positioner movement x. For comparability both plots are then normalized to the maximum. The inset in Fig. 3.16 shows such a plot for the 10 μm SiO_2 sample. Here, we see two maxima in the laserline intensity, the first at 10 μm movement and the second at 16.5 μm movement. The maximum at the air/SiO_2 interface shows only about 15 % of the intensity compared to the intensity of the reflection observed at SiO_2/Si interface. This can easily explained by the different reflectivities. Fused silica has a refractive index at 532 nm of $n(SiO_2) = 1,4607$ [238, 239], while silicon has a much larger index of $n(Si) = 4.143$ [240]. Calculating the reflectivity R for normal incidence via the Fresnel-equation

$$R = \left(\frac{n_2 - n_1}{n_2 + n_1}\right)^2 \tag{3.23}$$

yields at the air/SiO_2 interface $R = 0.035$ and $R = 0.23$ at the SiO_2/Si interface. Here, the reflection at the air/SiO_2 interface is only about 15% compared to the second, which fits very well with the observed intensity ratio.

The main Fig. 3.16 shows the thickness of the SiO_2 layer as a function of measured thickness by the positioner movement x. According to Equ. 3.21 the points should be on a linear slope with the slope $n(SiO_2)/n(\text{air})$. Because $n(\text{air}) \approx 1$, which is indeed fulfilled. Fitting a linear slope reveals $n(SiO_2) = 1.45 \pm 0.05$, which fits well with the literature data for SiO_2, which is given as $n(SiO_2) = 1,4607$ for 532 nm wavelength [238, 239].

Figure 3.17 shows a scan on a multilayer structure with 500 nm cubic GaN grown on 10.4 μm 3C-SiC on a silicon substrate. Here, between the surface signal and the signal from the silicon substrate a positioner

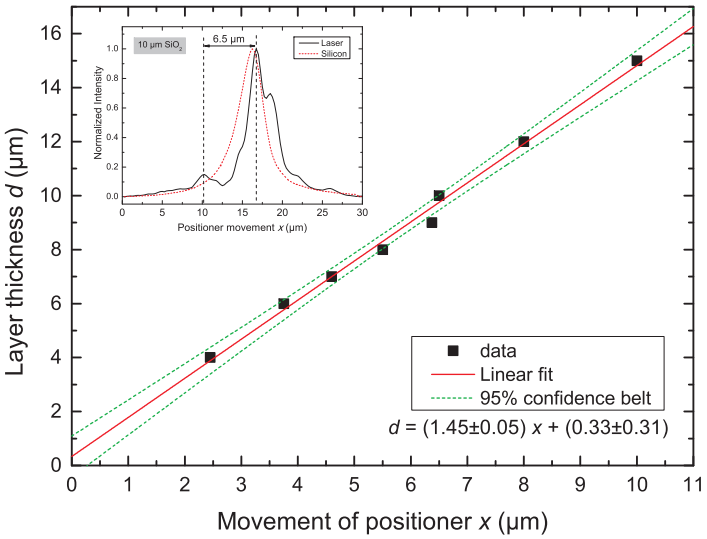

Fig. 3.16 Layer thickness d as a function of positioner movement x required to see the maxima in the reflected laser light from the air/SiO_2 and SiO_2/Si interfaces. The inset shows the line scan obtained on the 10 μm sample.

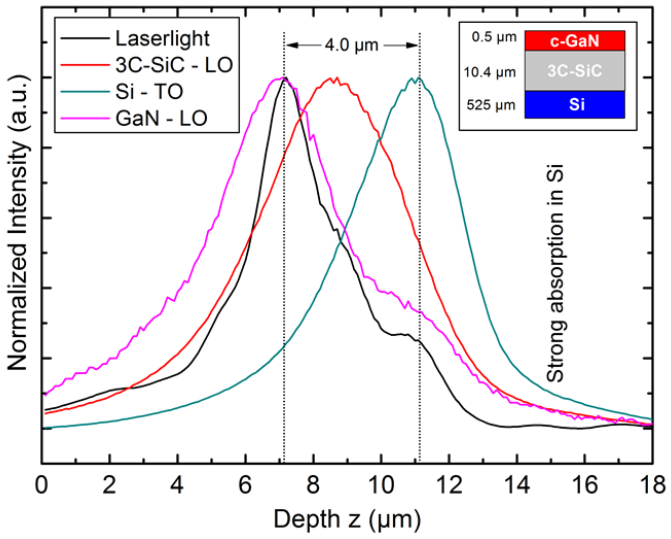

Fig. 3.17 Result of a axial confocal Raman line scan on a multilayer structure of 500 nm cubic GaN grown on 10.4 μm 3C-SiC on a silicon substrate. Scanning the complete multilayer structure results in about 4 μm positioner movement to scan the complete structure.

movement of 4 μm is required. Taking the refractive index for 3C-SiC of $n(\text{3C-SiC}) = 2.675$ [216] into account, yields a thickness of $d = n(\text{3C-SiC}) \cdot 4\mu\text{m} = 10.7\mu\text{m}$, which is a reasonable well result taking the depth resolution into account.

With this model we are able to obtain the right depth in most experiments. The model was verified for the numerical aperture $NA = 0.7$ and due to the nature of Gaussian optics the model should be correct for numerical aperture smaller than this. However for larger NA one should be cautious. Here, Gaussian optics is not the right tool anymore to describe focused beams. Instead one has to consider point spread function models to accurately describe intensity distribution in the focus. One could speculate, that due to the universal nature of optical path length conservation, the correction for depth may still hold true. However, large numerical apertures combined with high refracting and/or birefringent materials, will result in heavily distorted foci (compared to a Gaussian beam), which has been analyzed in many simulations [241–243]. Large birefringence may even result in polarization dependent focusing or a double focus for a given system.

Chapter 4

Spectroscopic analysis

After the discussion of the basic background of this work in the previous two chapters, this chapter will now present the first major experimental results. In this chapter the results of the spectroscopic analysis on the two material systems, $LiNbO_3$/$LiTaO_3$ and the $KTiOPO_4$ material family will be presented. This analysis presents the basis for the interpretation of the spatially resolved analysis on waveguides and domain structures in the following chapters.

A short notice is given regarding the units and nomenclature. In many works concerning Raman spectroscopy the frequency shift - usually called *Raman shift* - with respect to the Rayleigh scattered laser light is noted in wavenumbers in units of cm^{-1} instead of frequency. Frequency and wavenumber are directly proportional to the energy and each other. Due to this fact in many works *frequency* and *wavenumber*, although not being exactly the same thing, are used synonymously to name the Raman shift. If not noticed otherwise, this nomenclature will also be used here and *frequency*, *Raman shift* and *wavenumber* will be used synonymously in this work.

4.1 $LiNbO_3$ and $LiTaO_3$

$LiNbO_3$ and $LiTaO_3$ are studied for several decades with Raman spectroscopy in numerous publications. Nevertheless, there is still an ongoing debate about the correct assignment and spectral positions of phonon modes in this material system. Therefore the first part of this section is dedicated to the assignment of phonons in this material. The second part will then deal with the spectral signatures of doping in $LiNbO_3$ and its interpretation. The correct assignment of phonon modes to the symmetry species and the identification of their longitudinal or transverse character, as well as the exact knowledge of their spectral position is important for further analysis and the general understanding of the material system. In particular the phonon frequencies and intensities are directly connected to the electro-optic constants [48] and the dielectric properties [36, 37].

4.1.1 Phonons in the $LiNbO_3$ system

In their ferroelectric phase $LiNbO_3$ and $LiTaO_3$ are described in an orthorhombic unit cell containing two formula units. This results in 30 vibrational degrees of freedom and hence 27 optical phonons. With respect to group theory the vibrations for this system at the Brillouin zone center can be subdivided in the irreducible representations A_1, A_2 and E as follows

$$\Gamma_{vib} = 4A_1(\mathrm{R, IR}) + 5A_2 + 9E(\mathrm{R, IR}). \tag{4.1}$$

Table 4.1 Observable phonon modes and Raman tensor elements for back scattering configurations in $LiNbO_3$ and $LiTaO_3$.

Scattering configuration	Symmetry species	Tensor element	
		TO	LO
x(y,y)$\bar{x}$	A_1-TO, E-TO	a^2+c^2	
x(y,z)$\bar{x}$	E-TO	d^2	
x(z,y)$\bar{x}$	E-TO	d^2	
x(z,z)$\bar{x}$	A_1-TO	b^2	
y(x,x)$\bar{y}$	A_1-TO, E-LO	a^2	c^2
y(x,z)$\bar{y}$	E-TO	d^2	
y(z,x)$\bar{y}$	E-TO	d^2	
y(z,z)$\bar{y}$	A_1-TO	b^2	
z(x,x)$\bar{z}$	A_1-LO, E-TO	c^2	a^2
z(x,y)$\bar{z}$	E-TO	c^2	
z(y,x)$\bar{z}$	E-TO	c^2	
z(y,y)$\bar{z}$	A_1-LO, E-TO	c^2	a^2

Here, the four A_1 modes are infrared (IR), as well as Raman active (R) and represent vibrations, which conserve the crystal symmetry during the vibration. The five A_2 vibrations are completely silent in Raman and IR. The nine E type phonons are twofold degenerate. They are IR, as well as Raman active. Because both, A_1 and E modes, are both Raman and IR active, the vibrations are associated with long range electric fields. This results in the lift of the LO-TO degeneracy at the zone center. Therefore, the usual way of numbering Raman modes in $LiNbO_3$ and $LiTaO_3$ counts four A_1-TO modes, four A_1-LO modes, as well as nine E-TO modes and E-LO modes. In total 22 fundamental Raman modes are expected to appear in the spectra.

As discussed in Sec. 3.1 polarization-dependent Raman scattering in crystals can be described in terms of Raman tensors. $LiNbO_3$ and $LiTaO_3$ crystallize in the symmetry group C_{3v}. The Raman tensors for this group is given by [196, 197, 244]

$$A_1(z)=\begin{pmatrix} a & 0 & 0\\ 0 & a & 0\\ 0 & 0 & b\end{pmatrix}, E(y)=\begin{pmatrix} c & 0 & 0\\ 0 & -c & d\\ 0 & d & 0\end{pmatrix}, E(-x)=\begin{pmatrix} 0 & -c & -d\\ -c & 0 & 0\\ -d & 0 & 0\end{pmatrix}. \tag{4.2}$$

Here, the letter in brackets denotes the direction of propagation of the phonons. The A_1 phonons, for example, propagate in z-direction. Knowing the propagation direction allows further to distinguish TO and LO modes depending on the scattering geometry. The scattering configurations and the corresponding symmetry species for $LiNbO_3$ and $LiTaO_3$ are summarized in Tab. 4.1. One can see, that E-type phonons are mainly expected for crossed polarizations, while A-type phonons are expected in parallel configurations. Due to symmetry reasons, E-LO modes can only be observed in a single scattering configuration. Overall, by comparing the available scattering geometries one should be able to unambiguously distinguish E- and A_1-type modes.

The basic Raman spectra for all scattering configurations in $LiNbO_3$ and $LiTaO_3$ are shown in Figs. 4.2 and 4.1, respectively. Each spectrum is labeled by the respective scattering geometry in Porto's notation and the expected symmetry species according to Tab. 4.1. For a better comparability of the spectra, the dark count level has been subtracted and the spectra have been normalized to maximum. For better visibility the single spectra are then plotted with an offset of 0.5. Because the Raman tensor (and the dielectric tensor) is symmetric, there is no difference expected between crossed polarizations, which is confirmed in the experiment. It holds z(x,y)$\bar{z}$ = z(y,x)$\bar{z}$. Consequently only one of each spectrum is shown.

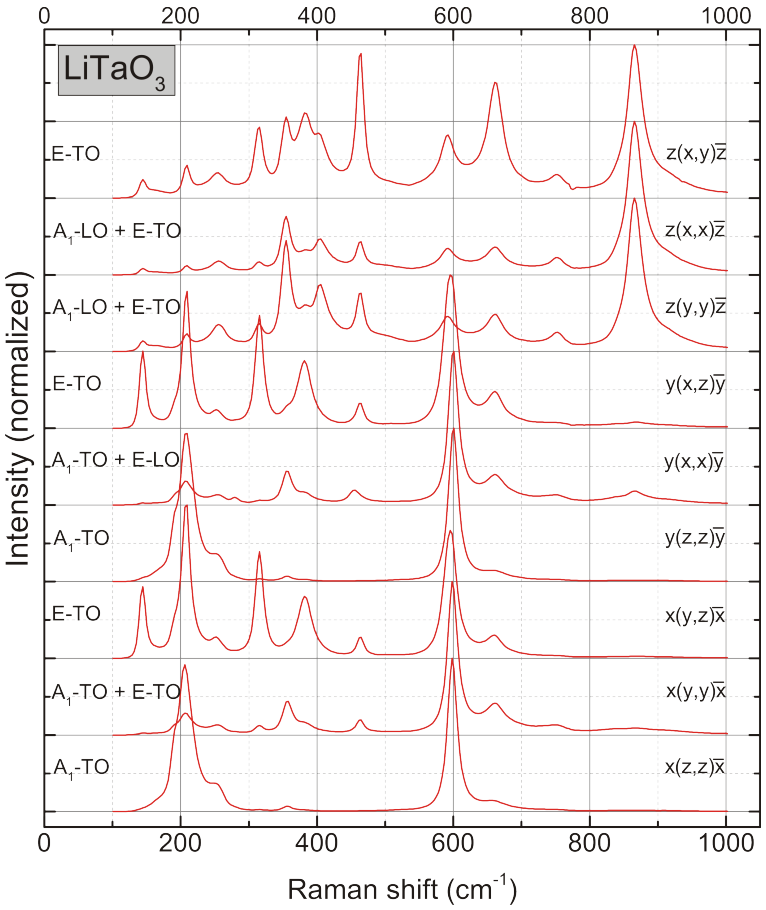

Fig. 4.1 Complete set of back-scattering Raman spectra of $LiTaO_3$.

At first glance one can immediately see, that the spectra of $LiNbO_3$ and $LiTaO_3$ show many similarities with respect to peak position, relative intensities and general spectral shape. This can be expected, because both materials are isostructural at room temperature as discussed before in Sec. 2.1 and the main difference is the substitution of tantalum ions with niobium ions.

A closer examination of the spectra reveals four clearly identifiable A_1-TO phonons for both materials. They can be best identified in the x(z,z)$\bar{\text{x}}$ and y(z,z)$\bar{\text{y}}$ configuration, which exclusively is expected to show A_1-TO modes. In the recorded spectra for $LiNbO_3$ these peaks are centered at 252, 273, 331 and 632 cm^{-1} and at 206, 252, 357 and 598 cm^{-1} for $LiTaO_3$, respectively. Commonly these modes are enumerated A_1-TO_1 to A_1-TO_4 from low to high wavenumbers. The measured Raman shifts are in very good agreement with literature [245, 76, 22, 246–248, 44] and can unambiguously be identified.

A similar observation is made for the A_1-LO modes. Longitudinal A_1 modes propagate along the z-axis. Therefore, the corresponding A_1-LO modes can only be observed for z(x,x)$\bar{\text{z}}$ and z(y,y)$\bar{\text{z}}$ in back-scattering geometries. Due to the selection rules also E-type phonons are present in these spectra. By careful comparison the Raman shifts of the A_1-LO modes are detected at 274, 330, 422 and 871 cm^{-1} for $LiNbO_3$ and 255, 355, 403 and 866 cm^{-1} for $LiTaO_3$. The enumeration is alike to the TO modes with A_1-LO_1 to A_1-LO_4 from low to high wavenumbers. The A_1-LO appear generally weak in intensity compared to the E-TO modes of the same scattering geometry, with the exception of the A_1-LO_4, which dominates the spectra and is even visible as a

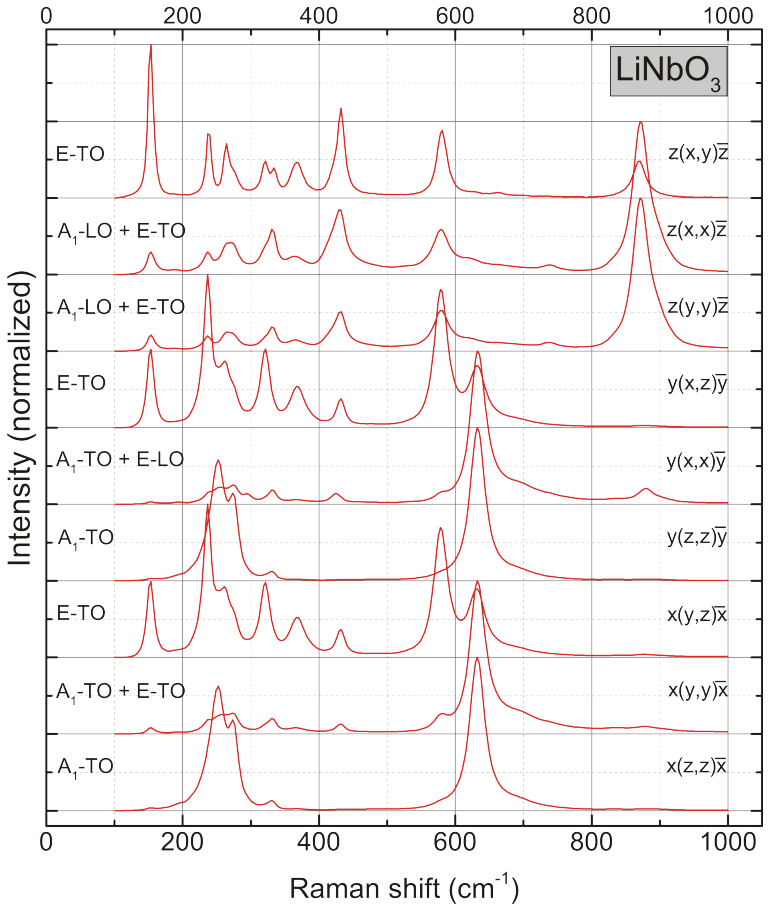

Fig. 4.2 Complete set of back-scattering Raman spectra of $LiNbO_3$.

leakage mode in z(x,y)$\bar{z}$ crossed polarization geometry. Overall, again the vibrations can be clearly assigned to the A_1-LO symmetry and correspond with the observations in literature [245, 76, 22, 246–248, 44].

These things are different, when the E-type phonons are concerned. The E modes are best observed in the crossed polarization geometries, where no A_1 modes are present, e.g. z(x,y)$\bar{z}$ or x(y,z)$\bar{x}$ which show E-TO modes. But the modes are also present for parallel polarization, e.g. z(y,y)$\bar{z}$ together with the A_1 species. Therefore, by carefully comparing all geometries, a concise identification should be possible. However, this analysis reveals only seven peaks unambiguously belonging to E-TO modes in $LiNbO_3$ and eight peaks in $LiTaO_3$ out of the total E-TO modes expected. These are centered at 150, 237, 263, 320, 367, 432 and 580 cm^{-1} in $LiNbO_3$ and 144, 210, 255, 315, 383, 462, 592 and 660 cm^{-1} in $LiTaO_3$. Indeed, when we look into literature the modes noted above are agreed on by most authors to be E-TO modes, whereas the missing modes are proposed to be at various spectral positions. And this issue has been pointed out by several authors [249, 47, 245, 250].

Indeed if we examine the spectra in Fig. 4.2 and 4.1 in closer detail there are still multiple candidates for the missing modes. In the z(y,y)$\bar{z}$ configuration both materials show a peak around 740 cm^{-1}, where selection rules suggest an E-TO. Alike in z(x,y)$\bar{z}$ shows for both materials a peak in the range between 150 and 200 cm^{-1}, which is shown in detail later in Fig. 4.15. A shoulder in this range is also visible for $LiTaO_3$ in x(y,z)$\bar{x}$, while in $LiNbO_3$ a strong candidate for a missing E-TO mode is a shoulder at 610 to 620 cm^{-1} in z-incident

configuration. This is of particular interest, as this spectral range has been found to be very sensitive to the presence of ferroelectric domain walls and can be used for Raman imaging [54, 46, 251, 252]. Because none of these features appear in all geometries, it is difficult to assign them to fundamental modes, as other explanations, e.g. defect or stoichiometry related modes or combination bands, are possible.

Thus, in literature many authors have tried to assign the missing modes. In the first extensive Raman analysis of $LiNbO_3$ and $LiTaO_3$ Kaminow and Johnston (1967 and 1968) assigned two peaks at 92 and 620 cm^{-1} in $LiNbO_3$ [48] and 74 cm^{-1} [253] in $LiTaO_3$ to the missing E-TO modes. In the same year Barker et. al. [44] suggested the fundamental E-TO modes in $LiNbO_3$ at 299 and 880 cm^{-1}, while they suggested the feature at 177 and 610 cm^{-1} to be a mixed phonon propagating at 45° with respect to the z-axis. In IR spectroscopy they observed an E-TO at 660 cm^{-1}, but they could not verify whether the structure in their Raman spectra at 670 cm^{-1} is fundamental or a combination band. The spectral features in IR they observed at 686 and 692 cm^{-1} they suggested to be combination bands. In 1972 Claus et. al. [254] identified the structures at 668 and 743 cm^{-1} to be E-TO modes, while Yang et. al. (1987) [246] suggested these structures to be combination bands in $LiNbO_3$ and $LiTaO_3$. Instead they concluded based on their directional analysis of both materials that the E-TO modes at 152 cm^{-1} (142 cm^{-1}) in $LiNbO_3$ ($LiTaO_3$) are the superposition of two E-TO modes and therefore explain the apparent absence of one mode in both systems. Based on their spectroscopy on stoichiometric and congruent $LiNbO_3$ and a temperature dependent analysis Ridah et. al. (1997) [247] concluded any structures in the 100 cm^{-1} and 700 cm^{-1} ranges to be related to two phonon processes, while the fundamental modes are at 177 and 610 cm^{-1}. Alike Repelin et. al. (1999) [76] named the frequencies of the missing E-TOs to be 180 and 610 cm^{-1} in $LiNbO_3$, while suggesting 180 cm^{-1} to be the frequency of the missing mode in $LiTaO_3$. But in their comparison of $^6LiNbO_3$ vs $^7LiNbO_3$ and $LiTaO_3$, they concluded no E-TO in the region above 650 cm^{-1} in $LiTaO_3$, but instead two overlapping E-TO modes at 597 cm^{-1}. In 2006 Shi et. al. [47] noted the problem of many different assignments. In their analysis of $LiTaO_3$ they detected no band at 90 cm^{-1} in $LiTaO_3$ and a fundamental mode at 190 cm^{-1}. In their review article Fontana and Bourson [22] named modes at 186 and 738 cm^{-1} to be the missing E-TOs and did not mention the contradictory assignments in literature.

Just like in experiments also in theoretical work many contradicting assignments have been stated. For example Caciuc et al. [255] and Parlinski et. al. [256] calculated 167 and 617 cm^{-1} and 423 and 690 cm^{-1} to be fundamental E-TO frequencies. Based on calculated Raman spectra and a detailed literature review Hermet et. al. (2007) [249] concluded that one missing mode at 677 cm^{-1} has a vanishing intensity in $LiNbO_3$ and therefore cannot be detected. The other missing mode they concluded to be part of two superpositioned peaks at 370 and 384 cm^{-1}, which usually cannot be detected separately in Raman or IR-spectroscopy, because one is strong in IR spectroscopy, while the other is dominating in Raman experiments. Hence, in either experiment one always dominates and superimposes the other mode. This suggestion was experimentally checked by Margueron et. al. [245] in 2012 by low temperature Raman spectroscopy, where they could show that the peak at 370 cm^{-1} in $LiNbO_3$ and 380 cm^{-1} $LiTaO_3$ can indeed by separated into a weak and strong peak in a low temperature environment, however only for stoichiometric material. Alike the peak at 660 cm^{-1} was shown to vanish in intensity with growing Nb-content in mixed crystals, while in IR a signature of a TO phonon remains at 660 cm^{-1} for $LiNbO_3$. For E-LO modes the situation is even more complicated, as they appear in only one back scattering geometry. They are generally weak in intensity compared to E-TO modes and the spectrum containing E-LO modes is therefore prone to leakage modes [245].

The goal of this work is now to review the assignments made by Margueron et. al. and Hermet et. al. based on our data and to make a definite assignment of phonon modes. We address this issue with calculated Raman

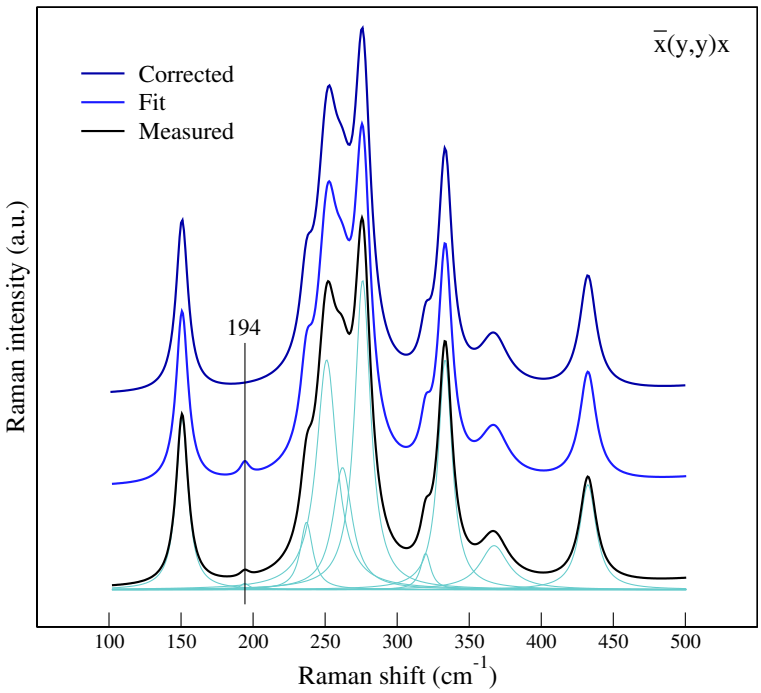

Fig. 4.3 The graph shows how the experimental data was corrected for comparison with the calculated spectra. For the correction, the measured spectra have been fitted with a Lorentzian function and all non-fundamental and LO related peaks have been neglected.

spectra (intensity and wavenumber) by ab-initio-theory and by the analysis mixed of crystals by experiment and theory in the next two chapters.

4.1.2 Theoretical calculation of Raman Spectra

As we have seen, there is a major unclarity about the correct assignment of phonons in the $LiTaO_3$ - $LiNbO_3$ crystal system. Therefore, to gain more insight the Raman spectra - i.e. intensity and spectral position - have been calculated in a DFT framework. The calculation was developed and performed by S. Sanna and S. Neufeld and so far successfully applied to $LiNbO_3$ and $LiTaO_3$ [70] and Au nanowires on silicon [257]. As we will now discuss, the calculated Raman spectra enables to understand some of the peculiarities in assignment as discussed above and helps to establish a concise assignment of the phonon modes.

The method used in this analysis allows to calculate fundamental Raman spectra of TO modes [70]. However, it does not include the long-range electric fields that accompany longitudinal phonons. For this reason, we limit ourselves to the investigation of transverse modes. Therefore, to have an accurate comparison of experimental and theoretical data, the experimental data needs to be corrected for any LO modes, as well as any non fundamental modes, e.g. multi-phonon scattering peaks. Here, the procedure is displayed in Fig. 4.3. All features in each analyzed spectrum were fitted with a Lorentzian function. Then all features, which were identified as non-fundamental or LO related, are neglected and the corrected spectrum has been recalculated based on the fitting parameters.

Figure 4.4 shows a comparison of the calculated Raman spectra for all tensor elements of both material with the measured spectra. Here, the calculated modes can be assigned and named unambiguously, while the modes in the experimental spectra are labeled with respect to the assignment by Margueron et. al. and

Hermet et. al. (see Sec. 4.1.4). For the calculated spectra it should be noted, that the ab initio theory yields the intensity as a scalar and the center frequency for each mode, but no value for the FWHM, which even in the experiment is dependent for each mode on many properties, such as temperature, crystal composition and stoichiometry. Therefore, for the simulated spectra a FWHM of 12 cm^{-1} was assumed for every mode. A FWHM of 12 cm^{-1} represents a typical average observed also in the experiment for stoichiometric material, where FWHM between 10 cm^{-1} for the E-TO_1 and 20 cm^{-1} for the A_1-TO_4, for example, have been observed in our analysis for stoichiometric $LiNbO_3$. Qualitatively the calculated spectra show a good agreement with the experiment and the calculation is able to reproduce the typical observed spectral shapes. Quantitatively the calculation yields frequencies with a typically deviation of 10 cm^{-1}. The calculated and measured frequencies are summarized in the section summary in Sec. 4.1.4 and will not be further discussed here.

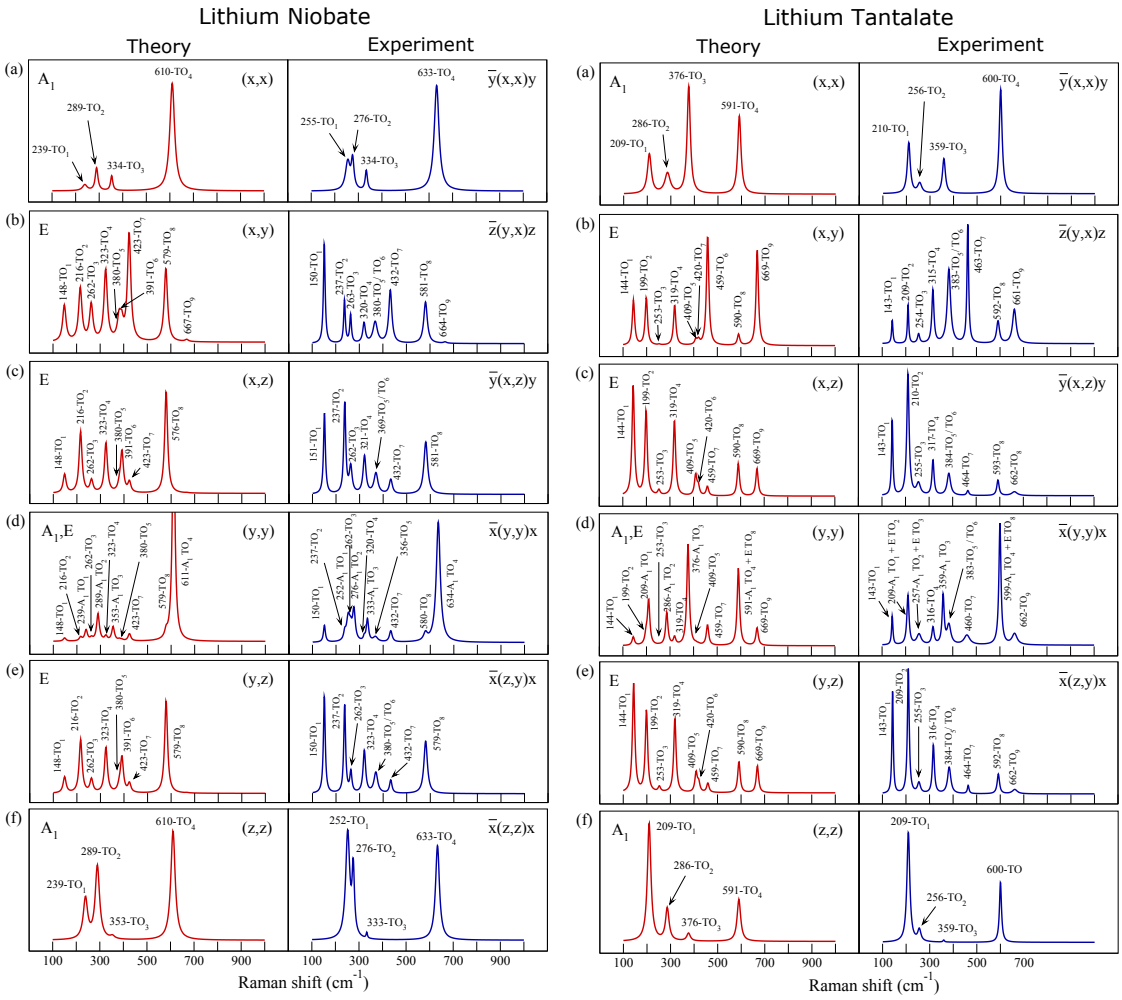

Fig. 4.4 Calculated Raman spectra based on the method from Ref. [70].

In the previous section it was stated, that in lithium niobate only seven of nine E-TO modes are consistently identified in literature. One of these modes is the highest frequency E-TO mode, the E-TO_9. This discrepancy can be solved by comparing the calculated and experimental spectra of $LiNbO_3$ and $LiTaO_3$. Theory predicts for $LiTaO_3$ the E-TO_9 to appear at 669 cm^{-1} with a fairly high intensity comparable to the neighboring E-TO_8

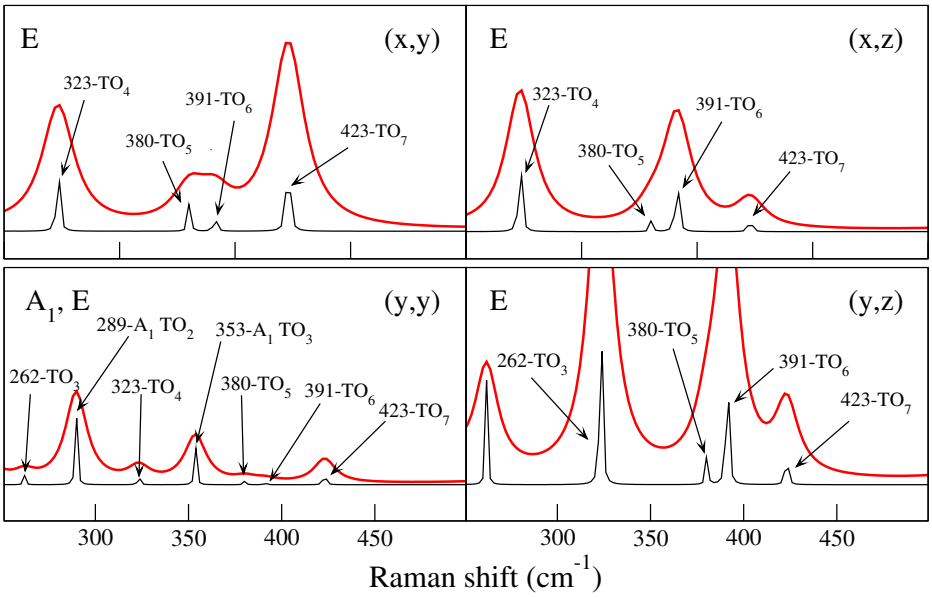

Fig. 4.5 Enlargement of the calculated $LiNbO_3$ Raman spectra of Fig. 4.4a) for all scattering configurations allowing the detection of the *E*-TO modes. The red line corresponds to the spectra shown in Fig. 4.4, the black curve shows the exact position of the Raman peaks. The Raman intensity is expressed in arbitrary units.

or even higher in some scattering configurations, e.g. in z(y,x)$\bar{z}$. This is confirmed for the experiment, where the E-TO_9 is observed as a fairly intense peak at 661 cm^{-1}, as seen in Fig. 4.4c in the z(y,x)$\bar{z}$ configuration. If we now observe this mode in lithium niobate, theory shows the E-TO_9 at almost the same frequency (667 cm^{-1}), but with almost vanishing intensity for all scattering configurations. Therefore in the experiment, the E-TO_9 is usually not detectable and other features, such as a multi-phonon related peak around 740 cm^{-1} or a shoulder centered about 620 cm^{-1} has been mistaken for this particular vibration. As we will see in the next chapter for mixed crystals we can demonstrate that this peak vanishes with increasing Nb content confirming the behavior of the E-TO_9.

Why does the E-TO_9 behave so differently in $LiNbO_3$ compared to $LiTaO_3$? As seen from the atomic displacements patterns shown in Figs. 4.9 and 4.13 in the next chapter the E-TO_9 represents a distortion of the oxygen cage and is a pure vibration of the oxygen cage. Because no Nb or Ta is involved in the vibration and the electronic binding forces are similar, this mode has almost the same frequency in both materials. Yet, the mode shows a massively different behavior in terms of intensity. This may be explained by the different bond length and electron affinity of Nb vs Ta. While the Nb-O bond length is 2.02 Å the Ta-O length of about 1.99 Å is slightly shorter. Here, in $LiTaO_3$ the E-TO_9 represents a larger relative distortion of the Ta-O bond length. The electron affinity of Ta is smaller, than those of Nb - meaning the Ta-O bond is of more covalent nature, which may be associated with a larger change in polarizability and hence a larger Raman scattering cross section.

The story of the second mode with unclear assignment in both, $LiNbO_3$ and $LiTaO_3$, can also be solved with the help of the theoretical calculation. In the theory as well as the experiment it is possible to identify the first four Raman modes (E-TO_1 to E-TO_4) for both materials by comparing the spectra. When we examine the next two E-TO phonons in the theoretical analysis, we find for both materials the E-TO_5 and E-TO_6 to be adjacent and only to be separated by 11 cm^{-1}. A detailed view of the calculated spectra for $LiNbO_3$ is shown in Fig. 4.5. Here, one can clearly see that the E-TO_5 and E-TO_6 do overlap in the calculated spectra (solid red

line) for an arbitrary width of $12\,cm^{-1}$. The overlapping should allow a separation in the experiment. However, for neither configuration both modes have comparable intensity and one always dominates the other. This can be seen from the black curves, which show the exact position and intensities of the modes. In total this results in apparently one detectable band in the experiment. Indeed in the experiment it was not possible to fit the peak conclusively with two Lorentzian, therefore it was treated as a single peak. Although we are not able to distinguish both peaks in our investigation we can still spot minor differences. While theory suggests for the (y,x) and (y,y) geometries a dominating E-TO_5, the E-TO_6 should be of higher intensity in the (x,z) and (y,z) geometries. Indeed in the experiment on $LiNbO_3$ we find for the z(y,x)$\bar{z}$ geometry the fitted peak centered at $367\,cm^{-1}$, while for x(y,z)$\bar{x}$ the peak is centered at a slightly higher frequency at $369\,cm^{-1}$. Our theoretical investigation is confirmed by recent low temperature spectroscopy [245] and previous theoretical results [249]. In conclusion the combination band of the E-TO_5 and E-TO_6 will be labeled E-$TO_{5/6}$ for the remainder of this work.

So far, we have established a mode assignment and have identified the "missing" modes. To confirm our mode assignment and to further study the material systems, $LiNb_{(1-x)}Ta_xO_3$ mixed crystal will now be analyzed over the complete compositional range and the measured frequencies will be compared with DFT based calculations.

4.1.3 $LiNb_{(1-x)}Ta_xO_3$ mixed crystals

In general, mixed crystals offer a way to control material properties via composition. For example in the field of semiconductors mixed crystals, e.g. AlGaAs oder AlGaN, are a standard procedure for material property tailoring, in particular the band gap. Also in the more relevant field of ferroelectric piezoceramics, e.g. $Pb(Zr_xTi_{1-x})O_3$, components are mixed to control piezoelectric and many other properties [258]. Alike in (linear) integrated optics, silicon oxynitride (SiO_xN_y) is widespread used to fabricate high index contrast waveguide structures. This enables high mode confinements and small bending radii [259]. However, mixed crystalline materials for use in nonlinear (integrated) optics mixed have not been studied extensively. $LiNb_{(1-x)}Ta_xO_3$ mixed crystals presents a perfect model system for such a study. What makes $LiNb_{(1-x)}Ta_xO_3$ particular interesting is the control not only of the refractive index, but of the birefringence by composition. $LiTaO_3$ is positively birefringent, while $LiNbO_3$ is negatively birefringent. Therefore, a compound with $x = 0.93 - 96$ exists with vanishing birefringence at room temperature, which has been shown in experiment and theory [260–262]. The resulting material is an optically isotropic crystal that retains the exclusive advantages of ferroelectrics, such as the large electro-optic and nonlinear coefficients [263].

However, there are not many studies dealing with $LiNb_{(1-x)}Ta_xO_3$. Most studies have focused on crystal growth and lattice parameters [264, 263, 69], as well as the thermal expansion characteristics [263] and Curie temperature of the systems have been determined [263, 265]. Furthermore, the refractive indices and birefringence have been determined [261, 260]. More recently, crystals growth with alternative methods has been investigated. Here, near-stoichiometric mixed crystals have been obtained [69, 265]. The Li stoichiometry has been determined experimentally and found to be between the values observed for . The linear and nonlinear optical susceptibilities have been calculated by the chemical bond method [266] and ab initio theory [262]. Furthermore, the zone center frequencies of A_1 phonons have been calculated [267].

To study the phonons and Raman spectra of the LN material system further, $LiNb_{(1-x)}Ta_xO_3$ mixed crystals have been grown and studied by Raman spectroscopy and theory. The mixed crystal used in this experiment have been grown by the group of Prof H. Zhang by Y. Wang and H. Yu (all Shandong University, Jinan, PR China) and precharacterized with x-ray diffraction, before being sent to Paderborn to be studied by Raman

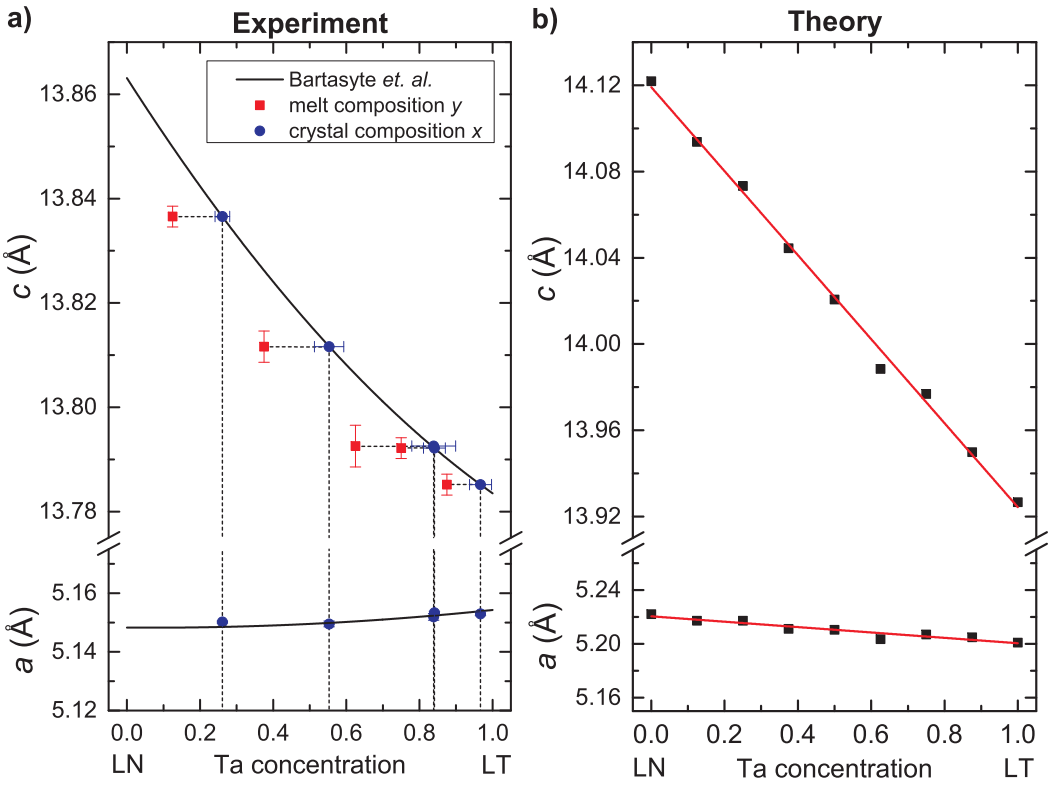

Fig. 4.6 a) Measured and b) DFT LNT lattice parameters as a function of the Ta concentration. The red squares are the measured lattice parameters plotted with respect to the melt composition y. The solid line shows the crystal composition x as extrapolated from Eq. 4.3.

spectroscopy. The theory was provided by S. Neufeld and S. Sanna. Due to the high computational demand for calculating the large unit cells required to represent mixed crystal, the theoretical results represented in this chapter will be limited to calculated gamma-point frequencies. More details regarding the calculation method can be found in the respective publications [70, 267, 268].

Crystal growth and lattice parameters

The niobium atom can be substituted by the electronically almost identical Tantalum atom leading to LNT mixed crystals over the complete compositional range [263, 69, 260]. The crystals in this study have been grown by the Czochralski method from a melt, which was obtained from mixed commercial $LiNbO_3$ and $LiTaO_3$ powders as discussed in more detail in Ref. [268]. The crystals were pulled from the melt by using a c-axis oriented lithium niobate crystals as seed. Melt compositions with $LiNbO_3$/$LiTaO_3$ proportion of 0.125:0.875, 0.25:0.75, 0.375:0.625, and 0.625:0.375 were used. The obtained crystals were then cut and polished along the main axes. The set of mixed crystals was completed by commercially obtained congruent $LiNbO_3$ and $LiTaO_3$.

The samples were pre-characterized with XRD measurements. The XRD measurements confirm well formed crystals in the lithium niobate crystal structure and allow to determine the (hexagonal) lattice parameters, which are summarized in Tab. 4.2. For lithium niobate tantalate mixed crystals it was previously observed by several authors, that the crystals grow tantalum rich, which means that the tantalum atom is more likely to be built into the crystal, than to remain in the liquid phase [264, 263, 69]. Therefore, the initial melt composition y is not identical with the actual tantalum percentage $x = [\mathrm{Ta}]/([\mathrm{Ta}]+[\mathrm{Nb}])$ in the crystals and as a prerequisite

Table 4.2 Measured $LiNb_{1-x}Ta_xO_3$ hexagonal lattice parameters with respect to the Ta concentration in the melt y and the actual Ta concentration in the crystals x.

Ta concentration in melt y	Ta concentration in crystal x	Lattice parameters c in Å	a in Å
0.125	0.261 ± 0.02	13.837 ± 0.002	5.150
0.375	0.553 ± 0.04	13.812 ± 0.003	5.150
0.625	0.839 ± 0.06	13.793 ± 0.004	5.152
0.75	0.841 ± 0.03	13.792 ± 0.002	5.153
0.875	0.967 ± 0.03	13.785 ± 0.002	5.153

for the Raman analysis the tantalum percentage x needs to be determined. The hexagonal lattice parameter c is known from literature to heavily depend on the crystal composition in $LiNb_{1-x}Ta_xO_3$ and the exact composition dependence of c is known in literature. This information can be used to calibrate the crystal composition.

In their work Bartasyte *et. al.* have analyzed the relationship for stoichiometric and congruent mixed crystals [69] and found the following non-vegard relationship with a slight bowing of the form

$$p(x) = xp_{\mathrm{LT}} + (1-x)p_{\mathrm{LN}} + bx(1-x), \tag{4.3}$$

where p_{LT} and p_{LN} describe the lattice parameters for pure $LiNbO_3$ and $LiTaO_3$. For congruent material Bartasyte *et. al.* determined the bowing parameter $b = -0.03$ for the lattice parameter c and $b = -0.007$ for cell parameter a. Based on the commonly accepted hexagonal lattice parameters for congruent $LiNbO_3$ and $LiTaO_3$ [76–79, 69] we have determined the tantalum percentage in our crystals, i.e. $a_{\mathrm{LT}} = 5.1543$ Å, $c_{\mathrm{LT}} = 13.7835$ Å, $a_{\mathrm{LN}} = 5.1483$ Å and $c_{\mathrm{LN}} = 13.8631$ Å.

The calculation is graphically displayed in Fig. 4.6a). Here, the measured lattice parameters are plotted with respect to the melt composition and projected on the assumed literature behavior shown as a solid line. Based on the standard error in the measurement, also the error in the determined crystal composition can be estimated by projecting the confidence interval of the measurements on the assumed behavior. The results are summarized in Tab. 4.2. The observed differences in crystal composition versus the melt compositions are largest for small Ta percentages, where a $y = 0.125$ result in a more than double as large crystal composition $x = 0.261$, while gradually decreasing to the Ta rich side. This is a behavior also observed by other authors [263] before.

The experimentally determined lattice parameters, the calibrated Ta crystal composition and the results from the theoretical calculation are plotted in Fig. 4.6a) and b). Here, the theoretical calculation reveals an almost vegard-like decrease of the lattice parameters c in accordance with the experimental data. In contrast to this, the lattice constant a is only affected in a minor way by mixing. The decrease in the lattice constant can be explained in terms of a smaller covalent radius of the Ta^{5+} vs Nb^{5+} (1.46 Å vs 1.47 Å), as well as stronger, and therefore shorter Ta-O bonds compared to Nb-O bonds (1.997 Å vs 2.038 Å), as revealed by the calculation. Interestingly, the lattice parameter a shows an opposing behavior in the calculation vs. the measurements, which may be explained by the congruent nature of the grown crystals, while the calculation only refers to stoichiometric crystals. The calculation suggest an vegard-like behavior with no pronounced bowing, which is in agreement with Bartasyte *et. al.*, who show that the bowing is much less pronounced for stoichiometric mixed crystals [69].

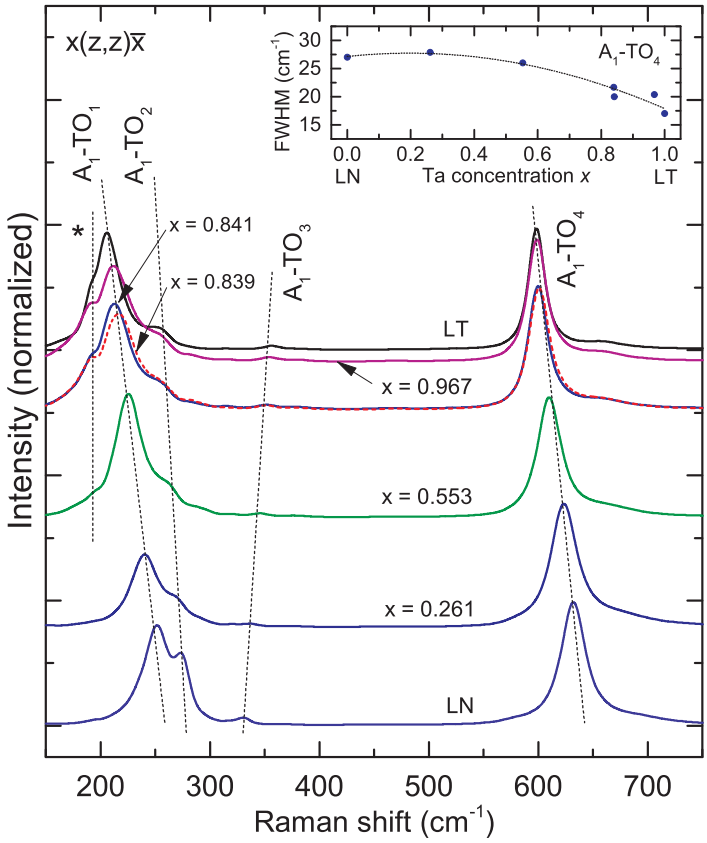

Fig. 4.7 Normalized Raman spectra obtained in x(z,z)$\bar{x}$ scattering geometry showing the behavior of A_1-TO modes in $LiNb_{1-x}Ta_xO_3$ mixed crystals. For better visibility the spectra have been separated by an artificial offset proportional to the Ta content x. Four A_1-TO modes predicted by the theory can be identified in all spectra. The inset shows the measured FWHM of the A_1-TO_4 mode as a function of the Ta concentration, showing a clear decrease for Ta rich crystals.

A_1-type phonons

As the Ta ration x in the crystals is now determined, the vibrational analysis can be performed and the previously established phonon assignment from Sec. 4.1.2 can be verified and further refined based on the mixed crystal analysis. Figure 4.7 shows the x(z,z)$\bar{x}$ spectra of the grown mixed crystals compared with the spectra of $LiNbO_3$ and $LiTaO_3$. As seen before, these geometry provides exclusively A_1-TO phonons, which are easy to identify. For comparison, the dark count has been subtracted and the spectra have been normalized to the maximum. For better visibility and to highlight the influence of the stoichiometric position, the spectra a separated by an artificial offset proportional to the Ta composition x. Here, the spectra of $LiNbO_3$ and $LiTaO_3$ are separated by a constant offset, while the mixed crystals are plotted in between with their baseline offset shifted proportional to the value of x.

For each composition, four peaks in a similar spectrum to the $LiNbO_3$ and $LiTaO_3$ can clearly be identified. The peaks all show a systematic shift with respect to composition and no change in general peak structure. Only for high Ta compositions an additional feature labeled with an asterisks is visible, which will be discussed further below. The inset shows the FWHM of the A_1-TO_4 mode as a function of Ta concentration. The FWHM was obtained by fitting a Lorentzian to the A_1-TO_4. The FWHM shows a clear decrease towards $LiTaO_3$. This observation can also be made for other modes (also E-type phonons) and may be explained by a better Li stoichiometry for Ta rich samples. The FWHM of the phonon modes has been established in previous studies to be sensitive to the crystal stoichiometry [69, 269, 22]. This is in agreement with the observation of a better Li stoichiometry for congruently grown $LiTaO_3$ compared to congruent $LiNbO_3$.

The observed peak frequencies of the A_1-TO modes, as well as the A_1-LO phonon, which have been obtained in z(y,y)$\bar{z}$ and z(y,y)$\bar{z}$ configurations, are plotted for each phonon in Fig. 4.8a) and c) versus the Ta composition and are compared with the theoretical predictions in Fig. 4.8b). Here, the frequencies of the A_1-TO_1, A_1-TO_2 and A_1-TO_4 and the respective LO modes decrease, while the A_1-TO_3 increases in frequency. A general decrease in frequency should be expected, when the Nb atom is substituted by the almost double as massive Ta atom (92.92 a.u. vs 180.948 a.u.). Here, the three decreasing modes all involve displacement patterns involving directly or indirectly the Ta/Nb atom as shown in Fig. 4.9, where the atomic displacements are shown. The A_1-TO_3, however, involves a rigid rotation of the oxygen cage in the xy-plane. It increases in frequency due to the stronger Ta-O bonds and shorter Ta-O bond lengths. Theory generally suggest the same trends and the same magnitude of the shift, however does not suggest a shift for the A_1-TO_2 mode. This may be explained by the congruent nature of the crystal, as the A_1-TO_2 mode involves the oxygen cage, as well as the lithium atoms as shown in Fig. 4.9 all in a motion along the z-axis of the crystal. Therefore, it may be more affected by the presence of Li vacancies and Nb antisites, as discussed in more detail in the paper [268]. The LO-phonons show a similar behavior compared to their TO counterparts, however the LO_4 shows a much less pronounced shift. This can be easily understood due to the dielectric properties as predicted by the Lyddane-Sachs-Teller relation and discussed at the end of the chapter.

E-type phonons

Figure 4.10 shows the spectra taken in x(y,z)$\bar{x}$ geometry, where selection rules only allow for E-TO phonons. In agreement with the discussion in 4.1.1, only seven out of nine E-TO modes can be identified for $LiNbO_3$, while for $LiTaO_3$ eight modes can be identified. The spectra show that the E-TO_9 mode vanishes with decreasing Ta percentage, but does not show a pronounced shift. This is also seen in other scattering geometries, e.g. in Fig. 4.16 below. This is in very good agreement with the previous discussion based on the intensities. Indeed, also no pronounced shift is predicted for the E-TO_9 as shown in Fig. 4.11.

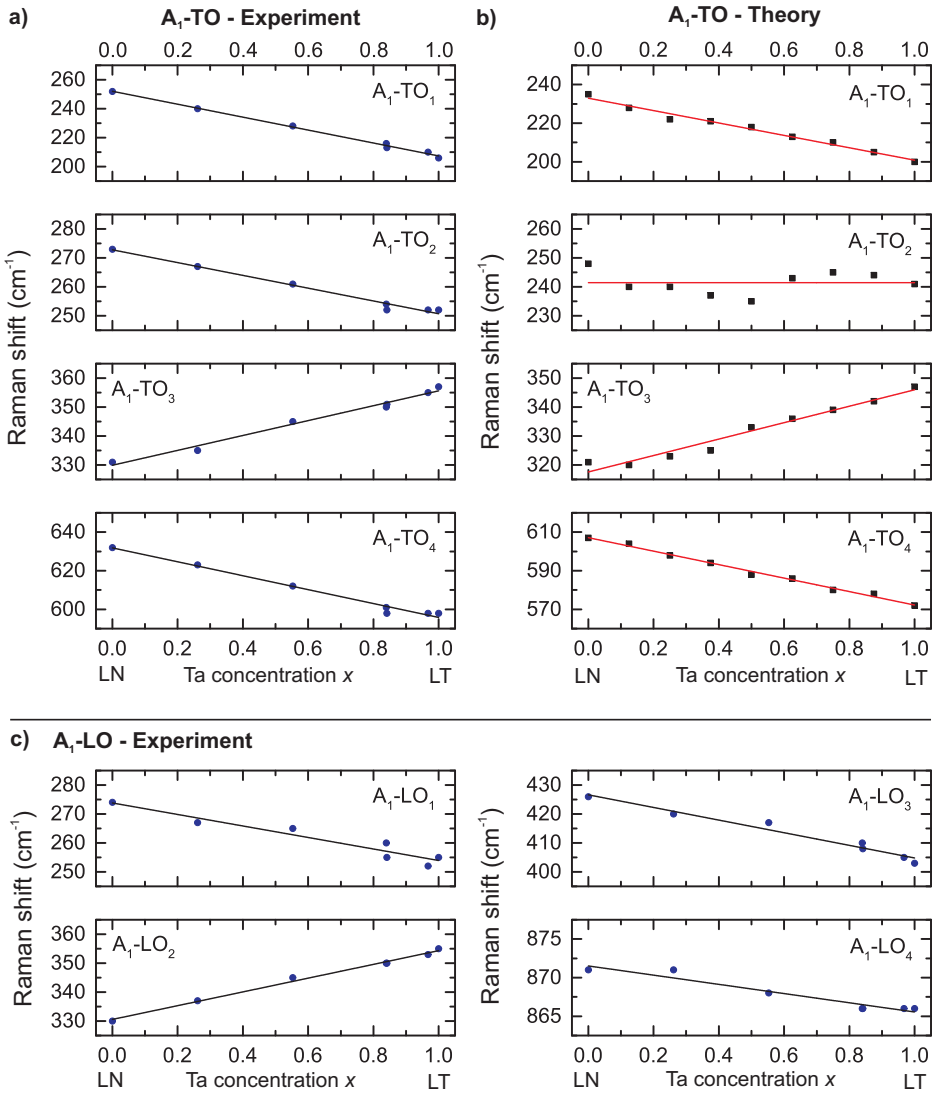

Fig. 4.8 Experimentally measured phonon frequencies of the A_1-TO modes as a function of the Ta concentration x (a) and corresponding theoretical predictions (b). In (c) the experimental measured A_1-LO phonon frequencies are displayed, which are not covered by our model.

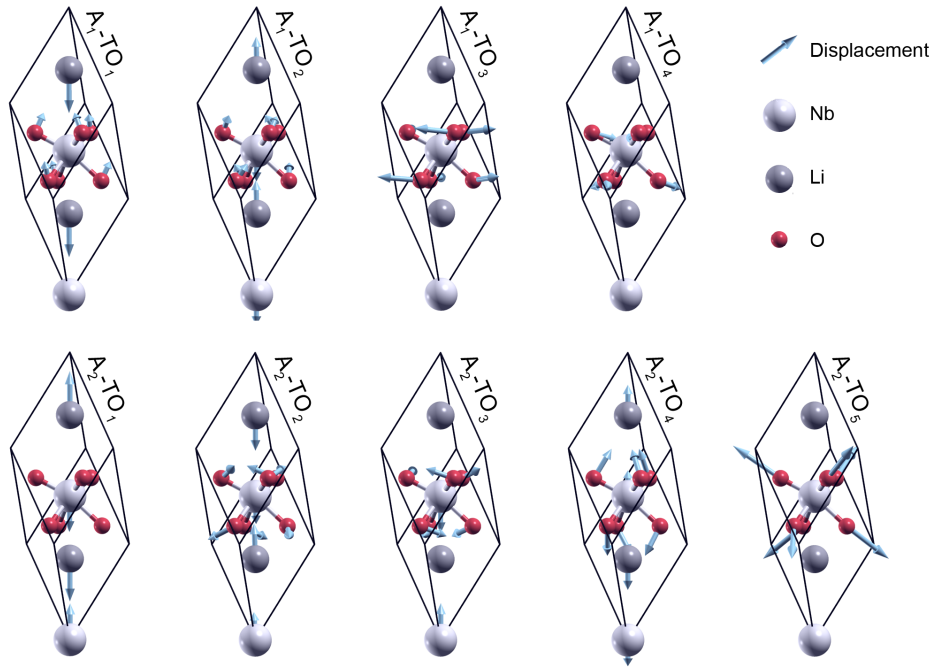

Fig. 4.9 Eigenvectors of the transversal phonon modes with A_1 symmetry (top) and A_2 symmetry (bottom). Nb/Ta atoms in white, Li in gray and O in red. The arrows represent the atomic displacement direction [268].

Using the same approach as in the previous chapter, one can calculate the intensity of the E-TO_9 mode in mixed crystals. As a prove of concept, this was performed $LiTa_{0.5}Nb_{0.5}O_3$, which can be realized in a single rhombohedral unit cell containing two formula units. Indeed, a decrease in intensity for the mixed compound in both shown configurations in Fig. 4.12. The intensity decrease seems to be proportionally larger than the composition would suggest, in similar to the experimental observation in Fig. 4.16. Here, the E-TO_9 only becomes dominant compared to the E-TO_8 intensity for $x > 0.5$. This behavior confirms the assignment of the E-TO_9 previously established.

The other disputed assignment regards the E-TO_5 and E-TO_6 modes. Instead of two modes, at room temperature only one broad peak is visible, which is created from the overlap of both modes, as discussed in the previous chapters in more detail. This combined feature was labeled E-$TO_{5/6}$ before. Indeed, if we follow this peak with the Ta percentage in Fig. 4.10 we see, that it shifts with increasing Ta concentration from about 370 cm^{-1} in $LiNbO_3$ to 380 cm^{-1} in $LiTaO_3$ without changing shape. This suggest, that the two underlying peaks do shift together in unity. Indeed, this is also what the DFT theory for mixed crystals suggest as seen in Fig. 4.11. Here, the measured position of the E-$TO_{5/6}$ is plotted together with the values for the E-TO_5 and E-TO_6 determined by Margueron *et. al.* [245]. Here, one can see that the interpolation of the literature values, as well as the center frequency determined in this experiment fit well with each other and the theory behavior. Here, theory suggest that both peaks shift by about 10 cm^{-1} from $LiNbO_3$ to $LiTaO_3$ in unity without changing the difference in position.

Again, the observed shifts of the different modes can be best explained and understood based on the displacement patterns displayed in Fig. 4.13. Most modes show a reduction in frequency, such as the E-TO_1, -TO_2, TO_3, TO_4, and TO_9, which all involve the Nb/Ta atom. Therefore these modes react to the increased mass of the Ta atom compared to the Nb atom. The E-TO_5, -TO_6, TO_7, and TO_8 mainly involve the oxygen cage and are therefore heavily influenced by the stronger Ta-O bond, compared to the Nb-O bond in a similar

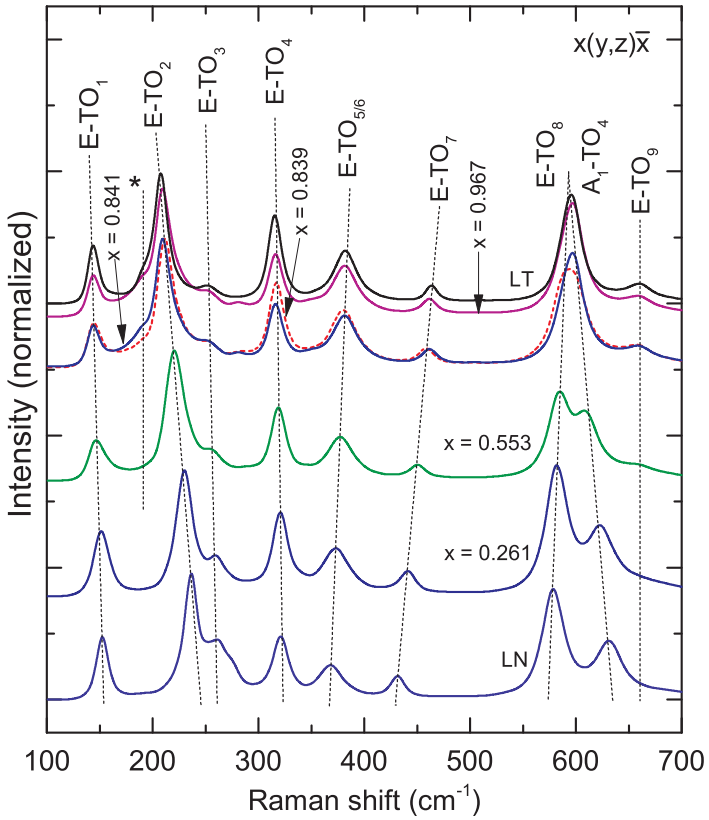

Fig. 4.10 Normalized Raman spectra obtained in the x(y,z)$\bar{x}$ scattering geometry showing the E-TO modes in $LiNb_{1-x}Ta_xO_3$ mixed crystals. The spectra have been separated with an artificial offset proportional to the Ta content x. Besides the E-modes, an A_1-TO4 leakage mode can be seen at high frequencies, resulting from an incomplete suppression of detection light. Peak assignment is carried following recent investigations [245, 70, 249].

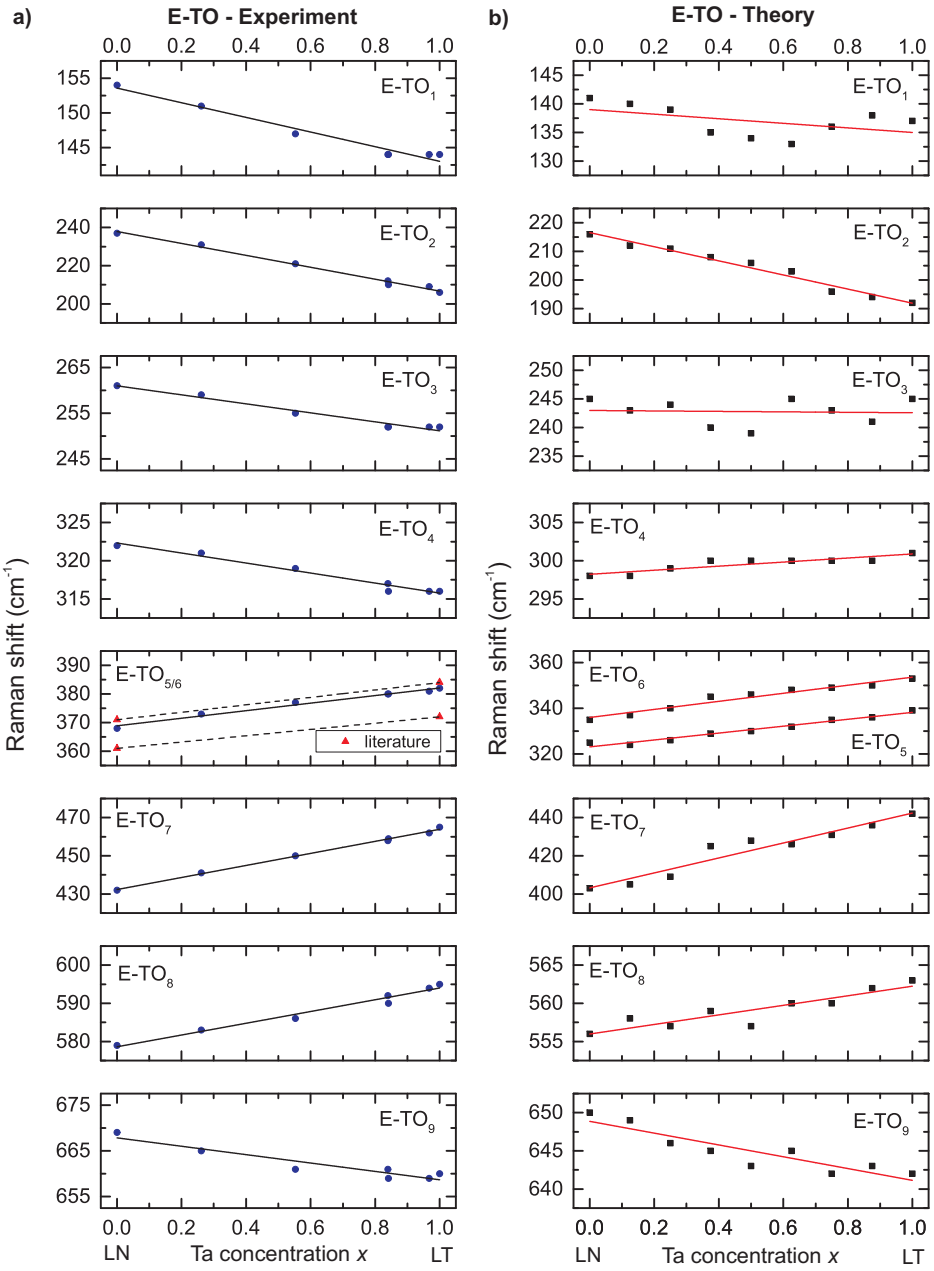

Fig. 4.11 Experimentally measured E-TO phonon frequencies in $LiNb_{1-x}Ta_xO_3$ mixed crystals as a function of the Ta concentration x (a), and comparison with the calculated values (b). $E\text{-}TO_5$ and $E\text{-}TO_6$ can only be resolved in low temperature Raman spectroscopy. Recent literature data of this resonance is shown for comparison [245].

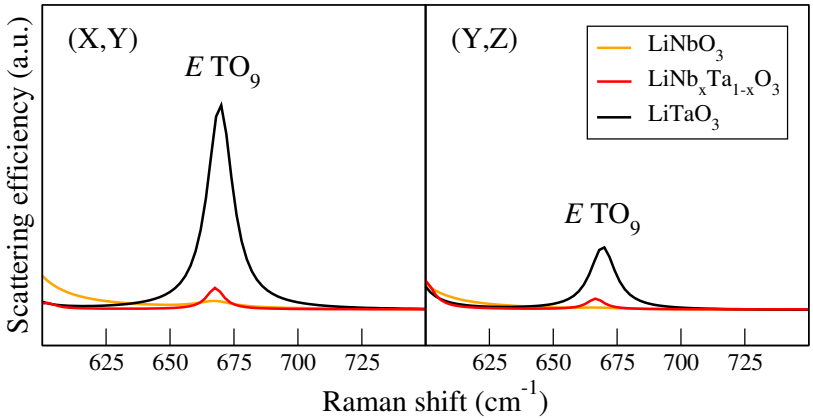

Fig. 4.12 Comparison of the theoretical intensity of the E-TO$_9$ mode for $LiNbO_3$, $LiTaO_3$, and $LiNb_{0.5}Ta_{0.5}O_3$. Here, these three composition can be represented with a single unit cell.

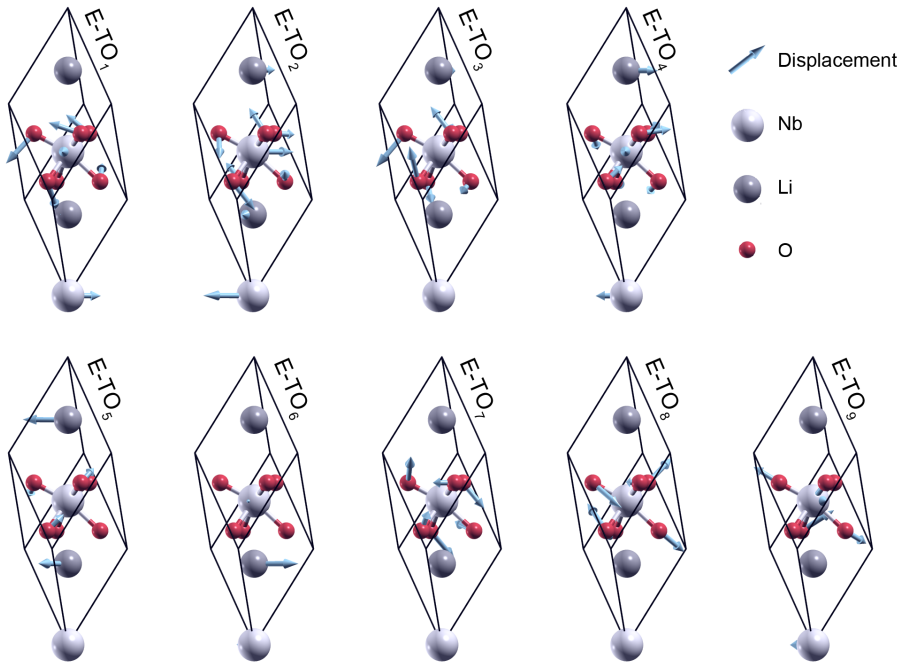

Fig. 4.13 Eigenvectors of the transversal phonon modes with *E* symmetry. Arrows represent the atomic displacement direction, color coding as in Fig. 4.9.

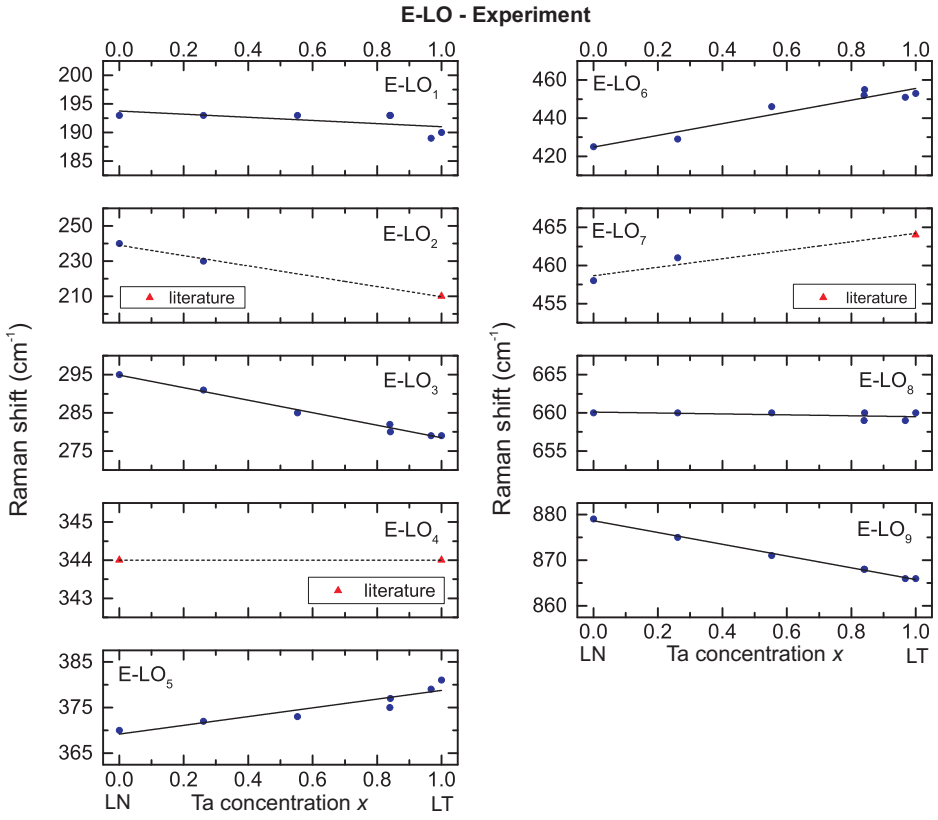

Fig. 4.14 Experimentally measured E-LO phonon frequencies in $LiNb_{1-x}Ta_xO_3$ mixed crystals as a function of the Ta concentration x. E-LO modes can only be detected in a single scattering configuration and are weak in intensity. For the sake of completeness our results are complemented by recent literature data [245].

way as the A_1-TO_3. The theory in general predicts the magnitude and direction of the shifts correctly. The only exception are the E-TO_3 and E-TO_4, which both do shift in the experiment, however show no or a slight opposing shift in the theory. Both modes involve a large displacement of the lithium ion. Here, the difference between experiment and theory may be atleast partially explained by the non-stoichiometric nature of the experimentally investigated samples compared to the simulated crystals, which are perfectly stoichiometric due to the small supercell, which does not allow to accurately account for the real stoichiometry in crystals.

The E-LO modes have also been investigated experimentally. They can only be detected in y(x,x)$\overline{y}$ and do generally appear weak and often in a spectrum with E-TO leakage modes, as also observed by other authors [245]. In our spectra we observe E-TO leakage modes apart from the A-TO modes, which both may overlap with the weak E-LO modes. Nevertheless, in our experiment we can unambiguously detect the E-LO_1, -LO_3, -LO_5, -LO_6, -LO_8, and -LO_9. While the E-LO_2 and -LO_7 could only be detected for Nb rich samples and will be masked by merging with generally stronger A-TO modes and leakage E-TO modes. The E-LO_4 could not be detected in our experiment. For these modes, the literature values from Ref. [245] have been added to obtain a complete set of data. For the incomplete sets, such as the E-LO_2, the literature data fit well with the projected behavior. This suggests also a vegard-like behavior for all E-LO modes. Here, we observe for several modes shifts of different magnitude or even direction, when compared to their TO counterparts. This is a result of the different dielectric properties of $LiNbO_3$ and $LiTaO_3$ in the xy-plane and will further be discussed in Sec. 4.1.3.

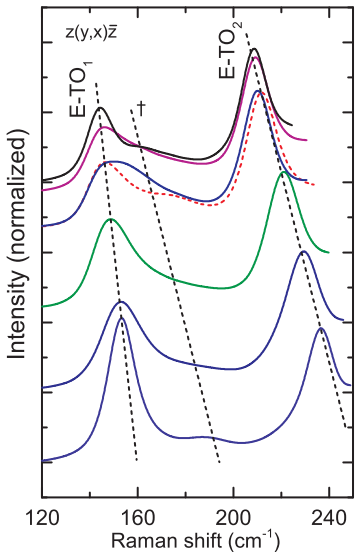

Fig. 4.15 Detailed view of the frequency range between the E-TO_1 and E-TO_2 modes. A broad structure shifting to lower frequencies on Ta rich samples is labeled by a dagger. This spectral feature is related to a two phonon process and heavily depends on stoichiometry [270, 247, 47]. Small variations in stoichiometry explain the slightly varying shapes obtained for different compositions.

Further spectral features

Up to this point we have assigned all first order peaks and have confirmed the assignment established in the previous chapter based on the analysis of $LiNb_{(1-x)}Ta_xO_3$ mixed crystals. Apart from this first order Raman features the spectra of $LiNbO_3$, $LiTaO_3$ and $LiNb_{(1-x)}Ta_xO_3$ show more features, as highlighted by an asterisk in Fig. 4.7. Several of such features are known and have been observed by many authors and have even been identified as the "missing" first-order peaks, as discussed in 4.1.1. We will now briefly discuss the compositional behavior of these features. In the low frequency range (< 200 cm^{-1}) we can identify two structures. The first structure appears for z-incident configurations at around 190 cm^{-1} in $LiNbO_3$. It is also visible in the fundamental spectra in Sec. 4.1.1. The compositional behavior of this feature is displayed in Fig. 4.15 for z(x,y)$\bar{z}$ geometry. The feature appears to shift to about 160 cm^{-1} in $LiTaO_3$. This feature does not fit with any first order Raman feature. Previous research has suggested that it is related to a two photon process due to its temperature behavior [270, 247]. Furthermore, the complete E-TO_1 range including this feature has been found to be sensitive to Li stoichiometry [47, 271].

In the low frequency another feature can be observed in x- or y-incident spectra. Here, as displayed in Fig. 4.7 for Ta rich samples (< 0.553) a feature at 190 cm^{-1} becomes visible, which does not appear to shift, but increases with increasing Ta content. A feature in this range has been observed before for $LiTaO_3$ even for stoichiometric material [245, 246]. Its intensity behavior is somewhat similar to a peak around 740 to 750 cm^{-1} observed for z-incident spectra in both, $LiTaO_3$ and $LiNbO_3$, which previously has often been misinterpreted as a first order peak. As seen in Fig. 4.16 and in Sec. 4.1.1 it is much more pronounced in $LiTaO_3$. Therefore, it often has been assigned to the missing E-TO_9. In our analysis, this peaks seems to be at a slightly higher frequency in $LiTaO_3$ than in $LiNbO_3$. It even appears for some mixed compositions, that it is composed of two features. Alike the feature in the 190 cm^{-1} range, these features are attributed to two-phonon processes due to their temperature and stoichiometry behavior [270, 247].

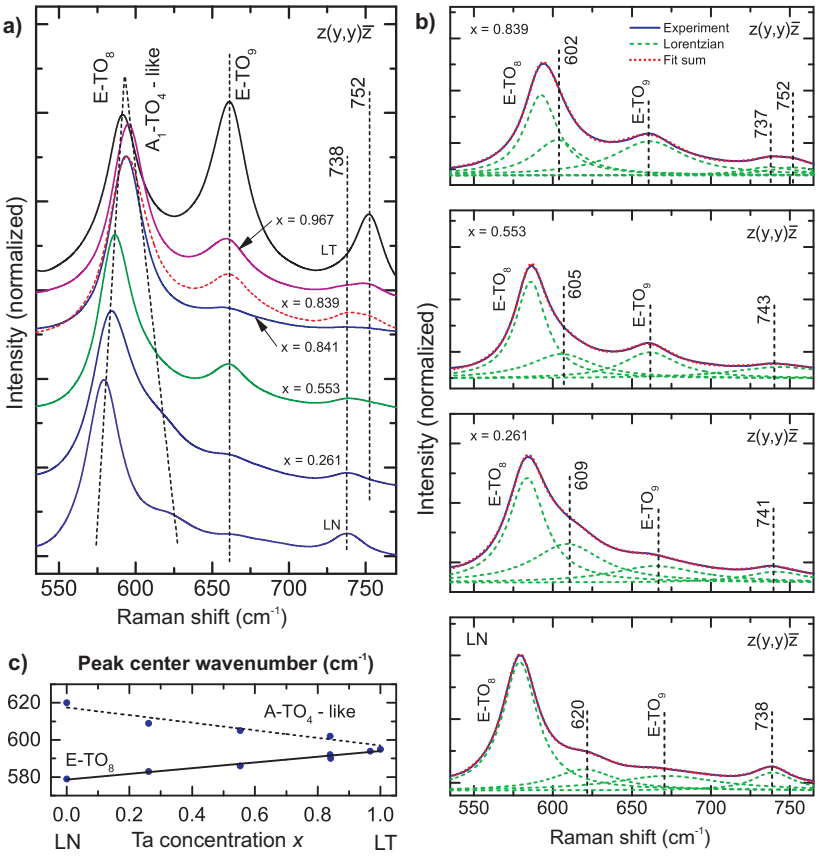

Fig. 4.16 (a) Close up of the spectral range from 535 to 770 cm^{-1} in z(y,y)$\bar{z}$. The spectra have been normalized to the E-TO8 mode intensity to warrant comparability. (b) Lorentzian fits of the represented spectral range, which highlights the shift of the features in the 600 - 620 cm^{-1} range. (c) Shift of the central frequency of the E-TO_8 and A_1-TO_4-like mixed LO-TO mode.

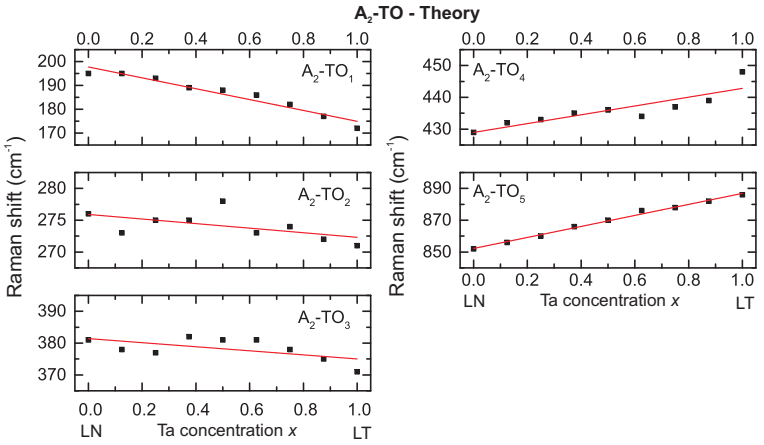

Fig. 4.17 Calculated frequencies of the A_2-phonons with respect to Ta concentration x.

In the context of imaging Raman of ferroelectric domain walls, probably the most interesting feature is the broad shoulder of the E-TO_8 visible in z(x,x)$\bar{z}$ and z(y,y)$\bar{z}$ in $LiNbO_3$ centered around 620 cm^{-1}. This range is shown in more detail in Fig. 4.16. For comparison the intensities have been normalized to the E-TO_8 intensity. In the spectrum the compositional dependence of the E-TO_9, as well as the discussed shifts can be seen. The intensity of the 620 cm^{-1} feature has been found to be very sensitive to the presence of ferroelectric domain walls [46, 251, 272–274] enabling high contrast images of domain walls. It should be noted, that such a feature has not been detected in $LiTaO_3$, where apparently only fundamental modes appear to be sensitive to domain walls. Furthermore, this feature was found to be very sensitive to stoichiometry and becomes sharper in stoichiometric material [76, 247]. Due to these observations and its frequency position in the > 600 cm^{-1} range lead to the assumption, that this peak was the missing E-TO_9, because it somewhat fitted with theory and IR spectroscopy results [249, 255]. However, as seen in this work, it is no first order Raman peak. As seen from the analysis in Fig. 4.16 it shifts to lower frequencies with increasing x and finally overlaps with the E-TO_8 peak.

Therefore, we suggest that this peak is an A_1-TO_4 mixed E-TO_8 mode, which propagates at oblique angles. It is excited due to the k-vector and polarization distribution in the focused laser beam [275–277]. The shoulder shows the same shift behavior as the A_1-TO_4 mode, which is for $LiTaO_3$ at almost the same frequency as the E-TO_8. The idea of this mode to be a mixed mode fits very well with observation of the angular dispersion behavior of the E-TO_8 and A_1-TO_4 mode as observed by Yang *et. al.* [246], which shows no directional dispersion for $LiTaO_3$ and a mixed mode for $LiNbO_3$. Therefore such a shoulder is not visible in $LiTaO_3$, while being strong in $LiNbO_3$. In $LiTaO_3$ it is superimposed with the E-TO_8. Recently it was demonstrated that the intensity of this shoulder, as well as the E-TO_8 peak position depends on the focusing in $LiNbO_3$, i.e. the chosen numerical aperture [278]. Furthermore, this explains, why this peak was detected by various authors in a broad frequency range from 610 to 630 cm^{-1} [76, 247, 48] and why it strongly reacts to the Li-stoichiometry [247]. Here, the different experimental setups and the numerical apertures are the reason.

For completeness, also the Γ-point frequencies of the optical silent A_2 modes have been calculated and are shown in Fig. 4.17. Alike the previously discussed A_1 and E-type modes, we see a frequency dependence, which can be understood in terms of the displacement patterns previously shown in Fig. 4.13. In this context, the A_2-TO_1, A_2-TO_2 and A_2-TO_3 decrease in frequency due to the involvement of the Nb/Ta atoms, while the A_2-TO_4 and A_2-TO_5 decrease due to the stronger binding forces in the Ta-O bonds.

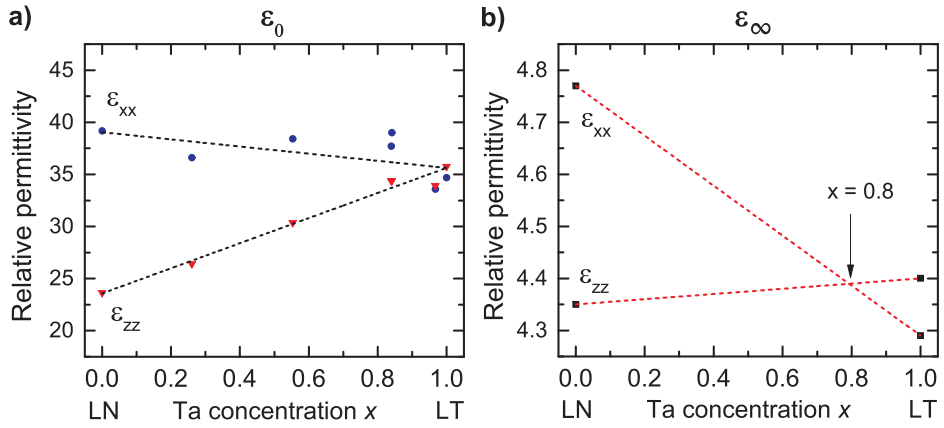

Fig. 4.18 The compositional dependence of the static dielectric permittivity estimated by Eq. 4.4. The extraordinary permittivity ε_{zz} shows a strong dependence on the Ta content, while the ordinary permittivity ε_{xx} is almost constant.

Dielectric properties

The complete assignment of all phonon frequencies allows also to analyze the behavior of the dielectric properties with respect to crystal composition. In this context, the well established Lyddane-Sachs-Teller (LST) relation [36, 37] provides a way to estimate the phononic contribution to the permittivity. In contrast to methods based on the IR reflectivity spectrum, the LST only requires knowledge about the phonon frequencies (both LO and TO), but no information about phonon damping. In its generalized form the LST connects the frequencies of the LO ω_{LO}^j and TO phonons ω_{TO}^j with the ratio of the high-frequency ε_∞ and static permittivity ε_0. It is given by

$$\varepsilon_0 = \varepsilon_\infty \cdot \prod_j \left(\frac{\omega_{LO}^j}{\omega_{TO}^j} \right). \tag{4.4}$$

The dielectric tensor for C_{3v} symmetry of lithium niobate is given by

$$\varepsilon = \begin{pmatrix} \varepsilon_{xx} & 0 & 0 \\ 0 & \varepsilon_{xx} & 0 \\ 0 & 0 & \varepsilon_{zz} \end{pmatrix} \tag{4.5}$$

and reflects its birefringent nature with a value along the ordinary and extraordinary axis, respectively. To estimate the static permittivity and the phononic influence on it, the high frequency dielectric permittivity of Lithium niobate and tantalate needs to be known. As lithium niobate is an insulator, it can be estimated from the refractive index in the optical range, which is on the order of $n_{LN} \approx 2.3$ and $n_{LT} \approx 2.2$, which would yield a high frequency permittivity on the order of ≈ 5 for both materials. For a more refined calculation of the static permittivity, the high frequency permittivity has been calculated with hybrid DFT for $LiNbO_3$ and $LiTaO_3$. Here, for $LiNbO_3$ the calculation results in $\varepsilon_{xx} = 4.77$ and $\varepsilon_{zz} = 4.35$, while for $LiTaO_3$ we obtain $\varepsilon_{xx} = 4.29$ and $\varepsilon_{zz} = 4.40$. These values slightly underestimate the values from literature, however shown similar trends and differences as the literature values, as summarized in Tab. 4.18. Our approach even accurately predicts and optical isotropic material for $x \approx 0.8$, which is in good agreement with previous experimental and theoretical approaches. For the calculation we now assume a vegard-like behavior for ε_∞ as displayed in Fig. 4.18b).

Table 4.3 Summary of the high frequency and static permittivity calculated for the end compounds LN and LT, respectively. The obtained values are in good agreement with literature [245, 44, 279, 48, 280, 55].

	ε_0		ε_∞	
	This work	Literature	This work	Literature
ε_{xx} (LN)	39.2 ± 5.7	40.2-42.5	4.77	5.0
ε_{zz} (LN)	23.6 ± 1.8	23.7-26	4.35	4.6
ε_{xx} (LT)	34.7 ± 5.2	39.6-42	4.29	4.50
ε_{zz} (LT)	35.8 ± 2.7	35.9-40	4.40	4.53

Table 4.4 Summary of the experimentally and theoretically determined Raman shifts for all fundamental modes. The corresponding experimental determined LO frequencies are also noted. Because the E-TO_5 and TO_6 can not be distinguished in the experiment, the sum peak frequency is noted. All Raman shifts in wavenumbers in cm^{-1}.

	$LiNbO_3$			$LiTaO_3$		
	Experiment	Theory	LO	Experiment	Theory	LO
A_1-TO_1	252-255	239	274	209-210	209	255
A_1-TO_2	275-276	289	330	256-257	286	355
A_1-TO_3	333-334	353	422	359-360	376	403
A_1-TO_4	633	610	871	600	591	866
E-TO_1	150-151	148	191	143	144	190
E-TO_2	237	216	237	210	199	-
E-TO_3	262-263	262	297	254-257	253	279
E-TO_4	320-321	320	-	315-317	319	-
E-$TO_{5/6}$	367-369	380/391	369/428	383-384	409/420	381/453
E-TO_7	432	423	428/456	460-465	459	-
E-TO_8	580-581	579	-	592	590	660
E-TO_9	664	667	877	661-662	669	866

Within the approach, we obtain static permittivity values for $LiNbO_3$ $\varepsilon_{xx} = 39.2 \pm 5.7$ and $\varepsilon_{zz} = 23.6 \pm 1.8$ and we obtain $\varepsilon_{xx} = 34.7 \pm 5.2$ and $\varepsilon_{zz} = 35.8 \pm 2.7$ for $LiTaO_3$, which are in good agreement with observations in literature [245, 44, 279, 48, 280, 55]. The data for the mixed crystals displayed in Fig. 4.18 suggest a vegard-like behavior with no pronounced bowing within our confidence bars. On the Ta rich side, one can see an almost isotropic crystal in the static frequency regime, similarly to the observations in the optical (high) frequency regime.

4.1.4 Conclusion

In this chapter we have now established a complete assignment of all phonon modes in the $LiNbO_3$/$LiTaO_3$ material system. Based on a rigorous theory and experiment comparison, we show that this assignment is able to explain all observations in good agreement with observations from literature. This demonstrates that a rigid theory combined with the experiment allows to understand observed spectra unambiguously. The determined experimental and theoretical phonon frequencies are summarized in Tab. 4.4. The assignment and complete understanding of the phonon spectrum in the $LiNbO_3$/$LiTaO_3$ material system now forms the foundation for further analysis in the next Sections.

Table 4.5 Raman selection rules for the complete set of back-scattering geometries calculated based on the Raman tensors for the KTP family. The last column gives a relative estimate for the tensor element squares deduced from the experiment. The observed intensities are normalized to d^2-element from A_2-symmetry.

Symmetry species	Scattering geometry	Tensor elements	Norm. Intensity in KTP (Experiment)
A_1-LO	z(x,x)$\bar{z}$	a^2	1.8
A_1-LO	z(y,y)$\bar{z}$	b^2	9.0
A_1-TO	y(x,x)$\bar{y}$	a^2	4.2
A_1-TO	x(y,y)$\bar{x}$	b^2	11.2
A_1-TO	x(z,z)$\bar{x}$	c^2	26.3
A_2	z(x,y)$\bar{z}$	d^2	1.0
B_1-TO	y(x,z)$\bar{y}$	e^2	1.9
B_2-TO	x(y,z)$\bar{x}$	f^2	10.2

4.2 $KTiOPO_4$ family

The second material system, which is analyzed in this work is the $KTiOPO_4$ material family. As discussed in chapter 2.2 the crystal structure of the KTP family is fairly complex. In particular the unit cell of $KTiOPO_4$ contains eight formula units, which leads up to 189 vibrational degrees of freedom. From the viewpoint of group theory all of these vibrations can be further subdivided into several irreducible representation [281]

$$\Gamma_{vib} = 47A_1(\mathrm{R,\,IR}) + 48A_2(\mathrm{R}) + 47B_1(\mathrm{R,\,IR}) + 47B_2(\mathrm{R,\,IR}). \tag{4.6}$$

As seen from equation 4.6 all of the phonons are Raman active. Unfortunately no symmetry reduces, e.g. by degeneracy, the total number of observable phonons. Therefore, complex spectra are expected. The Raman tensors for the orthorhombic point group C_{2v} are

$$A_1 = \begin{pmatrix} a & 0 & 0 \\ 0 & b & 0 \\ 0 & 0 & c \end{pmatrix}, A_2 = \begin{pmatrix} 0 & d & 0 \\ d & 0 & 0 \\ 0 & 0 & 0 \end{pmatrix},$$
$$B_1 = \begin{pmatrix} 0 & 0 & e \\ 0 & 0 & 0 \\ e & 0 & 0 \end{pmatrix}, B_2 = \begin{pmatrix} 0 & 0 & 0 \\ 0 & 0 & f \\ 0 & f & 0 \end{pmatrix}. \tag{4.7}$$

The experiments will be performed again in back scattering. Similar to Section 4.1.1 the scattering configurations and expected phonons are summarized in Tab. 4.5. As seen from the table in each scattering geometry only one symmetry species will appear. Longitudinal optical phonons can only be observed in back scattering for A_1 symmetry, because only this symmetry species has tensor elements on the main diagonal.

Fundamental spectra for $KTiOPO_4$, $KTiOAsO_4$ and $RbTiOPO_4$ have been recorded in all geometries. These spectra are displayed in Figs. 4.19, 4.20, and 4.21. For qualitative comparison all spectra have been normalized to the maximum, after the dark count level had been subtracted. The spectra have been recorded between 100 and 1200 cm^{-1}, where the lower boundary is determined by the absorption edge of the notch filter. No additional spectral features has been recorded above 1200 cm^{-1} in neither spectrum. For better visibility the spectra are separated by an offset of 0.5 and labeled with the respective scattering geometry and symmetry species.

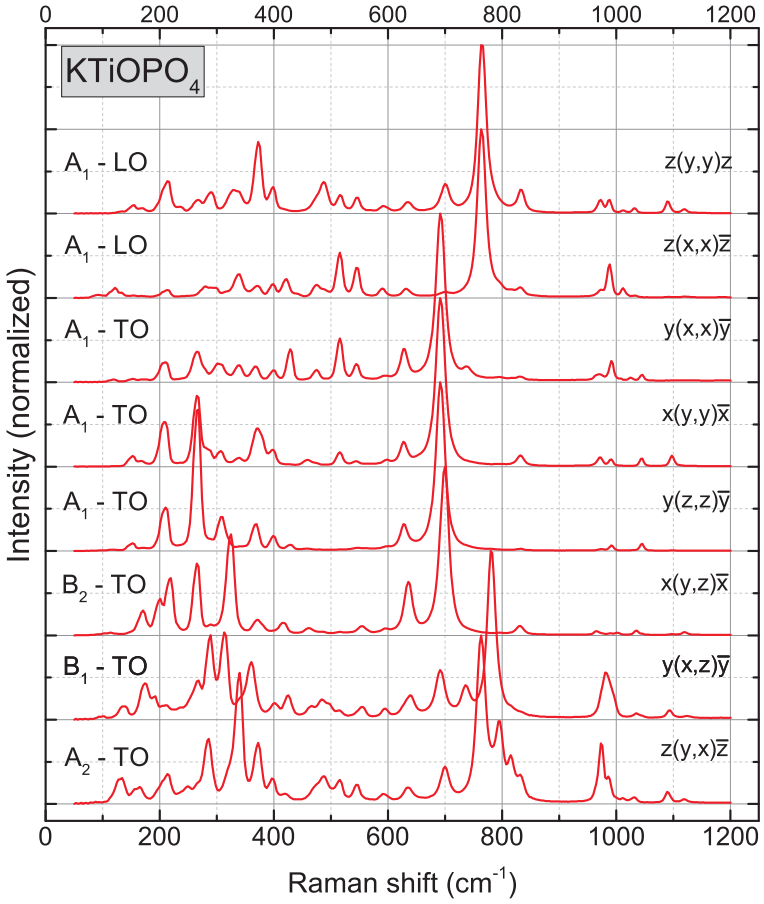

Fig. 4.19 Complete set of back-scattering Raman spectra of KTP.

As suggested by group theory, each spectrum in any symmetry species shows a complex shape with many overlapping peaks. In close examination, the more than 40 expected peaks can be identified in the individual spectra. Despite the complex shape many similarities, not only between the individual materials, but also between the various symmetry species can be observed. One key feature in all spectra is a dominating peak in the 650-800 cm^{-1} range. The second most intense features are usually located in the 200-400 cm^{-1} range, while the area in between (400-600 cm^{-1}), as well as the low frequency range ($< 200\,cm^{-1}$) shows no prominent features. Of particular interest is the high wavenumber range. Here, $KTiOPO_4$ and $RbTiOPO_4$ show frequencies up to 1120 cm^{-1}, while for $KTiOAsO_4$ no features for wavenumbers larger than >950 cm^{-1} can be detected. This indicates that the exchange of arsenic for phosphorous has a larger effect on the crystal properties, then the exchange of rubidium and potassium. Overall, the detected spectra agree well with the observations made in literature [281–284]. Apart from the spectra, also the relative intensities of the single scattering configuration have been determined for $KTiOPO_4$, which are summarized in Tab. 4.5. Here, as expected, the strongest signal is observed from the A_1-TO symmetry phonons detected parallel to the z-axis. This can be expected as the largest polarizabilities are parallely oriented to the spontaneous polarizations. The weakest signal comes from A_2 phonons, which display only 5% of the strongest A_1-TO intensity. This should be somewhat explainable by the fact that A_2 modes are Raman-active only and are not to be expected to show LO-TO splitting. Hence, the induced dipole moments are smaller, than in the other species leading to a lower intensity.

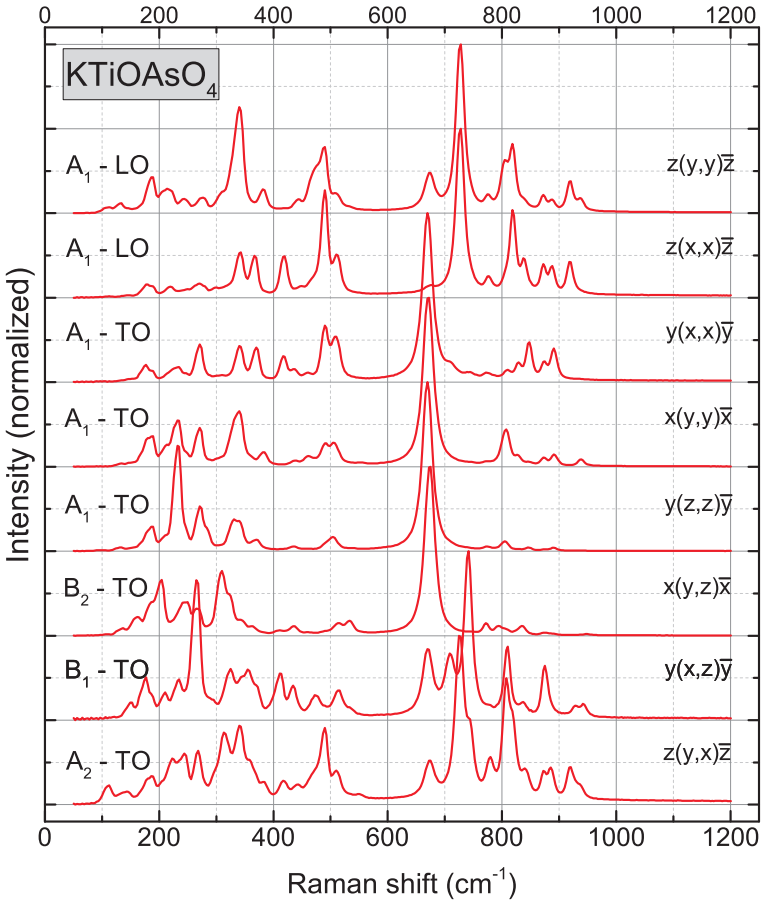

Fig. 4.20 Complete set of back-scattering Raman spectra of KTA.

We now want to examine the spectra in more detail and see, whether we can understand the similarities and differences of the spectra. In Fig. 4.22 several spectra of $KTiOPO_4$ (black), $RbTiOPO_4$ (red) and $KTiOAsO_4$ (green) are plotted together, which were taken in the same scattering configuration, respectively. Again, the spectra have been normalized and are displayed with a slight offset for better visibility.

Fig. 4.22a) shows the A_1-TO spectra taken in y(z,z)$\bar{y}$. The spectra look very similar with the dominant peak in the 600 to 700 cm^{-1} range and a group of four roughly equally-spaced medium intensity peaks between 200 to 400 cm^{-1}. While the spectra of $KTiOPO_4$ (black, bottom) and $RbTiOPO_4$ (red, center) are almost identical with regards to major peak positions and intensity, the spectrum of $KTiOAsO_4$ (green, top) shows larger differences. Here, the dominating peaks appear all shifted to lower frequency for the y(z,z)$\bar{y}$ spectrum, while pronounced differences especially in the high frequency range are visible. Similar observations can be made for the other symmetry species. For example for the second most intense B_2-TO symmetry species (Fig. 4.22c) the spectra of $KTiOPO_4$ and $RbTiOPO_4$ appear almost identical, while most peaks only show a slight red-shift of typically less than 10 cm^{-1}, while the $KTiOAsO_4$ shows larger differences. For the case of the A_1-LO spectra the spectra of each material looks more distinct and different (Fig. 4.22d). This may be understood in terms of different dielectric properties of the materials, because the LO-TO splitting is directly dependent on the dielectric properties, as formulated in the Lyddane-Sachs-Teller Relation [36, 37].

The fairly slight differences in the spectra of $KTiOPO_4$ and $RbTiOPO_4$ can easily be explained based on the crystal structures. The only differences in terms of crystal structure between those materials is the exchange

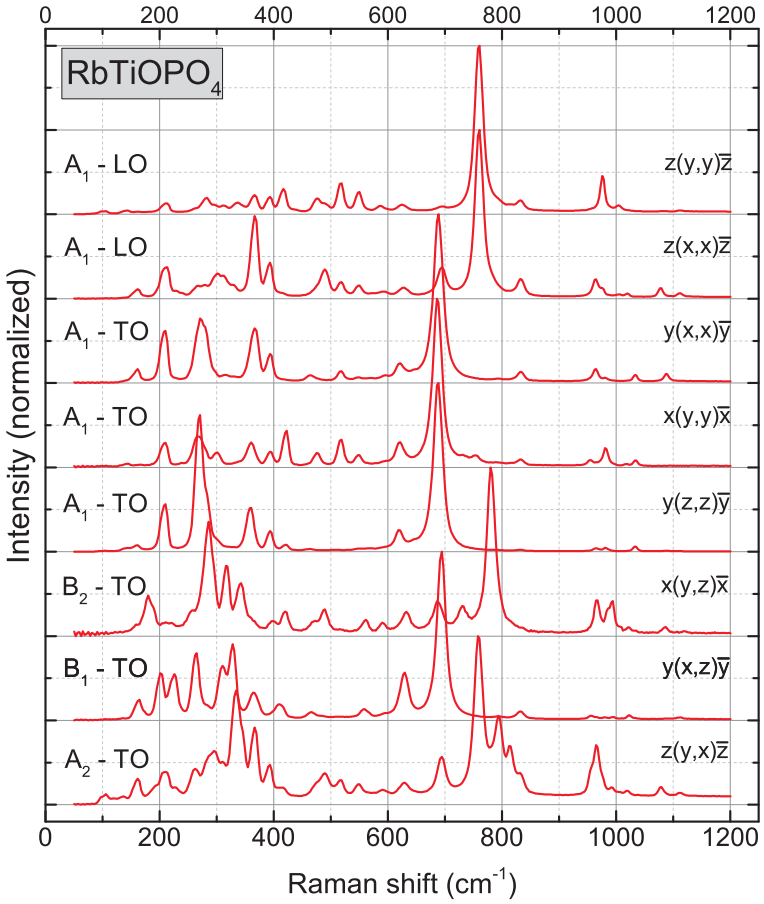

Fig. 4.21 Complete set of back-scattering Raman spectra of RTP.

of the potassium ion for rubidium ions, which are situated in cavities in between the PO_4 tetrahedrons and TiO_6 octahedrons. The Rb^+ and K^+ ions are only weakly bound to their sites and do not have a major influence on the overall bonding structure in the crystal. Therefore, the spectral signature of both materials appear almost identical in most symmetry species. Nevertheless for many dominating peaks a slight red shift is observed for $RbTiOPO_4$ compared to $KTiOPO_4$. This can be explained in terms of the larger crystallographic unit cell and larger lattice parameters due to the larger ionic radius of the Rb^+ ion, as sumarized in Tab. 2.1. This leads to longer bond lengths and therefore to a decrease in frequency for many features. The vibrations involving directly the Rb^+ ion are also expected to have a lower frequency due to the almost doubled mass compared to the potassium. Because the Rb^+ and K^+ ions are only weakly bound to their sites, the frequency of their respective vibrations are expected to be in the lower frequency range, which has also been observed in literature [282, 158]. The spectrum of $KTiOAsO_4$ shows larger differences. Here, in general a large redshift for all modes can be seen. This large redshift observed in many features can be explained in a similar way. The larger mass and ionic radius of the As ion leads to even larger lattice parameters and lower overall frequencies for many dominant vibrations.

As we have seen, overall differences of the crystal spectra can be understood, without microscopic insight on the actual vibrational patterns. Nevertheless, a theoretical investigation similar to those performed in $LiNbO_3$ would be very helpful for a deeper insight in the vibrational properties of of $KTiOPO_4$. However, so far no DFT investigation of the vibrational properties for any member of the $KTiOPO_4$ family is available. To get at least

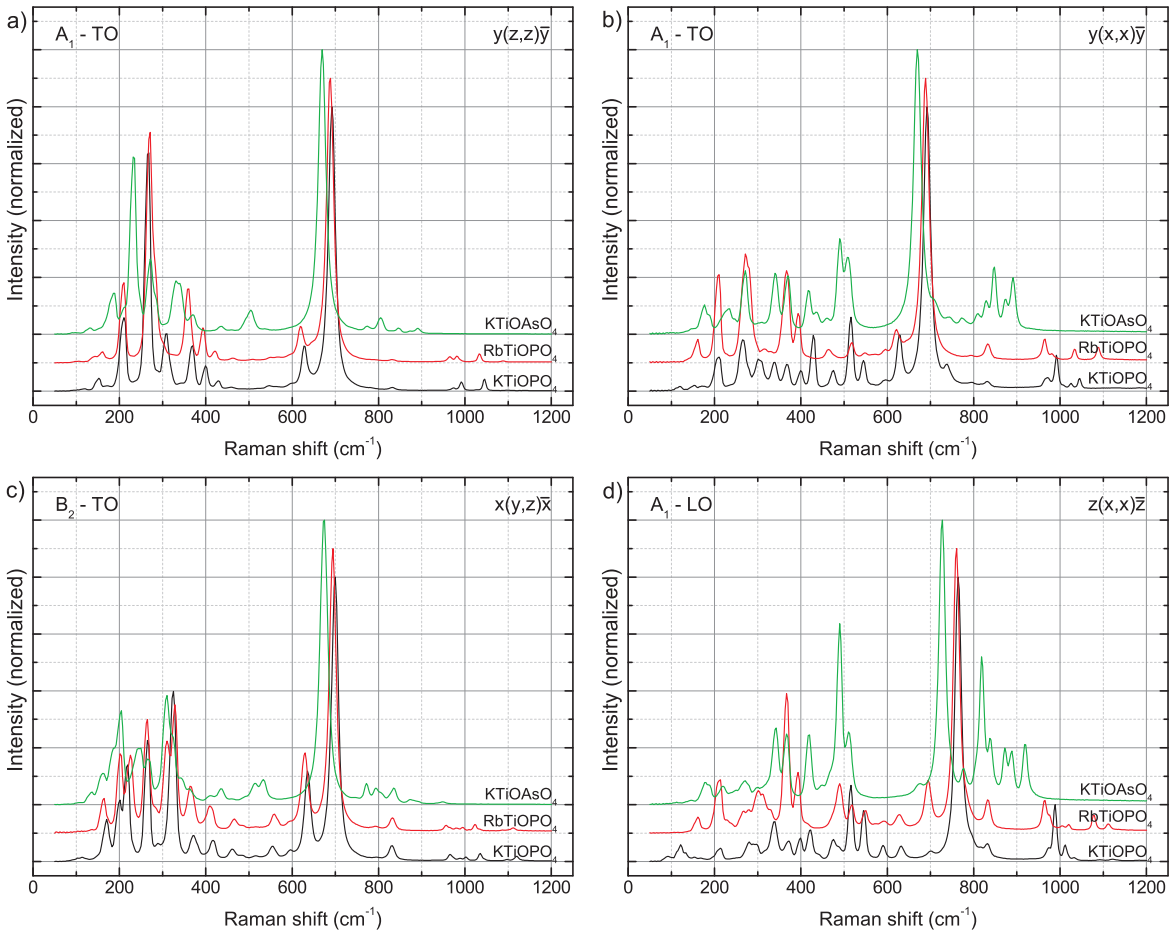

Fig. 4.22 Comparsison of the Raman spectra of $KTiOPO_4$ (black, bottom), $RbTiOPO_4$ (red, middle) and $KTiOAsO_4$ (green, top) taken in the same scattering configurations.

some more insight in the vibrational properties an internal mode assignment can be done for $KTiOPO_4$. An internal mode assignment means, that the spectral features observed in the Raman spectrum will be related to vibrational modes of substructures of the crystal lattice. In the case of $KTiOPO_4$, the crystal can be divided in the TiO_6 octahedron, the PO_4 tetrahedron and the potassium ion residing on sites in between. We will now briefly discuss this model, as it was proposed by Kugel *et. al.* [282] with respect to our data.

A free and symmetric octahedral molecule has six independent vibrations usually referred to as $\nu_1(TiO_6)$ to ν_6 (TiO_6), of which three are Raman active while the others three are infrared active [282]. These are displayed in Fig. 4.23. The octahedron inside the crystal is distorted in the ferroelectric phase, with its symmetry lowered to C_1. It further occupies two crystallographic sites. In detail four medium length Ti-O bonds in the range of 1.95 to 2.07 Å are reported. Along the z-axis one short length bond of about 1.7-1.8 Å and a long bond of about 2.0-2.15 Å are observed [282, 159]. As a result all selection rules are broken and modes of all six types are observable in Raman spectroscopy. Further the lowered symmetry results in a break-up of degenerated modes. In detail from the non-degenerated $\nu_1(TiO_6)$ mode up to two peaks are expected due to the two crystallographic sites of the octahedron [282]. The $\nu_2(TiO_6$) vibration is twofold-degenerate in the molecular case, hence, taking the two crystal sites into account, up to four Raman bands may be connected to this vibration in the Raman spectrum of KTP. Similarly the three-fold degenerated $\nu_3(TiO_6)$ to $\nu_6(TiO_6)$ might be connected to

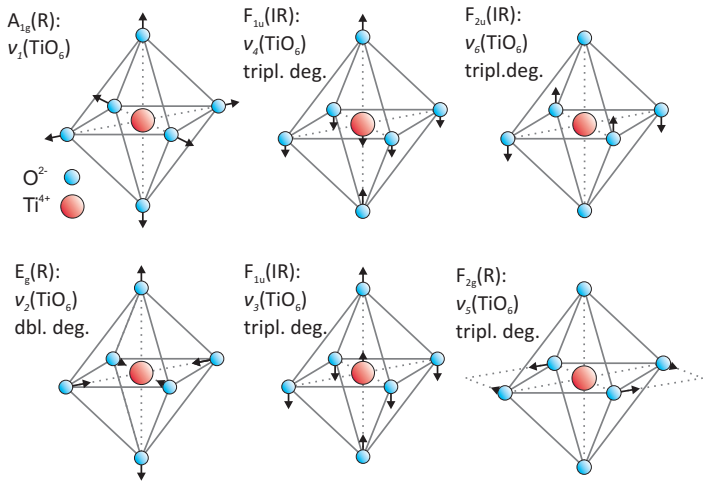

Fig. 4.23 Vibrational modes of a free, symmetric octahedral TiO_6 molecule. Here, the Raman and IR activity and the degeneracy is denoted.

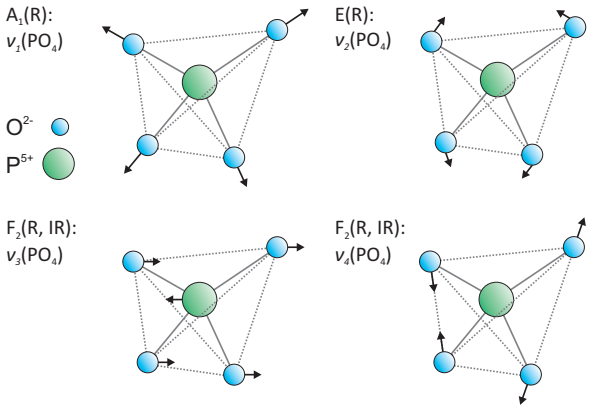

Fig. 4.24 Vibrational modes of a free, symmetric tetrahedral PO_4 molecule. Here, the Raman and IR activity and the degeneracy is denoted.

up to six peaks each. The $\nu_1(TiO_6)$ vibration is a total symmetric breathing mode of the octahedron. Due to its high symmetry and intrinsic Raman activity in the molecular case it is expected to be of high intensity. In literature it is unambiguously identified [281, 282] to arise as the highest peak in most spectra. For $KTiOPO_4$ this is, for example, found at 693 cm^{-1} in the A_1-TO spectra and 764 cm^{-1} $KTiOPO_4$ as the corresponding A_1-LO. It further might be connected to the high intense peak in the B_2 spectrum. The assignment of the other vibrations is less consistent in literature. Based on a review of different scattering experiments by several authors in KTP and related compounds, e.g. $KTiOAsO_4$, $CsTiOAsO_4$, or $TlTiPO_4$ [158, 281–287, 25], we suggest the following assignment: The $\nu_2(TiO_6)$ and $\nu_3(TiO_6)$ are usually referred to some low intensity peaks surrounding the high intensity $\nu_1(TiO_6)$ peaks at 600-690 cm^{-1} and 830 - 840 cm^{-1}, respectively. The other vibrations $\nu_4(TiO_6)$ to $\nu_6(TiO_6)$ are said to be related to medium to high intensity peaks in the 200 to 400 cm^{-1} range. Here, the $\nu_6(TiO_6)$ is stated to be most likely connected to peaks appearing at various frequencies in all configurations at 200-220 cm^{-1}, best seen as a double feature in the B_2-TO spectrum. The $\nu_5(TiO_6)$ is connected to high intensity peaks around 260-270 cm^{-1}, while the $\nu_4(TiO_6)$ related signatures are found to be of medium intensity in the 300 to 340 cm^{-1} range.

Of probably more interest is the PO_4 tetrahedron, because the spectra in Fig. 4.22 allows for a direct comparison of the $KTiOAsO_4$ and $KTiOPO_4$ spectra. In contrast to the TiO_6 octahedron, the PO_4 tetrahedron is nearly symmetric with average P-O bond length of 1.54 Å in the $KTiOPO_4$ crystal [288]. A free, symmetric tetrahedral molecule has four vibrational normal modes numerated $\nu_1(PO_4)$ to $\nu_4(PO_4)$, of which all are Raman active. These are displayed in Fig. 4.24. The PO_4 tetrahedron $\nu_1(PO_4)$ mode is a total symmetric breathing mode of A_1 symmetry, while the $\nu_2(PO_4)$ is of E-symmetry. Just like the TiO_6 octahedron the PO_4 tetrahedron occupies two indifferent crystallographic sites inside the $KTiOPO_4$ crystal structure. Therefore, two peaks are expected in the spectrum for the $\nu_1(PO_4)$ and $\nu_2(PO_4)$ modes, each. The $\nu_3(PO_4)$ and $\nu_4(PO_4)$ vibrations are of F_2 symmetry and are both triply degenerated. Due to the two crystal sites of the tetrahedron and the break-up of degeneracy, up to six peaks are expected from each of these modes. Comparing the Raman spectra of $KTiOAsO_4$ and $KTiOPO_4$ reveals main spectral changes in the ranges of 300 - 550 cm^{-1} and > 900 cm^{-1}, while other features are less affected [284, 281]. This is in agreement with calculations by Herzberg, who calculated the frequencies of a PO_4 tetrahedron from ν_1 to ν_4 to be 980 cm^{-1}, 363 cm^{-1}, 1082 cm^{-1} and 515 cm^{-1} [289]. Based on this we suggest the $\nu_2(PO_4)$ to be related to some medium intensity peaks at 360 - 400 cm-1, e.g. the dominant feature in B_1 symmetry. Up to six peaks are expected to arise from the $\nu_4(PO_4)$ mode, which are found as several low intensity peaks in the 450 to 600 cm^{-1} range. Due to the large number of peaks in the different scattering configurations a more precise assignment is difficult. This is different in the high wavenumber range, where only the $\nu_1(PO_4)$ and $\nu_3(PO_4)$ are expected. Comparing the obtained peak frequencies in the area, in fact shows several groups of peaks in the respective spectral ranges. Comparing $KTiOAsO_4$ spectra with $KTiOPO_4$ spectra in the > 900 cm^{-1} range also shows a heavy modification of this spectral ranges, clearly showing the origin of these peaks in the PO_4 vibrations. However, due to the largely different intensities in the scattering geometries it appears difficult to clearly assign the peaks.

The potassium ion is only weakly bound to its site. Hence, only low frequency contributions are expected [282]. Comparing the spectra of $KTiOPO_4$, $TlTiOPO_4$ and $RbTiOPO_4$ reveal low intensity peaks mainly located in the region < 350 cm^{-1} to be related to the K^+ ion [282, 158]. This is also seen in the spectra in this work, only minor differences are observed, where the global shift of most modes is attributed to the slightly larger unit cell, while certain modes are modified more largely. It can be speculated, whether further features in the low frequency region are related to vibrations of complete substructures, e.g. chains tetrahedrons and octahedrons, which displace as a whole with respect to the lattice. Such vibrations are expected to be low frequency, due to the large masses involved.

In conclusion, the internal mode assignment allows to understand the qualitative structure of the spectrum, as well as to some degree quantitative statements. Alike, some general considerations, such as the atomic masses and unit cell parameters, allow to understand the differences and similarities between the three materials. However, for a deeper understanding of the Raman spectrum and involved changes and the material properties of the material family in general, it will be inevitable to perform investigation with ab-initio theory. The internal mode assignment, as well as the spectra presented here, present a good reference for further investigation.

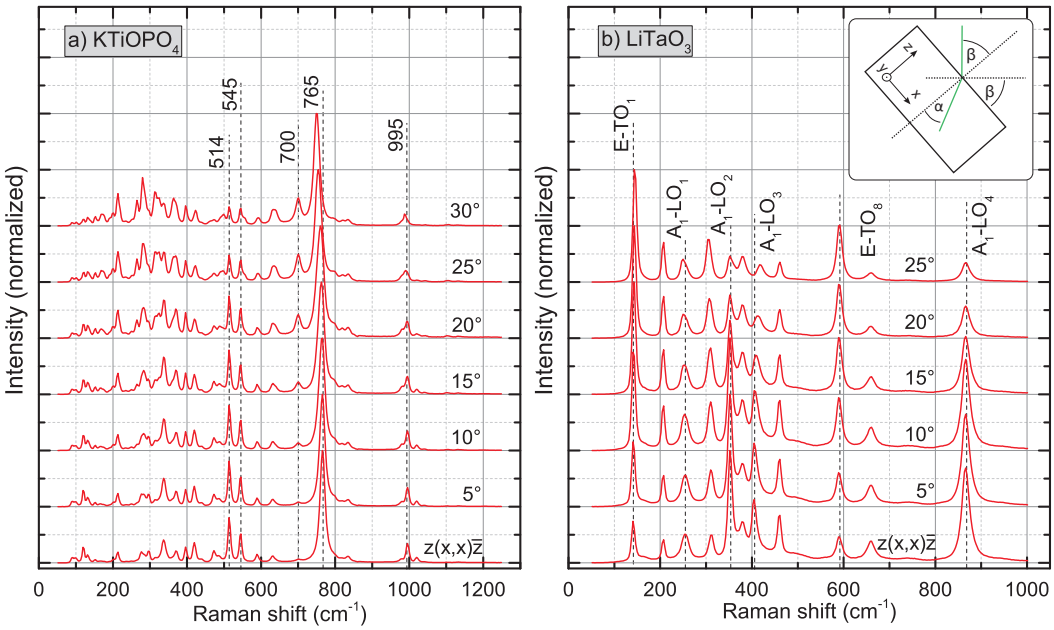

Fig. 4.25 Typical angular resolved spectra for a) $KTiOPO_4$ and b) $LiTaO_3$. The 0° spectrum is taken in the geometry specified at the bottom, while the other spectra are obtained by tilting the sample in five degree steps and keeping the polarization fix with respect to the 0° measurement. The specified angle is measured with respect to the inner angle β as given in the inset in b).

4.3 Directional dependent Raman spectroscopy

In polar crystals, like LN, LT or KTP, the phonon spectrum will change as a function of the propagation angle of the phonons, which is called directional dispersion. In the context of directional dispersion [290, 254, 246, 291–293] two types of phonons are distinguished. The first type are *ordinary* phonons, which do not shift and vary in spectroscopy under various angles, and the second are *extraordinary* phonons, which shift under angular observation. This is a prominent effect in polar materials, such as ferroelectrics, and can be understood as some phonons do couple to long range electric fields and is directly related to LO-TO splitting. The terms "ordinary" and "extraordinary" are chosen in analogy to the ordinary and extraordinary optical axes. Here, in particular phonons propagating parallel to the extraordinary axis, the axis of the internal field, are subject to changes, while in particular phonons in the ordinary plane are usually not subject to change. In this context KTP is a biaxial material, therefore extraordinary phonons are also expected in the xy-plane. For the total symmetric A_1 phonons in our three crystals this means for example that pure A_1-LO can only be observed parallel to the extraordinary axis (z-axis), while pure A_1-TOs can only be observed in the ordinary plane. For all other angles phonons of mixed type are observed. Therefore, measuring the angular dispersion allows to unambiguously identify all LO type phonons, as those will shift are vanish. This is very helpful in identifying and assigning phonons. As seen in the next Chapter, the angular resolved spectra are an important feature in the explanation of the domain wall contrast.

For the measurement procedure the samples either need to be polished to obtain facets with various angles or the sample is tilted with respect to the fixed measurement axis. If the latter is performed, it should be noted that the outer tilt angle β does not represent the angle α at which the phonon is excited. Due to refraction at the

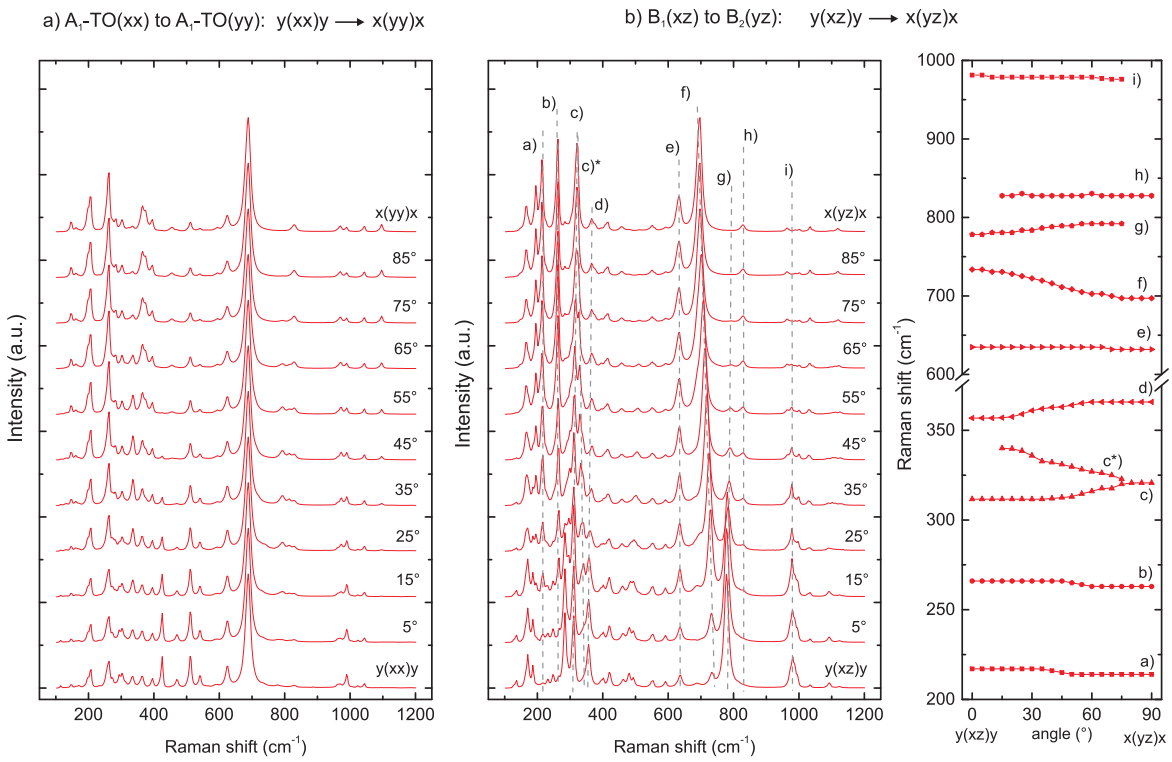

Fig. 4.26 Complete angular dispersion in the xy-plane of the KTP crystal. Here, one can clearly see that a) A_1-TO phonons in y(x,x)$\bar{y}$ to x(y,y)$\bar{x}$ show no change, while the B_1 phonons y(x,z)$\bar{y}$ show a clear angular dispersion to B_2 in x(y,z)$\bar{x}$ geometry.

surface, the angle is changed according to the inset in Fig. 5.3. The angles however can easily be corrected by using Snell's law

$$n_{\text{Luft}} \sin(\beta) = n_{\text{Material}} \sin(\alpha). \tag{4.8}$$

For example lithium niobate has a extraordinary refractive index at 532 nm of approximately $n = 2.23$. This means that the spectrum at $\alpha = 20°$ means the sample needs to be tilted by 47°. Alike, the corrections can be performed for $KTiOPO_4$ or $LiTaO_3$. The biggest disadvantage of this issue is that due to internal reflection only maximum angles of approximately 27° for $LiNbO_3$ and $LiTaO_3$ and 33° for $KTiOPO_4$ can be achieved. To measure a complete set with angles in the 30° to 60° range at least one facet with a 45° angle with respect to the desired axis needs to be polished.

Figure 5.3 a) and b) show a series of spectra taken every 5° of internal angle for KTP and LT. The spectra are simply normalized to maximum after the dark counts had been subtracted and separated by and artificial offset. Both 0° angle spectra show A_1-LO phonons in z(x,x)$\bar{z}$ (in the case of LT also E-TO modes). The theory of directional dispersion says now that this is the only geometry in which pure A_1-LO can be detected, as detection and excitation is parallel to the optical axis. If the sample is tilted mixed LO-TO modes at intermediate frequencies are seen. Indeed, when the sample is tilted shifts can be observed for $LiTaO_3$ and $KTiOPO_4$. The observations for lithium tantalate is in agreement with observations in literature [254, 246]. For KTP so far no observations exist. The presented measurement shows the dominating peak at 765 cm^{-1} is clearly an extraordinary A_1-LO mode.

In the case of directional dispersion, KTP is an interesting case, because it is a biaxial material. Here, extraordinary phonons are also expected in the xy-plane. In parallel polarization configurations (y(x,x)$\overline{y}$, y(z,z)$\overline{y}$, x(z,z)$\overline{x}$ and x(z,z)$\overline{x}$) always pure A_1-TO phonons are expected and therefore no directional dispersion is expected. However, in the crossed polarization configurations either B_1 (y(x,z)$\overline{y}$) or B_2 (x(y,z)$\overline{x}$) can be detected, therefore a directional dispersion is expected. Figure 4.26 shows a complete set for A_1-TO phonons and B_1/B_2 phonons. Here, the spectra for the A_1 phonons is almost independent of the angle with small except for some minor intensity variations and no shifts apparent shifts can be detected. For B_1/B_2 phonons in Fig. 4.26b), however, many clear shifts and intensity changes can be seen. Here, extra-ordinary phonons clearly appear in the xy-plane.

Chapter 5

Imaging Spectroscopy

In the previous chapter, we have focused on the spectroscopic analysis of the materials. Here, general properties of the materials were analyzed, where a spatial analysis and mapping was not necessary. Now, the imaging capability of the setup is used. In the context of integrated nonlinear optics in ferroelectric materials there are two major topics, where spatially resolved, imaging spectroscopy can provide useful insight into material properties. The first topic is the visualization of ferroelectric domain walls. Since the first experimental demonstrations of Raman imaging on ferroelectric domain walls, this technique has proven to be very useful due to its non-invasive nature and three dimensional resolution. Despite the widespread use, the actual mechanism providing a contrast to domain walls in Raman spectroscopy is not well understood.

In this chapter, we analyze periodically poled $LiNbO_3$, periodically poled $LiTaO_3$ and various periodically poled and unpoled $KTiOPO_4$ samples with and without waveguides. The $LiNbO_3$ and $LiTaO_3$ analysis were mainly performed on two commercially acquired samples. Both samples were poled and fabricated by *Deltronic Crystals, Inc*. The various $KTiOPO_4$ samples were fabricated and provided by the group of C. Silberhorn. The main cooperation partners were C. Eigner and L. Padberg. Details about the samples, if necessary for understanding, are provided in the respective sections.

5.1 Unraveling the DW contrast mechanism in Raman spectroscopy

In the last decade Raman microscopy has been applied to visualize and analyze ferroelectric domain structures in numerous materials [50, 252, 46, 273, 269, 272, 251, 54, 294, 295, 274, 296–299]. A connection between the phonon spectra and domain walls (DW) was probably first noted by Dierolf *et.al.* in 2004 [50], while performing luminescence microscopy on periodically poled Er-doped lithium niobate. In particular in lithium niobate ($LiNbO_3$) and lithium tantalate ($LiTaO_3$) this method has seen widespread use in many experiments since then. This method makes use of the fact that in particular the intensity - and to a lesser extend the frequency or FWHM - of certain Raman modes is heavily influenced by the presence of domain walls. These intensity variations can then be mapped to create an image of the domain structure. In confocal application, Raman microscopy offers an intrinsic three-dimensional resolution and is non-invasive, which are great advantages when compared to other widespread methods for domain imaging like selective etching or piezo-response force microscopy techniques. Despite the use of Raman microscopy for imaging of ferroelectric domain walls the mechanism, which results in a changed phonon spectrum at the DW, is not entirely understood. A detailed

understanding of the underlying contrast mechanism is inevitable for an interpretation of results and identifying possible deviations from the usual behavior.

The first explanation for the contrast was given by Fontana et. al. [269] shortly after the first papers showing domain wall imaging by Raman microscopy appeared. In the years preceding the first Raman experiments on ferroelectric domain walls, large strain fields in the vicinity of domain walls in $LiNbO_3$ and $LiTaO_3$ have been observed [51, 300], as well as predicted theoretically [301]. Furthermore, luminescence mapping experiments revealed large internal fields along domain walls [50, 295]. The model by Fontana *et. al.* now suggests that these strain fields and/or the local electric fields will lead to changed Raman scattering efficiency, which they identify as elasto-optic and electro-optic coupling. In classical theory the Raman intensity of a certain vibration n is associated with the polarizability change $d\alpha/dQ^n$ with respect to the normal coordinates Q^n of the vibration [196, 197]. Fontana et. al. showed that strain ds and local electric field dE will lead to additional terms in the polarizability change. The total polarizability including strains and electric fields is then given as [269]

$$\frac{d\alpha_{ij}}{dQ^n} = \frac{d\tilde{\alpha}_{ij}}{dQ^n} + \left(\frac{\partial \alpha_{ij}}{\partial s_{lm}} ds_{lm} + \frac{\partial \alpha_{ij}}{\partial E_k} dE_k \right) \frac{1}{dQ^n}. \tag{5.1}$$

Taking the aforementioned strains and local electric fields at domain walls into account [51, 300, 301], this model in principle can explain why a change in intensity is observable with Raman spectroscopy, because any local strain or electric field will influence Raman intensity. However, the predictability of the model is limited at first glance. Many factors need to be known to calculate the response of specific phonons, such as the local strain and electric field, as well as the polarizability change (or susceptibility in the case of crystalline materials). Here, a particular issue is also that some suspected non first order peaks also show sensitivity to domain walls, most prominent the 620 cm^{-1} line in $LiNbO_3$ formerly thought to be the E-TO_9 [70, 268, 249] (See also Sec. 4.1.1). Another somewhat open question is the size and magnitude of the strain field around domain walls. Experiments show that with applied electric fields, strain fields spanning up to 100 μm are observed by Bragg topography [51, 300], however Ginzburg-Landau-Devonshire theory only predicts strain fields only to be a few unit cells wide [301, 144]. Alike, ab-initio analysis of ferroelectric domain walls, show domain wall width - defined as the sign change of the spontaneous polarization - to be only a few unit cells wide [302, 303]. These theory results are in agreement transmission electron studies, showing domain transitions to be a few unit cells wide [304–306]. Nevertheless, people observed with Raman microscopy domain wall signatures, which are larger, than their optical resolution [54, 294]. Their observation fits with high resolution mapping of the refractive index and birefringence or electric fields around domain walls, where signatures on the order of several microns around a DW have been detected [52, 50, 295]. Measurements with nonlinear microscopy even suggest that the width of DW signatures depend on material properties and fabrication, e.g. annealing [204]. As we can see here, the observations are manifold and complex.

A completely different explanation for the contrast behavior of domain walls in Raman spectroscopy was presented in 2012 by Stone and Dierolf [251]. In their model they understand the domain wall as a large, planar defect. Planar defects are associated with a quasi-momentum q_{DW} normal to the defect plane, as shown in Fig. 5.1. This will lead to a change of selection rules. In particular, oblique-propagating phonons, some with mixed LO-TO character, can participate in the scattering process. If we analyze the momentum conservation within the bulk material for back-scattering situation, as in a typical Raman Imaging experiment, we get the situation displayed in Fig. 5.1a). Here the momenta of the incident k_i and scattered k_s and the phonon q_a are all collinear. The situation changes, if a domain with a quasi-momentum is concerned. Figure 5.1b) shows the situation for z-cut incident scattering at a 180° domain wall, which is a typical geometry for the investigation of periodically poled LN or KTP. Here, the additional defect momentum q_{DW} now will result in phonons q_b to participate in

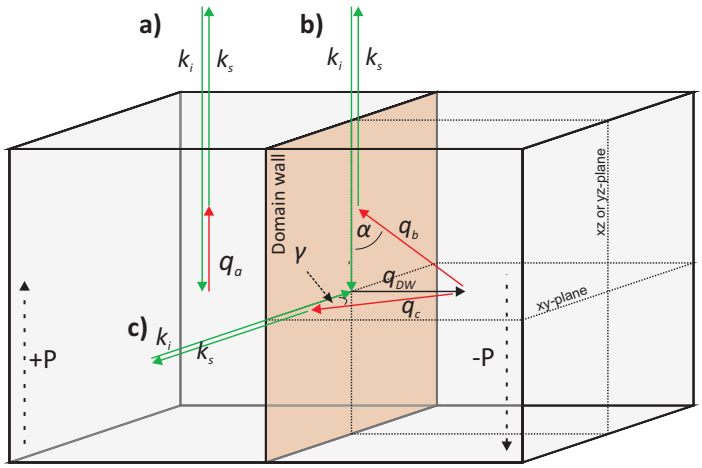

Fig. 5.1 Contrast mechanism as proposed by Stone and Dierolf [251]. In their model, they understand the DW as a large planar defect associated with a quasi momentum. This leads to a relaxation of selection rules at DWs giving rise to a changed Raman spectrum.

the scattering process, which are propagating at oblique angles with respect to the crystals axis. As Yang et. al. experimentally demonstrated [246] in their analysis of the directional dispersion of $LiTaO_3$ and $LiNbO_3$, Raman spectra - intensity and peak positions - change heavily, when measured at different angles. The effect is in particular large, when changing from z-incident, which allows for observation of strong A_1-LO peaks, to x- or y- incident direction, which allows for the observation of the respective lower frequency A_1-TO phonons. This fits with the observation that A_1-LO phonons decrease in intensity at domain walls. In their discussion Stone and Dierolf could then connect specific spectral ranges and phonons with changes observed by Yang et. al. [246]. The apparent major advantage of this explanation for the contrast mechanism is that the substructure of the domain wall is of no concern for the model.

We have now two different models, which both provide an explanation for the contrast observed at domain walls. In this context, Fontana et. al. model connect the spectral changes to the *microscopic* structure of the DW, while Stone and Dierolf see the contrast in the DW as a *macroscopic* object, where the micro-physical properties of the domain wall play no role. In our work we have investigated the spectra of the domain walls in z-cut and y-cut of $LiNbO_3$ and $LiTaO_3$, as well as $KTiOPO_4$ in the context of these two models. Here, we have measured angular dependent Raman spectra for a systematical comparison with DW spectra to address the macroscopic model of Stone and Dierolf, while the microscopic model is addressed based on DFT approach.

5.1.1 Raman Imaging and Directional dispersion

For this work three samples were analyzed. The periodically poled lithium niobate and lithium tantalate samples are obtained commercially via *Döhrer Elektrooptik* and fabricated by *Deltronic Crystals, Inc.*. The lithium niobate crystal features a period length of $\Lambda = 28.3\mu$m and a duty cycle of 60 : 40, while the Lithium tantalate crystal is poled with a period length of $\Lambda = 28.9\mu$m with a duty cycle of 50 : 50. Both samples are fabricated from congruent material. To enable the optical analysis both samples have been polished on one z-face and one y-face, respectively. Here, the polishing step also makes sure that any etching pattern remaining from fabrication is removed. The KTP sample was fabricated in the in-house technology in Paderborn by electric field poling from a contact electrode. A similar sample has been analyzed before [294]. It features a period length of $\Lambda = 16.7\mu$m and a duty cycle of approximately 70 : 30. Again, for optical analysis the z-face and one

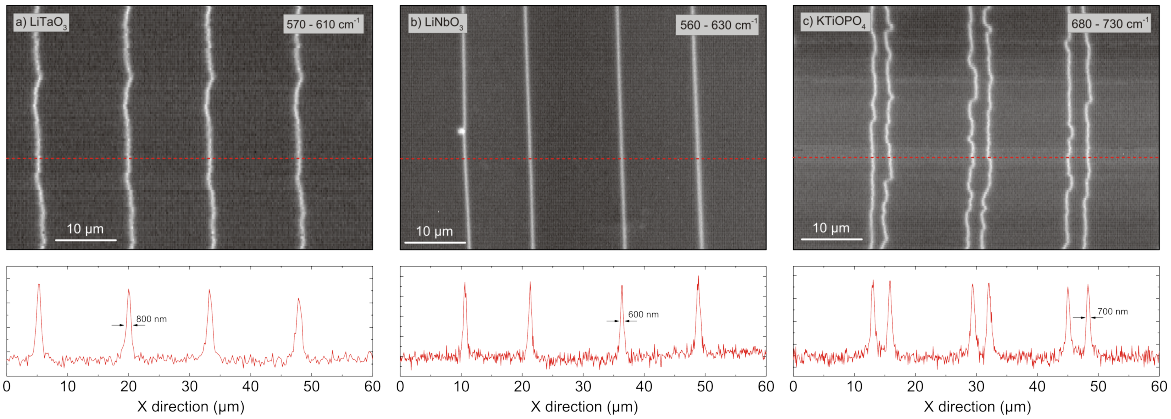

Fig. 5.2 Raman imaging is demonstrated for the $LiNbO_3$, $LiTaO_3$, and $KTiOPO_4$ sample. Each image is created using the integrated intensity in a specified spectral range of the Raman spectrum, which was identified by previous authors to give high contrast images of domain walls. The graph below each image, gives a cross section along the red, dashed line. Here, typical FWHM of the domain wall signatures between 600 and 800 nm are seen.

y-face has been polished. Here, all samples have domain walls oriented parallel to the y-axis according to Fig. 3.7.

Figure 5.2 demonstrates Raman imaging of ferroelectric domain walls on all three samples. Here, on each sample spectra in a 60 by 40 μm^2 (x by y) region were recorded every 100 nm orthogonal to the DWs (x-direction) and 250 nm steps parallel to the DWs (y-direction) with integration times of 1000 ms. For the scans, the focus was placed typically 5 to 10 μm below the sample surface, to ensure that no surface related effects will interfere with the measurements. The spectra were taken in a defined polarization described in Porto's notation as $z(x,x)\bar{z}$. For each material, certain parts in the spectrum are known, which show a systematic decrease or increase in intensity at a DW relative to a bulk spectrum. A straightforward and convenient method to generate images of domain wall is to integrate the intensity in such a spectral range. This integrated intensity is then plotted in a false-color image to reveal the domain structure. For our images we chose spectral ranges, which are known to provide an increased signal at DWs for each material. In detail, for LT we chose the range of 570 to 610 cm^{-1} [274], in LN the region from 560 - 630 cm^{-1} [46, 269, 252] and for KTP the region of 560 - 630 cm^{-1} is chosen [294], which all are known to provide a good contrast. Figure 5.2a) - c) shows the obtained images for our three samples. Here, the period length differences as well as the different duty cycles can be seen. Below each image a plot of the intensity profiles along the red, dashed line is given. Here, the signatures of the domain walls can be seen to clearly stand out from noise. The DW signatures show full width at half maxima (FWHM) of 600 to 800 nm. Here, the width is moderated by the resolution limit of optical microscopy and not by the size of the domain wall, which is significantly smaller than this. This already fits well with the idea and observations with other methods, e.g. PFM, where the domain transitions has been determined to be 20 - 80 nm for LN or KTP [307].

Based on the images and line scans performed in Fig. 5.2, the positions of single Domain walls were identified. On these locations Raman spectra were taken and compared with spectra taken in the bulk regions in between. In Figure 5.3c) and d) two examples for a DW spectrum for $KTiOPO_4$ and $LiTaO_3$ in $z(x,x)\bar{z}$ geometry are shown. Here, the DW spectrum is given in dashed green lines, while the bulk reference spectrum is plotted as a solid black line. Here, the differences appear only very minor, which is consistent with literature. To better highlight the differences, it is convenient to plot the difference spectrum. Here, the spectrum of the bulk is

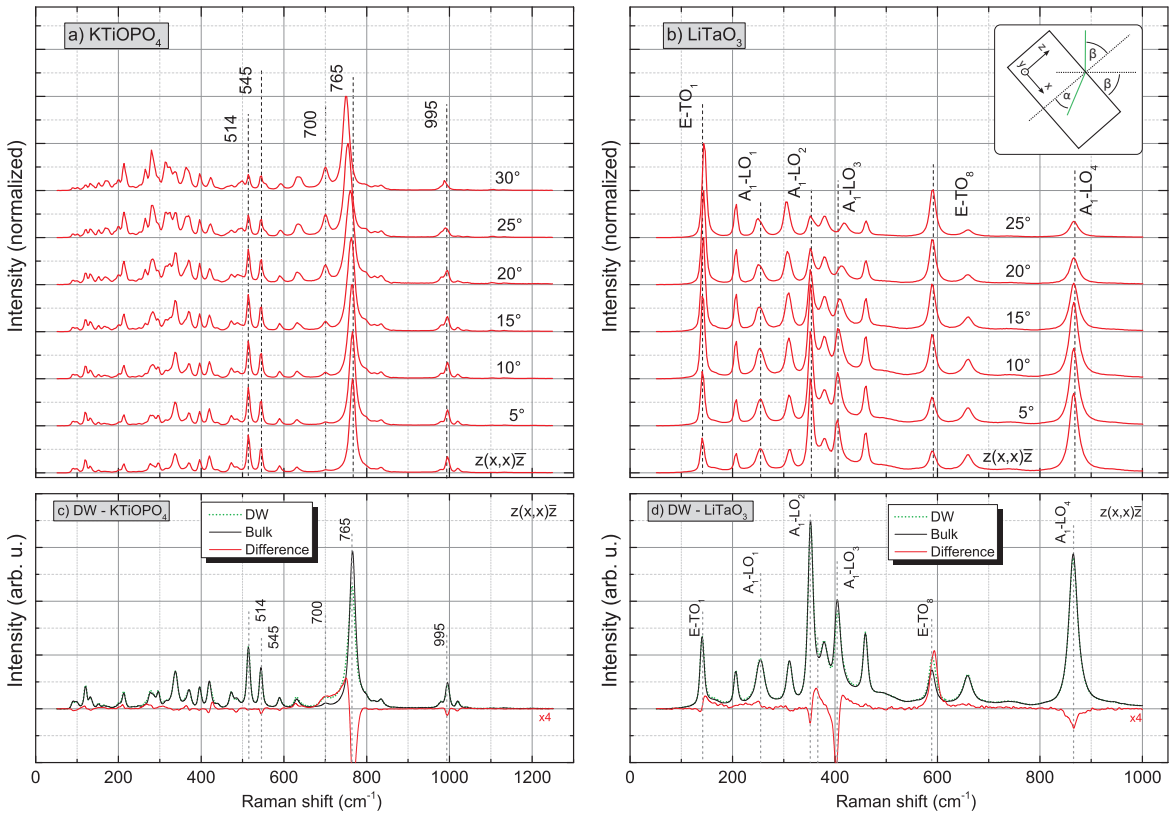

Fig. 5.3 a) and b) show the angular dependent Raman spectra of KTP and LT. Here, the crystal is tilted with respect by an angle with respect to the x- and z-axis, while the light polarization is kept fix according to the 0° scattering geometry z(x,x)$\bar{z}$.

subtracted from the DW spectrum ($I(DW) - I(bulk)$). This plot highlights, how the spectrum at the domain wall changes. For even better visibility this spectrum is multiplied by four and plotted beneath. This now allows to spot the differences quite easily. In KTP, for example, the region around 700 cm^{-1} from approximately 680 to 730 cm^{-1} shows an enhanced signal at the domain wall. This is exactly the region and behavior, which is used to create the plot in Fig. 5.2c).

As discussed above, the contrast for domain walls is explained by Stone and Dierolf in terms of a relaxation of the selection rules by treating the domain wall as a large, planar defect. Here, phonons propagating at oblique angles with respect to the wall will also participate in the scattering. To reconstruct the spectra expected at domain walls it is therefore necessary to actually measure the spectra of phonons propagating at oblique angles. For this, the samples were mounted on the goniometer stage and the sample was tilted around the y-axis according to the inset in Fig. 5.3b) with respect to the fixed optical axis. In Fig. 5.3 a) and b) show a series of spectra taken every 5° of tilting. Due to internal reflection only spectra up to approximately 25° in LN and LT and 30° in KTP could be taken, see Sec. 4.3 for more details. The light polarization in the experimental setup was kept fixed according to the starting scattering geometry, which in this case was x(z,z)$\bar{x}$. The spectra are simply normalized to maximum after the dark counts had been subtracted. For better visibility they are separated by 0.5 with respect to the normalization maximum for a first, qualitative comparison. This enables to compare the changes in the directional dependent spectra with the spectra of the domain walls. For easy comparison some spectral features have been highlighted. Here, the modes in $LiNbO_3$ and $LiTaO_3$ are

assigned with numerations, which are usually used in literature. And the assignment is based on the most recent works [245, 268, 70, 249]. For $KTiOPO_4$ no generally accepted assignments and numbering of all phonons are available, therefore the approximate mode frequencies are given, which allows for the convenient comparisons.

In the DW spectrum of $KTiOPO_4$ (Fig. 5.3c) one of the most prominent changes is the decrease and shift to lower frequencies of the 765 cm^{-1} phonon, while the mode at 700 cm^{-1} increases relative to this dominant peak. Alike, smaller changes for the 545 or 995 cm^{-1} can be spotted. In $LiTaO_3$ similar is observed, when comparing the angular dependent spectra (Fig. 5.3b) and the changes in the DW spectrum (Fig. 5.3d). Here, the most drastic changes at the DW spectrum are observed for the A_1-LO_2, LO_3, LO_4 and E-TO_8 modes. Indeed, these can be connected to the changes, which are observed in the angular resolved spectra. Here, the A_1-LO_2, A_1-LO_3 and A_1-LO_4 decrease and shift, as they are all extraordinary modes [246, 254]. The A_1-LO_3 shifts to higher frequencies and presents a LO-TO mixed mode, which at 90° eventually will merge with the E-TO_7 peak. Similar to this, the E-TO_8 shows a slight shift in the DW spectrum to higher frequency and an intensity increase. At 90° angle this mode will become the A_1-TO_4, which explains the strong reaction of this mode at the domain wall. Our observations allow - in agreement with the model by Stone and Dierolf - to explain most features of the domain wall spectrum.

Now, we investigate this behavior systematically for all geometries in z-cut and for all three materials. The top panels in Figs. 5.4a)-i) show the measured DW difference spectrum and a respective bulk spectrum for reference. The measured DW difference spectrum is calculated as described above and again multiplied by four for better visibility. It should be noted that it is in the correct proportion to the bulk spectrum. Only the bulk and the difference spectra are given, because the difference of the DW to the bulk spectrum is only minor.

The explanation for the contrast mechanism now associates the spectra of oblique propagating phonons with the DW spectrum. To systematically analyze this behavior, we have measured the angular resolved spectra at 0° and 25° and plotted them in the bottom panels in Figs. 5.4a)-i). Here, the 0° spectrum is identical with the bulk spectrum in the respective geometry, while the 25° spectrum represents the largest angle spectrum, which could be measured for all samples. The model for the contrast mechanism states that at the domain wall oblique-propagating phonons will be present in the Raman spectrum. Therefore, we now assume that the 25° spectrum is the spectrum of an 'ideal' domain wall and calculate the difference spectrum of the two spectra ($I(25°) - I(0°)$). The result is plotted below for an easy comparison with the measured DW spectra. For this calculation, the 0° and 25° spectra, both, have been normalized to maximum. As the domain wall region is smaller, than the focus spot size, this difference spectrum needs to be reduced. This is done by dividing it by four. This normalization provides a similar intensity of the calculated difference spectrum compared to the bulk spectrum, as the measured DW spectrum in the top panels show.

This goal of this calculation is to highlight any differences and to provide a spectrum for a quick and easy comparison. It should not be understood as an unrestrained, quantitative way to calculate the domain wall spectra. Here, two major limitations arise from our simple approach. First, we assume that only the 25° spectrum does represent the domain wall. For a more accurate modeling, more than just a single spectrum may need to be weighed in. Here, the weighing factor may depend on the quality of the domain wall and the actual magnitude of the DW quasi-momentum q_{DW}. However, the biggest issue, which prevents an accurate calculation, is the normalization of the spectra before the calculation. In our plot, the angular resolved spectra have just been normalized to maximum, because in absolute intensities, the 25° spectrum usually is much weaker in intensity, due to the large excitation angle. Here, a lot of intensity is lost due to reflection (see the inset in Fig. 5.3). This requires a normalization. As however, no mode can be assumed to be unchanged during the angular resolved measurement, any normalization may induce artifacts. For a better normalization in the future, for example, the Rayleigh peak may be used, which in our setup is blocked by a Notch filter.

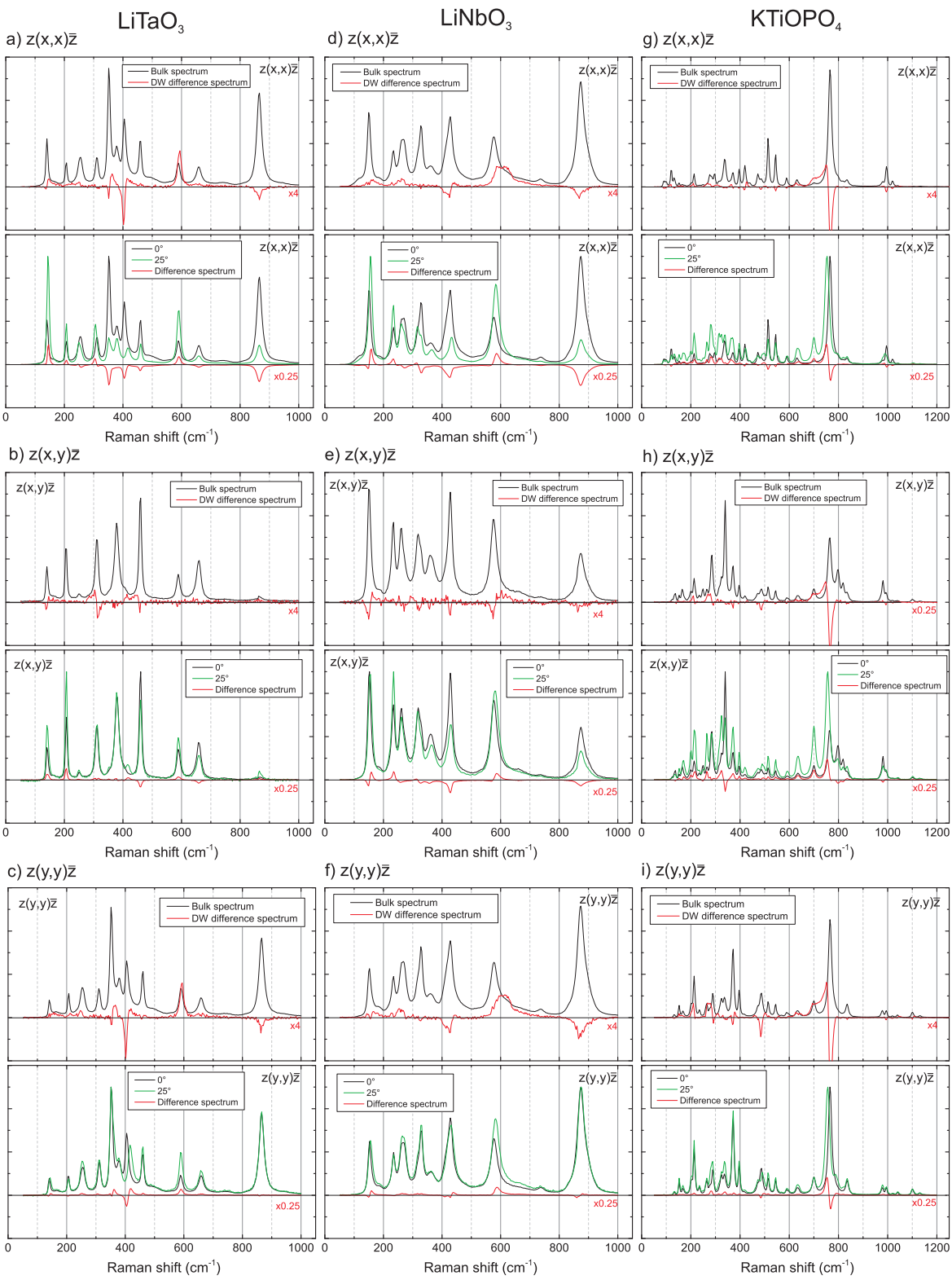

Fig. 5.4 The figure shows the spectral signatures of domain walls on z-cut for all three materials in the top spectra. Here, in black a bulk spectrum is given for reference, while the red line denotes the difference spectrum calculated from the measured DW spectrum ($I(DW) - I(bulk)$). Below are the 0° and 25° angular resolved spectra, where 0° is the spectrum in the given scattering geometry. Here, to highlight differences, also a difference spectrum is given ($I(25°) - I(0°)$).

Despite these limitations, the accordances we achieve with this approach are surprisingly large. Let us take for example the spectra of $LiNbO_3$ in Fig. 5.4 d) and f). Here, the measurement of the DW shows an increase in the 620 cm^{-1} region, while the A-LO_3 at $\approx$ 430 cm^{-1} and the A-LO_4 at 870 cm^{-1} show a decrease. This is well reproduced in the difference spectra of the angular dispersions. Similar, can be seen for $LiTaO_3$ or KTP, where several very pronounced modes of A_1-LO character decrease and shift, while the spectral regions, where after full rotation to y- or x-incident strong A_1-TO peaks are expected, strong increases are seen and predicted. That A_1-LO modes show a particular pronounced reaction, is easily understandable, because pure A_1-LO modes are only allowed for scattering geometries parallel to the optical axis [290]. Therefore, a strong shift and mixed LO-TO character for these modes is expected with any off-axis scattering. Alike, the A_1-TO counterparts will appear as the most intense modes in scattering geometries parallel to the xy-plane.

The predictions for the crossed polarizations (z(x,y)$\bar{z}$) in the center row are somewhat less conclusive for LN and LT. This is however, expected as they show E-TO modes. The E modes for LN and LT should have no pronounced directional shifts as expected, as the E-TO modes are ordinary modes and also will appear after the respective full turn. However, at crossed polarization geometries from x- or y-incident different E-TO modes with different intensities (a different tensor element) will be excited, which explains the changes in intensities. Shifts and certain features, like the shoulder at 620 cm^{-1} in LN also appear for this polarization, which are observed are mainly due to not fully suppressed depolarizations or due to focusing [278]. The problem that normalization will influence the calculated angular difference spectra, can best be seen in Fig. 5.4 f), where the strong mode at 860 cm^{-1} is expected to decrease in the top panel, however does not decrease in the bottom panel, as it is the mode used for normalization in the 0° and 25° spectrum. Instead a slight shift of the mode center of a few cm^{-1} is indicated, which is also observed in the top panel DW difference spectrum. Overall, this model appears to be able to explain most of the peculiarities.

So far, the model by Stone and Dierolf can explain the changes observed at domain walls fairly well and allows to predict the contrast behavior. The differences between our prediction and the actual DW spectra are mainly explained by the difficult normalization of the angular resolved spectra, as well as by the arbitrary selection of just the 25° angular resolved spectrum for comparison. The next questions is, if this model can also be applied to y-incident investigations of domain walls.

5.1.2 Domain walls on y-cut surfaces

As far, as we know all Raman studies on ferroelectric domain walls in either of the discussed crystals here, have been performed for z-incident Raman spectroscopy only [50, 46, 273, 269, 272, 251, 54, 294, 295, 274, 296–298, 252, 299]. Here, most images in literature have been obtained by either making use of one the A_1-LO phonons, the E-TO_8 phonon in $LiTaO_3$ or the 620 cm^{-1} region in $LiNbO_3$, all of which behaviors at the DW can be explained by the model of Stone and Dierolf and linked to the directional dispersion, as discussed before. In principal, also a contrast for domain walls in x-cut or y-cut geometries as shown in Fig. 5.1c) should be observable, if the directional dispersion will show significant changes at the DW. In this contest, Figure 5.1c) shows that scattering at the DW may excite mixed phonons propagating in the xy-plane (or ordinary plane) of the crystal. Here, for A_1 phonons purely TO phonons will be excited, for which no directional dependence do exist, e.g. tilting from from y(z,z)$\bar{y}$ to x(z,z)$\bar{x}$ will give the same spectra. Alike, E-TO phonons in crossed as well as parallel configurations show no directional dispersion. Phonons, which have no directional dispersion, are knows as ordinary phonons in the sense of Ref. [290]. The only exception for LN and LT are the E-LO phonons, which are however very weak and difficult to detect [245]. This is also seen in the Raman tensors for E-TO and A-TO phonons, where in y- or x-cut always the same elements are addressed. The ordinary

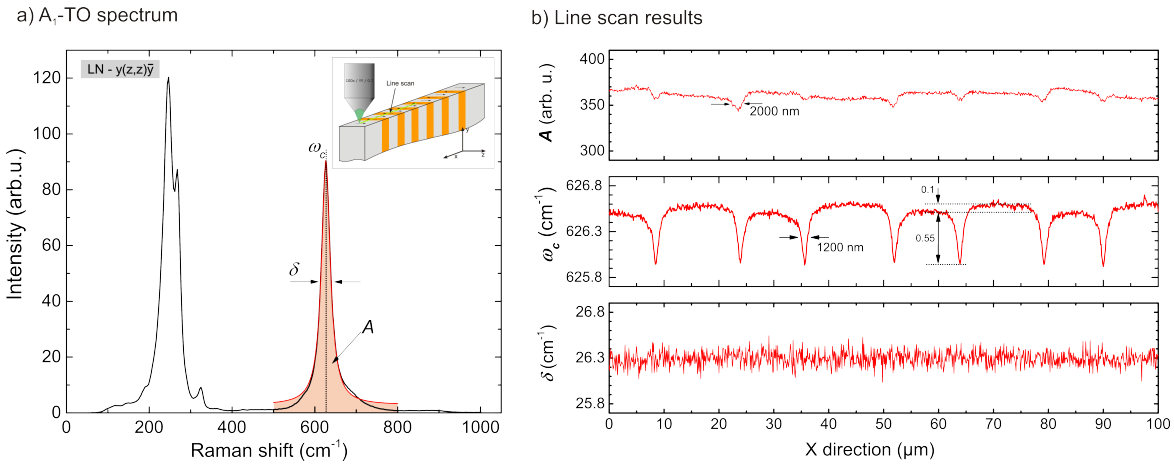

Fig. 5.5 a) Raman spectrum taken in y(z,z)$\bar{y}$ for $LiNbO_3$. The A-TO_4 line has been fitted with a Lorentzian function. The inset demonstrates the measurement geometry, in which y-cut domains have been investigated. b) Fitting results of a line scan on the $LiNbO_3$. The domain walls are associated with a clear shift of the peak frequency, while in the intensity only a light imprint can be seen.

nature of the phonons in the xy-plane has been experimentally demonstrated for Lithium niobate and tantalate [246, 254] and is in line with our observations, when measuring angular dependent spectra. If the model of Stone and Dierolf entirely describes the contrast at the DW, only very slight changes are expected at a DW, and these will only be seen for the weak E-LO modes. In this context $KTiOPO_4$ is different, because it is a biaxial crystal described by a three index ellipsoid, rather than a two-index ellipsoid. This also means that extraordinary phonons, i.e. phonons with a directional dependence [290], for rotations around the z-axis do exist. This is indeed what we have demonstrated in Sec. 4.3, where a phononic dispersion for the crossed polarizations between B_1 and B_2 phonons is observed, but not for A_1 phonons. Therefore, for the scattering geometry of y(x,z)$\bar{y}$ a contrast based on the model by Stone and Dierolf is expected as the only geometry.

To verify these ideas, line scans are performed in y-cut geometry for all samples and in all geometries as shown in the inset in Fig. 5.5a). As we expected only a small contrast for the DWs, the intensity this time has not just been integrated in the convenient method in various, but selected lines have been fitted with a Lorentzian function of the form

$$I(\omega) = \frac{A}{2\pi} \frac{\delta}{(\omega^2 - \omega_c^2) + \delta^2/4}, \tag{5.2}$$

where the prefactor A gives the integrated intensity of the line, ω_c is the resonance or peak frequency and δ specifies the full width at half maximum (FWHM) of the line. This allows to investigate line shifts, the intensities and FWHMs with respect to the domain structure. Figure 5.5 shows the result of such an investigation of a line scan of 100 μm for $LiNbO_3$. Here, the A_1-TO_4 line highlighted in Fig. 5.5a) has been investigated. While the intensity A only shows a slight connection to the domain walls, in the peak frequency ω_c a clear shift can be seen. The period length of 28.3 μm and the 40:60 duty cycle are reproduced very well, which demonstrates that domain wall imaging on y-cut is indeed possible, however the observed contrast here, is different from what we have expected and have previously seen for z-cut.

For each sample, such line scans have been performed in all three scattering geometries and several modes have been investigated for connections to the domain walls. Here, Fig. 5.6 shows an example for one mode in

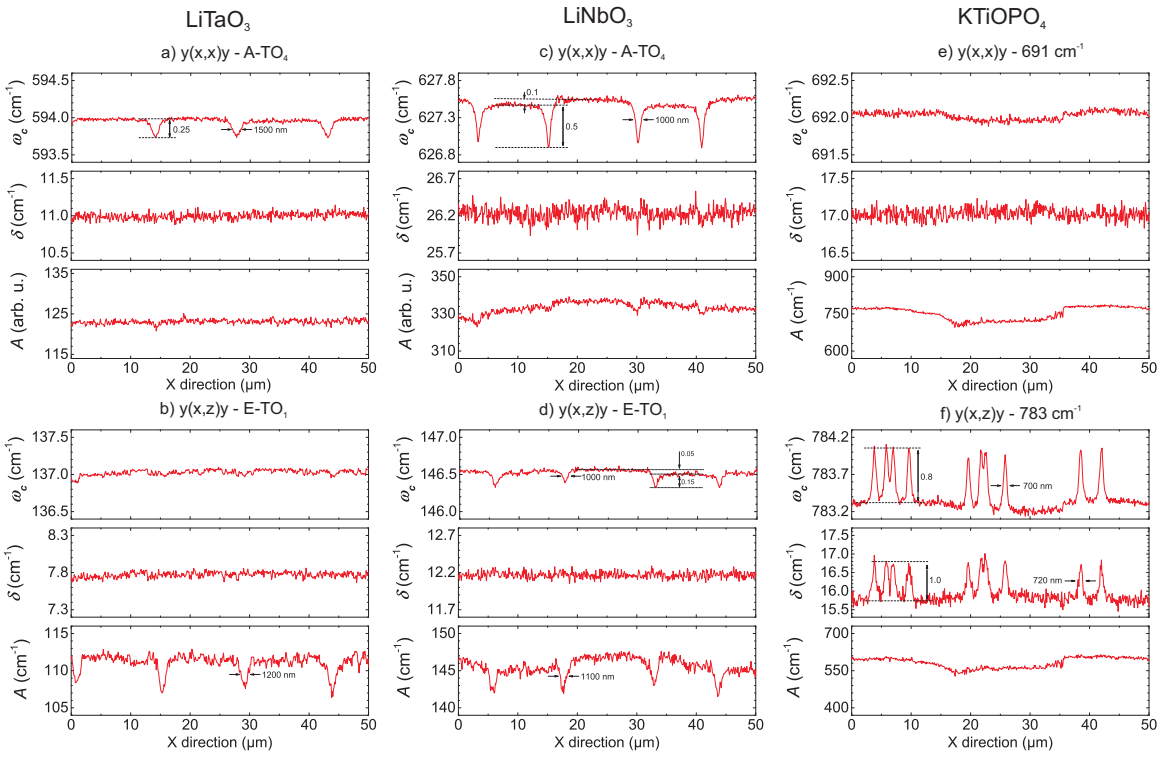

Fig. 5.6 The figure shows examples of results of lines scans for all three materials. Here, each phonon gives rise to a specific signature related to the presences of domain wall. While the DW signatures in $LiTaO_3$ and $LiNbO_3$ appear wider in y-cut, than z-cut, the DW signatures of KTP is of the same order. Here, however only a contrast for $y(x,z)\overline{y}$ is observed.

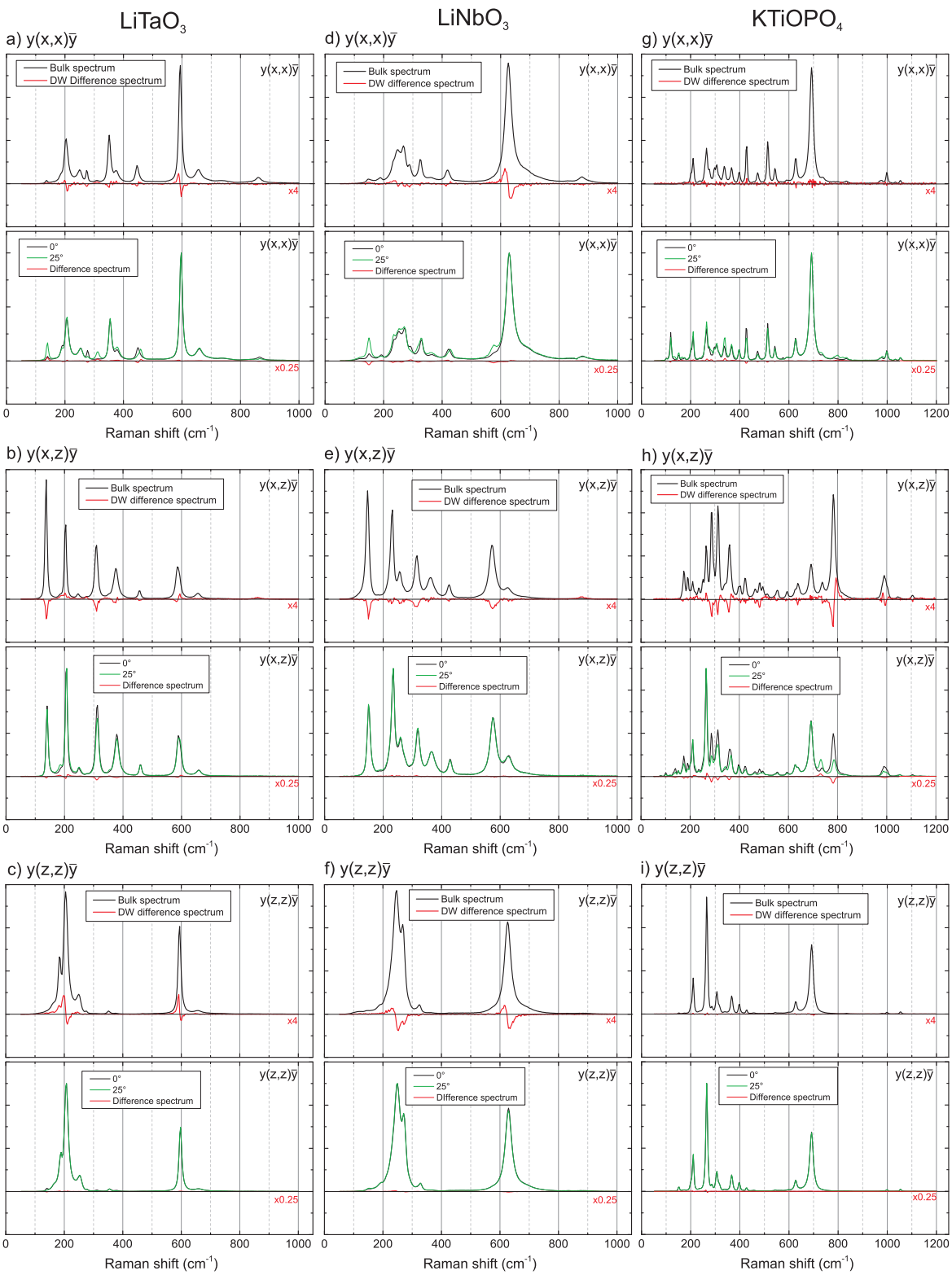

Fig. 5.7 The figure shows the spectral signatures of domain walls on y-cut for all three materials in the top spectra. Here, in black a bulk spectrum is given for reference, while the red line denotes the difference spectrum calculated from the measured DW spectrum ($I(DW) - I(bulk)$). Below are the 0° and 25° angular resolved spectra, where 0° is the spectrum in the given scattering geometry. Here, to highlight differences, also a difference spectrum is given ($I(25°) - I(0°)$).

y(x,x)$\overline{y}$ and y(x,z)$\overline{y}$ polarization. Based on these line scans, the locations of individual domain walls could be identified and the respective spectra could be taken.

Like in the previous section, Figure 5.7a)-i) shows in the top panels the measured difference spectra and a bulk spectrum for reference, while in the bottom panels the respective difference spectrum based on the angular resolved spectra is presented. Here, the difference spectra have been calculated in the similar manner, as discussed above. While we see in the top panels for all geometries significant changes in the difference spectra for $LiTaO_3$ and $LiNbO_3$, the angular resolved difference spectra indicate almost no changes, except for slight changes in E-LO modes in the y(x,z)$\overline{y}$ spectra in LN and LT. This is in agreement with the expectations discussed at the beginning of this section. In agreement with our predictions in KTP we only observe significant changes in the domain wall spectrum for y(x,z)$\overline{y}$ geometry in Fig. 5.7h), which also shows as the sole geometry a significant change in the directional dispersion in the bottom panel. In this context, it appears that the directional dispersion can only explain the behavior of KTP and to a slight degree of the weak E-LO in LN and LT, while the major changes in the LN and LT spectra remain not explained. To explain this behavior, we need to take a look again at the line scans of DWs presented in Fig. 5.6.

While the signatures of the domain walls for $KTiOPO_4$ show in y-cut a similar width of $KTiOPO_4$ of 700 nm in y-cut, we observe half widths between 1000 nm and 2000 nm in Figs. 5.7 and 5.5 for $LiNbO_3$ and $LiTaO_3$. Which is significantly larger, than the results previously observed in z-cut (Fig. 5.2). It should be stressed again at this point that the results for z-cut and y-cut, both, have been obtained on the same samples and with the same experimental setup. Despite that, we observed apparently larger domain wall signatures depending on the geometry and analyzed parameter. Indeed, even for z-cut these different ranges can be observed, if the right phonons and parameters are analyzed, as demonstrated in Fig. 5.8. The suggests that we have a different mechanism (with longer range) being responsible for this type of contrast, than the mechanism previously discussed by Stone and Dierolf. And this mechanism is at least in our experiment only present in $LiNbO_3$ and $LiTaO_3$, but not in $KTiOPO_4$. Indeed, if we take a look at the domain wall spectra (Fig. 5.7), we see significant changes in the DW spectra in all geometries for $LiNbO_3$ and $LiTaO_3$, but for $KTiOPO_4$ only in the y(x,z)$\overline{y}$ geometry in agreement with the presence of directional dispersion in this geometry. In contrast to this, the changes in the domain wall spectra for $LiNbO_3$ and $LiTaO_3$ can not be connected to the angular resolved spectra. Here, the explanation may be the aforementioned strain and/or electric fields, which have been discussed together with the microscopic model for the DW contrast of Fontana et. al. [269].

Indeed, in particular in congruent $LiNbO_3$ and $LiTaO_3$ a multitude of effects have been observed in the vicinity of domain walls. Here, strain fields in the order of 10 microns have been observed by x-ray topography spanning around domain walls [51, 300]. As $LiNbO_3$ and $LiTaO_3$ are piezo-electric this strain will likely be associated with an electric field. Indeed electric fields are present in the region of domains walls in congruent lithium niobate, as demonstrated by Dierolf et. al. with luminescence microscopy [144, 54]. Here, they detected fields of up to 6 kV/mm in a 4 μm range around the domain wall, while they could detect a long range electric field of up to 10 kV/mm before and still 4 kV/mm after annealing in a up to 20 μm wide region around the domain wall. These strain and electric fields are usually believed to be the reason behind changes in birefringence and refractive index from 3 to 20 μm around domain walls have been observed for both materials [52, 308, 54]. Alike, it is very reasonable that these strain and electric fields will influence the Raman spectrum, which is exactly the background of the first model for the DW contrast proposed by Fontana et. al. [269], which was discussed in the introduction [269]. The longer range of up to 2 μm fit well with the idea of strain being behind the contrast. Why is no such behavior observed for $KTiOPO_4$ in our experiment? Here, the reason may lay in the specific material properties of $KTiOPO_4$, which is known for its very high ionic conductivity [159]. If now any strains (inducing an electric field by the piezoelectric effect) or electric fields in general are present

in $KTiOPO_4$, they will be masked soon by a charge rearrangement. Some authors even report smaller domain wall width for $KTiOPO_4$, than $LiNbO_3$ [307].

The presence of (large) electric fields and their influence on the Raman spectrum in lithium niobate also allows to understand another observation. In the line scans of lithium niobate in Figs. 5.6c), d) and Fig. 5.5 one can see in the peak frequencies of the respective modes, do not only show a contrast for the domain wall, but apparently also a difference between domains of a different polarity. Here, for the A_1-TO phonon a difference of $\Delta\omega_c = 0.1$ cm^{-1} is seen, while for the E-TO_1 phonon a shift of $\Delta\omega_c = 0.05$ cm^{-1} is detected. This fits very well with the result of an experiment made by Stone et. al., who analyzed the Raman spectrum of z-cut stoichiometric and congruent lithium niobate under applied electric fields before and after poling [309]. Therefore, they applied an electric field along z-direction and measured the Raman spectrum from this direction. They detected for all of their analyzed phonons a linear shift of the mode frequency with respect to the applied electric field, as well as a frequency difference between domains of different orientations. Depending on the phonon they detected differences $\Delta\omega_c$ between 0.24 and 0.64 cm^{-1}. These differences they interpreted in terms of known residual fields in recently switched domains. Here, a lot of previous poling experiments in lithium niobate and tantalate have shown that the coercive field for forward and backward is different [136–138]. This is explained in terms of defect complexes with a defect polarization, which is not inverted during poling [102]. Therefore, the effective spontaneous polarization is different between recently switched and grown domains. This easily explains the frequency difference in domain of different polarity. According to Stone et. al. the proportionality constants between frequency shift and electric field β have values between 0.01 to 0.03 cm^{-1}mm/kV for most modes. Unfortunately, they did not provide data for A_1-TO_4, because they measured from z-cut, which only shows A_1-LO modes. However, a β between 0.01 to 0.03 cm^{-1}mm/kV will correspond to an internal field of 3 - 10 kV/mm based on the A_1-TO_4 of $\Delta\omega_c = 0.1$ cm^{-1}, which is certainly a reasonable magnitude for the internal fields in congruent material [136–138, 144]. Taking their proportionality constant for the E-TO_1 and assuming it can also be applied in y-cut spectra, we obtain an internal electric field of 2 kV/mm with $\beta = 0.024$ cm^{-1}mm/kV and $\Delta\omega_c = 0.05$ cm^{-1}. Certainly, defect complexes and internal fields are also known from lithium tantalate [136–138]. Why is then no different peak levels in the domains observed for lithium tantalate in our experiment? The reason here, may be the different sample fabrication, which we unfortunately can not comprehend, as the $LiTaO_3$ and $LiNbO_3$ sample were commercially acquired. From literature, it is for example known that defect complexes can rearrange with high temperature annealing [102, 54] and therefore this leveling will likely do vanish. These are things, however, which can be addressed in future work.

As mentioned, even for z-cut incident it can be shown that both mechanisms are present. Here, different response length can be observed. Figure 5.8 shows an investigation of the peak frequency, integrated intensity and FWHM for the E-TO_8 (≈ 580 cm^{-1}) and TO_1 (≈ 151 cm^{-1}) phonon from z-cut in lithium niobate in z(y,y)$\bar{\text{z}}$ and z(x,y)$\bar{\text{z}}$. Here, for the E-TO_8 in z(y,y)$\bar{\text{z}}$ we detect an increase in all three properties. In particular, the peak frequency shift is one of the largest, which we have detected in this work of 1.5 cm^{-1}. Here, these properties only change over 600 - 700 nm, which is in the limit of optical resolution similar to Fig. 5.2. The increase of peak frequency, integrated intensity and FWHM can easily be understood in terms of relaxed selection rules based on the model by Stone and Dierolf. Here, the shift, intensity increase and even the FWHM increase is expected. For the E-TO_1 in z(y,y)$\bar{\text{z}}$ geometry, we only detect very minor influences of the domain wall. Both observations are agreement with the spectra in Fig. 5.4. The situation, however is different for the spectrum in z(x,y)$\bar{\text{z}}$ crossed light polarization/detection. Here, the same peaks have been analyzed, which yield completely different results. In agreement with the difference spectrum in 5.4e) the E-TO_8 shows a decrease at the domain wall, while in the intensity an asymmetric shift to higher frequencies is observed. Here, the

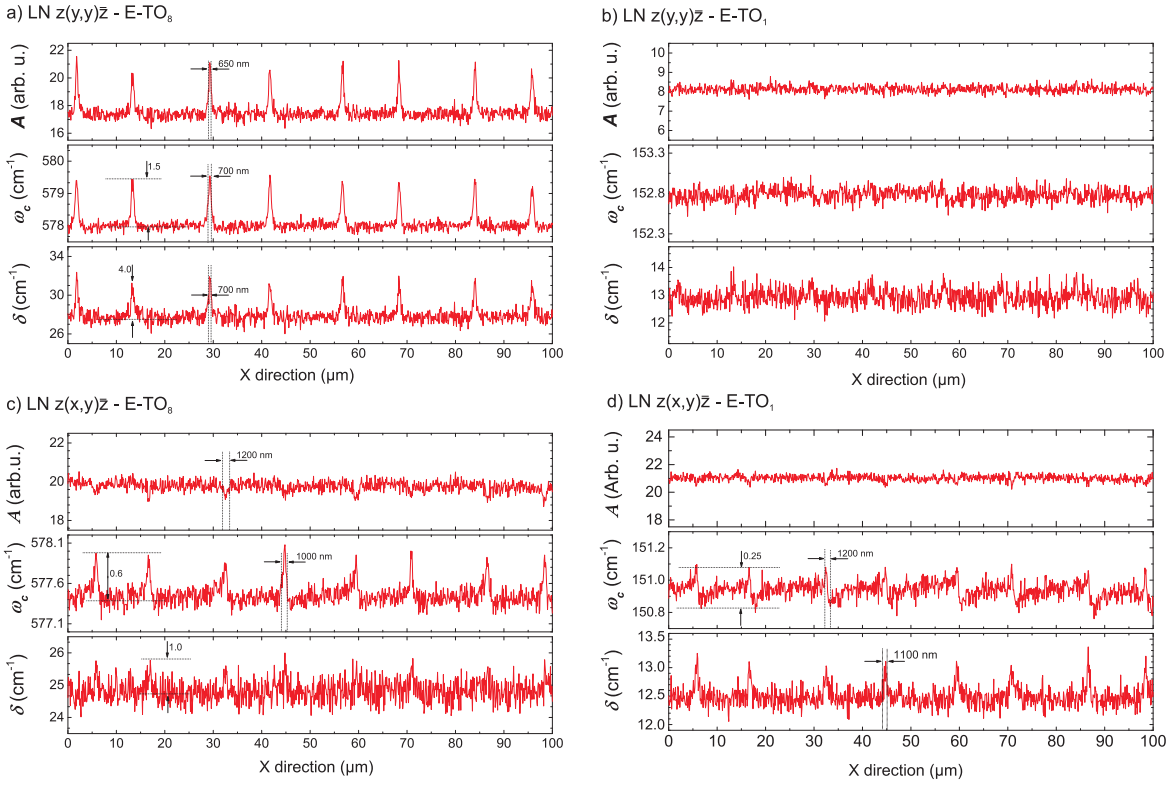

Fig. 5.8 We have investigated the peak frequency, integrated intensity and FWHM for the E-TO_8 and TO_1 phonon from z-cut in lithium niobate in z(y,y)$\bar{z}$ and z(x,y)$\bar{z}$.

spatial width of the domain wall signatures are larger ($<$ 1000 nm) than in z(y,y)$\bar{z}$, which again indicates that these shift can not be understood in terms of directional dispersion and lifted selection rules. As mentioned already before, the E-TO modes detected z(x,y)$\bar{z}$ should not show a pronounced directional dispersion, as these modes are of ordinary type. Even, better an unusual behavior is seen for the results of the E-TO_1 in crossed polarization in Fig. 5.8c). While the point spectrum in Fig. 5.4e) suggested a slight shift to higher frequencies at the domain wall, we now see here that we actually see a sawtooth pattern, where the frequency apparently increases towards the domain wall and decrease within 1200 nm across the DW. This is definitely not explained by a change in selection rules. According to the data of Stone et. al. [309] the frequency drop of $\Delta\omega = 0.25$ cm^{-1} refers to a drop in electric field of approximately 10 kV/mm, which according to our data then rises again towards the next domain transition. Although, it should be noted that Stone et. al. only applied field along the z-axis of the crystals. Here, the direction of the E-field is currently unclear and it is possible that the E-TO phonons in z(x,y)$\bar{z}$ geometry may couple to off-optical-axis electric fields. The range of the influence of the domain wall, appears in this case to be in the order of 10-20 microns, which is in agreement with the observations by Dierolf et. al. [144]. This hints that many things are left to understand in the substructure of the domain transition in lithium niobate and tantalate, as well as the role of fabrication history (annealing) or defects.

In conclusion, we have demonstrated that *both* models for the contrast of domain wall are needed to explain the effects observed. It depends on the scattering geometry, if the macroscopic or microscopic effects, and the specific phonon and property, i.e. shift, FWHM or intensity, if the macroscopic or microscopic effects will define the contrast. This raises two question for further investigation. Is the strain and field related domain wall contrast for $LiNbO_3$ and $LiTaO_3$ different, i.e. less pronounced, for stoichiometric and/or annealed material or even vanishes completely, which seems likely at this point? Alike, one can speculate if the physical width of the domain wall signatures of $LiNbO_3$ and $LiTaO_3$ is influenced by annealing or stoichiometry, i.e. in stoichiometric or annealed material the signatures will appear as small as the optical resolution permits ($<$ 600 nm).

5.1.3 Atomistic simulations

We have seen that electric fields and strain are an likely explanation DW contrast in at least $LiNbO_3$ and $LiTaO_3$, which is in agreement with the view of Fontana et. al. [269]. In order to enable an actual qualitative and quantitative prediction based on this view, we study the effect of aforementioned influences of strain and local electric fields in the vicinity of domain walls on the Raman spectra in terms of a simple atomistic model. The model was developed in cooperation with S. Neufeld from the group of S. Sanna. The basic idea is that we assume that the crystal structure at the domain wall is an extrapolated structure between the paraelectric (PE) and ferroelectric (FE) phase of the rhombohedral unit cell. This is somewhat reasonable as the spontaneous polarization needs to vanish at the domain transitions, which is a quasi-paraelectric state. The lattice vectors as well as atomic coordinates are linearly interpolated between their respective PE and FE values by

$$\vec{a}(\xi) = \xi \cdot \vec{a}_{FE} + (1-\xi) \cdot \vec{a}_{PE}. \tag{5.3}$$

This is displayed in Fig. 5.9. The calculations are then performed similar to Ref. [70], where the Raman spectra of TO modes are calculated. More details will be found in the to be published paper.

Since the changes of strain and internal polarization in the vicinity of a domain wall are considered to be relatively small (in the order of 10^{-4} [54]), only values of $\xi = 1$ (pure ferroelectric state) and $x = 0.95$ are considered in this work. A lattice distortion of that size accounts for strain values of $\varepsilon_{x,y} = 3.8 \cdot 10^{-4}$ and

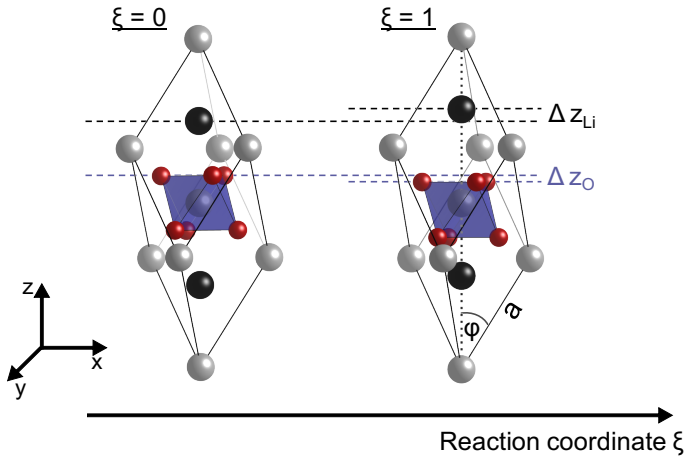

Fig. 5.9 Rhombohedral unit cell of LN/LT for different states along the reaction coordinate ξ between the ferroelectric ($\xi = 1$) and paraelectric phase ($\xi = 0$). O atoms are indicated in red, while white and black circles represent Nb/Ta and Li respectively. Note the displacement $\Delta\, z_O$ between the oxygen octahedron and the central niobium along the ferroelectric z-axis as well as the displacement $\Delta\, z_{Li}$ of the lithium sublattice. Rhombohedral lattice constants ϕ and a are indicated.

$\varepsilon_z = -7 \cdot 10^{-4}$ in the case of LN and $\varepsilon_{x,y} = 3.3 \cdot 10^{-4}$ and $\varepsilon_z = -3.7 \cdot 10^{-4}$ for LT. The internal polarization additionally decreases by $\Delta P_{LN} = 33.77$ mC/m^2 and $\Delta P_{LT} = 25.73$ mC/m^2 with respect to the ferroelectric phase. Raman spectra as well as difference spectra between the two geometries are summarized in Fig. 5.10. The largest contribution to the difference signal in (x,x) as well as (z,z) polarization can be observed to stem from A_1-TO modes. This can be explained by generally larger overlaps between the A_1-TO eigenvectors and the paraelectric-ferroelectric displacement vector (94 % and 69 % in case of the A_1-TO_1-mode of LN and LT respectively). A stronger overlap would result in a weakening of the restoring force and thus in a higher modulation of the phonon frequency. Frequency shifts between 2 cm^{-1} and 13 cm^{-1} can be observed throughout all spectra. Noticeable intensity shifts of A_1-TO modes appear exclusively within the A_1-TO_2 mode at 255 cm^{-1} ($x = 1$) and 250 cm^{-1} ($x = 0.95$) with an intensity increase from $\xi = 1$ to $\xi = 0.95$ of up to 31 % and 40 % for LN and LT respectively.

Comparing the results for theory, suggest an influence of strain on almost all modes. In particular large is the effect on the A_1-TO modes, which are directly associated with the ferroelectric properties (soft mode behavior [310–313]). Therefore, a strong and pronounced reaction of these modes is very reasonable. Comparing the results from the model spectra in Fig. 5.10 with the measured spectra indeed show a lot similarities on the A_1-TO modes. Here, the theoretical model suggests a shift to lower frequencies for all A_1-TO modes, which is also observed in the experiment and yields an explanation for the observed behaviors. Theory also suggests effects on nearly all E-TO modes. Here, however the accordance is less distinct. In the experiment, we observe first of all for all modes a decrease in intensity, while theory also suggests a shift. Here, the theory however suggests shifts of smaller magnitude, which may not be resolvable in experiment. Here, the largest shift is predicted for the E-$TO_{5/6}$ double peak at approximately 350 cm^{-1} for LT and 340 cm^{-1} for LN, which shows a shift to higher frequencies in contrast to all other modes. Indeed, this is also observed in Fig. 5.7b) for LT and to a lesser degree also for LN.

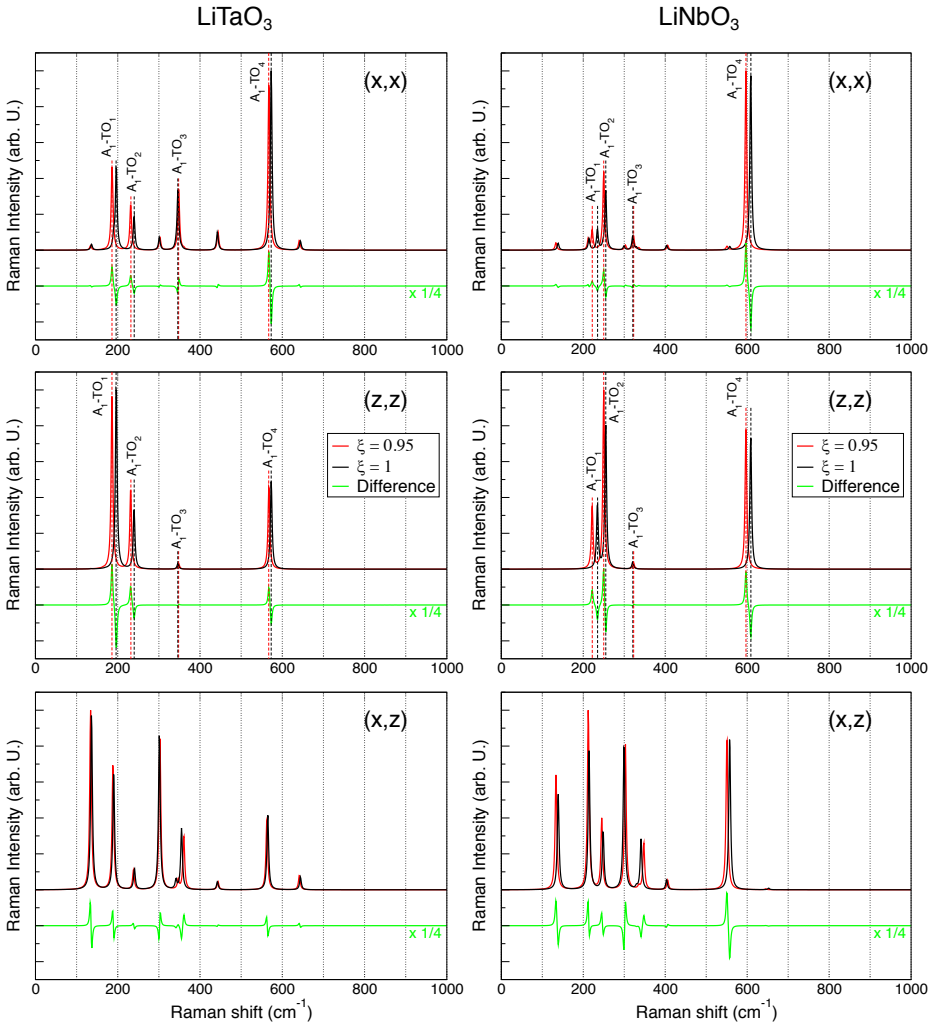

Fig. 5.10 Theoretical Raman spectra of LN/LT in three different polarization configurations. Spectra of both materials in their ferroelectric phase ($\xi = 1$) as well as in a distorted geometry corresponding to a displacement of 5 % along the ferroelectric-paraelectric reaction pathway ($\xi = 0.95$) are depicted alongside their corresponding difference spectra. Peak centers of A_1-TO modes are indicated by black/red lines.

In conclusion, we can see that even such a simple model already has explanatory qualities. Of course, a refining of the model including different types or directions of strain is indicated, which may in the future allows for a deeper understanding of the domain wall surroundings in $LiNbO_3$ and $LiTaO_3$.

5.1.4 Limits and open questions

As seen in this work, we have been able to understand the contrast at domain walls by a combination of a macroscopic model, where the DW modifies the selection rules, and a microscopic model, where microscopic strain and electric fields influence the Raman spectrum. Although our work is able to explain the general behavior of the contrast mechanism in poled, volume crystals, there are many peculiarities, which may be considered in future work. The first question is the role of surfaces. For example, in previous works there has been a contrast observed between recently switched ('as-poled') and virgin ('as-grown') domains [272, 252]. In these works, the contrast to the domain polarity has been explained in terms of residual surface charges, which is likely taking the work of Stone et. al. into account [309]. Related to this, different Raman spectra for +z and -z surfaces on lithium niobate have been predicted theoretically and observed in the experiments [314]. As a result a different contrast or spectrum for certain phonons may arise when measuring close to the surface. In previous work even a change in the sign of the contrast has been observed, i.e. the E-TO_8 showed a decrease at the domain wall measured close to the surface, while a decrease at the DW in depth was observed [315]. In our work here, we have deliberately analyzed data measured well away from the surface to exclude any surface related effects. Therefore, further studies may be carefully performed and interpreted, when analyzing contrast or the signatures of specific phonons in surface near regions. Alike, the imaging of ferroelectric domains in thin films [49] or ridge structures [225, 205] may vary from volume crystals due to pronounced surface effects. In the past, domains of head-to-head, tail-to-tail or arbitrary inclination have been observed with PFM and Cherenkov second-harmonic generation [316], which may will yield a different contrast mechanism in Raman microscopy.

But even in bulk regions, well away from surfaces, other factors may influence the Raman imaging of domain walls. In this context, previous work has also shown that point defects allocate at and in the vicinity of domain walls and domain walls do interact heavily with defects [54]. In this context, recent work by Nataf et. al. on Mg-doped $LiNbO_3$ could show that the actual domain wall signature also depends on defects and defect concentration [317]. Defects may influence contrast and sensitivity to domain walls or may even more alter the spectrum itself. In the context of defects, Raman spectroscopy is one of the prime methods to analyze doping, defects and stoichiometry in lithium niobate or tantalate [22]. In this work, we have analyzed domain structures in congruent material and no qualitative differences were observed in comparison to the previous work by Stone and Dierolf, who analyzed domain walls in near stoichiometric material [251]. This fits with the macroscopic nature of this explanation, where the substructure of the domain wall is of no concern. However, the contrast observed for y-cut $LiNbO_3$ and $LiTaO_3$ may completely change in stoichiometric material due to the absence of defects or fields, somewhat similar to the absence of contrast in y-cut $KTiOPO_4$ for some geometries. Indeed, there is a lot of experimental work, which shows that the internal fields in $LiTaO_3$ and $LiNbO_3$ are significantly smaller in near stoichiometric material [137, 136, 138]. In the context of defects, also the influence of annealing may be studied. Previous works based on nonlinear microscopy has shown that the DW-related signatures may be broadened before annealing, suggesting a more inhomogeneous domain interface [204]. Here, the question is, how this may affect the contrast in Raman spectroscopy, because of the changed defect structure and hence a changed quasi-momentum.

Related to the question of defects in the context of domain imaging by Raman spectroscopy are also wave guiding structures, which can be created in lithium niobate and tantalate by in-diffusion of metal ions, e.g. titanium, proton exchange or ion bombardment. Here, all these methods do nothing else than to deliberately create internal or external defects. Here, the localized presence of defects will likely influence the Raman spectrum. As seen in literature, not only domain structures will be visualized in Raman imaging, but also the waveguides structures themselves. Here, it is likely that domain wall contrast will change. In KTP waveguide fabrication is done by ion-exchange of the potassium ions, e.g. by rubidium. Due to the high mobility of the potassium ions along z-direction large rubidium concentrations are possible, which results effectively in $K_{1-x}Rb_xTiOPO_4$ mixed crystals, which will result in heavily modified Raman spectra. Here, images of domain structures in waveguides may be analyzed with caution, as the contrast mechanism will be influenced.

Lastly, the experimental setup itself may influence contrast and imaging. Here, of particular importance is the numerical aperture. Using a high NA objective lens results in a distribution of k-vectors in the excitation field in the focus area. Therefore, phonons propagating at oblique angles may be excited even in the bulk area. Here, a change in the Raman spectrum for different NAs in $LiNbO_3$ and $KTiOPO_4$ has been nicely demonstrated by Tuschel [278]. This may influence the contrast observed for domain walls, as signatures of oblique propagating phonons are already present in the bulk spectra. This effect may be considered in further work. In this context, it may be interesting to investigate domain walls by z-polarization microscopy via radially polarized light [276, 275]. This will allow to access y-cut and x-cut spectra from z-cut directions by radially polarized light, which will completely circumvent the mechanism of Stone and Dierolf, or investigate y- and x-cut spectra only by azimuthally polarized light.

5.1.5 Summary and Conclusion

In this work we have systematically performed Raman spectroscopy on ferroelectric domain structures in $LiNbO_3$, $LiTaO_3$ and $KTiOPO_4$. Here, the goal was to obtain an extensive insight in the mechanism, which alters the Raman spectrum in the vicinity of domain walls and allows for visualization of domain structures. In the past, two opposing models have been proposed to explain the contrast mechanism. One model suggests microscopic changes at a DW, e.g. electric fields, strain fields or defects, to be responsible for the difference in the Raman spectrum, while the second model proposes a macroscopic change of selection rules, which enables oblique phonons with mixed LO-TO character to participate in scattering. Our research demonstrates that both models play a role in domain wall contrast and need to be employed for a throughout understanding of the domain wall spectra. Here, the macroscopic model best explains differences seen in A_1-LO phonon, which are of extra-ordinary character (see Refs. [254, 246, 290–293]) with a pronounced directional dispersion. Basically by measuring angular resolved spectra, one can quickly predict the behavior of certain phonons at domain transitions. Microscopic changes in electric fields and strain manifest themselves mainly in micrometer-scale shifts of phonon frequencies and changes in intensity, which are qualitatively different from any changes due to relaxed selection rules. A microscopic model best explains differences in the spectra of ordinary phonons at domain walls, which show no directional dispersion. We can even identify two different response length scales for each effect. While strains or electric fields may span several micron around the domain wall, the change of selection rules appears to be localized only at the domain transition itself. Here, the width of the domain wall signature in the measurements is only limited by the diffraction limit of microscopy. Different response length indeed have been proposed in the past for different methods and properties [54]. In the context of the microscopic model, we present a simple atomistic model of strain and electric fields. While we can connect several changes in the spectrum to our atomistic model, it certainly does not fully comprehend the

system yet. Nevertheless, this proposes the path, how to simulate and understand the domain wall spectrum on a microscopic scale.

5.2 Investigation of $KTiOPO_4$

5.2.1 Rb-exchanged waveguides in $KTiOPO_4$

Introduction

Low loss waveguides allow the interconnection of passive or active optical structures without any coupling losses and therefore form the foundation of any integrated optical device. In integrated nonlinear optics waveguides allow to reach the high power densities necessary for any nonlinear effect with low absolute powers, while at the same time efficiently collecting the (sometimes) weak signal and idler beams. In the $KTiOPO_4$ material family waveguide fabrication has been demonstrated with various different methods. The methods range from depositing high refractive index material strips, e.g. tantalum pentaoxide Ta_2O_5, on top of $KTiOPO_4$ [318], creating index barriers of damaged crystalline material, e.g by ion irradiation [319–321] or high power laser beams [322], to ionic exchange methods. In particular, the ion exchange offers practical advantages and low losses. Here, one makes use of the possibilities offered by the large material family and the high mobility of the potassium atom, which can easily be exchanged by other similar atoms to effectively create mixed crystals. This has also the particular advantage that the nonlinear properties are retained. To create waveguides in $KTiOPO_4$ the potassium can be exchanged either by monovalent atoms, like rubidium, cesium or, thallium, or by divalent atoms, like barium or strontium [323, 324, 175]. Compounds with the named monovalent atoms are also part of the material family. This means that the ion exchange may effectively be understood as the formation of mixed crystals, e.g. $Rb_xK_{1-x}TiOP_4$ mixed crystals will be created for Rb exchange in $KTiOPO_4$. In contrast to monovalent atoms, the divalent barium comes with a peculiarity. barium exchanged in $KTiOPO_4$ is accompanied with domain inversion on -c surfaces [324–326]. In the past this has been used to create segmented, periodically poled waveguide in on fabrication step. However, the segmented nature of the waveguide will lead to comparatively high losses, as well as the domain inversion is often not as deep as the waveguide segments [325], which further limits the efficiency. In contrast to this for Rb exchanged waveguides losses down to 0.4 db/cm have been achieved [175]. And for Rb waveguides poling has been demonstrated by various methods [327, 326], which therefore is the method of choice for this work.

In this work, we have investigated Rb-exchanged waveguides fabricated on a flux grown $KTiOPO_4$ substrate. The sample was fabricated by C. Eigner. Here, waveguides of various width have been fabricated on a single substrate based on the process established by other authors [175, 170]. In preparation of the ion exchange, the fKTP substrate is covered on both c-surfaces in a titanium layer deposited by e-beam evaporation sputtering. Exchange is possible on either +c or -c surfaces. The titanium layer on the desired surface is then structured by a photo-lithographic mask and subsequent EDTA etching. As a result strips of various width (from 1.5 μm up to 40 μm) running along the x-axis are left uncovered by the titanium on the +c surface of the sample. The ion exchange is then performed in a melt of $RbNO_3/KNO_3/Ba(NO_3)_2$ at approximately 330 to 350°C for typically 60 minutes [326, 327, 175, 328]. Depending on the desired depth and profiles the process parameters need to be adjusted. Typical depth of a few μm are achieved with the aforementioned parameters. The addition of potassium nitrate in the melt should slow the Rb diffusion and serve as a buffer against potassium out-diffusion, because one of the main defects in $KTiOPO_4$ is a potassium non-stoichiometry [31, 182]. The Barium in low concentrations has been observed to serve as a catalyst for diffusion, as well as to homogenize diffusion profiles [170, 328, 323]. After waveguide fabrication, the Ti layer is removed completely and the end facets (x-faces) have been polished for the subsequent microscopy investigations.

Now, the goal is to investigate the properties of the waveguides of various width with μ-Raman spectroscopy. It is expected that mixed crystal of the form $Rb_xK_{1-x}TiOP_4$ are formed. In this context, Raman spectroscopy

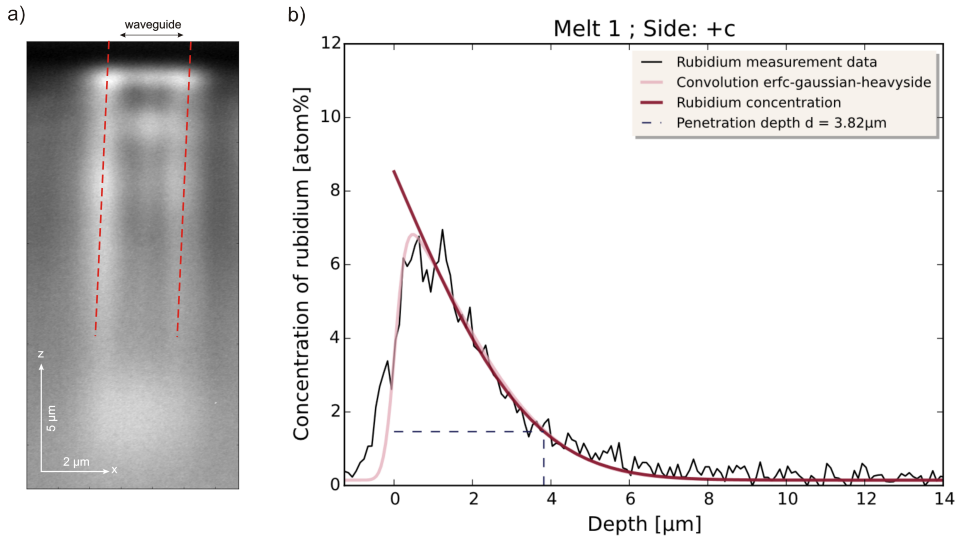

Fig. 5.11 a) Micrograph of a 3.5 μm wide waveguide, which is back-lit by a white LED. The light from the LED is coupled in the waveguide and excites guided modes. Here, guided light is not only seen in the upper part of the waveguide, where the strongest Rb-concentration and the largest refractive index change is expected, but also along the waveguide/bulk interfaces (dashed lines). This indicates a large, unexpected refractive index increase at the interface, which may be caused by strain [329, 330]. b) Typical Rb-concentration profile measured by EDX. Here, clearly the expected complementary error function profile is seen, which yields a depth of 3.82 μm [331].

should in principal enable to determine the Rb stoichiometry x based on the line shift, similar, for example, to the lithium niobate mixed crystals [268] (See Sec. 4.1.3). However, Raman spectroscopy is not only sensitive to stoichiometry. Any changes in crystal properties should have an imprint also in the Raman spectrum, e.g. strain, dielectric properties or disorder. Strain may manifest itself in line shifts [29, 28, 25, 287] and/or intensity variations [269] (See also Sec. 5.1), more disorder and a worse (K/Rb) stoichiometry in change in FWHM of Raman lines. Within this chapter, we will explore the possibilities of Raman analysis in this context and present the first extensive study on this topic.

In this context, previously two observations have been made, where the Raman analysis may provide additional insight [329, 331, 330]. Previously, EDX measurements have been performed by L. Padberg on similar samples to determine the diffusion depth and the Rb concentration profiles. This measurements confirm that the diffusion profile yields the expected complementary error-function as shown in Fig. 5.11b). However, it was noted that the diffusion depth for Rb-exchanged waveguides also depends on the waveguide width. In particular, small waveguides (1.5 μm width) appear to show a stronger diffusion and therefore larger depth, compared to wider waveguides. Here, a systematic decrease in diffusion depth is observed with increasing width. Can something similar also be observed with Raman spectroscopy? Related to this is a second observation. Here, the waveguiding in the waveguides have been investigated with microscopy by M. Santandrea. For this a white light provided by an LED was coupled into the waveguide and the guided light was imaged on the other sight by projecting the image on a CCD chip. The white light from the LED should excite many superimposing guided modes. An example for a 3.5 μm wide waveguide provided by M. Santandrea is shown in Fig. 5.11a). The EDX measurements suggest the largest Rb-concentration at the surface and decrease with depths. Hence, the most strongly confined guided modes are expected close to the waveguide surface. However, also strongly guided light is seen stretching deep into the crystal along the waveguide/bulk interface as highlighted by the

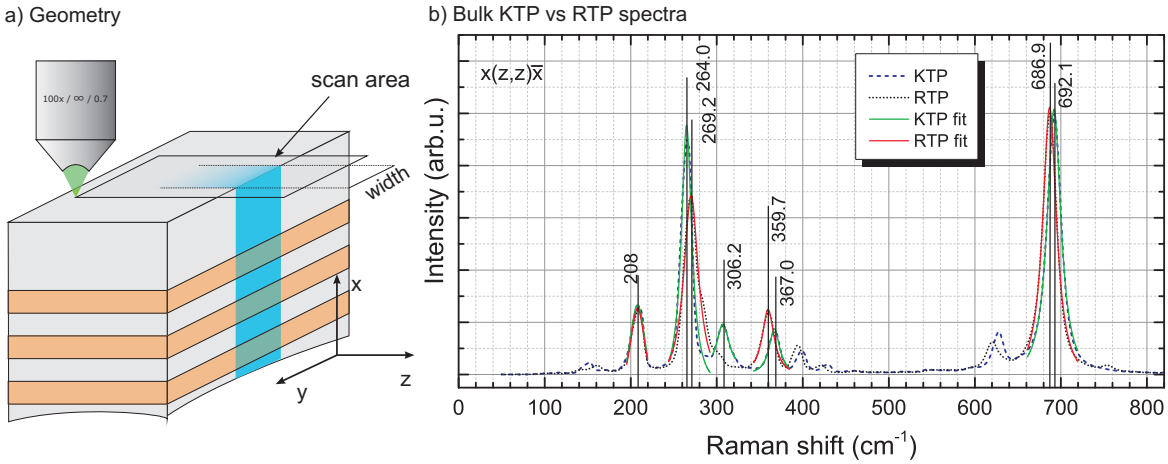

Fig. 5.12 a) Measurement geometry for the analysis of the diffusion profiles in Rb-exchanged waveguides in $KTiOPO_4$. b) Comparison of typical Raman spectra in x(z,z)$\bar{x}$ geometry for bulk $KTiOPO_4$ and bulk $RbTiOPO_4$. Highlighted and fitted are five different modes, which are analyzed for the imaging procedure.

dashed lines in Fig. 5.11a). Here, more light is guided that in the central node. This indicates that there might be an additional refractive index enhancement at the waveguide/bulk material interfaces. It should be stressed that the EDX measurements show no difference in Rb distribution with respect to the lateral dimension of the waveguide (y-axis). Similar Rb-diffusion profiles are obtained independent of the x-position of the lateral position in the waveguide. Here, the refractive index change may be caused by a strained interface, which is somewhat likely due to the large ionic radius of the Rb^+ ion compared to K^+ and the absence of lateral diffusion. For the Raman experiments this means that strain may result in additional shifts of phonon frequencies at the interfaces or that the strain induced dielectric changes will also result in intensity changes in Raman intensity along the interface.

While Raman studies on $KTiOPO_4$ and related compounds have been performed regularly, studies of ion exchanged waveguides are rare. So far, other authors have observed the appearance of new lines in Cs:$KTiOPO_4$ and Rb:$KTiOPO_4$, as well as a broadening of the lines [332–334]. In a Raman imaging study by Tuschel segmented waveguides were analyzed three dimensionally with confocal Raman spectroscopy. However, the images were attained by fitting a complete reference spectrum to the obtained spectra. This allowed for easy and fast visualization of the segmented waveguides, but limits the further insight in crystal properties [335]. In lithium niobate the situation is different. Here, confocal Raman imaging was applied to laser-written waveguides by several authors. Here, based on a detailed analysis of the modes and numerical simulations it was possible to fit the strain and damage profiles based on the Raman spectra [45, 27, 336, 337]. The goal of this present work is now to provide the foundation for a similar level of understanding of Rb-exchanged $KTiOPO_4$.

Figure 5.12a) shows the measurement geometry of the μ-Raman experiment. No pinhole was applied for this measurement series, due to the depth homogeneity of the sample in this geometry. The samples are mounted upright with their x-axis parallel to optical axis of the objective lens. This enables to investigate the samples with the best (lateral) resolution offered by diffraction limited microscopy. Here, the lateral width of the focus spot is smaller than < 500 nm. This is compatible with the previously performed EDX analysis [331]. Furthermore, it can be assumed that the samples are homogeneous along the x-axis. For better optical axis the x-faces have been polished. The waveguides chosen for analysis are identified in the optical microscope mode of the Raman setup. They can be made visible in the microscope by diffuse illumination provided by a

Table 5.1 Summary of the mode frequencies of modes for $KTiOPO_4$ and $RbTiOPO_4$, as measured in the experiment and compared to literature. All Raman shifts in wavenumbers in cm^{-1}.

Experiment		Watson [281]	
$KTiOPO_4$	$RbTiOPO_4$	$KTiOPO_4$	$RbTiOPO_4$
208.0	208.0	212.8	211.6
264.2	269.2	268.0	270.8
306.2	vanished	309.2	vanished
367.0	359.7	370	361.4
692.1	686.9	692.8	687.2

simple LED mounted below the samples similar to Fig. 5.11. For maximum Raman signal the focus was placed approximately 1 μm below the surface, which was determined by the maximum of the reflected laser light. We have performed Raman scans on four small (1.5, 2.5, 3.5, 4.5 μm, respectively) and one wide waveguide (40 μm width). For the small waveguides Raman images of 25 by 15 μm^2 (Y by Z) and 25 by 50 μm^2 (Y by Z) for the 40 μm waveguide. The step width was 200 nm in each direction. The measurement is performed in a fixed excitation and detection polarization, here the scattering geometry in Porto's notation is $x(z,z)\overline{x}$. Here x and -x denotes the k-vector of the incoming and detection direction, while (z,z) defines the light polarization (vector of the electric field) for (excitation, detection) all given in crystal coordinates. This scattering geometry allows for the detection of the phonons with the largest Raman scattering cross-section and shows A_1-TO modes. This geometry was chosen, as it is dominated by only a few, very intense peaks, which allows for easy analysis and fitting.

For reference, two bulk samples of $KTiOPO_4$ and $RbTiOPO_4$ were spectroscopically investigated in $x(z,z)\overline{x}$ geometry. This provides a baseline for interpretation of the Raman spectra of the waveguides, for example if shifts or intensity variations originate from the Rb exchange or from strain. Figure 5.12b) shows a comparison of the Raman spectrum of bulk $KTiOPO_4$ and bulk $RbTiOPO_4$ taken in the 0 cm^{-1} to 800 cm^{-1} range. No peaks below 100 cm^{-1} can be detected due to the Notch filter suppressing the elastically scattered light in the spectrometer. The intensity of both spectra appears very similar in the original experiment, where the $RbTiOPO_4$ spectrum appeared about 20% stronger, which can be seen as very similar. Here, the spectra are normalized to the maximum peak for better comparison. The spectrum of $KTiOPO_4$ shows five highlighted peaks at 208, 264.2, 306.2, 367, and 692.1 cm^{-1}. The spectrum of $RbTiOPO_4$ looks almost identical, which is expected because only the Rb atom is switched, while the crystal symmetry and structure remains the same. Consequently, the many peaks are subject to slight shifts or intensity variation due to the changed bonding length (larger unit cell of $RbTiOPO_4$) and doubled mass of Rb compared to K. Hence, no large differences are seen for the general shape of the spectrum. However, many peaks have shifted to lower frequencies due to the larger mass of the Rb, as well increased bond length. The peaks detected for $KTiOPO_4$, appear in $RbTiOPO_4$ now at 208, 269.2, 359.7 and 686.9 cm^{-1}. The peak formerly seen at 306.2 cm^{-1} has shifted to lower frequency and has almost vanished. If we now assume that the Rb-K exchange is the only thing, which influences the spectrum of the waveguide, we can now expect that the 208 cm^{-1} shows no shift, while the other modes are all subject to shifts and further the 306.2 cm^{-1} peak is expected to vanish. The measured intensities of KTP compared to RTP is observed to be comparable, which can easily be understood due to the very similar electronic properties. Therefore, for the analysis of the waveguides no large differences will be expected.

Watson compared the spectra of $RbTiOPO_4$ and $KTiOPO_4$. He detected the 208 cm^{-1} mode at 212.8 cm^{-1} in $KTiOPO_4$, while at a slightly *lower* frequency at 211.6 in $RbTiOPO_4$, which contradicts our observation. The 264 (367; 692.1) cm^{-1} mode he detected at 268.0 (370; 692.8) cm^{-1} in $KTiOPO_4$ and shifted to 270.8 (361.4;

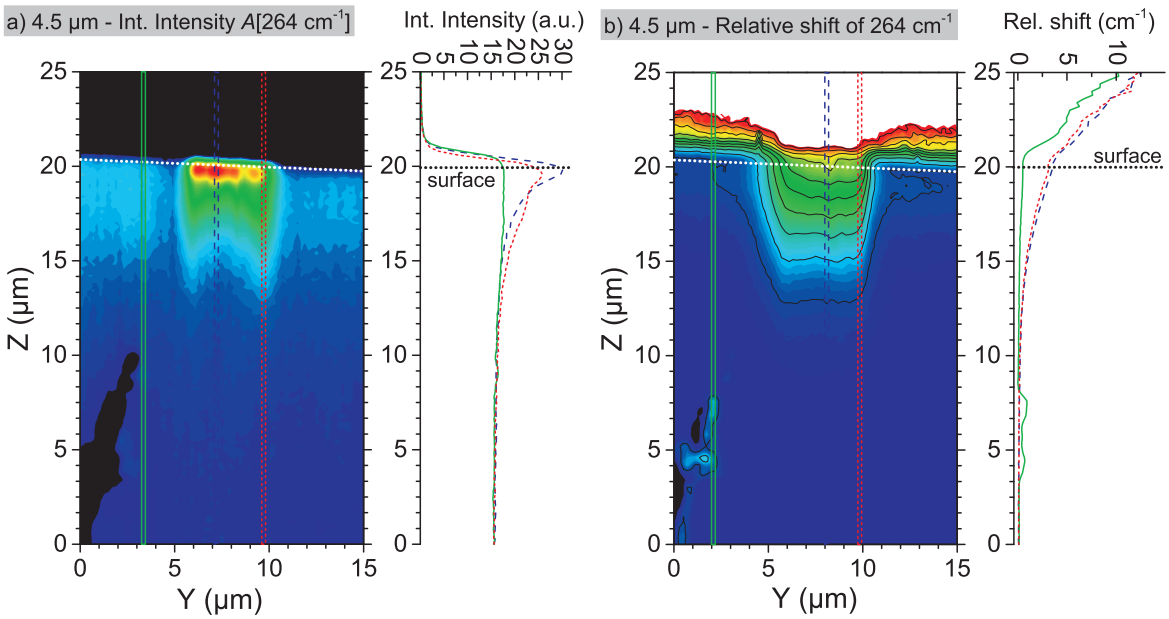

Fig. 5.13 a) Plot of the integrated intensity of the 264 cm^{-1} and profile lines at three different positions. b) Relative shift of the 264 cm^{-1} band with respect to the bulk value.

687.2) cm^{-1} in $RbTiOPO_4$ in agreement with our observation. Alike, the peak at 306.2 cm^{-1} is at 309.2 cm^{-1} in $KTiOPO_4$ and vanished in $RbTiOPO_4$. He detects a slightly different magnitude in most shifts, this is either explained in a different stoichiometry (quality) of the crystals compared in our experiment and study. Here, the most common defect in the $KTiOPO_4$ family is a potassium deficiency, which may influences the position of the peaks. Secondly, Watson performed the experiment in a 90° scattering configuration (x(z,z)y), which may also explain some differences. The results are summarized in Tab. 5.1. Nevertheless, with the exception of the 208 cm^{-1}, he detected the same general trends for the other four modes. Because the wafers, where the waveguides have been fabricated in, and the $KTiOPO_4$ and $RbTiOPO_4$ sample are from the same vendor, we assume a comparable quality (stoichiometry) for both materials. Therefore, we use our measured values as reference for the upcoming analysis.

Results on 4.5 μm waveguide

With this baseline the waveguides can now be investigated. For the evaluation now, in each spectrum the specified lines are fitted with a single Lorentzian profile

$$I(\omega) = \frac{A}{2\pi} \frac{\Gamma}{(\omega^2 - \omega_c^2) + \Gamma^2/4}, \tag{5.4}$$

where A is proportional to the amplitude (or integrated intensity below the line), ω_c denotes the resonance frequency (in this case the Raman shift of each mode) and Γ quantifies the full width at half maximum (FWHM) of the line. As a result, we can now plot the intensity, FWHM and peak frequency for each mode as a function of spatial position.

Figure 5.13 shows the plot of the integrated intensity (a) and relative shift of the 264 cm^{-1} with respect to the $KTiOPO_4$ bulk frequency exemplary for the 4.5 μm waveguide. The intensity and shift are represented as false color images, where *red* denotes a high intensity (large shift) and *blue* a low intensity (no shift compared to

the bulk frequency), respectively. In 5.13a) the waveguide appears as a region of increased intensity compared to the bulk $KTiOPO_4$ below and adjacent to the waveguide. The plotted profile lines show three intensity profiles. One profile measured over the bulk region (green, solid), one through a hot spot in the waveguide center (blue, large dashes), where the intensity is almost enhanced by 100 %, and a profile along the waveguide/bulk interface (red, short dashes). Here, the influence of exchange is detected much deeper in z-direction, compared to the center hot spot. The overall plot also demonstrates how we define the air/crystal interface in this and the following plots. It is defined as the point, where the intensity in the bulk region has reached a constant level. This line is then highlighted as a white, dotted line in the relative shift and FWHM plots to provide an equal baseline for all plots. A particular striking feature in Fig. 5.13a) is the shape of the waveguide in the intensity plot. Here, the waveguide appears in a pronounced inverted u-shape shape, very similar to the micrograph of the waveguide in Fig. 5.11 . In contrast to this, the inverted u-profiled shape can not be seen for the peak frequency plot. Here, we see a systematic increase in the frequency towards the surface and in the waveguide region, which one can expect for a Rb-exchanged area. However, the region, where a frequency shift is seen, is larger than the actual exchanged area. Here, we see a trapezoid shape of increased intensity. This may indicate a strained region, which we will later discuss in more detail. In the profile lines, it can be seen that the frequency stays almost constant in the bulk outside of the waveguide (green solid line), while decreasing from a value of about 4.5 cm^{-1} relative shift at the surface to the bulk level within 7-8 μm. Above the highlighted surface line, the fit indicates a heavy increase in mode frequency. This is an artifact in fitting due to heavily decreasing intensity, the fit does not converge anymore. In this region typically a diverging FWHM and shift is seen. Therefore, above the highlighted surface line (white, dotted line), the values have no physical meaning.

Figures 5.14 and 5.15 show now the complete set of results on the 4.5 μm of all five previously identified modes. Here, the analysis and definition of surface has been performed as described above. The first row shows the integrated intensities, the second row the respective shifts and the last row the determined FWHM for each mode. The fit of the intensity shows for all modes, except the 306 cm^{-1}, a general increase with only minor differences. Remarkably, the relative intensity enhancement appears to be a general effect for all modes and appears to have no dependency on the analyzed modes. The intensity enhancement appears to be similar in magnitude for any mode and is seen for nearly all modes, as displayed in Fig. 5.19. In contrast to the other modes, the 306 cm^{-1} mode vanishes in the waveguide region (Fig. 5.14c), while adjacent to the waveguide a region of significantly enhanced intensity is observed. The vanishing is in agreement with the prediction for $Rb_xK_{1-x}TiOPO_4$.

The situation is different, if we concern the peak shifts. Here, we see a specific and distinctly different behavior for each mode. As discussed above, the 264 cm^{-1} reacts in the expected way, so do the 306 and 367 cm^{-1} peaks. Both show a slight decrease in frequency, as suggested before. The other two modes, however, show a different behavior. The 208 cm^{-1} mode shows a steady increase of up about 3 cm^{-1} in the waveguide region, which was neither expected from the bulk crystal analysis, nor the literature. This may suggest that the shift is not explained by the formation of mixed crystals, but possibly by strain. Similar is observed for the 692.1 cm^{-1}. Here, we have expected a distinct shift to lower frequencies, yet we see an even increased frequency of about 2 cm^{-1} in the waveguide region. Here, the shift appears not the be moderated by the Rb-exchange, but by strain. It is very likely that these waveguides are strained, due to the different lattice constants of $RbTiOPO_4$ and $KTiOPO_4$ and the different ionic radii of Rb^+ and K^+, respectively [154, 159]. Here, a material with a larger lattice parameter and unit cell size ($RbTiOPO_4$) is positioned in a matrix by a material with a smaller lattice constant ($KTiOPO_4$), which results in compressive strain. Here, compressive strain leads to shorter bond lengths and increased frequencies in the majority of modes [287], which is exactly what we observe here. The trapezoid shape of several peak frequency plots also fits with this idea. Here, the strain is larger in magnitude,

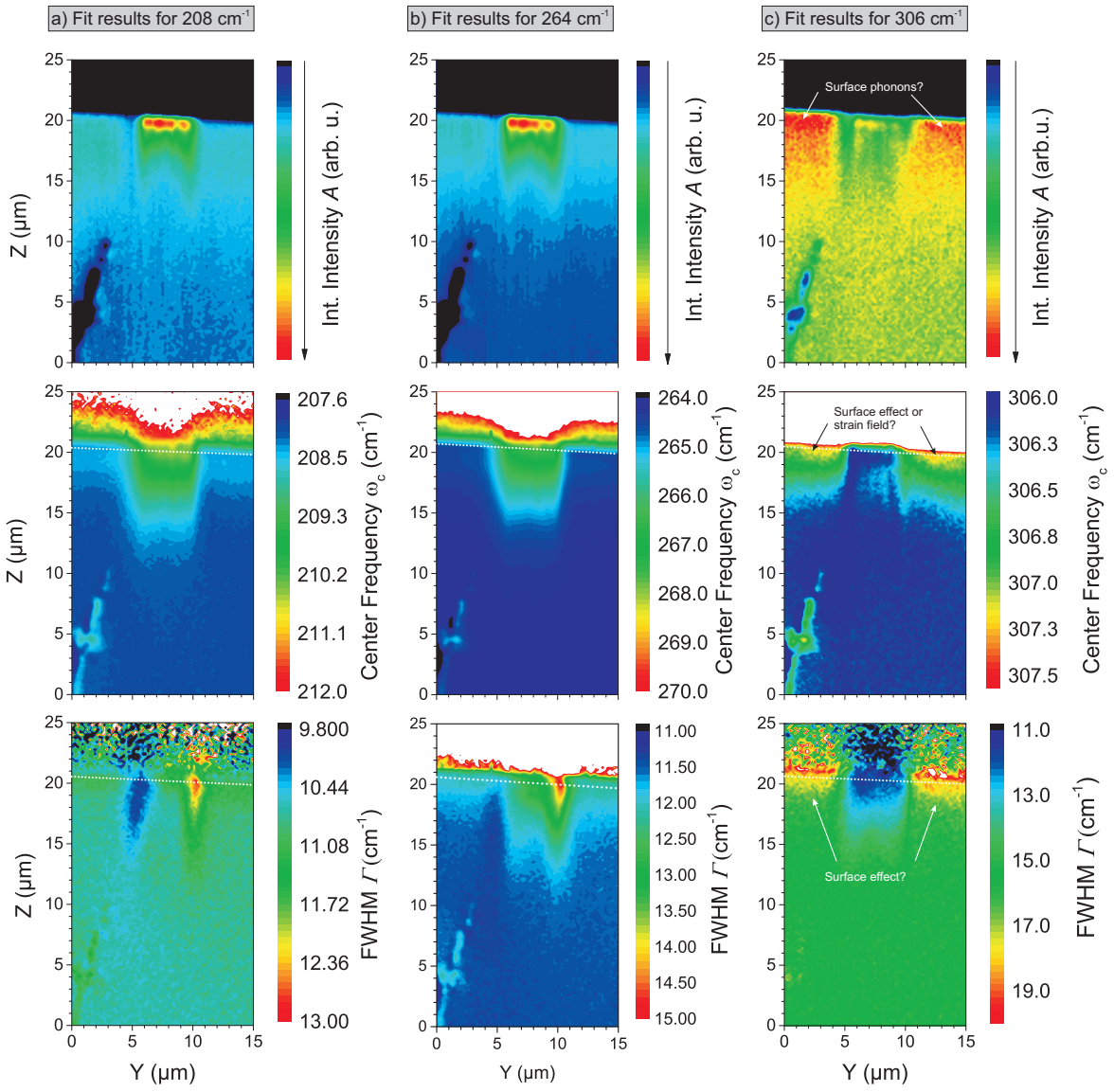

Fig. 5.14 The figures shows the fit results for the integrated intensity A, peak shift ω_c and FWHM Γ for the 208, 264 and 306.2 cm^{-1} modes. Each mode and parameter gives rise to specific signatures.

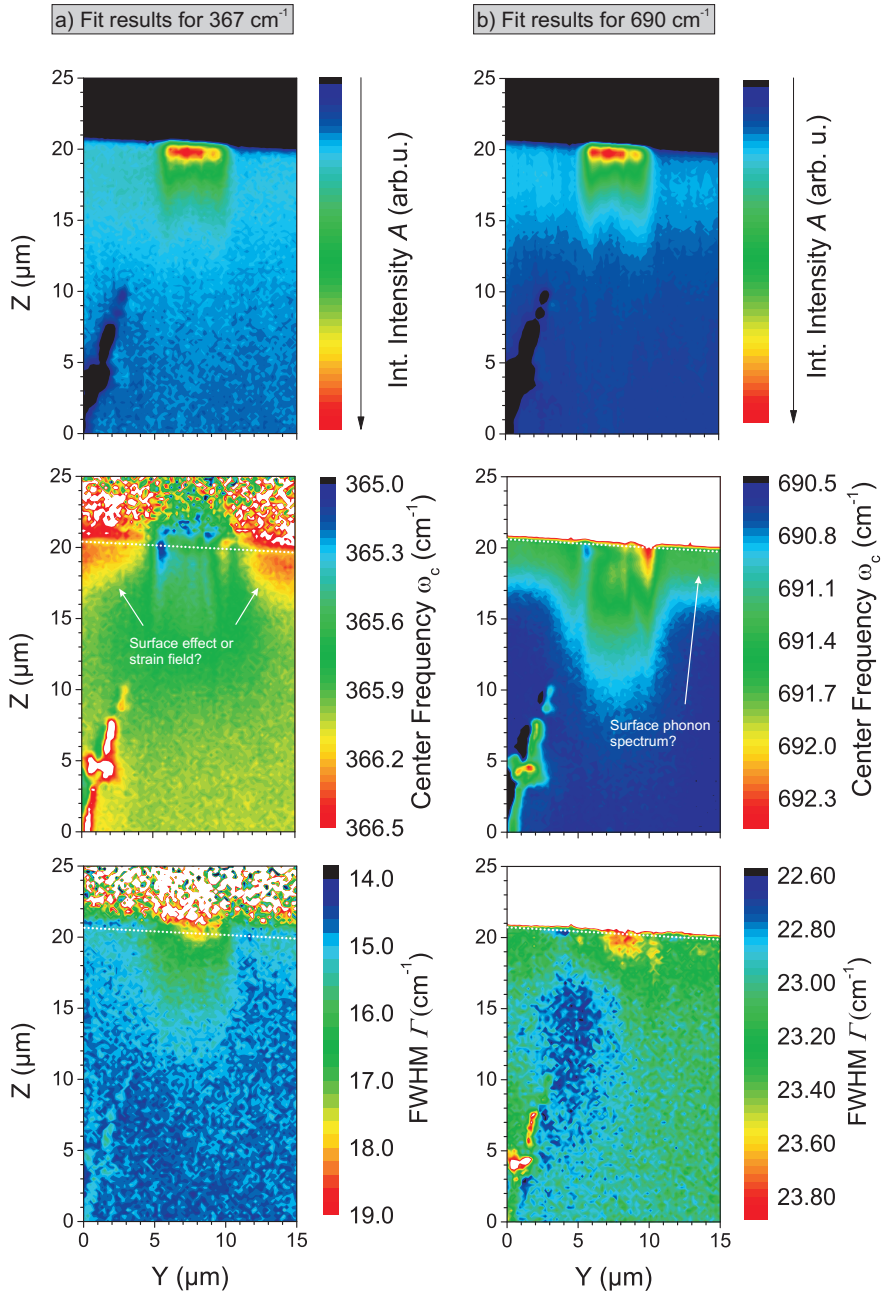

Fig. 5.15 The figures shows the fit results for the integrated intensity A, peak shift ω_c and FWHM Γ for the 367 and 692.1 cm^{-1} modes. Each mode and parameter gives rise to specific signatures.

as well as physical dimension, closer towards the surface. This can be explained by the larger Rb/K contrast closer to the surface at the waveguide/bulk interface. Strain will lead to an additional effect on the (linear and nonlinear) dielectric properties, i.e. the refractive index [338]. This would explain the inverted u-shaped refractive index profiles, but also Raman intensity plots, because the Raman intensity alike depends on the susceptibility. Previous work on laser written waveguides in lithium niobate or deposited silicon oxynitride on silicon suggest that strain fields may stretch 10-20 μm around waveguides [337, 28, 29]. The question is, if the structures seen in the shift of the 367 cm^{-1} or the second harmonic microscopy analysis, are also due to similar large strain fields around the waveguides.

In terms of changes in FWHM, we can distinguish two different behaviors. Here, the 208 and 264 cm^{-1}, both, show an change in FWHM at the waveguide/bulk interface, which suggest particular disorder in these region. This is somewhat reasonable, as this is also the strained region. In contrast to this, the other three modes show a change in the FWHM restricted to the waveguide region. Here, in particular for the non-vanishing 367 and 692 cm^{-1} we see an increase in FWHM, which is very typical for formation of mixed crystal or doped/ion exchanged material [333]. The basic idea is that the in-diffusion will disturb the long range crystallographic order, which relaxes the selection rules leading to an increased width of modes. In particular for Rb:$KTiOPO_4$ it is even known that the Rb will - at least in low concentrations - primarily occupy only one of the two crystallographically distinct lattice sites for K ions [177, 178]. This will likely lower the symmetry of the crystal and lead to higher disorder. This also fits with the results from second harmonic microscopy shown below.

Additionally to this, we see for the 306 cm^{-1} mode an increase of the FWHM in a 1-2 μm wide layer close to the surface. Similar observations can be made for the intensity or center frequencies of some modes as marked by arrows and comments in several plots in Figs. 5.14, 5.15 and even for the SH microscopy images in Fig. 5.18. Here, the effects length scales range from 1-5 μm along the z-direction. This result indicate that the polar surface of $KTiOPO_4$ is physically and/or chemically different from bulk material. Here, physically different can, for example, mean that the surface has a distinctly different phonon spectrum, as it was observed for lithium niobate. Here, the +c and -c surfaces have different reconstruction and distinctly different Raman spectra and properties [314, 339]. If one measures spectra close to the surfaces, it sounds reasonable that influences are visible. Even the measurement geometry used in this experiment was similar to the previous investigation of polar surfaces in $LiNbO_3$ [314]. However, also chemical differences of the surface layers in contrast to bulk material are possible. $KTiOPO_4$ is a ferroelectric. The spontaneous polarization will lead to a surface charge compensating for the outer electric field. As $KTiOPO_4$, however, features a large ionic conductivity, this surface charges will be screened by charge transfer. Here, either K^+ ions diffuse to the surface or away from it (depending on +c or -c orientation), leading to a compensating electric field. Obviously, this will change the K^+ stoichiometry in a surface layer, which may explain the effects we see in our plots. Alike, it is possible that the availability of K-vacancies, may lead to an in-diffusion of adsorbed air molecules.

The observation of surface effects means that one has to be particular cautious when using Raman spectroscopy for the investigation of diffusion profiles, because this surface effects on the Raman spectrum will overlap with effects from Rb-exchange. This may be the reason, why the 367 cm^{-1} (Fig. 5.15a) shows almost the same frequency in bulk, as in the waveguide region. From the bulk analysis we expected the mode to lower its frequency by more than 7 cm^{-1} for very high Rb concentrations. At the same time, we observed a frequency increase adjacent to the waveguide in a surface region. So both effects may cancel each other, which complicates the analysis as both effects can not unambiguously be distinguished. Further studies are required to analyze and understand the surface effects in this material, e.g. comparing +c and -c surfaces or analyzing effects of different treatments, which is however beyond the scope of this study.

So far, we can conclude that the majority of the analyzed modes and properties react in the way, which is expected for the formation of $Rb_xK_{1-x}TiOP_4$ mixed crystals. The observations are in agreement with the predictions based on the comparison of $RbTiOPO_4$ and $KTiOPO_4$ Raman spectra. Here, in particular the line shifts show a systematic behavior, which fits with the expected diffusion process. Alike, the FWHM of some modes shows an increased value in the waveguide region, which is typical for ion-exchanged and the formation of mixed crystals. This indicates an increased disorder in line with previous observation [333].

Width dependent results

As we have seen, every phonon we have analyzed so far shows a specific behavior with respect to the ion exchange. However, the analysis has shown that only the 264 cm^{-1} reacts to the Rb-exchange in the way, we expected and shows no pronounced surface related behavior. Alike, its FWHM only shows a pronounced influence at the waveguide/bulk interface, while it is less affected in the central region. Hence, for further analysis of waveguides of different width, we will restrict the analysis to the 264.0 cm^{-1} line.

Figure 5.16 shows the 264 cm^{-1} mode evaluated for all small waveguides (1.5 - 4.5 μm). The intensity plots in the first row show the waveguide region dominated by surface near hotspots, where a heavily enhanced Raman signal is observed. In the intensity plots we see for each waveguide, except the smallest, an inverted u-shaped intensity profile, where the intensity enhancement stretches deeper into the material at the waveguide/bulk interface, than in the center. For the 1.5 μm this cannot be resolved anymore, because the widths of the bulk/waveguide interface in the other plots are larger than 1 μm. Due to the color scale it is difficult to see that the intensity enhancement shows a systematic behavior with waveguide width. Here, the hotspots in the center of the waveguide appear brighter, the smaller the waveguide is. This behavior is plotted in Fig. 5.20. The FWHM for all modes shows a pronounced reaction at both sides of the waveguide, as previously observed. The area of increased or decrease FWHM is larger than 1 μm and therefore cannot be resolved for the smallest waveguide. Probably most interesting are the plots of the relative shifts. Here, again the trapezoid shape is observed fo every waveguide. Regarding the depth the plots indeed suggests a systematic behavior of width versus depths, similar to previous observation with EDX [331]. Here, the smallest waveguide is significantly deeper, than the larger ones. Alike, the maximum shift observed at the surface also appears to be dependent on the waveguide width. Here, the largest shift is seen for the smallest waveguide (Fig. 5.16, ~4.4 cm^{-1}, orange color), while gradually decreasing to the 4.5 μm (Fig. 5.16, ~3.6 cm^{-1}, yellow color), which is also plotted in Fig. 5.20.

The picture is completed with the analysis of the 40 μm waveguide depicted in Fig. 5.17. Here, hotspots are only visible at both waveguide/bulk interfaces, while the center of the waveguide is almost invisible in the intensity plot, as seen in Fig. 5.17a). This suggest that the intensity enhancement is not a sign of strain, but appears in regions of a strain gradient, which lowers symmetry and relaxes Raman selection rules. Therefore, we see only a marginal intensity variation in the middle of the waveguide, while the waveguide borders show significantly more Raman intensity. That we have an exchange region in between those hot spots and not two single waveguides 40 μm apart, can clearly be seen at the frequency shift of the 264 cm^{-1} phonon. Here, a gradual changing in frequency along the z-axis can be seen in the 40 μm wide center of the waveguide. At the same time, the FWHM plot again shows enhancements at the waveguide/bulk interface, while showing only a slight enhancement in the waveguide region. The comparison to the results of the 1.5 μm waveguide shows that the small waveguide has to be treated like a completely strained region, which is in size comparable to the hotspots of the 40 μm waveguide.

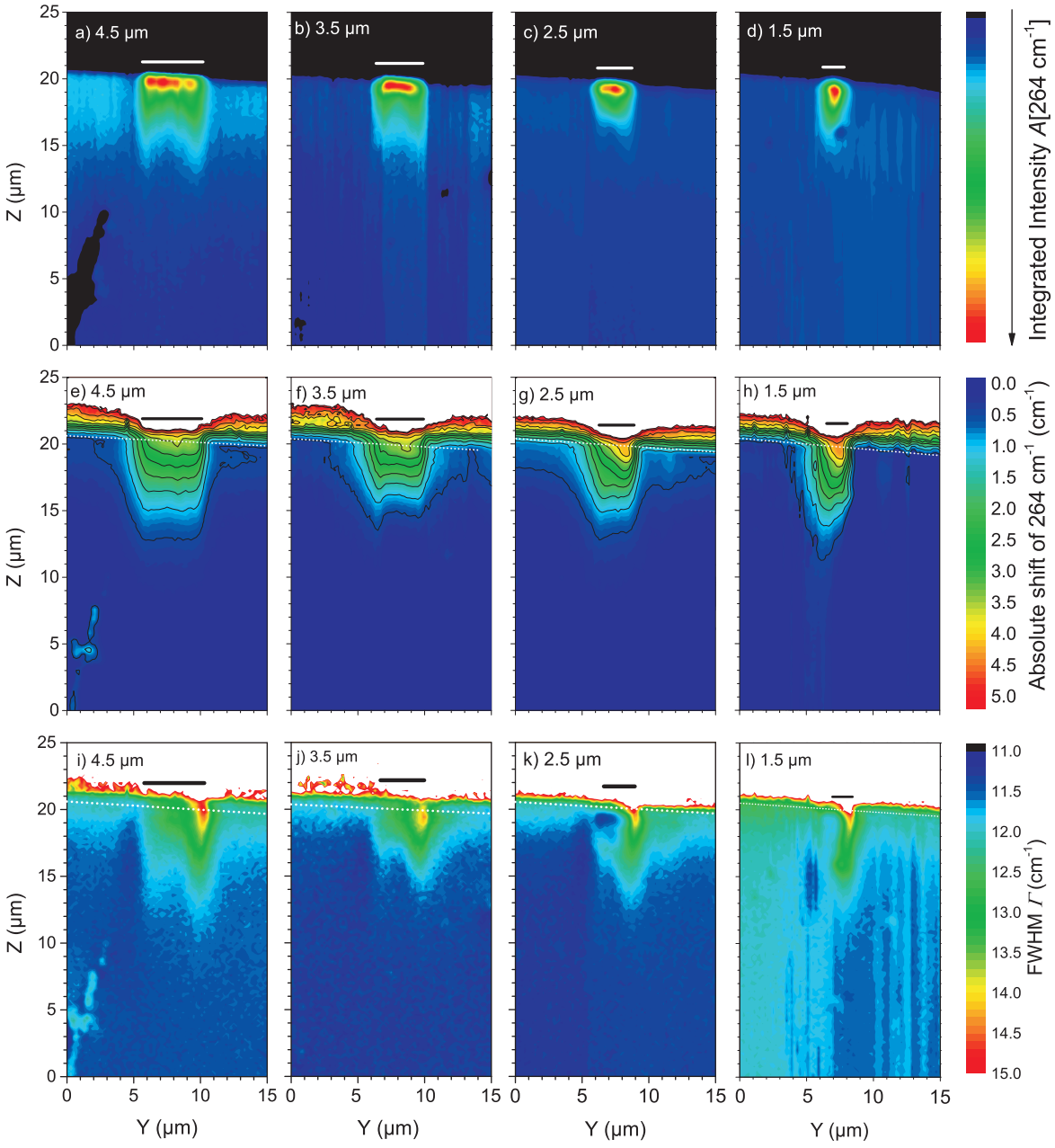

Fig. 5.16 a)-d) Integrated intensity of the 264 cm^{-1} mode for different waveguide width. e)-h) Determined shift of the 264 cm^{-1} with respect to the bulk frequency. Here, blue (0 cm^{-1}) would refer to $KTiOPO_4$, while red (5.2 cm^{-1}) would be expected for $RbTiOPO_4$ (see Fig. 5.12b). Fig. i)-l) shows the FWHM as determined by the fitting. The black and white bars are scale bars at the length of the respective waveguide width for easy size comparison.

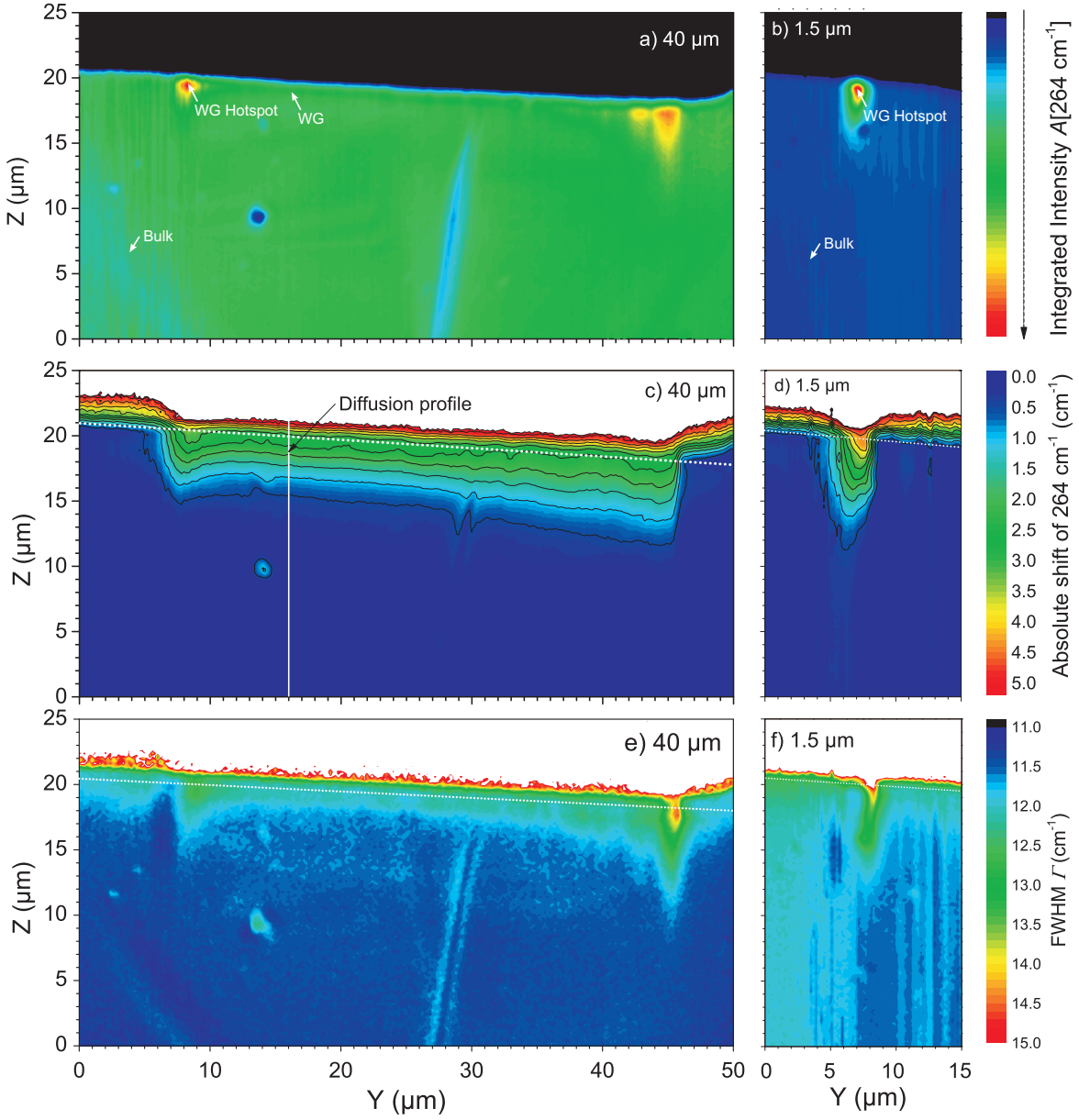

Fig. 5.17 The figure shows the results for the 264 cm^{-1} mode on the 40 μm waveguide. For comparison, the results of the 1.5 μm waveguide are shown.

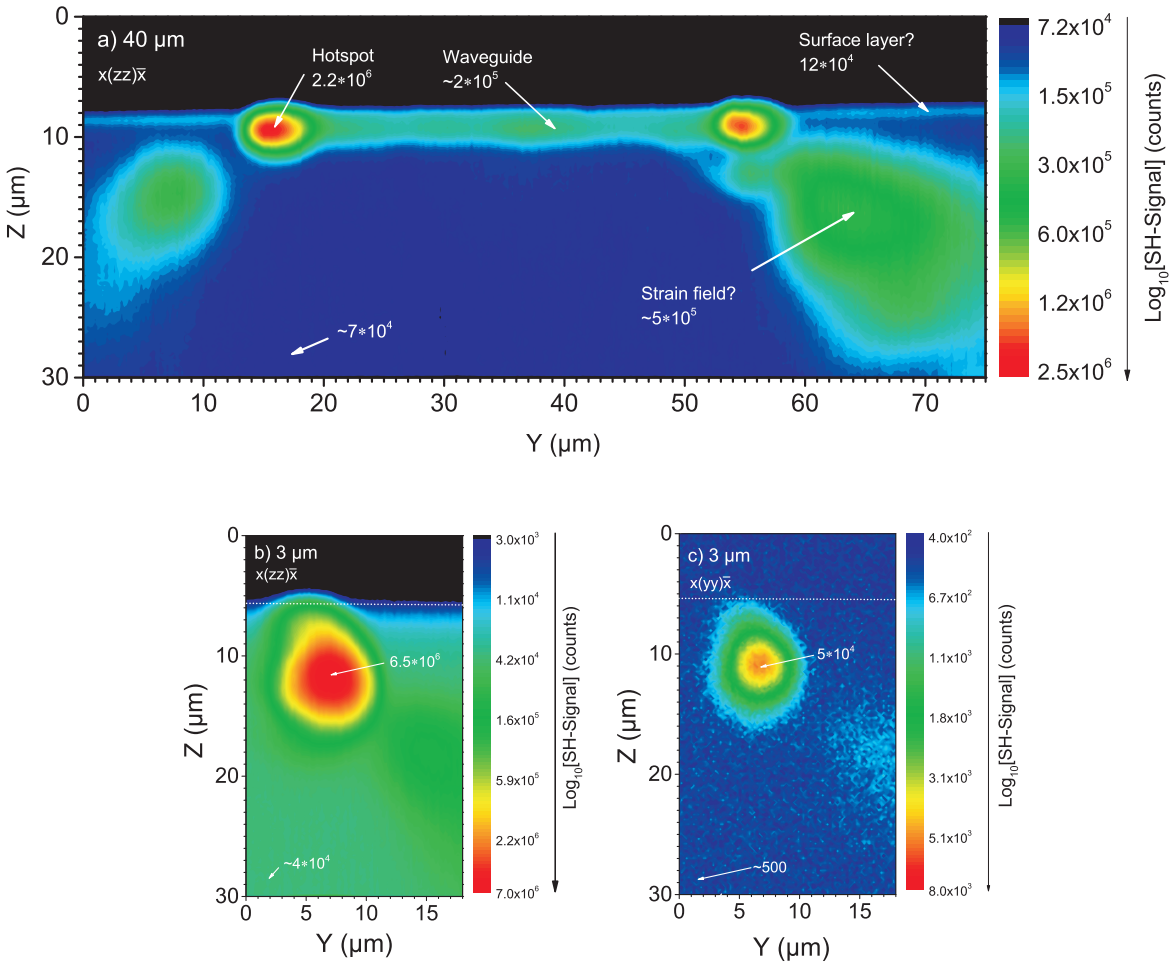

Fig. 5.18 The figure shows second harmonic maps of the 40 μm channel (a) and two scans of a 3 μm waveguide (b&c) in two different polarization. For better comparability, the counts of a few selected coordinates are highlighted. While x(z,z)$\bar{x}$ geometry allows for SH generation, the x(y,y)$\bar{x}$ should give no signal. Yet a nonlinear signal in the waveguide is detected, which can be understood by lowering the crystal symmetry by ion-exchange or strain [17].

Second harmonic microscopy

To conclude the Raman analysis, the 40 μm and a further 3 μm wide waveguide are investigated with Second harmonic (SH) microscopy. Second harmonic generation is very sensitive to changes in crystal symmetry [53] and therefore may provide additional information. The general measurement geometry is the same, as for the Raman analysis. The scans were performed with a numerical aperture of $NA = 0.65$ and step width of 200 nm in y- and z-direction. The relatively low NA should give no rise to a polarization component along z-direction, otherwise observed for strong focusing ($NA \geq 0.9$). The samples are mounted with their x-face parallel to the optical axis of the objective lens, similar to Fig. 5.12 and the detection is performed in backscattering geometry. Further information about the layout of the setup may be found in Refs. [116, 204, 205, 74].

Figure 5.18a) shows a 75 by 30 μm^2 (SH) scan of the 40 μm channel in x(z,z)$\bar{x}$ geometry. Please note the logarithmic intensity scale on all figures. Again, intensity hotspots appear at the waveguide/bulk material interface. Here, an intensity of $> 2.0 \cdot 10^6$ counts is detected compared to $\approx 7 \cdot 10^4$ in the general bulk level. The

detector dark count level is ≈ 500. The enhancement at the hotspot is almost three orders of magnitude! This may be understood in a breaking of crystal symmetry due to a strain gradient. Additionally, in the waveguide region an increased signal is detected, highlighting the breaking of symmetry. Outside of the waveguide region a thin surface layer of enhanced signal is detected, which may indicate a chemically or physically different surface layer similar to previous observation based on the evaluation of some Raman modes, e.g. Fig. 5.15b). It appears as if from the hotspots two lobes of enhanced signal spread into the bulk material ($\approx 5 \cdot 10^5$ counts). This may be interpreted as large strain fields induced by the waveguide. The strain fields lower the symmetry of the crystal and change the susceptibility, which leads to an increased SH signal. The strain fields have dimensions of more than 10-20 μm, which is, however, not suprising. For laser written waveguides in $LiNbO_3$ strain fields (and changes in refractive index) of a similar dimensions have been detected around the laser damaged region [337].

Figures 5.18b) and c) show two scans of a 3 μm waveguide in x(z,z)$\bar{x}$ and x(y,y)$\bar{x}$ geometries. The x(z,z)$\bar{x}$ geometry shows qualitatively the same result, as the 40 μm waveguide. Again, we see a hotspot of significantly enhanced SH signal, which is in magnitude and diameter even larger, than the hotspots of the 40 μm waveguide. This suggests an even stronger strain gradient in a small waveguide, compared to the large waveguide and is in agreement with the observations from the Raman analysis, e.g. Fig. 5.20. More interesting is the x(y,y)$\bar{x}$ geometry. Here, second harmonic generation is forbidden for the *mm*2 orthorhombic crystal class, as the $d_{22} = 0$ element is zero, which is shown in the following equation. An excitation along y-direction only induces a polarization in z-direction, but no signal in y-direction, which is detected in this scattering geometry. Indeed, outside of the waveguide only the detector dark count level of ≈ 500 counts is detected. However, in the waveguide region a clear signal of 5000 - 6000 counts is detected. This can be explained that according to

$$\begin{pmatrix} P_x \\ P_y \\ P_z \end{pmatrix} = \begin{pmatrix} 0 & 0 & 0 & 0 & d_{15} & 0 \\ 0 & d_{22} \neq 0 & 0 & d_{24} & 0 & 0 \\ d_{31} & d_{32} & d_{33} & 0 & 0 & 0 \end{pmatrix} \begin{pmatrix} 0 \\ E_y^2 \\ 0 \\ 0 \\ 0 \\ 0 \end{pmatrix} = \begin{pmatrix} 0 \\ d_{22}E_y^2 \neq 0 \\ d_{31}E_y^2 \end{pmatrix} \tag{5.5}$$

the d_{22} needs to be nonzero ($d_{22} \neq 0$). This can be understood as a lowering of symmetry in the crystal. The next lower-symmetry crystal class with $d_{22} \neq 0$ is the triclinic crystal class 1, which has nonzero elements overall. This suggest that the exchange will increase the crystal disorder, which is in agreement with the observation of increased Raman mode FWHM in the waveguide region. However, the changes in Fig. 5.18c) are rather small compared to the several orders of magnitude intensity increase supposedly introduced by strain. Overall this first SH microscopy results suggest that appropriate analysis of the nonlinear data, including additional polarizational scans, can supplement the Raman measurements and may allow to understand the type and direction of strain by symmetry arguments. However, further analysis is indicated.

Discussion

Figure 5.19 compares the spectra of bulk and from a hotspot in a waveguide for the 1.5 μm (a) and 40 μm (b) waveguides. Additionally a spectrum from the waveguide regions of the 40 μm is also given. The spectra are normalized to the intensity of the highest bulk peak (264 cm^{-1}). The spectra show that the hotspot spectrum is - apart from the reported slight shifts - almost identical in terms of peak intensities and structures. For the hot spot spectrum just a general increase by the same factor in intensity for all modes is observed. This explains, why all

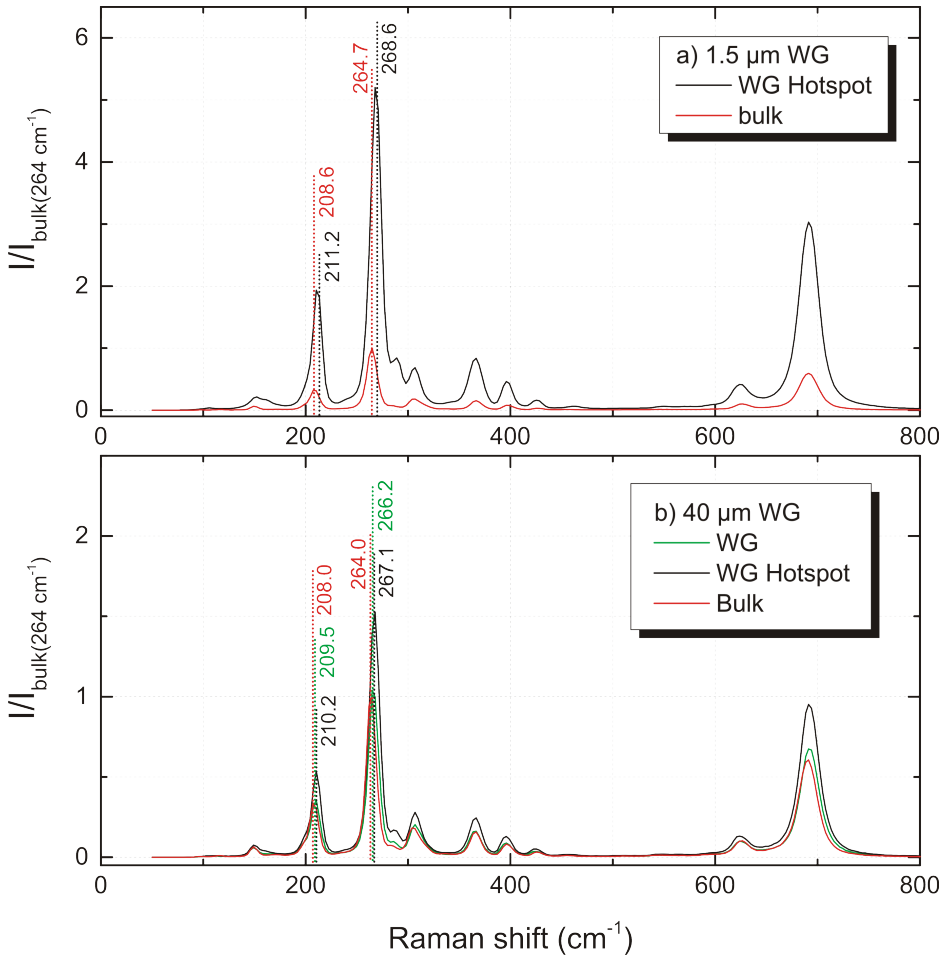

Fig. 5.19 The figure compares two as-measured spectra from bulk and a hotspot for the 1.5 μm and 40 μm waveguides (WG). For the 40 μm waveguides (WG) further a spectrum from the waveguide region is taken. The positions of the spectra are highlighted in Fig. 5.17.

intensity plots (except the 306 cm^{-1}) in Figs. 5.14 and 5.15 look almost identical. Interestingly, the spectrum of the 40 μm waveguide region (5.19b) shows almost the same intensity as the bulk spectrum. This suggest that the intensity enhancement here, is a phenomenon related to the strain gradient at the border of the waveguide, and not directly connected to the Rb-exchange. Therefore, the intensity enhancement represents no category to measure the Rb-content. Figure 5.20 compares the relative hotspot intensity for all five measured waveguide (black squares). Here, a systematic increase for smaller waveguide is seen substantiating the connection to the strain gradient. Apparently nearly no intensity enhancement is seen for the waveguide center of the 40 μm waveguide. Here, the measured data point is almost at the bulk intensity line.

One of the driving questions of this whole analysis was, if measuring the behavior of certain Raman lines, allows to determine the rubidium concentration. The analysis of the $LiTa_xNb_{1-x}O_3$ mixed crystals in Sec. 4.1.3 has shown that the determined Raman frequency of certain modes should exhibit a Vegard-like behavior with respect to concentration [268]. Rb-exchanged waveguide should also be representable by $Rb_xK_{1-x}TiOP_4$ mixed crystals. Therefore, the Rb concentration $x = [Rb]/([Rb]+[K])$ should also be measurable based on peak frequencies. For the 264.0 cm^{-1} mode we expect a shift to 269.2 cm^{-1} in $RbTiOPO_4$. Therefore, the concentration may be interpolated with a Vegard-behavior as

$$\omega_x = (1-x)\cdot\omega_{\mathrm{KTP}} - x\cdot\omega_{\mathrm{RTP}} = 264.0\ \mathrm{cm}^{-1} + 5.2\ \mathrm{cm}^{-1}\cdot x. \tag{5.6}$$

In the 40 μ waveguide, we determined a relative frequency shift for this mode of 2.8 cm^{-1} (see Fig. 5.19). This yields an $x = 2.8/5.2 \approx 0.53$, which sounds reasonable. However, in the hotspot we detect a larger shift of 3.3 cm^{-1}. This can mean either that we have a higher surface concentration in the borders or we see an additional effect of strain. The EDX analysis suggests no location dependent Rb-concentration profile, therefore strain is the likely explanation for the hotspots.

The small waveguide all have similar dimensions, as the hotspot of the 40 μm waveguide. For the smallest waveguide we see a systematic increase of the surface-near mode frequency of up to 4.4 cm^{-1} (Fig. 5.20). This raises the question if the systematic behavior of higher frequency shift in a smaller waveguide is either caused by a systematic increase of strain or by a systematic increase in surface concentration or by both. Therefore, one has to be cautious if equation 5.6 is true for the small waveguides or if a correction factor for strain needs to be applied.

The results suggest that the change in Raman frequency of the 264 cm^{-1} line is directly proportional to the Rb concentration. However, as strain also heavily influences the line positions, such an analysis may only be performed in the supposedly unstrained central region of the 40 μm waveguide. If the frequency change is proportional to the Rb concentration, then this will allow to determine the diffusion parameter. As a proof of concept, a line profile is obtained from the central region of the 40 μm waveguide as highlighted in Fig. 5.19c). This is shown in Fig. 5.21. Here, z = 0 was positioned according to process described in Fig. 5.13. The solution of Fick's law of diffusion for the case of one dimensional diffusion and with the boundary condition of a constant surface concentration is given by a complementary error function $1 - erf = erfc$. This is the appropriate description in this case, as lateral diffusion can be neglected in $KTiOPO_4$ [175]. The fitted function is given by

$$y(z) = y_0\,(1 - erf(z/b)) + y_{offset}. \tag{5.7}$$

Here, b denotes the diffusion depth. The function describes the observed behavior fairly well. The actual surface concentration may even be higher, than shown here, but can not be determined due to limited optical

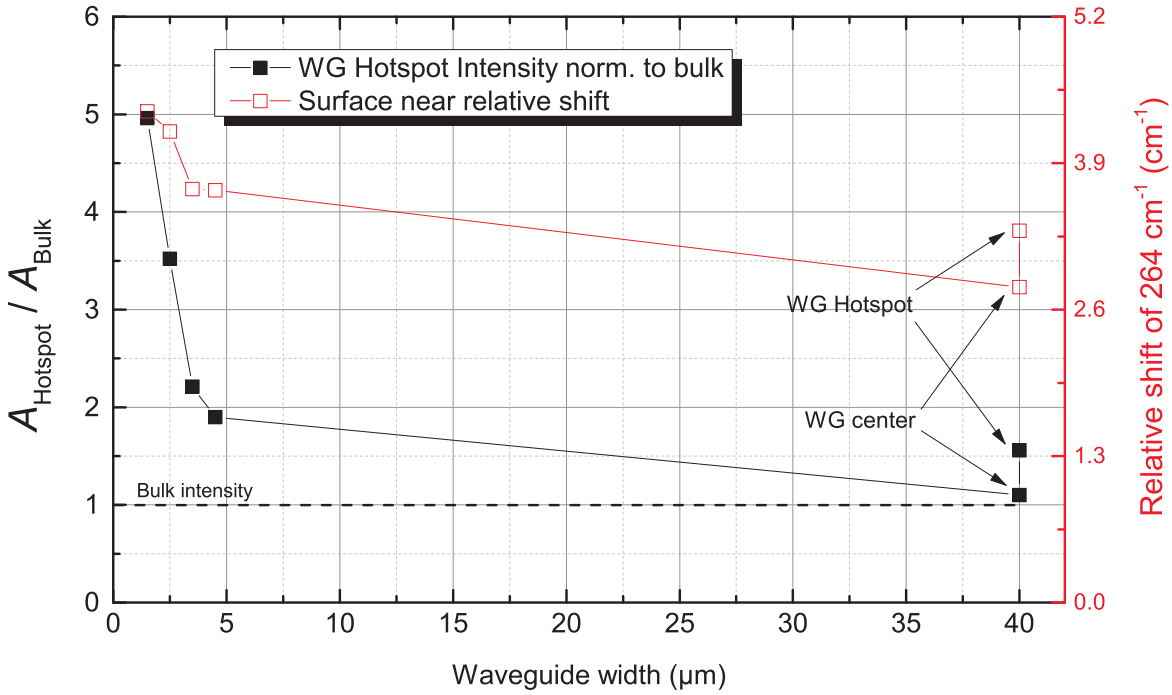

Fig. 5.20 The graph shows the determined relative shifts of the 264 cm^{-1} at the surface and the hotspot intensities with respect to the waveguide width. For the 40 μm waveguide two values are given, one from the hotspot and one from the waveguide center.

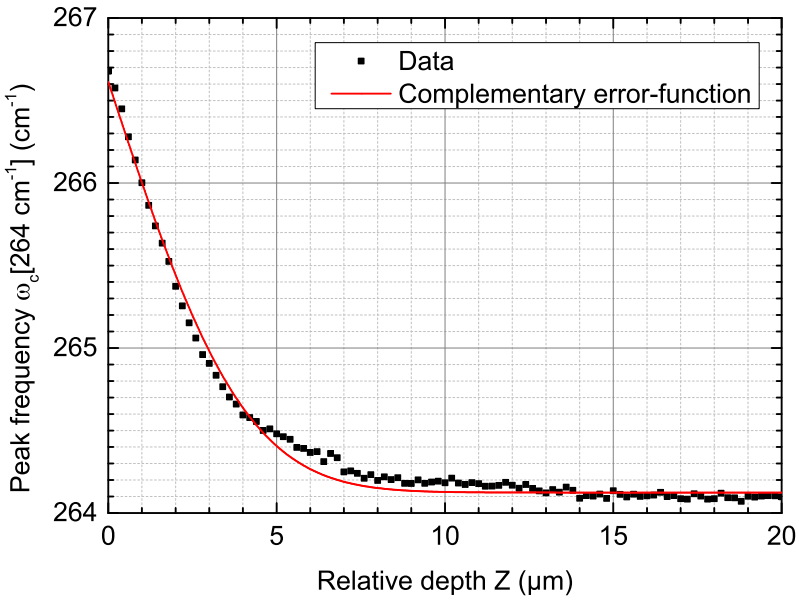

Fig. 5.21 The graph shows the frequency shift of the 264 cm^{-1} line as a function of relative depth taken from the 40 μm waveguide. The origin of the profile is highlighted in Fig. 5.17 c).

resolution. From the fit, we obtain $b = 4.4\ \mu$m, which is reasonable compared to the 3.82 μm shown in the EDX profile. It holds

$$b = \sqrt{2Dt}, \tag{5.8}$$

where D is the diffusion parameter and t is the diffusion time, which was $t = 60$ minutes in this case. Based on this, we calculate a diffusion parameter of $D = 0.08\ \mu\text{m}^2/\text{min} \approx 1.3 \cdot 10^{-9}\ \text{cm}^2/\text{s}$. The obtained depth $b = 4.4\ \mu$m and diffusion constant for an exchange time of 60 minutes and exchange temperature of 350 °C lie well in the range of values typically reported in literature [175, 324, 323]. This shows that Raman microscopy is in principle capable of determining diffusion profiles. However, we have also seen that the position and shape of peaks is influenced by chemical or physical surface effect, strain or possible by stoichiometry and defects, which will overlap with effects induced by a Rb-K exchange.

Conclusion

We have investigated Rb-exchanged waveguides in KTP of various width with imaging Raman spectroscopy and nonlinear microscopy. Here, we could detect signs for structural changes related to the Rb-exchanged, but also changes which are allegedly resulting from strain and, which are not limited to the Rb-exchanged region. The previous analysis with EDX has shown that for neither waveguide width a connection between diffusion depth and position in the waveguide is observed, i.e. the Rb-exchange depth at the WG/bulk interface is the same as in the center of the waveguide [331]. This effects we do not see with Raman spectroscopy or second harmonic microscopy. On the contrary, we often see systematic changes in the spectrum (FWHM, peak shift or integrated intensity) which are not explained by the ion exchange alone, for example by unexpected or contradicting phonon behavior and much larger physical dimensions of spectral changes compared to waveguide sizes. Here, the results from Raman spectroscopy and SH microscopy suggest strain fields. These are likely due to the large compositional change and size differences between the Rb^+ and K^+ ions. Even more, the Rb-exchange lead to a more disordered system, e.g. seen in increased mode FWHM or broken SH selection rules. We have seen that we can determine diffusion parameters from Raman spectroscopy. However, as the phonon modes are not only influenced by the Rb-exchange, but by many other effects, the pure determination of diffusion parameters should be left for methods, which are specifically and only sensitive to chemical elements, like EDX or mass spectroscopy techniques. The power of confocal Raman spectroscopy and nonlinear microscopy lie in the combination of a noninvasive measurement with real three dimensional resolution with a combined sensitivity for stoichiometry effects, strain, disorder, but also periodic poling [294]. This combination can provide very valuable insight in the interaction of these effects. For example, one of the next steps should be three dimensional analysis of poled waveguides. In this context first results are shown and analyzed in the next section.

The analysis of the waveguides have revealed strains. Previous work on lithium niobate or in silicon oxynitride structures have shown that the connection of strain fields and refractive index changes can be modeled [30, 28, 29, 337, 45, 336, 27]. Here, these models may be transferable to $KTiOPO_4$, however the spectrum of $KTiOPO_4$ is much more complex. A major issue is the missing complete assignment of phonon modes to certain atomic displacement patterns. Furthermore, the magnitude of certain material properties, e.g. the Grüneisen parameters, are not known. The Grüneisen parameter basically connects the frequency shift of any phonon with the strain (or pressure). However, only one study of the pressure dependence of the Raman spectrum of $KTiOPO_4$ exist so far [287], but no estimation of the Grüneisen parameters have been given for any modes. In this context, DFT simulation can provide a solution, as they would allow to predict the changes in the

Raman spectrum in strained material, as well as provide displacement patterns for each mode. This information can be used to quantify the strain in the waveguides, which in turn may be used as input parameters for further DFT simulations to model and understand the changes in refractive index.

5.2.2 Perdiodically poled Rb-exchanged waveguides

So far, we have demonstrated that confocal Raman spectroscopy can be used to visualize ferroelectric domain structures in $KTiOPO_4$, as well as to analyze the stoichiometry and other effects, e.g. strain, in Rb-exchanged waveguides. The simplest integrated nonlinear device is the combination of both, i.e. a periodically poled waveguide. In this context Raman spectroscopy represents a method, which is sensitive to both, the stoichiometry change, i.e. the waveguide, the periodic poling, as well as other effects, such as strain. Furthermore, the three dimensional resolution of confocal microscopy enables to investigate these properties non destructively and without any specific sample preparation in layers below the sample's surface, while methods like PFM [340] or selective etching [341] reveal only the quality of the surface near domain structure. This is a major limitation of those methods, as the quality of poling in the complete waveguide affects the conversion efficiency.

In the following analysis a Rb exchanged poled waveguide will be analyzed. Periodically poled waveguides in $KTiOPO_4$ can be obtained in two possible ways. Either, a previously exchanged waveguide is poled, or a previously poled crystal is exchanged afterwards. Both methods have been demonstrated and come with their own technological challenges [327, 326]. The sample in this study was first exchanged, than poled. Here, the Rb exchange will lower the conductivity in the regions of exchange, e.g. the conductivity of $RbTiOPO_4$ is two to three orders of magnitude smaller than $KTiOPO_4$ [342, 174]. For bulk doped Rb:$KTiOPO_4$ with doping concentrations of 0.3 % a reduction in ionic conductivity of two orders of magnitude was observed [343]. Furthermore, the exchange may improve stoichiometry further lowering the conductivity. Therefore, during poling the main potential drop will be observed at the (only surface near $\approx 10\mu$m) waveguides, where the coercive field will be reached much earlier than in the rest of crystal. As a result, the waveguides will be periodically poled, while the bulk crystal is not inverted. This opens the questions, if the domain inversion reaches as deep as the Rb-exchange, which can not be answered by surface sensitive methods.

For the analysis, a 40 μm by 10 μm (x by y) was taken over a 1.5 μm wide waveguide. For the scan the focus is placed slightly below the surface (about 1 μm), which is determined by the maximum of the laser line. Here, Raman spectra with an integration time of 3000 ms per spectra were taken with step width of 200 nm in x-direction and 400 nm in y-direction. The spectra were taken in $z(x,x)\bar{z}$ geometry, which is known to provide information about domain walls [294]. Figure 5.22 shows three confocal Raman images based on the integrated intensities of a different line. The lines are highlighted in the spectrum in Fig. 5.25. To obtain these images, the spectral channels in a $\pm$ 10 cm^{-1} interval around these lines were used, which is the convenient method to visualize ferroelectric domain walls in $KTiOPO_4$ and other materials [294, 46, 274, 272]. The obtained intensities are then used to generate false color images.

Figure 5.22a) is based on the 150 cm^{-1} line, which has not been observed to be sensitive to ferroelectric poling in $KTiOPO_4$ in previous work by the author [294]. Due to its low frequency and intensity this phonon is assumed to be connected to the K^+/Rb^+ ion [281, 282]. Indeed, in the image one can identify the 1.5 μm wide waveguide centered running from left to right in the image. The waveguide itself appears as a region of slightly enhanced intensity compared to the bulk crystal signal and is highlighted by two dashed lines. Furthermore, an area of decreasing signal adjacent to the waveguide is found. These regions are about 1.5 μm wide and follow the waveguide. Similar observations are made for the other two modes in Figs. 5.22b) and c). A possible explanation may be a strain field spanning around the waveguide. Because the Rb-exchange mainly takes place

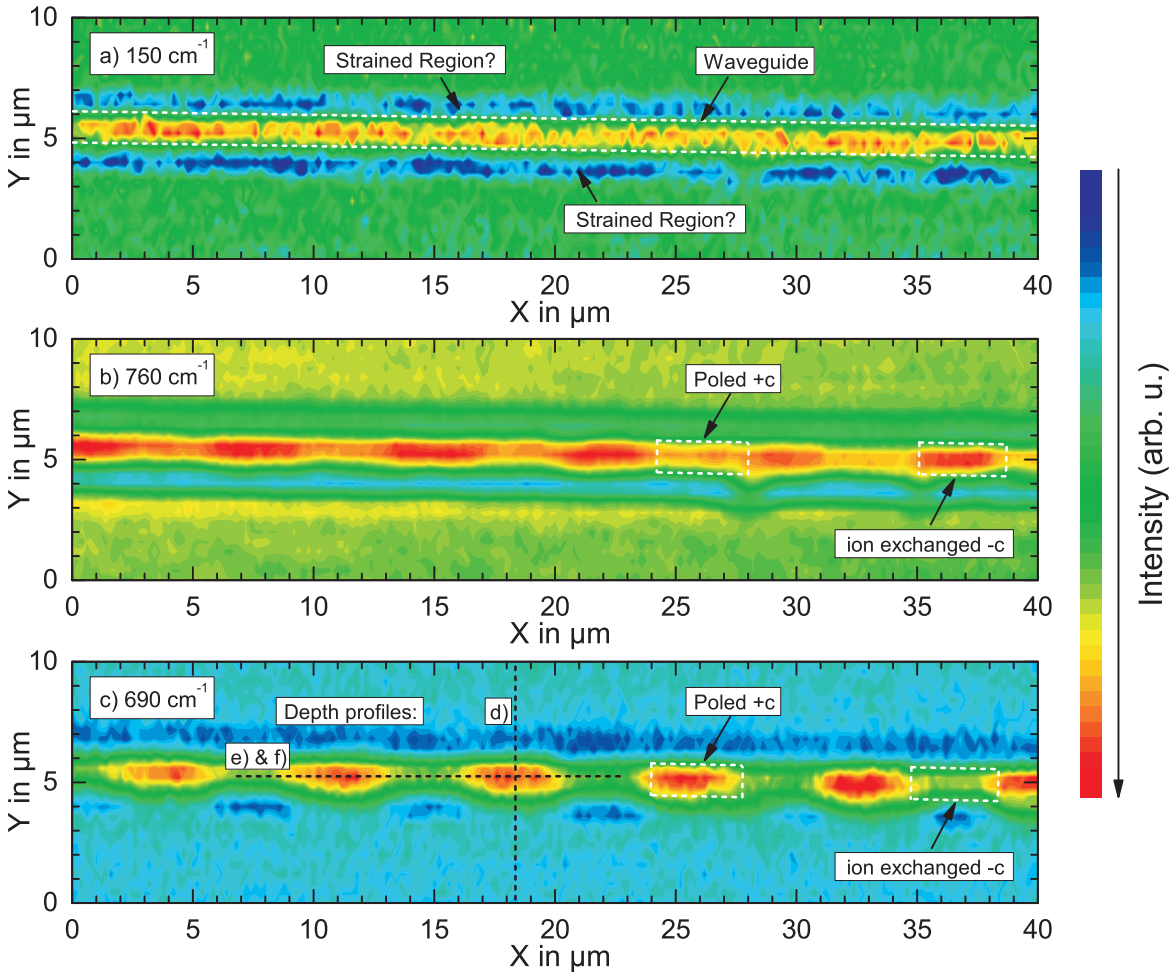

Fig. 5.22 Confocal Raman images of a periodically poled 1.5 μm wide Rb-exchanged waveguide in $KTiOPO_4$, which was poled after waveguide fabrication. The images are based on the integrated intensities of the named modes in a $\pm$ 10 cm^{-1} interval. Figures a) to c) are based on different phonons, each showing a different behavior.

along the z-axis due to the high conductivity, it is likely that the waveguide and its surrounding regions are strained. Here, the strain comes from the massively different lattice parameter of $RbTiOPO_4$ compared to $KTiOPO_4$ due to the much larger Rb^+ ion [154]. And as observed in the previous Section, $Rb_xK_{1-x}TiOPO_4$ with x up to 0.9 is possible. This will likely result in large strains, especially in small waveguides. Strain has been observed before, to be responsible for changes in intensity in Raman spectroscopy [269].

In contrast to the 150 cm^{-1}, the intensities of the 690 cm^{-1} and 760 cm^{-1} lines, which are displayed in Fig. 5.22b) and c), have been observed to change in the vicinity of ferroelectric domain walls. Here, the 760 cm^{-1} decreases, while the 690 cm^{-1} mode increases [294] at a domain wall. Indeed, we see for both modes in the 1.5 μm wide waveguide region a periodic variation of their intensities. In this context five periods are visible, which allows to estimate the poling period on the order of $\Lambda = (7.8 \pm 0.3)\mu$m, which fits well the production parameters. Even more, we can clearly see that both phonons react complementary to each other as expected. This behavior is highlighted by the white, dashed rectangles in Figs. 5.22b) and c). Together with the fact that other phonons, e.g. the 150 cm^{-1} phonon, do not show any periodic behavior, this confirms that the periodic

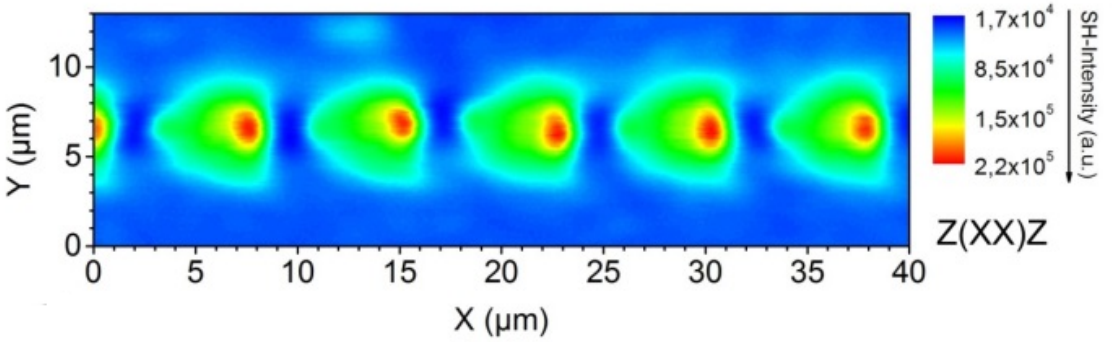

Fig. 5.23 Second harmonic scan of the same 1.5 μm waveguide as presented before. Again, we can not distinguish between domain walls and the waveguide, but rather see only a general enhancement of the signal in the apparently poled regions. However, we see again also a signal variation adjacent to the waveguide, this time however pronounced around the poled areas. This may be explained by strain field stretching far out of the actual waveguide region, which are further modulated by the poling. Here, the actual mechanisms remains elusive so far [17].

signal can only be explained in terms of periodic domain inversion. It should be noted that previously Raman spectroscopy was observed to be mainly sensitive to domain walls [294]. Instead, we see here a complete signal enhancement or decrease for the whole inverted domain. Here, two domain walls are expected to be parallel to the waveguide border, while the other two domain walls are orthogonal to the waveguide. An inverted domain should resemble therefore something like the dashed boxes in Figs. 5.24. This discrepancy can be explained first by the limits of optical resolution. Even for an infinitesimal small domain wall, the convolution of the optical beam with the (infinitesimal wide) domain wall will result in minimum width for a domain wall of $\Delta \approx 600 - 800$ nm. This can be seen in 5.1, where the smallest DW signatures were $\Delta \approx 600$ nm. Because the maximum width of the domain here is limited by the waveguide width of 1.5 μm, it is clear that this may only be incompletely resolved. Nevertheless, Fig. 5.24 d) and e) suggest a slightly enhanced signal at the suspected domain interfaces. Taking then also the strains induced by the waveguide interface into account, it becomes clear that the actual substructure of the combined domain-wall-$Rb_xK_{1-x}TiOPO_4$-waveguide-bulk-$KTiOPO_4$ interface is very complex and will overlap with each other. This is also seen in the unpoled region, where the signal is enhanced compared to the bulk signal, despite the absence of domain walls. This is also seen in the difference Spectra in Fig. 5.25.

More important, than the surface structure of the periodic poling, is the penetration depth of the inverted domains. To answer this question two cross-sections as denoted by the black dashed line in Fig. 5.22c) were taken. Here, one cross-section parallel to the waveguide and one orthogonal through a poled region were taken. Here, for the two scans the step-width along x and y was chosen to be 200 nm, while in depth (z-direction) steps of 250 nm were chosen. The scan was started about 2 μm above the surface, which was determined by the maximum of the laser reflection. The results for the two cross-sections are shown in Figs. 5.24 d)-f). Here, the plot of the 690 cm^{-1} line is shown for the orthogonal scan, while two plots for the parallel cross-section are shown based on the 690 cm^{-1} and 760 cm^{-1}. For this analysis the focus is only on the DW sensitive lines. The dashed lines define the surface as determined by the maximum of the laser reflection in a different plot not shown here. When focusing through a refraction surface, the actual focus position (AFP), does differ from the nominal focus position (NFP) [235–237]. To accurately determine the penetration depth of the waveguide and

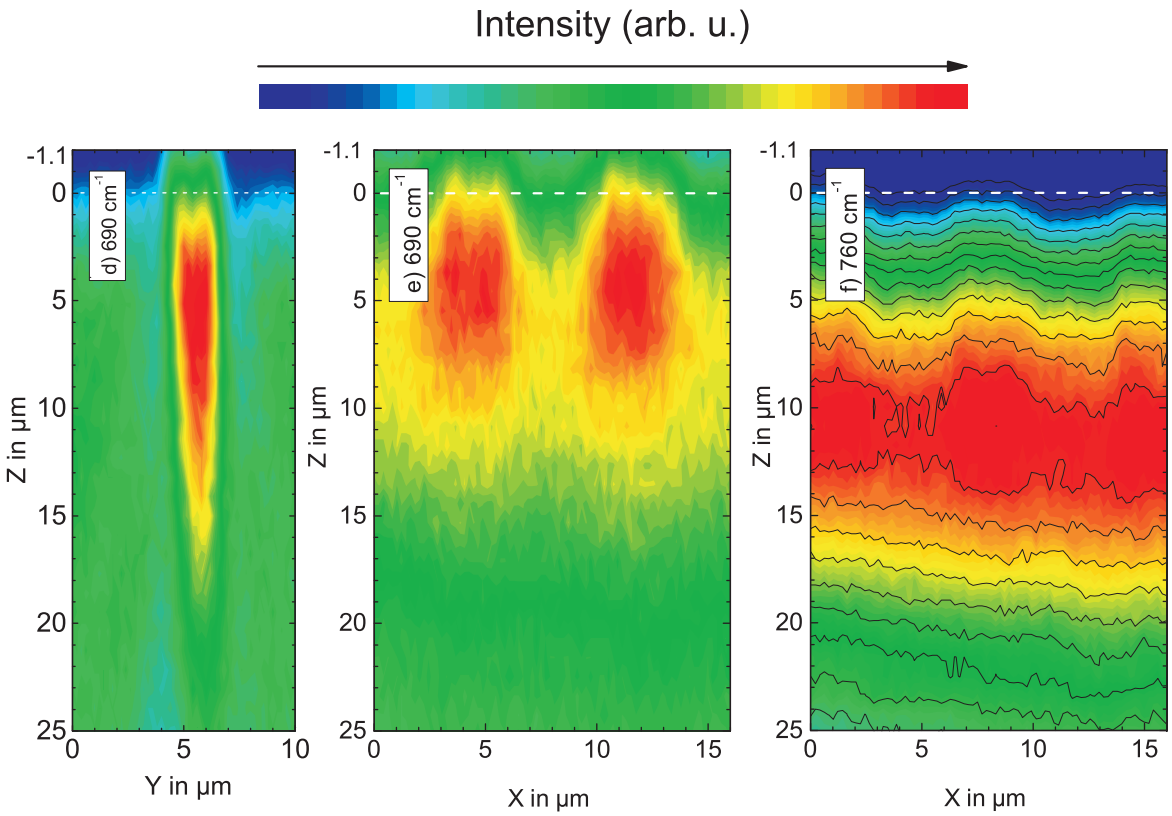

Fig. 5.24 Confocal cross sections through the waveguide and along the lines shown in Fig. 5.22c) based on the domain wall sensitive 690 cm^{-1} and 760 cm^{-1} lines.

poling, this needs to be corrected. Here, basically optical path length conservation applies and the AFP can be calculated by multiplying the NFP, which is determined in this experiment by the actuator movement, with the ratio of the refractive indices $n_{KTP}/n_{air}(532\text{nm}) \approx 1.78$ [344]. Therefore, the z-scaling changes at the surface as shown by the dashed line. Below the dashed line one tick refers to 1 μm, while above to 0.55 μm.

Figure 5.24 d) shows the orthogonal cross section of a poled area. Here, a large signal enhancement and a drop-shaped structure can be seen down to 15-20 μm. In the upper 10 μm the outer boarders are almost parallel to the z-axis, suggesting a homogeneous inversion parallel to the Rb-exchange area. Close to the surface, even two slight increase along the y-axis can be seen, which may can be interpreted as the domain boarders. Below 10 μm the area of signal increase gets smaller and somewhat resembles the typical structure of surface near domains having a tapered structure into the materials.

To determine the penetration depth of the poling, the 5.24 e) and f) are more useful. Here, again the two complementary behaving 690 cm^{-1} and 760 cm^{-1} are shown. In both images a periodic signal variation indicating the poling down to 13 μm depth can be seen, which presents an upper boarder of the inverted domain depth. Depending on, where the XZ cross section was taken, the actual poling may even reach somewhat deeper as seen in Fig. 5.24 d). Nevertheless, a depth of 13 μm coincides well with the typical penetration depth of significant amounts ($> 1\%$) of Rb, which shows that the waveguides are completely poled. As an interesting note, the two phonon modes apparently have their maximum intensity in different depth. Here, the 760 cm^{-1} can be considered a LO mode due to its shifting behavior in angular resolved spectroscopy (4.3), while the 690 cm^{-1} line appears to be a TO phonon, only visible in the spectrum due to z-polarization components in the

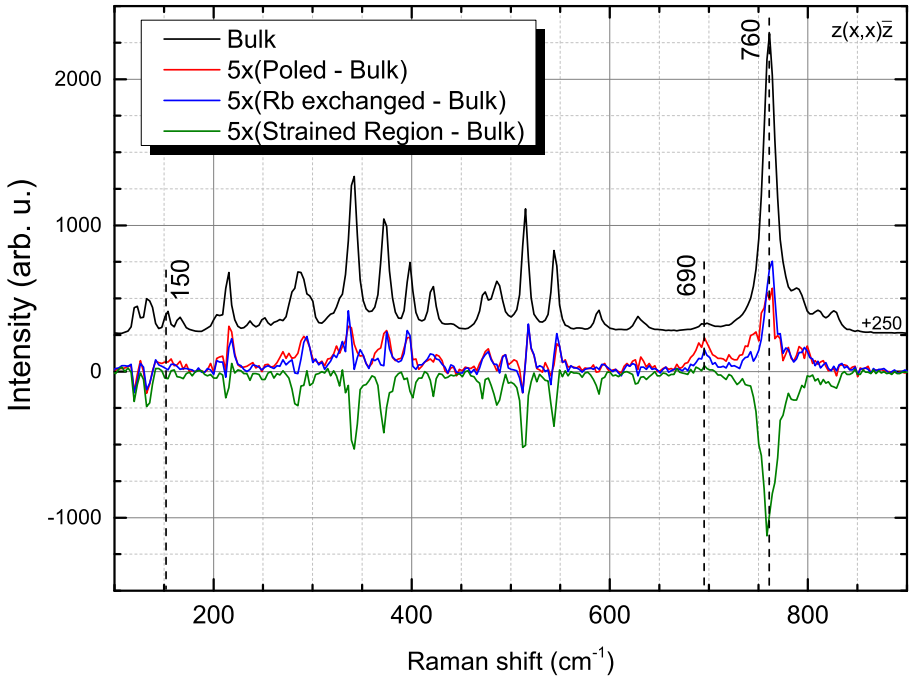

Fig. 5.25 Exemplary difference Raman spectra for each region in the scans in Fig. 5.24. Here, the black line shows a typical bulk spectrum. The other three spectra show the difference of a poled region, an exchanged region and the strained region with respect to the bulk spectrum. For better visibility the difference spectra are multiplied by five and the bulk spectrum has an artificial offset.

focused beam [278]. Its strong sensitivity to the waveguide and poling period, may be explained by relaxed selection rules at domain walls or the waveguide border [251].

In conclusion, we have demonstrated that confocal Raman spectroscopy allows to visualize and distinguish poled waveguides in a simple and reliable way. Here, it was found that domain inversion appears to reach through most of the exchanged region in depth, which is a prerequisite for efficient nonlinear devices. Furthermore, signs for strain adjacent to the waveguides region are detected, which may be expected from the different unit cell parameters of $RbTiOPO_4$ versus $KTiOPO_4$. Here, further work with Raman spectroscopy may will allow to quantify and analyze the strain in more detail, as it had been done in other materials such as silicon/silicon onynitride, lithium tantalate or lithium niobate [27–30].

Chapter 6

Conclusion

In this work confocal Raman spectroscopy supported by DFT and second harmonic microscopy was applied to investigate specific problems in the common ferroelectric materials $LiNbO_3$, $LiTaO_3$ and $KTiOPO_4$. The overall goal was to achieve an improved and deepened understanding of the material properties, the role of defects and domain boundaries. On the long term a throughout understanding of the material properties and various influences is a corner stone towards improved fabrication and sophisticated devices.

In the context of fundamental Raman spectroscopy in the $LiNbO_3$ family the driving question is the contradictory phonon assignments, which introduces an uncertainty in any analysis based on Raman spectroscopy. Based on an extensive analysis of Raman data of pure and mixed crystals, as well as atomistic simulations and an extensive review of literature data it was possible to explain all fundamental features in the Raman spectra of both, pure crystals and mixed crystals. Here, the theoretical results could be brought in excellent agreement with the experiment. This enabled to solve the case of the "missing" phonon modes, to thoroughly understand the spectra of mixed crystals, as well as to analyze the dielectric properties of the crystals. In conclusion, this analysis serves as an excellent example of the explanatory power of a combined experimental and theoretical approach.

In the field of imaging Raman microscopy of ferroelectrics one of the major questions concerns the differences of the spectra of ferroelectric domain walls compared to bulk material. Here, in this work it could be shown in this work that the spectral difference between domain wall and bulk spectra can be traced back to two distinctly different effects. First, there is a change in selection rules at the domain boundary, secondly local strains and electrical fields, which are known to exist in the vicinity of domain walls in LN and LT for some time, induce distinct differences in the spectra. In this context a simple atomistic approach even allows to qualitatively and quantitatively address these changes. The understanding of the underlying mechanism finally allows to use Raman spectroscopy of domain walls for more than mere imaging. An analysis of the underlying contrast mechanism provides a firm basis for more in-depth analysis of domain boundaries with Raman spectroscopy.

The second part of the Raman imaging chapter evaluates Raman spectroscopy for the analysis of Rb-exchanged waveguides and addresses the issue of suspected strain in those waveguide structures. While methods such as EDX are only sensitive to the Rb/K stoichiometry, Raman effect analyzes the phonon spectrum, which is sensitive to strain, stoichiometry or crystal quality. In this context, we could find that Raman is not just sensitive to the stoichiometry, but provides information about the previously suspected strain. Because Raman spectroscopy is a noninvasive method and is also sensitive to domain structures, it is an ideal method to

assess the quality of periodically poled waveguides in its entirety. This is clearly demonstrated on a study on a periodically poled waveguide.

Outlook

In the context of spectroscopic analysis, a joint theoretical-experimental investigations greatly contributed to a throughout understanding of the Raman spectrum of the $LiNbO_3$-$LiTaO_3$ system. In contrast to this, the understanding of the Raman spectrum of the $KTiOPO_4$ family is still in a rudimentary state. Here, the presented internal mode assignment allows to understand some general features of the spectra. However, to reach a more mature level of understanding atomistic modeling is inevitable. This will also greatly contribute to the analysis of the spectra of waveguide. In this context a clear assignment of phonons will help to distinguish stoichiometric effects and quantify the effects of strain. Alike, theory can provide Grüneisen parameters to quantify the strain. Which in turn may be used as an input parameters to calculate the refractive index changes, which are suspected to be induced by strain. On the long term this might allow a full modeling of the effects of strain similar to Refs. [45, 336, 345, 337, 28, 29].

The work on the domain walls has provided a general understanding of the contrast mechanism at domain walls. In particular it has revealed a likely presence of strain fields and strain at domain wall. In this context however, the magnitude, orientation and type of the electric fields and strain are still not clear. This is crucial for more accurate DFT simulations. This raises the question, whether the effects of this strain and the electric fields, respectively, can be influenced by doping or annealing in lithium niobate. Furthermore, the question is, if they are also observable in stoichiometric material. A further important consequence, may be that these strain or electric field will have an effect on the smallest possible period length in the fabrication of domain grids. We have observed signatures of domain walls with widths in the order of 1000 - 2000 nm. The question is, if this range also defines a type of DW-DW interaction length limiting a smallest domain period in regular LN. Here, certainly annealing, poling at elevated temperatures (to prevent the building of frustrated defect complexes) or use of stoichiometric material maybe investigated. In this context possibly in-situ observations of Raman spectra under the application of electric fields not only along the polar direction, as in Ref. [309], but along all axis are necessary for the refinement of the atomistic model.

An improvement of the experimental methods can be achieved by making use of radially or axially polarization, which can be used for a z-polarized excitation and detection scheme [276, 275]. This will give access to the larger tensor elements in Raman even in a z-cut geometry. The data analysis process can be improved by deconvolution based on a better knowledge of the light distribution in the focus. These methods will be in particular needed in the context of ultra-short domain periods and thin films.

List of figures

List of tables

References

[1] S. E. Miller. Integrated Optics: An Introduction. *Bell Syst. Tech. J.*, 48(7):2059–2069, sep 1969.

[2] E. A. J. Marcatili. Dielectric Rectangular Waveguide and Directional Coupler for Integrated Optics. *Bell Syst. Tech. J.*, 48(7):2071–2102, sep 1969.

[3] J. E. Goell. A Circular-Harmonic Computer Analysis of Rectangular Dielectric Waveguides. *Bell Syst. Tech. J.*, 48(7):2133–2160, sep 1969.

[4] E. A. J. Marcatili. Bends in Optical Dielectric Guides. *Bell Syst. Tech. J.*, 48(7):2103–2132, sep 1969.

[5] P. A. Franken, A. E. Hill, C. W. Peters, and G. Weinreich. Generation of Optical Harmonics. *Phys. Rev. Lett.*, 7(4):118–119, aug 1961.

[6] P. D. Maker, R. W. Terhune, M Nisenoff, and C. M. Savage. Effects of Dispersion and Focusing on the Production of Optical Harmonics. *Phys. Rev. Lett.*, 8(1):21–22, jan 1962.

[7] J. A. Giordmaine. Mixing of Light Beams in Crystals. *Phys. Rev. Lett.*, 8(1):19–20, jan 1962.

[8] J. A. Armstrong, N. Bloembergen, J. Ducuing, and P. S. Pershan. Interactions between Light Waves in a Nonlinear Dielectric. *Phys. Rev.*, 127(6):1918–1939, sep 1962.

[9] G. D. Boyd, Robert C. Miller, K. Nassau, W. L. Bond, and A. Savage. LiNbO3: An Efficient Phase Matchable Nonlinear Optical Material. *Appl. Phys. Lett.*, 5(11):234–236, dec 1964.

[10] R. C. Miller, G. D. Boyd, and A. Savage. Nonlinear optical interactions in LiNbO3 without double refraction. *Appl. Phys. Lett.*, 6(4):77–79, feb 1965.

[11] J. A. Giordmaine and R. C. Miller. Tunable Coherent Parametric Oscillation in LiNbO3 at Optical Frequencies. *Phys. Rev. Lett.*, 14(24):973–976, jun 1965.

[12] A. Zukauskas, A. L. Viotti, C. Liljestrand, V. Pasiskevicius, and C. Canalias. Cascaded counter-propagating nonlinear interactions in highly-efficient sub-μm periodically poled crystals. *Sci. Rep.*, 7(1):1–8, 2017.

[13] C. Canalias and V. Pasiskevicius. Mirrorless optical parametric oscillator. *Nat. Photonics*, 1(8):459–462, aug 2007.

[14] A. Christ, A. Eckstein, P. J. Mosley, and C. Silberhorn. Pure single photon generation by type-I PDC with backward-wave amplification. In *CLEO/Europe - EQEC 2009 - Eur. Conf. Lasers Electro-Optics Eur. Quantum Electron. Conf.*, volume 17, pages 1–6. IEEE, jun 2009.

[15] A. Eckstein, A. Christ, P. J. Mosley, and C. Silberhorn. Highly Efficient Single-Pass Source of Pulsed Single-Mode Twin Beams of Light. *Phys. Rev. Lett.*, 106(1):013603, jan 2011.

[16] A. Gatti, T. Corti, and E. Brambilla. Temporal coherence and correlation of counterpropagating twin photons. *Phys. Rev. A*, 92(5):053809, nov 2015.

[17] P. Mackwitz. Private Communication, 2017.

[18] C. V. Raman and K. S. Krishnan. A New Type of Secondary Radiation. *Nature*, 121(3048):501–502, mar 1928.

[19] T. Frey, D. J. As, M. Bartels, A. Pawlis, K. Lischka, A. Tabata, J. R. L. Fernandez, M. T. O. Silva, J. R. Leite, C. Haug, and R. Brenn. Structural and vibrational properties of molecular beam epitaxy grown cubic (Al, Ga)N/GaN heterostructures. *J. Appl. Phys.*, 89(5):2631–2634, mar 2001.

[20] H. Harima. Properties of GaN and related compounds studied by means of Raman scattering. *J. Phys. Condens. Matter*, 14(38):R967–R993, sep 2002.

[21] M. Rüsing, T. Wecker, G. Berth, D. J. As, and A. Zrenner. Joint Raman spectroscopy and HRXRD investigation of cubic gallium nitride layers grown on 3C-SiC. *Phys. status solidi*, 253(4):778–782, apr 2016.

[22] M. D. Fontana and P. Bourson. Microstructure and defects probed by Raman spectroscopy in lithium niobate crystals and devices. *Appl. Phys. Rev.*, 2(4):040602, dec 2015.

[23] A. K. Arora, M. Rajalakshmi, T. R. Ravindran, and V. Sivasubramanian. Raman spectroscopy of optical phonon confinement in nanostructured materials. *J. Raman Spectrosc.*, 38(6):604–617, jun 2007.

[24] H. Richter, Z.P. Wang, and L. Ley. The one phonon Raman spectrum in microcrystalline silicon. *Solid State Commun.*, 39(5):625–629, aug 1981.

[25] Z. X. Shen, X. B. Wang, H. P. Li, S. H. Tang, and F. Zhou. Pressure-Induced Phase Transitions of KTiOAsO4 by Raman Spectroscopy. *Rev. High Press. Sci. Technol.*, 7:748–750, 1998.

[26] M. Panfilova, A. Pawlis, C. Arens, S. Michaelis de Vasconcellos, G. Berth, K.P. Hüsch, V. Wiedemeier, A. Zrenner, and K. Lischka. Micro-Raman imaging and micro-photoluminescence measurements of strain in ZnMgSe/ZnSe microdiscs. *Microelectronics J.*, 40(2):221–223, feb 2009.

[27] A. Ródenas, A. H. Nejadmalayeri, D. Jaque, and P. Herman. Confocal Raman imaging of optical waveguides in LiNbO3 fabricated by ultrafast high-repetition rate laser-writing. *Opt. Express*, 16(18):13979, sep 2008.

[28] I. De Wolf, H. E. Maes, and S. K. Jones. Stress measurements in silicon devices through Raman spectroscopy: Bridging the gap between theory and experiment. *J. Appl. Phys.*, 79(9):7148–7156, may 1996.

[29] I. De Wolf. Stress measurements in Si microelectronics devices using Raman spectroscopy. *J. Raman Spectrosc.*, 30(10):877–883, oct 1999.

[30] B. McMillen, K. P. Chen, and D. Jaque. Microstructural imaging of high repetition rate ultrafast laser written LiTaO3 waveguides. *Appl. Phys. Lett.*, 94(8):081106, feb 2009.

[31] J. R. Gandhi, B. Vijayalakshmi, M. Rathnakumari, and P. Sureshkumar. Growth of Pure and Mo Doped Potassium Titanyl Phosphate (KTP) Crystals:Influence of KTP/Flux Ratios on the Growth Morphology. *J. Miner. Mater. Charact. Eng.*, 10(08):683–691, 2011.

[32] N. Mironova-Ulmane, A. Kuzmin, I. Steins, J. Grabis, I. Sildos, and M. Pärs. Raman scattering in nanosized nickel oxide NiO. *J. Phys. Conf. Ser.*, 93(1):012039, dec 2007.

[33] N. Mironova-Ulmane, A. Kuzmin, I. Sildos, and M. Pärs. Polarisation dependent Raman study of single-crystal nickel oxide. *Open Phys.*, 9(4):1096–1099, jan 2011.

[34] D. J. Lockwood, G. Mischler, and A. Zwick. Raman scattering from magnons, electronic excitations and phonons in antiferromagnetic FeI 2. *J. Phys. Condens. Matter*, 6(32):6515–6533, aug 1994.

[35] V. G. Ivanov, M. V. Abrashev, N. D. Todorov, V. Tomov, R. P. Nikolova, A. P. Litvinchuk, and M. N. Iliev. Phonon and magnon Raman scattering in CuB2O4. *Phys. Rev. B*, 88(9):094301, sep 2013.

[36] R. H. Lyddane, R. G. Sachs, and E. Teller. On the Polar Vibrations of Alkali Halides. *Phys. Rev.*, 59(8):673–676, apr 1941.

[37] A.S. Chaves and S.P.S. Porto. Generalized Lyddane-Sachs-Teller relation. *Solid State Commun.*, 13(7):865–868, oct 1973.

[38] T. Kozawa, T. Kachi, H. Kano, Y. Taga, M. Hashimoto, N. Koide, and K. Manabe. Raman scattering from LO phonon-plasmon coupled modes in gallium nitride. *J. Appl. Phys.*, 75(2):1098–1101, jan 1994.

[39] H. Harima, S. I. Nakashima, and T. Uemura. Raman scattering from anisotropic LO-phonon-plasmon-coupled mode in n-type 4H- and 6H-SiC. *J. Appl. Phys.*, 78(3):1996–2005, 1995.

[40] Yu A. Pusep, M. T O Silva, J. R L Fernandez, V. A. Chitta, J. R. Leite, T. Frey, D. J. As, D. Schikora, and K. Lischka. Raman study of collective plasmon-longitudinal optical phonon excitations in cubic GaN and AlxGa1-xN epitaxial layers. *J. Appl. Phys.*, 91(9):6197–6199, may 2002.

[41] V. Deckert. Tip-Enhanced Raman Spectroscopy. *J. Raman Spectrosc.*, 40(10):1336–1337, oct 2009.

[42] R. M. Stöckle, Y. D. Suh, V. Deckert, and R. Zenobi. Nanoscale chemical analysis by tip-enhanced Raman spectroscopy. *Chem. Phys. Lett.*, 318(1-3):131–136, feb 2000.

[43] J. Steidtner and B. Pettinger. Tip-Enhanced Raman Spectroscopy and Microscopy on Single Dye Molecules with 15 nm Resolution. *Phys. Rev. Lett.*, 100(23):236101, jun 2008.

[44] A. S. Barker and R. Loudon. Dielectric Properties and Optical Phonons in LiNbO3. *Phys. Rev.*, 158(2):433–445, jun 1967.

[45] M. R. Tejerina, D. Jaque, and G. A. Torchia. μ-Raman spectroscopy characterization of LiNbO 3 femtosecond laser written waveguides. *J. Appl. Phys.*, 112(12):123108, dec 2012.

[46] G. Berth, W. Hahn, V. Wiedemeier, A. Zrenner, S. Sanna, and W. G. Schmidt. Imaging of the Ferroelectric Domain Structures by Confocal Raman Spectroscopy. *Ferroelectrics*, 420(1):44–48, jan 2011.

[47] L. Shi, Y. Kong, W. Yan, J. Sun, S. Chen, L. Zhang, W. Zhang, H. Liu, X. Li, X. Xie, D. Zhao, L. Sun, Z. Wang, J. Xu, and G. Zhang. Determination of the composition of lithium tantalate by means of Raman and OH- absorption measurements. *Mater. Chem. Phys.*, 95(2-3):229–234, feb 2006.

[48] I. P. Kaminow and W. D. Johnston. Quantitative Determination of Sources of the Electro-Optic Effect in LiNbO3 and LiTaO. *Phys. Rev.*, 160(3):519–522, aug 1967.

[49] P. Mackwitz, M. Rüsing, G. Berth, A. Widhalm, K. Müller, and A. Zrenner. Periodic domain inversion in x-cut single-crystal lithium niobate thin film. *Appl. Phys. Lett.*, 108(15):152902, apr 2016.

[50] V. Dierolf and C. Sandmann. Inspection of periodically poled waveguide devices by confocal luminescence microscopy. *Appl. Phys. B*, 78(3-4):363–366, feb 2004.

[51] T. Jach, S. Kim, V. Gopalan, S. Durbin, and D. Bright. Long-range strains and the effects of applied field at 180° ferroelectric domain walls in lithium niobate. *Phys. Rev. B*, 69(6):064113, feb 2004.

[52] S. Kim and V. Gopalan. Optical index profile at an antiparallel ferroelectric domain wall in lithium niobate. *Mater. Sci. Eng. B Solid-State Mater. Adv. Technol.*, 120(1-3):91–94, 2005.

[53] S. Cherifi-Hertel, H. Bulou, R. Hertel, G. Taupier, K. D. (Honorat) Dorkenoo, C. Andreas, J. Guyonnet, I. Gaponenko, K. Gallo, and P. Paruch. Non-Ising and chiral ferroelectric domain walls revealed by nonlinear optical microscopy. *Nat. Commun.*, 8:15768, jun 2017.

[54] V. Gopalan, V. Dierolf, and D. A. Scrymgeour. Defect–Domain Wall Interactions in Trigonal Ferroelectrics. *Annu. Rev. Mater. Res.*, 37(1):449–489, aug 2007.

[55] K. K. Wong, editor. *Properties of Lithium Niobate*. INSPEC, The Institution of Electrical Engineers, London, United Kingdom, 2002.

[56] T. Volk and M. Wöhlecke. *Lithium Niobate - Defects, Photorefraction and Ferroelectric switching*, volume 115 of *Springer Series in Materials Science*. Springer Berlin Heidelberg, Berlin, Heidelberg, 2008.

[57] A. Bartasyte, S. Margueron, T. Baron, S. Oliveri, and P. Boulet. Toward High-Quality Epitaxial LiNbO 3 and LiTaO 3 Thin Films for Acoustic and Optical Applications. *Adv. Mater. Interfaces*, 4(8):1600998, apr 2017.

[58] W. Sohler, H. Hu, R. Ricken, V. Quiring, C. Vannahme, H. Herrmann, D. Büchter, S. Reza, W. Grundkötter, S. Orlov, H. Suche, R. Nouroozi, and Y. Min. Integrated Optical Devices in Lithium Niobate. *Opt. Photonics News*, 19(1):24, jan 2008.

[59] M. Lawrence. Lithium niobate integrated optics. *Reports Prog. Phys.*, 56(3):363–429, mar 1993.

[60] K. Buse, A. Adibi, and D. Psaltis. Non-volatile holographic storage in doubly doped lithium niobate crystals. *Nature*, 393:665–668, 1998.

[61] F. S. Chen, J. T. LaMacchia, and D. B. Fraser. Holographic storage in lithium niobate. *Appl. Phys. Lett.*, 13(7):223–225, oct 1968.

[62] F. H. Mok. Angle-multiplexed storage of 5000 holograms in lithium niobate. *Opt. Lett.*, 18(11):915–917, 1993.

[63] S. Gong and G. Piazza. Design and Analysis of Lithium–Niobate-Based High Electromechanical Coupling RF-MEMS Resonators for Wideband Filtering. *IEEE Trans. Microw. Theory Tech.*, 61(1):403–414, jan 2013.

[64] V. M. Fridkin. Bulk photovoltaic effect in noncentrosymmetric crystals. *Crystallogr. Reports*, 46(4):654–658, jul 2001.

[65] M. Simon, St. Wevering, K. Buse, and E. Krätzig. The bulk photovoltaic effect of photorefractive :Fe crystals at high light intensities. *J. Phys. D. Appl. Phys.*, 30(1):144–149, jan 1997.

[66] A. M. Glass, D. von der Linde, and T. J. Negran. High-voltage bulk photovoltaic effect and the photorefractive process in LiNbO 3. *Appl. Phys. Lett.*, 25(4):233–235, aug 1974.

[67] M. Carrascosa, A. García-Cabañes, M. Jubera, J. B. Ramiro, and F. Agulló-López. LiNbO3: A photovoltaic substrate for massive parallel manipulation and patterning of nano-objects. *Appl. Phys. Rev.*, 2(4):040605, dec 2015.

[68] B Naranjo, J K Gimzewski, and S Putterman. Observation of nuclear fusion driven by a pyroelectric crystal. *Nature*, 434(7037):1115–7, 2005.

[69] A. Bartasyte, A. M. Glazer, F. Wondre, D. Prabhakaran, P. A. Thomas, S. Huband, D. S. Keeble, and S. Margueron. Growth of LiNb1-xTaxO3 solid solution crystals. *Mater. Chem. Phys.*, 134(2-3):728–735, jun 2012.

[70] S. Sanna, S. Neufeld, M. Rüsing, G. Berth, A. Zrenner, and W. G. Schmidt. Raman scattering efficiency in LiTaO3 and LiNbO3 crystals. *Phys. Rev. B*, 91(22):224302, 2015.

[71] F. W. H. Zachariasen. *Untersuchungen ueber die Kristallstrukturen von Sesquioxygen und Verbindungen ABO3*. PhD thesis, University of Oslo, 1928.

[72] B. T. Matthias and J. P. Remeika. Ferroelectricity in the Ilmenite Structure. *Phys. Rev.*, 76(12):1886–1887, dec 1949.

[73] H. C. Schweinler. Ferroelectricity in the Ilmenite Structure. *Phys. Rev.*, 87(1):5–11, jul 1952.

[74] G. Berth. *Visualisierung ferroelektrischer Domänenstrukturen in Lithiumniobat mittels konfokaler nichtlinearer Mikroskopie*. Phd thesis, University of Paderborn, 2010.

[75] R. S. Weis and T. K. Gaylord. Lithium Niobate: Summary of Physical Properties and Crystal Structure R. *Appl. Phys. A Mater. Sci. Process.*, 37(4):191–203, 1985.

[76] Y. Repelin, E. Husson, F. Bennani, and C. Proust. Raman spectroscopy of lithium niobate and lithium tantalate. Force field calculations. *J. Phys. Chem. Solids*, 60(6):819–825, jun 1999.

[77] S.C. Abrahams, E. Buehler, W.C. Hamilton, and S.J. Laplaca. Ferroelectric lithium tantalate—III. Temperature dependence of the structure in the ferroelectric phase and the para-electric structure at 940°K. *J. Phys. Chem. Solids*, 34(3):521–532, jan 1973.

[78] S.C. Abrahams, J.M. Reddy, and J.L. Bernstein. Ferroelectric lithium niobate. 3. Single crystal X-ray diffraction study at 24°C. *J. Phys. Chem. Solids*, 27(6-7):997–1012, jun 1966.

[79] Y. S. Kim and R. T. Smith. Thermal expansion of lithium tantalate and lithium niobate single crystals. *J. Appl. Phys.*, 40(11):4637–4641, 1969.

[80] P. Lerner, C. Legras, and J.P. Dumas. Stoechiométrie des monocristaux de métaniobate de lithium. *J. Cryst. Growth*, 3-4:231–235, jan 1968.

[81] J. R. Carruthers, G. E. Peterson, M. Grasso, and P. M. Bridenbaugh. Nonstoichiometry and Crystal Growth of Lithium Niobate. *J. Appl. Phys.*, 42(5):1846–1851, apr 1971.

[82] R. L. Barns and J. R. Carruthers. Lithium tantalate single crystal stoichiometry. *J. Appl. Crystallogr.*, 3(5):395–399, 1970.

[83] P. F. Bordui, R. G. Norwood, D. H. Jundt, and M. M. Fejer. Preparation and characterization of off-congruent lithium niobate crystals. *J. Appl. Phys.*, 71(2):875–879, jan 1992.

[84] P. F. Bordui, R. G. Norwood, C. D. Bird, and J. T. Carella. Stoichiometry issues in single-crystal lithium tantalate. *J. Appl. Phys.*, 78(7):4647–4650, oct 1995.

[85] X. Liang, X. Xuewu, C. Tow-Chong, Y. Shaoning, Y. Fengliang, and T. Y. Soon. Lithium in-diffusion treatment of thick LiNbO3 crystals by the vapor transport equilibration method. *J. Cryst. Growth*, 260(1-2):143–147, jan 2004.

[86] G. I. Malovichko, V. G. Grachev, L. P. Yurchenko, V. Ya. Proshko, E. P. Kokanyan, and V. T. Gabrielyan. Improvement of LiNbO3 Microstructure by Crystal Growth with Potassium. *Phys. Status Solidi*, 133(1):K29–K32, sep 1992.

[87] G. I. Malovichko, V. G. Grachev, E. P. Kokanyan, O. F. Schirmer, K. Betzler, B. Gather, F. Jermann, S. Klauer, U. Schlarb, and M. Woehlecke. Characterization of stoichiometric LiNbO3 grown from melts containing K2O. *Appl. Phys. A Solids Surfaces*, 56(2):103–108, feb 1993.

[88] K. Kitamura, J.K. Yamamoto, N. Iyi, S. Kirnura, and T. Hayashi. Stoichiometric LiNbO3 single crystal growth by double crucible Czochralski method using automatic powder supply system. *J. Cryst. Growth*, 116(3-4):327–332, feb 1992.

[89] A. Clairet, S. Oliveri, A. Almirall, T. Baron, W. Daniau, and A. Bartasyte. Characterization of single-port SAW resonators at 3.7 GHz based on epitaxial LiNbO3 layers. In *2017 Jt. Conf. Eur. Freq. Time Forum IEEE Int. Freq. Control Symp.*, pages 516–518. IEEE, jul 2017.

[90] O. F. Schirmer, M. Imlau, C. Merschjann, and B. Schoke. Electron small polarons and bipolarons in LiNbO 3. *J. Phys. Condens. Matter*, 21(12):123201, mar 2009.

[91] K. Lengyel, Á. Péter, L. Kovács, G. Corradi, L. Pálfalvi, J. Hebling, M. Unferdorben, G. Dravecz, I. Hajdara, Zs. Szaller, and K. Polgár. Growth, defect structure, and THz application of stoichiometric lithium niobate. *Appl. Phys. Rev.*, 2(4):040601, dec 2015.

[92] M. Imlau, H. Badorreck, and C. Merschjann. Optical nonlinearities of small polarons in lithium niobate. *Appl. Phys. Rev.*, 2(4):040606, dec 2015.

[93] H. Donnerberg, S. M. Tomlinson, C. R. A. Catlow, and O. F. Schirmer. Computer-simulation studies of intrinsic defects in LiNbO3 crystals. *Phys. Rev. B*, 40(17):11909–11916, dec 1989.

[94] N. Iyi, K. Kitamura, F. Izumi, J. K. Yamamoto, T. Hayashi, H. Asano, and S. Kimura. Comparative study of defect structures in lithium niobate with different compositions. *J. Solid State Chem.*, 101(2):340–352, dec 1992.

[95] S. C. Abrahams and P. Marsh. Defect structure dependence on composition in lithium niobate. *Acta Crystallogr. Sect. B Struct. Sci.*, 42(1):61–68, feb 1986.

[96] D. M. Smyth. Defects and transport in LiNbO 3. *Ferroelectrics*, 50(1):93–102, nov 1983.

[97] H. Donnerberg, S. M. Tomlinson, C. R. A. Catlow, and O. F. Schirmer. Computer-simulation studies of extrinsic defects in LiNbO3 crystals. *Phys. Rev. B*, 44(10):4877–4883, sep 1991.

[98] H. Xu, D. Lee, J. He, S. B. Sinnott, V. Gopalan, V. Dierolf, and S. R. Phillpot. Stability of intrinsic defects and defect clusters in LiNbO3 from density functional theory calculations. *Phys. Rev. B - Condens. Matter Mater. Phys.*, 78(17):1–12, 2008.

[99] Y. Li, S. Sanna, and W. G. Schmidt. Modeling intrinsic defects in LiNbO3 within the Slater-Janak transition state model. *J. Chem. Phys.*, 140(23):234113, 2014.

[100] Y. Li, W. G. Schmidt, and S. Sanna. Intrinsic LiNbO3 point defects from hybrid density functional calculations. *Phys. Rev. B*, 89(9):094111, mar 2014.

[101] Y. Li, W. G. Schmidt, and S. Sanna. Defect complexes in congruent LiNbO3 and their optical signatures. *Phys. Rev. B*, 91(17):174106, may 2015.

[102] S. Kim, V. Gopalan, K. Kitamura, and Y. Furukawa. Domain reversal and nonstoichiometry in lithium tantalate. *J. Appl. Phys.*, 90(6):2949–2963, 2001.

[103] H. Xu, D. Lee, S. B. Sinnott, V. Dierolf, V. Gopalan, and S. R. Phillpot. Structure and diffusion of intrinsic defect complexes in LiNbO3 from density functional theory calculations. *J. Phys. Condens. Matter*, 22(13):135002, apr 2010.

[104] V. Gopalan and M. C. Gupta. Origin and characteristics of internal fields in LiNbO 3 crystals. *Ferroelectrics*, 198(1):49–59, jun 1997.

[105] G. Bergmann. The electrical conductivity of LiNbO3. *Solid State Commun.*, 6(2):77–79, feb 1968.

[106] O. F. Schirmer, O. Thiemann, and M. Wöhlecke. Defects in LiNbO3—I. experimental aspects. *J. Phys. Chem. Solids*, 52(1):185–200, jan 1991.

[107] M. Bazzan and C. Sada. Optical waveguides in lithium niobate: Recent developments and applications. *Appl. Phys. Rev.*, 2(4):040603, dec 2015.

[108] G. I. Malovichko, V. G. Grachev, and O. F. Schirmer. The effect of iron ions on the defect structure of lithium niobate crystals grown from K2O containing melts. *Solid State Commun.*, 89(3):195–198, jan 1994.

[109] J. Hukriede, D. Kip, and E. Krätzig. Thermal fixing of holographic gratings in planar LiNbO3:Ti:Fe waveguides. *Appl. Phys. B Lasers Opt.*, 66(3):333–338, mar 1998.

[110] M.N. Armenise. Fabrication techniques of lithium niobate waveguides. *IEE Proc. J Optoelectron.*, 135(2):85, 1988.

[111] P.-K. Wei and W.-S. Wang. A TE-TM mode splitter on lithium niobate using Ti, Ni, and MgO diffusions. *IEEE Photonics Technol. Lett.*, 6(2):245–248, feb 1994.

[112] R. J. Holmes and D. M. Smyth. Titanium diffusion into LiNbO3 as a function of stoichiometry. *J. Appl. Phys.*, 55(10):3531–3535, may 1984.

[113] M. Minakata, S. Saito, M. Shibata, and S. Miyazawa. Precise determination of refractive-index changes in Ti-diffused LiNbO3 optical waveguides. *J. Appl. Phys.*, 49(9):4677–4682, sep 1978.

[114] H. Hu, R. Ricken, W. Sohler, and R. B. Wehrspohn. Lithium Niobate Ridge Waveguides Fabricated by Wet Etching. *IEEE Photonics Technol. Lett.*, 19(6):417–419, mar 2007.

[115] H.J. Lee and S.-Y. Shin. Lithium niobate ridge waveguides fabricated by wet etching. *Electron. Lett.*, 31(4):268–269, feb 1995.

[116] K. J. Spychala, G. Berth, A. Widhalm, M. Rüsing, L. Wang, S. Sanna, and A. Zrenner. Impact of carbon-ion implantation on the nonlinear optical susceptibility of LiNbO3. *Opt. Express*, 25(18):21444, sep 2017.

[117] O. Pea-Rodrguez, J. Olivares, M. Carrascosa, N. Garca-Cabaes, A. Rivera, and F. Agull-Lpez. Optical Waveguides Fabricated by Ion Implantation/Irradiation: A Review Optical Waveguides Fabricated by Ion Implantation/Irradiation: A Review. In *Ion Implant.* InTech, may 2012.

[118] J. Burghoff, S. Nolte, and A. Tünnermann. Origins of waveguiding in femtosecond laser-structured LiNbO3. *Appl. Phys. A*, 89(1):127–132, aug 2007.

[119] G. Poberaj, H. Hu, W. Sohler, and P. Günter. Lithium niobate on insulator (LNOI) for micro-photonic devices. *Laser Photon. Rev.*, 6(4):488–503, jul 2012.

[120] H. Hu, R. Ricken, and W. Sohler. Lithium niobate photonic wires. *Opt. Express*, 17(26):24261, dec 2009.

[121] L. Cai, S. L. H. Han, and H. Hu. Waveguides in single-crystal lithium niobate thin film by proton exchange. *Opt. Express*, 23(2):1240, jan 2015.

[122] H. Hu, R. Ricken, and W. Sohler. Low-loss ridge waveguides on lithium niobate fabricated by local diffusion doping with titanium. *Appl. Phys. B*, 98(4):677–679, mar 2010.

[123] M. Friedrich, W. G. Schmidt, A. Schindlmayr, and S. Sanna. Optical properties of titanium-doped lithium niobate from time-dependent density-functional theory. *Phys. Rev. Mater.*, 1(3):034401, aug 2017.

[124] V. Gericke, P. Hertel, E. Kraetzig, J. P. Nisius, and R. Sommerfeldt. Light-induced refractive index changes in LiNbO3:Ti waveguides. *Appl. Phys. B Photophysics Laser Chem.*, 44(3):155–162, nov 1987.

[125] A. M. Glass, I. P. Kaminow, A. A. Ballman, and D. H. Olson. Absorption loss and photorefractive-index changes in Ti:LiNbO3 crystals and waveguides. *Appl. Opt.*, 19(2):276, jan 1980.

[126] T. R. Volk, V. I. Pryalkin, and N. M. Rubinina. Optical-damage-resistant LiNbO3:Zn crystal. *Opt. Lett.*, 15(18):996, sep 1990.

[127] T. Volk, M. Wöhlecke, N. Rubinina, A. Reichert, and N. Razumovski. Optical-damage-resistant impurities (Mg, Zn, In, Sc) in lithium niobate. *Ferroelectrics*, 183(1):291–300, jul 1996.

[128] M. Aillerie, P. Bourson, M. Mostefa, F. Abdi, and M. D. Fontana. Photorefractive Damage in congruent LiNbO3. Part II. Magnesium doped Lithium Niobate Crystals. *J. Phys. Conf. Ser.*, 416:012002, 2013.

[129] N. V. Sidorov, M. N. Palatnikov, N. A. Teplyakova, A. A. Yanichev, A. A. Kruk, O. V. Makarova, O. Yu. Pikoul, and K. Bormanis. Structural and Optical Homogeneity in Lithium Niobate Crystals of Low Photorefractivity. *Ferroelectrics*, 484(1):55–61, aug 2015.

[130] N. V. Sidorov, M. N. Palatnikov, N. A. Teplyakova, A. A. Gabain, and I. N. Efremov. Photorefractive properties of congruent lithium niobate crystals doped with zinc. *Inorg. Mater. Appl. Res.*, 7(2):170–176, mar 2016.

[131] N. V. Sidorov, M. N. Palatnikov, A. A. Yanichev, R. A. Titov, and N. A. Teplyakova. Structural disorder and optical properties of congruent lithium niobate crystals doped with zink and boron. *Opt. Spectrosc.*, 121(1):36–44, jul 2016.

[132] K. Nakamura, J. Kurz, K. Parameswaran, and M. M. Fejer. Periodic poling of magnesium-oxide-doped lithium niobate. *J. Appl. Phys.*, 91(7):4528–4534, apr 2002.

[133] K. Lengyel, I. Kiss, L. Kovács, V. Szalay, and G. Corradi. Anomalous temperature dependence of the OH- absorption band in stoichiometric LiNbO3 crystals. *Vib. Spectrosc.*, 71:37–40, mar 2014.

[134] L. Kovács, V. Szalay, and R. Capelletti. Stoichiometry dependence of the OH- absorption band in LiNbO3 crystals. *Solid State Commun.*, 52(12):1029–1031, dec 1984.

[135] N. V. Sidorov, L. A. Bobreva, and M. N. Palatnikov. Concentration dependences of IR absorption spectra in the range of stretching vibrations of OH groups of congruent lithium-niobate crystals doped with zinc and magnesium. *Opt. Spectrosc.*, 123(2):258–263, aug 2017.

[136] Y.-L. Chen, J.-J. Xu, X.-Z. Zhang, Y.-F. Kong, X.-J. Chen, and G.-Y. Zhang. Ferroelectric domain inversion in near-stoichiometric lithium niobate for high efficiency blue light generation. *Appl. Phys. A Mater. Sci. Process.*, 74(2):187–190, feb 2002.

[137] A. Grisard, E. Lallier, K. Polgar, and A Peter. Low electric field periodic poling of thick stoichiometric lithium niobate. *Electron. Lett.*, 36(12):1043, 2000.

[138] K. Kitamura, Y. Furukawa, K. Niwa, V. Gopalan, and T. E. Mitchell. Crystal growth and low coercive field 180° domain switching characteristics of stoichiometric LiTaO3. *Appl. Phys. Lett.*, 73(21):3073–3075, nov 1998.

[139] V. Gopalan, T. E. Mitchell, Y. Furukawa, and K. Kitamura. The role of nonstoichiometry in 180° domain switching of LiNbO3 crystals. *Appl. Phys. Lett.*, 72(16):1981–1983, apr 1998.

[140] W. Sohler. Erbium-Doped Lithium Niobate Waveguide Lasers. *IEICE Trans. Electron.*, E88-C(5):990–997, may 2005.

[141] I. Baumann, S. Bosso, R. Brinkmann, R. Corsini, M. Dinand, A. Greiner, K. Schafer, J. Sochtig, W. Sohler, H. Suche, and R. Wessel. Er-doped integrated optical devices in LiNbO3. *IEEE J. Sel. Top. Quantum Electron.*, 2(2):355–366, jun 1996.

[142] C. W. Thiel, Y. Sun, R. M. Macfarlane, T. Böttger, and R. L. Cone. Rare-earth-doped LiNbO3 and KTiOPO4 (KTP) for waveguide quantum memories. *J. Phys. B At. Mol. Opt. Phys.*, 45(12):124013, jun 2012.

[143] V. Dierolf and C. Sandmann. Confocal two photon emission microscopy: A new approach to waveguide imaging. *J. Lumin.*, 102-103(SPEC):201–205, may 2003.

[144] V. Dierolf and C. Sandmann. Combined excitation emission spectroscopy of defects for site-selective probing of ferroelectric domain inversion in lithium niobate. *J. Lumin.*, 125(1-2):67–79, jul 2007.

[145] F. C. Zumsteg, J. D. Bierlein, and T. E. Gier. KxRb1-xTiOPO4: A new nonlinear optical material. *J. Appl. Phys.*, 47(11):4980–4985, 1976.

[146] G. Hansson, H. Karlsson, S. Wang, and F. Laurell. Transmission measurements in KTP and isomorphic compounds. *Appl. Opt.*, 39(27):5058, sep 2000.

[147] H. Vanherzeele and J. D. Bierlein. Magnitude of the nonlinear-optical coefficients of KTiOPO4. *Opt. Lett.*, 17(14):982–984, 1992.

[148] M. E. Hagerman and K. R. Poeppelmeier. Review of the Structure and Processing-Defect-Property Relationships of Potassium Titanyl Phosphate: A Strategy for Novel Thin-Film Photonic Devices. *Chem. Mater.*, 7(4):602–621, apr 1995.

[149] Y. Yang, D. Psaltis, M. Luennemann, D. Berben, U. Hartwig, and K. Buse. Photorefractive properties of lithium niobate crystals doped with manganese. *J. Opt. Soc. Am. B*, 20(7):1491, jul 2003.

[150] F. Laurell. Periodically poled materials for miniature light sources. *Opt. Mater. (Amst).*, 11(2-3):235–244, jan 1999.

[151] S. J. Crennell, J. J. Owen, C. P Grey, A. K Cheetham, J. A. Kaduk, and R. H. Jarman. Isomorphous substitution in non-linear optical KTiOPO4 . Powder diffraction and magic angle spinning nuclear magnetic resonance study of (K½Na½)TiOPO4 and (Rb½Na½)TiOPO4. *J. Mater. Chem.*, 1(1):113–119, 1991.

[152] S. J. Crennell, A. K. Cheetham, J. A. Kaduk, and R. H. Jarman. Isomorphous substitution in non-linear optical KTiOPO4: powder diffraction studies of K0.5RB0.5SnOPO4, K0.5Na0.5 Ti0.5Sn0.5OPO4, Na0.5Rb0.5 Ti0.5Sn0.5OPO4 and K0.5Rb0.5 Ti0.5Sn0.5OPO4. *J. Mater. Chem.*, 2(8):785, 1992.

[153] S. J. Crennell, J. J. Owen, A. K. Cheetham, J. A. Kaduk, and R. H. Jarman. A Combined X-Ray and Neutron Powder Diffraction Study of K(Ti0.5Sn0.5)OPO4. *Eur. J. Solid State Inorg. Chem.*, 28:397–407, 1991.

[154] P. A. Thomas, S. C. Mayo, and B. E. Watts. Crystal structures of RbTiOAsO4, KTiO(P0.58,As0.42)O4, RbTiOPO4 and (Rb0.465,K0.535)TiOPO4, and analysis of pseudosymmetry in crystals of the KTiOPO4 family. *Acta Crystallogr. Sect. B*, 48(4):401–407, 1992.

[155] P. A. Northrup, J. B. Parise, L. K. Cheng, L. T. Cheng, and E. M. McCarron. High-Temperature Single-Crystal X-ray Diffraction Studies of Potassium and (Cesium, Potassium) Titanyl Arsenates. *Chem. Mater.*, 6(4):434–440, apr 1994.

[156] J. Almgren, V. A Streltsov, A. N Sobolev, B. N Figgis, and J. Albertsson. Structure of and electron density in RbTiOAsO 4at 9.6 K. *Acta Crystallogr. Sect. B Struct. Sci.*, 55(5):712–720, oct 1999.

[157] S. C. Mayo, P. A. Thomas, S. J. Teat, G. M. Loiacono, and D. N. Loiacono. Structure and non-linear optical properties of KTiOAsO 4. *Acta Crystallogr. Sect. B Struct. Sci.*, 50(6):655–662, dec 1994.

[158] R. V. Pisarev, R. Farhi, P. Moch, and V. I. Voronkova. Temperature dependence of Raman scattering and soft modes in TlTiOPO4. *J. Phys. Condens. Matter*, 2(37):7555–7568, sep 1990.

[159] N. I. Sorokina and V. I. Voronkova. Structure and properties of crystals in the potassium titanyl phosphate family: A review. *Crystallogr. Reports*, 52(1):80–93, feb 2007.

[160] J. D. Bierlein and H. Vanherzeele. Potassium titanyl phosphate: properties and new applications. *J. Opt. Soc. Am. B*, 6(4):622, apr 1989.

[161] M. Yashima and T. Komatsu. Order-disorder and displacive components in the ferroelectric-paraelectric phase transition of potassium titanyl phosphate KTiOPO4. *Chem. Commun.*, 2009(9):1070, 2009.

[162] V. K. Yanovskii and V. I. Voronkova. Ferroelectric Phase Transitions and Properties of Crystals of the KTiOPO4 Family. *Phys. Status Solidi*, 93(2):665–668, 1986.

[163] D. K. T. Chu and H. Hsiung. Ferroelectric phase transition in KTiOPO4: An optical second-harmonic generation study. *Appl. Phys. Lett.*, 61(15):1766–1768, oct 1992.

[164] N. Angert, M. Tseitlin, E. Yashchin, and M. Roth. Ferroelectric phase transition temperatures of KTiOPO4 crystals grown from self-fluxes. *Appl. Phys. Lett.*, 67(13):1941–1943, sep 1995.

[165] M. Roth. Stoichiometry and Domain Structure of KTP-Type Nonlinear Optical Crystals. In *Springer Handb. Cryst. Growth*, pages 691–723. Springer Berlin Heidelberg, Berlin, Heidelberg, 2010.

[166] S. T. Norberg, P. A. Thomas, and M. G. Tucker. A neutron total scattering study of local coordination in KTiOPO4 from room temperature to 900 °C. *J. Phys. Condens. Matter*, 23(17):175401, may 2011.

[167] P. A. Thomas, A. M. Glazer, and B. E. Watts. Crystal structure and nonlinear optical properties of KSnOPO4 and their comparison with KTiOPO4. Erratum. *Acta Crystallogr. Sect. B Struct. Sci.*, 46(5):692–692, oct 1990.

[168] M. L. F. Phillips, W. T. A. Harrison, G. D Stucky, E. M. McCarron, J. C Calabrese, and T. E. Gier. Effects of substitution chemistry in the potassium titanyl phosphate (KTiOPO4) structure field. *Chem. Mater.*, 4(1):222–233, jan 1992.

[169] D. Xue and S. Zhang. Calculation of Second-Order Nonlinear Optical Coefficients of KTiOPO4 and KTiOAsO4. *J. Solid State Chem.*, 142(1):156–162, jan 1999.

[170] R. Wellendorf. *Kationenaustausch in K(TiO)PO4-Einkristallen im Kontakt mit Rb-haltigen Nitratschmelzen zur Erzeugung von mikrooptischen Strukturen*. PhD thesis, Bauhaus Universität Weimar, 1999.

[171] G. Rosenman, A. Skliar, D. Eger, M. Oron, and M. Katz. Low temperature periodic electrical poling of flux-grown KTiOPO4 and isomorphic crystals. *Appl. Phys. Lett.*, 73(25):3650–3652, dec 1998.

[172] J. D. Bierlein and C. B. Arweiler. Electro-optic and dielectric properties of KTiOPO4. *Appl. Phys. Lett.*, 49(15):917, 1986.

[173] J. Hellström, R. Clemens, V. Pasiskevicius, H. Karlsson, and F. Laurell. Real-time and in situ monitoring of ferroelectric domains during periodic electric field poling of KTiOPO4. *J. Appl. Phys.*, 90(3):1489, 2001.

[174] H. Karlsson, F. Laurell, and L. K. Cheng. Periodic poling of RbTiOPO4 for quasi-phase matched blue light generation. *Appl. Phys. Lett.*, 74(11):1519, 1999.

[175] J. D. Bierlein, A. Ferretti, L. H. Brixner, and W. Y. Hsu. Fabrication and characterization of optical waveguides in KTiOPO 4. *Appl. Phys. Lett.*, 50(18):1216–1218, may 1987.

[176] L. K. Cheng and J. D. Bierlein. KTP and isomorphs - recent progress in device and material development. *Ferroelectrics*, 142(1):209–228, jan 1993.

[177] P. A. Thomas, R. Duhlev, and S. J. Teat. A comparative structural study of a flux-grown crystal of K0.86Rb0.14TiOPO4 and an ion-exchanged crystal of K0.84Rb0.16TiOPO 4. *Acta Crystallogr. Sect. B Struct. Sci.*, 50(5):538–543, oct 1994.

[178] D. R. Allan, J. S. Loveday, R. J. Nelmes, and P. A. Thomas. A high-pressure structural study of potassium titanyl phosphate (KTP) up to 5 GPa. *J. Phys. Condens. Matter*, 4(11):2747–2760, mar 1992.

[179] E. L. Belokoneva, K. S. Knight, W. I. F. David, and B. V. Mill. Structural phase transitions in germanate analogues of KTiOPO4 investigated by high-resolution neutron powder diffraction. *J. Phys. Condens. Matter*, 9(19):3833–3851, may 1997.

[180] S. Sanna and W. G. Schmidt. Ferroelectric phase transition in LiNbO3: Insights from molecular dynamics. *IEEE Trans. Ultrason. Ferroelectr. Freq. Control*, 59(9):1925–1928, sep 2012.

[181] K. Toyoura, M. Ohta, A. Nakamura, and K. Matsunaga. First-principles study on phase transition and ferroelectricity in lithium niobate and tantalate. *J. Appl. Phys.*, 118(6):064103, aug 2015.

[182] P. F. Bordui and J. C. Jacco. Viscosity and density of solutions used in high-temperature solution growth of KTiOPO4 (KTP). *J. Cryst. Growth*, 82(3):351–355, mar 1987.

[183] P.A. Morris, A. Ferretti, J.D. Bierlein, and G.M. Loiacono. Reduction of the ionic conductivity of flux grown KTiOPO4 crystals. *J. Cryst. Growth*, 109(1-4):361–366, feb 1991.

[184] V. D. Kugel, G. Rosenman, N. Angert, E. Yaschin, and M. Roth. Domain inversion in KTiOPO4 crystal near the Curie point. *J. Appl. Phys.*, 76(8):4823–4826, oct 1994.

[185] M. G. Roelofs. Identification of Ti3+ in potassium titanyl phosphate and its possible role in laser damage. *J. Appl. Phys.*, 65(12):4976–4982, jun 1989.

[186] D. J. Gardiner and P. R. Graves. *Practical Raman Spectroscopy*, volume 53. Springer Berlin Heidelberg, Berlin, Heidelberg, 1989.

[187] P. Y. Yu and M. Cardona. *Fundamentals of Semiconductors*. Graduate Texts in Physics. Springer Berlin Heidelberg, Berlin, Heidelberg, 2005.

[188] H. Günzler and H. M. Heise. *IR-Spektroskopie: Eine Einführung*. Wiley-VCH, Weinheim, 1996.

[189] B. R Masters. CV Raman and the Raman Effect. *Opt. Photonics News*, 20(3):40, mar 2009.

[190] A. Smekal. Zur Quantentheorie der Streuung und Dispersion. *Naturwissenschaften*, 16(31):612–613, aug 1928.

[191] H. A. Kramers and W. Heisenberg. Über die Streuung von Strahlung durch Atome. *Zeitschrift für Phys.*, 31(1):681–708, feb 1925.

[192] G. Landsberg and L. Madelstam. Eine neue Erscheinung bei der Lichtzerstreuung in Krystallen. *Naturwissenschaften*, 16(28):557–558, jul 1928.

[193] C. V. Raman. A new radiation. *Proc. Indian Acad. Sci. - Sect. A*, 2:387–398, 1928.

[194] K. W. F. Kohlrausch. *Der Smekal-Raman-Effekt*. Springer Berlin Heidelberg, Berlin, Heidelberg, 1931.

[195] R. W. Wood. Wave-length Shifts in Scattered Light. *Nature*, 122(3071):349–349, sep 1928.

[196] W Demtröder. *Laserspektroskopie*, volume 4. Springer Berlin Heidelberg, Berlin, Heidelberg, 2007.

[197] H. Kuzmany. *Solid-State Spectroscopy*. Springer Berlin Heidelberg, Berlin, Heidelberg, 2009.

[198] E. Burstein, F. A. Johnson, and R. Loudon. Selection Rules for Second-Order Infrared and Raman Processes in the Rocksalt Structure and Interpretation of the Raman Spectra of NaCl, KBr, and NaI. *Phys. Rev.*, 139(4A):A1239–A1245, aug 1965.

[199] P. A. Temple and C. E. Hathaway. Multiphonon Raman spectrum of silicon. *Phys. Rev. B*, 7(8):3685–3697, 1973.

[200] K. Uchinokura, T. Sekine, and E. Matsuura. Critical-point analysis of the two-phonon Raman spectrum of silicon. *J. Phys. Chem. Solids*, 35(2):171–180, jan 1974.

[201] W. Nolting. *Grundkurs Theoretische Physik 5/2*. Springer-Lehrbuch. Springer Berlin Heidelberg, Berlin, Heidelberg, 2015.

[202] W. Nolting. *Grundkurs Theoretische Physik 5/1*. Springer-Lehrbuch. Springer Berlin Heidelberg, Berlin, Heidelberg, 2009.

[203] P. F. Bernath. *Spectra of atoms and molecules*. Oxford University Press, New York, 2005.

[204] G. Berth, V. Quiring, W. Sohler, and A. Zrenner. Depth-Resolved Analysis of Ferroelectric Domain Structures in Ti:PPLN Waveguides by Nonlinear Confocal Laser Scanning Microscopy. *Ferroelectrics*, 352(1):78–85, jul 2007.

[205] G. Berth, V. Wiedemeier, K.-P. Hüsch, L. Gui, H. Hu, W. Sohler, and A. Zrenner. Imaging of Ferroelectric Micro-Domains in X-Cut Lithium Niobate by Confocal Second Harmonic Microscopy. *Ferroelectrics*, 389(1):132–141, oct 2009.

[206] H. Harima, T. Inoue, S. Nakashima, H. Okumura, Y. Ishida, S. Yoshida, T. Koizumi, H. Grille, and F. Bechstedt. Raman studies on phonon modes in cubic AlGaN alloy. *Appl. Phys. Lett.*, 74(2):191–193, jan 1999.

[207] D. W. Feldman, James H Parker, W J Choyke, and Lyle Patrick. Phonon Dispersion Curves by Raman Scattering in SiC, Polytypes 3C, 4H, 6H , 15R, and 21R. *Phys. Rev.*, 173(3):787–793, 1968.

[208] K. Karch, P. Pavone, W. Windl, O. Schütt, and D. Strauch. Ab initio calculation of structural and lattice-dynamical properties of silicon carbide. *Phys. Rev. B*, 50(23):17054–17063, dec 1994.

[209] M. Giehler, M. Ramsteiner, O. Brandt, H. Yang, and K. H. Ploog. Optical phonons of hexagonal and cubic GaN studied by infrared transmission and Raman spectroscopy. *Appl. Phys. Lett.*, 67(6):733–735, aug 1995.

[210] P. Giannozzi, S. de Gironcoli, P. Pavone, and S. Baroni. Ab initio calculation of phonon dispersions in semiconductors. *Phys. Rev. B*, 43(9):7231–7242, mar 1991.

[211] M. Kuball. Raman spectroscopy of GaN, AlGaN and AlN for process and growth monitoring/control. *Surf. Interface Anal.*, 31(10):987–999, oct 2001.

[212] L. Bergman and R. J. Nemanich. Raman Spectroscopy for Characterization of Hard, Wide-Bandgap Semiconductors: Diamond, GaN, GaAlN, AlN, BN. *Annu. Rev. Mater. Sci.*, 26(1):551–579, aug 1996.

[213] S. Blumenthal, M. Bürger, A. Hildebrandt, J. Förstner, N. Weber, C. Meier, D. Reuter, and D. J. As. Fabrication and characterization of two-dimensional cubic AlN photonic crystal membranes containing zincblende GaN quantum dots. *Phys. status solidi*, 13(5-6):292–296, may 2016.

[214] R. M. Kemper, T. Schupp, M. Häberlen, T. Niendorf, H.-J. Maier, A. Dempewolf, F. Bertram, J. Christen, R. Kirste, A. Hoffmann, J. Lindner, and D. J. As. Anti-phase domains in cubic GaN. *J. Appl. Phys.*, 110(12):123512, dec 2011.

[215] H. Nagasawa, M. Abe, K. Yagi, T. Kawahara, and N. Hatta. Fabrication of high performance 3C-SiC vertical MOSFETs by reducing planar defects. *Phys. status solidi*, 245(7):1272–1280, jul 2008.

[216] P. T. B. Shaffer. Refractive Index, Dispersion, and Birefringence of Silicon Carbide Polytypes. *Appl. Opt.*, 10(5):1034, may 1971.

[217] H. Han, L. Cai, and H. Hu. Optical and structural properties of single-crystal lithium niobate thin film. *Opt. Mater. (Amst).*, 42:47–51, apr 2015.

[218] F. Sulser, G. Poberaj, M. Koechlin, and P. Günter. Photonic crystal structures in ion-sliced lithium niobate thin films. *Opt. Express*, 17(22):20291, oct 2009.

[219] L.-T. Cai, H. Hu, A. Gorbach, Y.-W. Wang, and W. Ding. Highly-efficient Broadband Second Harmonic Generation in Compact Fiber-integrated Thin-film LiNbO3 Nano-waveguides. In *Conf. Lasers Electro-Optics*, page SM3M.6, Washington, D.C., 2017. OSA.

[220] Z. Chen, Y. Wang, Y. Jiang, R. Kong, and H. Hu. Grating coupler on single-crystal lithium niobate thin film. *Opt. Mater. (Amst).*, 72:136–139, oct 2017.

[221] C. Wang, M. J. Burek, Z. Lin, H. A. Atikian, V. Venkataraman, I.-C. Huang, P. Stark, and M. Lončar. Integrated high quality factor lithium niobate microdisk resonators. *Opt. Express*, 22(25):30924, dec 2014.

[222] A. Guarino, G. Poberaj, D. Rezzonico, R. Degl'Innocenti, and P. Günter. Electro–optically tunable microring resonators in lithium niobate. *Nat. Photonics*, 1(7):407–410, jul 2007.

[223] P. O. Weigel, M. Savanier, C. T. DeRose, A. T. Pomerene, A. L. Starbuck, A. L. Lentine, V. Stenger, and S. Mookherjea. Lightwave Circuits in Lithium Niobate through Hybrid Waveguides with Silicon Photonics. *Sci. Rep.*, 6(1):22301, apr 2016.

[224] P. Weigel and S. Mookherjea. Hybrid Silicon / Lithium Niobate Waveguide Micro-chips Stable to 300C. In *Conf. Lasers Electro-Optics*, page SM3K.1, Washington, D.C., 2017. OSA.

[225] L. Gui, H. Hu, M. Garcia-Granda, and W. Sohler. Local periodic poling of ridges and ridge waveguides on X- and Y-Cut LiNbO3 and its application for second harmonic generation. *Opt. Express*, 17(5):3923, mar 2009.

[226] H. Steigerwald, Y. J. Ying, R. W. Eason, K. Buse, S. Mailis, and E. Soergel. Direct writing of ferroelectric domains on the x- and y-faces of lithium niobate using a continuous wave ultraviolet laser. *Appl. Phys. Lett.*, 98(6):062902, feb 2011.

[227] S. Sonoda, I. Tsuruma, and M. Hatori. Second harmonic generation in electric poled X-cut MgO-doped LiNbO3 waveguides. *Appl. Phys. Lett.*, 70(23):3078–3080, jun 1997.

[228] T. Kishino, R. F. Tavlykaev, and R. V. Ramaswamy. 70+ μm deep domain inversion in X -cut LiNbO3 and its use in a high-speed bandpass integrated-optic modulator. *Appl. Phys. Lett.*, 76(26):3852–3854, jun 2000.

[229] G. Li, Y. Chen, H. Jiang, and X. Chen. Broadband sum-frequency generation using d_33 in periodically poled LiNbO_3 thin film in the telecommunications band. *Opt. Lett.*, 42(5):939, mar 2017.

[230] A. Rao, A. Patil, M. Malinowski, J. Chiles, S. Khan, A. Honardoost, S. Toroghi, G. F. Camacho-Gonzalez, P. Rabiei, and S. Fathpour. Electro-optic and second-order nonlinear effects in thin film lithium niobate on silicon. In *2017 IEEE Photonics Soc. Summer Top. Meet. Ser.*, volume 21, pages 151–152. IEEE, jul 2017.

[231] V. Ya Shur. Kinetics of ferroelectric domains: Application of general approach to LiNbO3 and LiTaO3. In *Front. Ferroelectr.*, volume 1, pages 199–210. Springer US, Boston, MA, 2007.

[232] R. W. Boyd. *Nonlinear Optics*. Academic Press, London, United Kingdom, 2003.

[233] E. Hecht. *Optics*. Addison-Wesley, 2001.

[234] R. Menzel. *Photonics: Linear and Nonlinear Interactions of Laser Light and Matter*. Springer Verlag Berlin, Heidelberg, New York, 2013.

[235] S. Hell, G. Reiner, C. Cremer, and E. H. K. Stelzer. Aberrations in confocal fluorescence microscopy induced by mismatches in refractive index. *J. Microsc.*, 169(3):391–405, mar 1993.

[236] K. Carlsson. The influence of specimen refractive index, detector signal integration, and non-uniform scan speed on the imaging properties in confocal microscopy. *J. Microsc.*, 163(2):167–178, aug 1991.

[237] T. D. Visser, J. L. Oud, and G. J. Brakenhoff. Refractive index and axial distance measurements in 3-D microscopy, 1992.

[238] I. H. Malitson. Interspecimen Comparison of the Refractive Index of Fused Silica. *J. Opt. Soc. Am.*, 55(10):1205, oct 1965.

[239] C.Z. Tan. Determination of refractive index of silica glass for infrared wavelengths by IR spectroscopy. *J. Non. Cryst. Solids*, 223(1-2):158–163, jan 1998.

[240] M. A. Green. Self-consistent optical parameters of intrinsic silicon at 300K including temperature coefficients. *Sol. Energy Mater. Sol. Cells*, 92(11):1305–1310, nov 2008.

[241] M. J. Nasse and J. C. Woehl. Realistic modeling of the illumination point spread function in confocal scanning optical microscopy. *J. Opt. Soc. Am. A*, 27(2):295, feb 2010.

[242] M. Jain, J.K. Lotsberg, J.J. Stamnes, and Ø. Frette. Effects of aperture size on focusing of electromagnetic waves into a biaxial crystal. *Opt. Commun.*, 266(2):438–447, oct 2006.

[243] M. Jain, J. K. Lotsberg, J. J. Stamnes, Ø. Frette, D. Velauthapillai, D. Jiang, and X. Zhao. Numerical and experimental results for focusing of three-dimensional electromagnetic waves into uniaxial crystals. *J. Opt. Soc. Am. A*, 26(3):691, mar 2009.

[244] J. Reinhold. *Quantentheorie der Moleküle: Eine Einführung*. Vieweg+Teubner, Wiesbaden, 2015.

[245] S. Margueron, A. Bartasyte, A. M. Glazer, E. Simon, J. Hlinka, I. Gregora, and J. Gleize. Resolved E-symmetry zone-centre phonons in LiTaO 3 and LiNbO 3. *J. Appl. Phys.*, 111(10):104105, may 2012.

[246] X. Yang, G. Lan, B. Li, and H. Wang. Raman Spectra and Directional Dispersion in LiNbO3 and LiTaO3. *Phys. status solidi*, 142(1):287–300, jul 1987.

[247] A. Ridah, P. Bourson, M. D. Fontana, and G. Malovichko. The composition dependence of the Raman spectrum and new assignment of the phonons in. *J. Phys. Condens. Matter*, 9(44):9687–9693, nov 1997.

[248] M. Friedrich, A. Schindlmayr, W G Schmidt, and S. Sanna. LiTaO3 phonon dispersion and ferroelectric transition calculated from first principles. *Phys. status solidi*, 253(4):683–689, apr 2016.

[249] P. Hermet, M. Veithen, and Ph. Ghosez. First-principles calculations of the nonlinear optical susceptibilities and Raman scattering spectra of lithium niobate. *J. Phys. Condens. Matter*, 19(45):456202, nov 2007.

[250] Y. Y. Li, H. L. Chen, G. J. Chen, C. L. Kuo, P. H. Hsieh, and W. S. Hwang. Investigation of the defect structure of congruent and Fe-Doped LiNbO3powders synthesized by the combustion method. *Materials (Basel).*, 10(4), 2017.

[251] G. Stone and V. Dierolf. Influence of ferroelectric domain walls on the Raman scattering process in lithium tantalate and niobate. *Opt. Lett.*, 37(6):1032, mar 2012.

[252] R. Hammoum, M.D. Fontana, P. Bourson, and V.Y. Shur. Characterization of PPLN-microstructures by means of Raman spectroscopy. *Appl. Phys. A*, 91(1):65–67, apr 2008.

[253] W. D. Johnston and I. P. Kaminow. Temperature dependence of raman and Rayleigh scattering in LiNbO3 and LiTaO3. *Phys. Rev.*, 168(3):1045–1054, apr 1968.

[254] R. Claus, J. Brandmüller, G. Borstel, E. Wiesendanger, and L. Steffan. Directional Dispersion and Assignment of Optical Phonons in LiNbO3. *Zeitschrift für Naturforsch. A*, 27(8-9):1187–1192, jan 1972.

[255] V. Caciuc, A. V. Postnikov, and G. Borstel. Ab initio structure and zone-center phonons in LiNbO 3. *Phys. Rev. B*, 61(13):8806–8813, apr 2000.

[256] K. Parlinski, Z. Q. Li, and Y. Kawazoe. Ab initio calculations of phonons in LiNbO3. *Phys. Rev. B*, 61(1):272–278, jan 2000.

[257] M. Liebhaber, B. Halbig, U. Bass, J. Geurts, S. Neufeld, S. Sanna, W. G. Schmidt, E. Speiser, J. Räthel, S. Chandola, and N. Esser. Vibration eigenmodes of the Au-5×2/Si(111) surface studied by Raman spectroscopy and first-principles calculations. *Phys. Rev. B*, 94(23):235304, 2016.

[258] G. H. Haertling. Ferroelectric Ceramics: History and Technology. *J. Am. Ceram. Soc.*, 82(4):797–818, apr 1999.

[259] K. Worhoff, L. T. H. Hilderink, A. Driessen, and P. V. Lambeck. Silicon oxynitride - A versatile material for integrated optics applications. *J. Electrochem. Soc.*, 149(8):F85–F91, 2002.

[260] I. G. Wood, P. Daniels, R. H. Brown, and A. M. Glazer. Optical birefringence study of the ferroelectric phase transition in lithium niobate tantalate mixed crystals: LiNb(1-x)Ta(x)O(3). *J. Phys. Condens. Matter*, 20(23):235237, 2008.

[261] F. Shimura. Refractive indices of LiNb1-yTayO3 single crystals. *J. Cryst. Growth*, 42(C):579–582, 1977.

[262] A. Riefer, S. Sanna, and W. G. Schmidt. LiNb1-xTaxO3 Electronic Structure and Optical Response from First-Principles Calculations. *Ferroelectrics*, 447(1):78–85, jan 2013.

[263] F. Shimura and Y. Fujino. Crystal growth and fundamental properties of LiNb(1-y)Ta(y)O3. *J. Cryst. Growth*, 38(3):293–302, jun 1977.

[264] K. Sugii, H. Koizumi, S. Miyazawa, and S. Kondo. Temperature variations of lattice parameters of LiNbO3, LiTaO3 and Li(Nb1-yTay)O3 solid-solutions. *J. Cryst. Growth*, 33(1):199–202, apr 1976.

[265] S. Huband, D. S. Keeble, N. Zhang, A. M. Glazer, A. Bartasyte, and P. A. Thomas. Crystallographic and optical study of LiNb 1-x Ta x O 3. *Acta Crystallogr. Sect. B Struct. Sci. Cryst. Eng. Mater.*, 73(3):498–506, jun 2017.

[266] D. Xue, K. Betzler, and H. Hesse. Dielectric properties of lithium niobate – tantalate crystals. *Solid State Commun.*, 115:581–585, 2000.

[267] S. Sanna, A. Riefer, S. Neufeld, W. G. Schmidt, G. Berth, M. Rüsing, A. Widhalm, and A. Zrenner. Vibrational Fingerprints of LiNbO3-LiTaO3 Mixed Crystals. *Ferroelectrics*, 447(March 2015):63–68, 2013.

[268] M. Rüsing, S. Sanna, S. Neufeld, G. Berth, W. G. Schmidt, A. Zrenner, H. Yu, Y. Wang, and H. Zhang. Vibrational properties of LiNb1-xTaxO3 mixed crystals. *Phys. Rev. B*, 93(18):184305, may 2016.

[269] M. D. Fontana, R. Hammoum, P. Bourson, S. Margueron, and V. Ya. Shur. Raman Probe on PPLN Microstructures. *Ferroelectrics*, 373(1):26–31, nov 2008.

[270] A. Ridah, M. D. Fontana, and P. Bourson. Temperature dependence of the Raman modes in LiNbO3 and mechanism of the phase transition. *Phys. Rev. B*, 56(10):5967–5973, sep 1997.

[271] U. Schlarb, S. Klauer, M. Wesselmann, K. Betzler, and M. Woehlecke. Determination of the Li/Nb ratio in lithium niobate by means of birefringence and Raman measurements. *Appl. Phys. A Solids Surfaces*, 56(4):311–315, apr 1993.

[272] P. Capek, G. Stone, V. Dierolf, C. Althouse, and V. Gopolan. Raman studies of ferroelectric domain walls in lithium tantalate and niobate. *Phys. status solidi*, 4(3):830–833, mar 2007.

[273] V. Ya Shur, P. S. Zelenovskiy, M. S. Nebogatikov, D. O. Alikin, M. F. Sarmanova, A. V. Ievlev, E. A. Mingaliev, and D. K. Kuznetsov. Investigation of the nanodomain structure formation by piezoelectric force microscopy and Raman confocal microscopy in LiNbO3 and LiTaO 3 crystals. *J. Appl. Phys.*, 110(5), 2011.

[274] V. Ya Shur and P. S. Zelenovskiy. Micro- and nanodomain imaging in uniaxial ferroelectrics: Joint application of optical, confocal Raman, and piezoelectric force microscopy. *J. Appl. Phys.*, 116(6):066802, aug 2014.

[275] Y. Saito and P. Verma. Polarization-Controlled Raman Microscopy and Nanoscopy. *J. Phys. Chem. Lett.*, 3(10):1295–1300, may 2012.

[276] Y. Saito, M. Kobayashi, D. Hiraga, K. Fujita, S. Kawano, N. I. Smith, Y. Inouye, and S. Kawata. z -Polarization sensitive detection in micro-Raman spectroscopy by radially polarized incident light. *J. Raman Spectrosc.*, 39(11):1643–1648, nov 2008.

[277] R. Ossikovski, Q. Nguyen, G. Picardi, J. Schreiber, and P. Morin. Theory and experiment of large numerical aperture objective Raman microscopy: application to the stress-tensor determination in strained cubic materials. *J. Raman Spectrosc.*, 39(5):661–672, may 2008.

[278] D. Tuschel. The Effect of Microscope Objectives on the Raman Spectra of Crystals. *Spectroscopy*, 32(9):14–23, 2017.

[279] A. S. Barker, A. A. Ballman, and J. A. Ditzenberger. Infrared Study of the Lattice Vibrations in LiTaO3. *Phys. Rev. B*, 2(10):4233–4239, nov 1970.

[280] T. Fujii, A. Ando, and Y. Sakabe. Characterization of dielectric properties of oxide materials in frequency range from GHz to THz. *J. Eur. Ceram. Soc.*, 26(10-11):1857–1860, 2006.

[281] G. H. Watson. Polarized Raman spectra of ktioaso4 and isomorphic nonlinear-optical crystals. *J. Raman Spectrosc.*, 22(11):705–713, nov 1991.

[282] G. E. Kugel, F. Bréhat, B. Wyncket, M. D. Fontana, G. Marnier, C. Carabatos-Nedelec, and J. Mangin. The vibrational spectrum of a KTiOPO4 single crystal studied by Raman and infrared reflectivity spectroscopy. *J. Phys. C Solid State Phys*, 21:5565–5583, 1988.

[283] M.J. Bushiri, V.P. Mahadevan Pillai, R. Ratheesh, and V.U. Nayar. Raman spectra of KTP crystal in an in situ electric field. *J. Phys. Chem. Solids*, 60(12):1983–1988, dec 1999.

[284] C.-S. Tu, A. R. Guo, R. Tao, R. S. Katiyar, R. Guo, and A. S. Bhalla. Temperature dependent Raman scattering in KTiOPO4 and KTiOAsO4 single crystals. *J. Appl. Phys.*, 79(6):3235, 1996.

[285] S. Furusawa, H. Hayasi, Y. Ishibashi, A. Miyamoto, and T. Sasaki. Raman Scattering Study of KTiOPO 4 (KTP) Single Crystal. *J. Phys. Soc. Japan*, 60(7):2470–2474, jul 1991.

[286] A. R. Guo, C.-S. Tu, Ruiwu Tao, R. S. Katiyar, Ruyan Guo, and A. S. Bhalla. Raman scattering in CsTiOAsO4 single crystal. *Ferroelectr. Lett. Sect.*, 21(3-4):71–77, jun 1996.

[287] G. A. Kourouklis, A. Jayaraman, A. A. Ballman, and M. Hill. A high pressure Raman study of KTP and pressure induced phase transition. *Solid State Commun.*, 62(6):379–382, 1987.

[288] I. Tordjman, R. Masse, and J. C. Guitel. Structure cristalline du monophosphate KTiPO5. *Zeitschrift fur Krist. - New Cryst. Struct.*, 139(1-2):103–115, 1974.

[289] G. Herzberg. *Infrared and Raman Spectra of Polyafomic Molecules*. Van Nostrand, New York, 1975.

[290] L Merten. Directional Dispersion of Extraordinary Optical Phonons of α-Quartz. *Phys. Status Solidi*, 28(1):111–119, 1968.

[291] J. Onstott and G. Lucovsky. Directional dispersion of extraordinary optical phonons in alpha-quartz in the frequency domain from 380 to 640 cm-1. *J. Phys. Chem. Solids*, 31(10):2171–2184, oct 1970.

[292] N. Kuroda and Y. Nishina. Directional dispersion of extraordinary phonons in layer compound InSe. *Solid State Commun.*, 30(2):95–98, apr 1979.

[293] D.J. Olechna. Directional dispersion of extraordinary optical phonons in uniaxial crystals. *J. Phys. Chem. Solids*, 31(12):2755–2763, dec 1970.

[294] M. Rüsing, C. Eigner, P. Mackwitz, G. Berth, C. Silberhorn, and A. Zrenner. Identification of ferroelectric domain structure sensitive phonon modes in potassium titanyl phosphate: A fundamental study. *J. Appl. Phys.*, 119(4):044103, jan 2016.

[295] Y. Zhang, L. Guilbert, and P. Bourson. Characterization of Ti : LiNbO3 waveguides by micro-raman and luminescence spectroscopy. *Appl. Phys. B*, 78(3-4):355–361, feb 2004.

[296] V. Ya Shur, D. S. Chezganov, M. S. Nebogatikov, I. S. Baturin, and M. M. Neradovskiy. Formation of dendrite domain structures in stoichiometric lithium niobate at elevated temperatures. *J. Appl. Phys.*, 112(10):104113, nov 2012.

[297] P. S. Zelenovskiy, M. D. Fontana, V. Y. Shur, P. Bourson, and D. K. Kuznetsov. Raman visualization of micro- and nanoscale domain structures in lithium niobate. *Appl. Phys. A*, 99(4):741–744, jun 2010.

[298] R. Hammoum, M. D. Fontana, P. Bourson, and V. Ya Shur. Raman micro-spectroscopy as a probe to investigate PPLN structures. *Ferroelectrics*, 352(1 PART 2):106–110, 2007.

[299] Y. Kong, J. Xu, B. Li, S. Chen, Z. Huang, L. Zhang, S. Liu, W. Yan, H. Liu, X. Xie, L. Shi, X. Li, and G. Zhang. The asymmetry between the domain walls of periodically poled lithium niobate crystals. *Opt. Mater. (Amst).*, 27(3):471–473, dec 2004.

[300] Kh. Hassani, M. Sutton, M. Holt, Y. Zuo, and D. Plant. X-ray diffraction imaging of strain fields in a domain-inverted LiTaO[sub 3] crystal. *J. Appl. Phys.*, 104(4):043515, 2008.

[301] D. A. Scrymgeour, V. Gopalan, A. Itagi, A. Saxena, and P. J. Swart. Phenomenological theory of a single domain wall in uniaxial trigonal ferroelectrics: Lithium niobate and lithium tantalate. *Phys. Rev. B*, 71(18):184110, may 2005.

[302] J. Padilla, W. Zhong, and D. Vanderbilt. First-principles investigation of 180° domain walls in BaTiO3. *Phys. Rev. B*, 53(10):R5969–R5973, mar 1996.

[303] B. Meyer and D. Vanderbilt. Ab initio study of ferroelectric domain walls in PbTiO3. *Phys. Rev. B*, 65(10):104111, 2002.

[304] C.-L. Jia, S.-B. Mi, K. Urban, I. Vrejoiu, M. Alexe, and D. Hesse. Atomic-scale study of electric dipoles near charged and uncharged domain walls in ferroelectric films. *Nat. Mater.*, 7(1):57–61, jan 2008.

[305] L.A. Bursill and Peng Ju Lin. Electron microscopic studies of ferroelectric crystals: Detection of weak symmetry elements. *Ultramicroscopy*, 18(1-4):235–240, jan 1985.

[306] Y. B. Chen, M. B. Katz, X. Q. Pan, R. R. Das, D. M. Kim, S. H. Baek, and C. B. Eom. Ferroelectric domain structures of epitaxial (001) BiFeO[sub 3] thin films. *Appl. Phys. Lett.*, 90(7):072907, 2007.

[307] J. Wittborn, C. Canalias, K. V. Rao, R. Clemens, H. Karlsson, and F. Laurell. Nanoscale imaging of domains and domain walls in periodically poled ferroelectrics using atomic force microscopy. *Appl. Phys. Lett.*, 80(9):1622–1624, 2002.

[308] T. Yang, Venkatraman Gopalan, P. Swart, and U. Mohideen. Direct Observation of Pinning and Bowing of a Single Ferroelectric Domain Wall. *Phys. Rev. Lett.*, 82(20):4106–4109, 1999.

[309] G. Stone, B. Knorr, V. Gopalan, and V. Dierolf. Frequency shift of Raman modes due to an applied electric field and domain inversion in LiNbO3. *Phys. Rev. B*, 84(13):134303, oct 2011.

[310] J.L. Servoin and F. Gervais. Soft vibrational mode in LiNbO3 and LiTaO3. *Solid State Commun.*, 31(5):387–391, aug 1979.

[311] C. Raptis. Assignment and temperature dependence of the Raman modes of LiTaO3 studied over the ferroelectric and paraelectric phases. *Phys. Rev. B*, 38(14):10007–10019, nov 1988.

[312] Y. Tezuka, S. Shin, and M. Ishigame. Hyper-Raman and Raman studies on the phase transition of ferroelectric LiTaO3. *Phys. Rev. B*, 49(14):9312–9321, 1994.

[313] H. R. Xia, S. Q. Sun, X. F. Cheng, S. M. Dong, H. Y. Xu, L. Gao, and D. L. Cui. Lattice vibrations and phase-transition soft mode in near stoichiometric lithium niobate crystals. *J. Appl. Phys.*, 98(3):033513, aug 2005.

[314] S. Sanna, G. Berth, W. Hahn, A. Widhalm, A. Zrenner, and W. G. Schmidt. Localised Phonon Modes at LiNbO3 (0001) Surfaces. *Ferroelectrics*, 419(0001):1–8, 2011.

[315] G. Berth. Joint IEEE ISAF-ECAPD-PFM 2012, 2012.

[316] T. Kämpfe, P. Reichenbach, M. Schröder, A. Haußmann, L. M. Eng, T. Woike, and E. Soergel. Optical three-dimensional profiling of charged domain walls in ferroelectrics by Cherenkov second-harmonic generation. *Phys. Rev. B*, 89(3):035314, jan 2014.

[317] G. F. Nataf, M. Guennou, A. Haußmann, N. Barrett, and J. Kreisel. Evolution of defect signatures at ferroelectric domain walls in Mg-doped LiNbO3. *Phys. status solidi - Rapid Res. Lett.*, 10(3):222–226, mar 2016.

[318] T. Doumuki, H. Tamada, and M. Saitoh. Phase-matched second-harmonic generation in a Ta2O5/KTiOPO4 waveguide. *Appl. Phys. Lett.*, 65(20):2519–2521, nov 1994.

[319] L. Zhang, P. J. Chandler, P. D. Townsend, Z. T. Alwahabi, S. L. Pityana, and A. J. McCaffery. Frequency doubling in ion-implanted KTiOPO 4 planar waveguides with 25% conversion efficiency. *J. Appl. Phys.*, 73(6):2695–2699, mar 1993.

[320] P. Bindner, A. Boudrioua, J. C. Loulergue, and P. Moretti. Formation of planar optical waveguides in potassium titanyl phosphate by double implantation of protons. *Appl. Phys. Lett.*, 79(16):2558–2560, oct 2001.

[321] C. Chen, C. E. Rüter, M. F. Volk, C. Chen, Z. Shang, Q. Lu, S. Akhmadaliev, S. Zhou, F. Chen, and D. Kip. Second harmonic generation of diamond-blade diced KTiOPO4 ridge waveguides. *Opt. Express*, 24(15):16434, jul 2016.

[322] F. Laurell, T. Calmano, S. Müller, P. Zeil, C. Canalias, and G. Huber. Laser-written waveguides in KTP for broadband Type II second harmonic generation. *Opt. Express*, 20(20):22308, sep 2012.

[323] M. G. Roelofs, P. A. Morris, and J. D. Bierlein. Ion exchange of Rb, Ba, and Sr in KTiOPO4. *J. Appl. Phys.*, 70(2):720–728, jul 1991.

[324] F. Laurell, M. G. Roelofs, W. Bindloss, H. Hsiung, A. Suna, and J. D. Bierlein. Detection of ferroelectric domain reversal in KTiOPO4 waveguides. *J. Appl. Phys.*, 71(10):4664–4670, 1992.

[325] M. G. Roelofs, A. Suna, W. Bindloss, and J. D. Bierlein. Characterization of optical waveguides in KTiOPO4 by second harmonic spectroscopy. *J. Appl. Phys.*, 76(9):4999–5006, nov 1994.

[326] Q. Chen and W.P. Risk. High efficiency quasi-phasematched frequency doubling waveguides in KTiOPO4 fabricated by electric field poling. *Electron. Lett.*, 32(2):107, 1996.

[327] M. Pysher, C. M. Kaleva, T. D Roberts, P. Battle, and O. Pfister. Broadband amplitude squeezing in a periodically poled KTiOPO4 waveguide. *Opt. Lett.*, 34(3):256, feb 2009.

[328] W. P. Risk. Fabrication and characterization of planar ion-exchanged KTiOPO4 waveguides for frequency doubling. *Appl. Phys. Lett.*, 58(1):19–21, jan 1991.

[329] M. Santandrea. Private Communication, 2017.

[330] C. Eigner. Private Communication, 2017.

[331] L. Padberg. Private Communication, 2017.

[332] I. Savatinova, S. Tonchev, T. Popov, E. Liarokapis, and C. C. Ziling. Raman study of Cs:KTiOPO 4 waveguides. *J. Phys. D. Appl. Phys.*, 27(7):1384–1389, jul 1994.

[333] I. Savatinova, I. Savova, E. Liarokapis, C. C. Ziling, V. V. Atuchin, M. N. Armenise, and V. M. N. Passaro. A comparative analysis of Rb:KTP and Cs:KTP optical waveguides. *J. Phys. D. Appl. Phys.*, 31(14):1667–1672, jul 1998.

[334] D. D. Tuschel, G. R. Paz-Pujalt, and W. P. Risk. Chemical bonding and atomic structure of Rb + exchanged KTiOPO 4 waveguides probed by micro-Raman spectroscopy. *Appl. Phys. Lett.*, 66(9):1035–1037, feb 1995.

[335] D. Tuschel. Three-Dimensional Raman Imaging of Ion-Exchanged Waveguides. *Spectroscopy*, 29(12):14–23, 2014.

[336] M. R. Tejerina and G. A. Torchia. Computation of the expansion parameters of femto-waveguides using a two dimensional μ-Raman map and guided modes. *J. Appl. Phys.*, 114(15):153106, oct 2013.

[337] M. R. Tejerina, D. Jaque, and G. A. Torchia. A 2D μ-Raman analysis of low repetition rate femto-waveguides in lithium niobate by using a finite element model. *Opt. Mater. (Amst).*, 36(5):936–940, mar 2014.

[338] J.-J. Yin, F. Lu, X.-B. Ming, Z.-H. Qin, and Y.-J. Ma. Theoretical modeling and experiment of refractive index change in He+ ion-implanted KTP waveguide. *Appl. Opt.*, 51(13):2400, may 2012.

[339] R. Hölscher, W. G. Schmidt, and S. Sanna. Modeling LiNbO3 Surfaces at Ambient Conditions. *J. Phys. Chem. C*, 118(19):10213–10220, may 2014.

[340] C. Canalias, V. Pasiskevicius, A. Fragemann, and F. Laurell. High-resolution domain imaging on the nonpolar y-face of periodically poled KTiOPO[sub 4] by means of atomic force microscopy. *Appl. Phys. Lett.*, 83(4):734, 2003.

[341] N. Argiolas, M. Bazzan, a. Bernardi, E. Cattaruzza, P. Mazzoldi, P. Schiavuta, C. Sada, and U. Hangen. A systematic study of the chemical etching process on periodically poled lithium niobate structures. *Mater. Sci. Eng. B*, 118(1-3):150–154, 2005.

[342] H. Karlsson and F. Laurell. Electric field poling of flux grown KTiOPO4. *Appl. Phys. Lett.*, 71(24):3474–3476, dec 1997.

[343] H. Kianirad, A. Zukauskas, T. Frisk, C. Canalias, and F. Laurell. Contact poling of Rb:KTiOPO4 using a micro-structured silicon electrode. *Opt. Express*, 23(2):636, jan 2015.

[344] K. Kato and E. Takaoka. Sellmeier and thermo-optic dispersion formulas for KTP. *Appl. Opt.*, 41(24):5040, aug 2002.

[345] M. R. Tejerina, K. Pereira da Silva, A. R. Goñi, and G. A. Torchia. Hydrostatic-pressure dependence of Raman-active optical phonons in Nd:Mg:LiNbO3. *Opt. Mater. (Amst).*, 36(2):581–583, dec 2013.

[346] C. Canalias, J. Hirohashi, V. Pasiskevicius, and F. Laurell. Polarization-switching characteristics of flux-grown KTiOPO4 and RbTiOPO4 at room temperature. *J. Appl. Phys.*, 97(12):124105, jun 2005.

[347] C. Canalias. *Domain Engineering in KTiOPO4*. PhD thesis, Royal Institute of Technology Stockholm, 2005.

[348] C.-L. Zhang, Z.-G. Hu, L.-X. Huang, W.-N. Zhou, Z. Lü, G. Zhang, Y.-C. Liu, Y.-B. Zou, F.-H. Lu, H.-D. Hou, S.-J. Qin, H.-X. Zhang, and L. Bai. Growth and optical properties of bulk KTP crystals by hydrothermal method. *J. Cryst. Growth*, 310(7-9):2010–2014, apr 2008.

[349] K. Vivekanandan, S. Selvasekarapandian, P. Kolandaivel, M.T. Sebastian, and S. Suma. Raman and FT-IR spectroscopic characterisation of flux grown KTiOPO4 and KRbTiOPO4 non-linear optical crystals. *Mater. Chem. Phys.*, 49(3):204–210, jul 1997.

[350] J. J. Carvajal, P. Segonds, A. Peña, J. Zaccaro, B. Boulanger, F. Díaz, and M. Aguiló. Structural and optical properties of RbTiOPO 4 :Nb crystals. *J. Phys. Condens. Matter*, 19(11):116214, mar 2007.

Appendix A

KTP wafer homogeneity

In Section 5.2.1 the Raman spectra of Rb-exchanged waveguides have been studied. Here, it was found that many modes react to the exchange of potassium for ion, as well as to strain induced by the exchange. Additionally, some hints were found, that the spectrum in the surface region shows its own peculiarities. Similarly, changes in the spectra have been observed from domain walls have been discussed in Secs. 5.1 and 5.2.2. In all cases, small changes in the Raman spectra have been used for visualization of said properties. The samples in this work are all fabricated from flux grown $KTiOPO_4$. For flux grown $KTiOPO_4$ previous work suggests, that certain properties can vary globally over the a complete wafer, e.g. the ionic conductivity [346, 347] or refractive index [348]. In particular, the ionic conductivity was found to have a parabolic distribution with a maximum in the center of a $KTiOPO_4$ wafer, while it decreases by almost a factor of two towards both sides. These variations was only dominant along the y-axis [346, 347]. This is explained by variations in K^+ stoichiometry induced during growth. Flux-grown, single $KTiOPO_4$ crystals are often grown from on seed on multiple sectors. This means, the crystals growth takes place in multiple directions around the central seed [165]. Due to different solubility of the components in the liquid and solid phase, as well as a temperature gradient towards the center of the crystals, this can result in a systematic variations of defects and stoichiometry from the center to the outer parts of a crystal, where the crystals is generally considered of better stoichiometry in the outer parts, leading to a decreasing conductivity [346, 347].

For the wafers analyzed in this work, no such variation in the conductivity was observed. Nevertheless, this could mean, that the defect concentration and stoichiometry, e.g. the K^+ vacancies, may have a systematic variation, over a wafer, which do not modify the ionic conductivity, but are still detectable by Raman spectroscopy. Here, indeed in literature differences in the spectra of $KTiOPO_4$ grown from different fluxes have been observed, which are thought to be from different stoichiometry [349]. Similar, doping $RbTiOPO_4$ with Nb ions leads to broadening of the Raman lines [350]. Therefore, it can be expected that Raman spectroscopy is sensitive to any systematic stoichiometry or defect variations.

To check, whether or not global variations over a complete waveguide can be detected, spatially resolved Raman spectroscopy was performed to analyze the homogeneity of the wafer. For the analysis, the focus was placed more than 20 μm below the surface in each measurement to avoid any surface related imprint on the spectrum. For this, Raman spectra 1 mm apart were taken over a complete RTP, as well as a KTP wafer, as shown in the insets in Figs. A.2 and A.1. Here, one scan was performed over the center of the waveguide parallel to the x and y-axes, respectively. In these spectra then the peak position, as well as the FHWM have been analyzed for multiple peaks, which both are typical criteria for stoichiometry in other materials. The exemplary results for one mode are plotted below each spectrum. Here, for neither mode we detect any

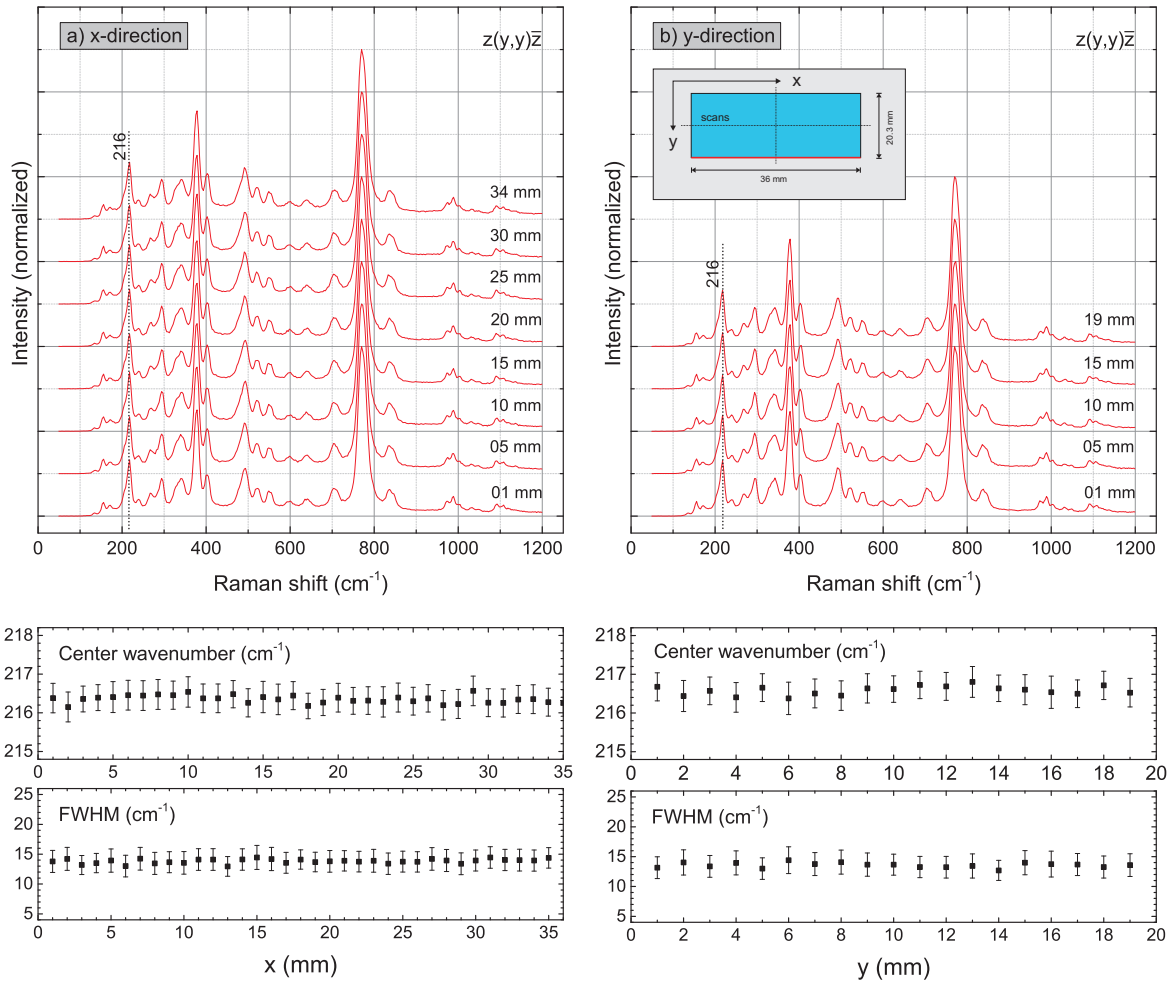

Fig. A.1 Z-cut Raman spectra of a $KTiOPO_4$ wafer with the dimensions of 36 mm (x) by 20.3 mm (y) have been taken at a line parallel to the x-direction (a) and y-direction (b), as indicated by the dotted lines in the inset in b). Here, no significant variations in the spectrum, i.e. spectral positions and FWHM of modes have been detected. As a representative, the determined peak positions and FWHM for the 216 cm^{-1} is plotted below for each plot.

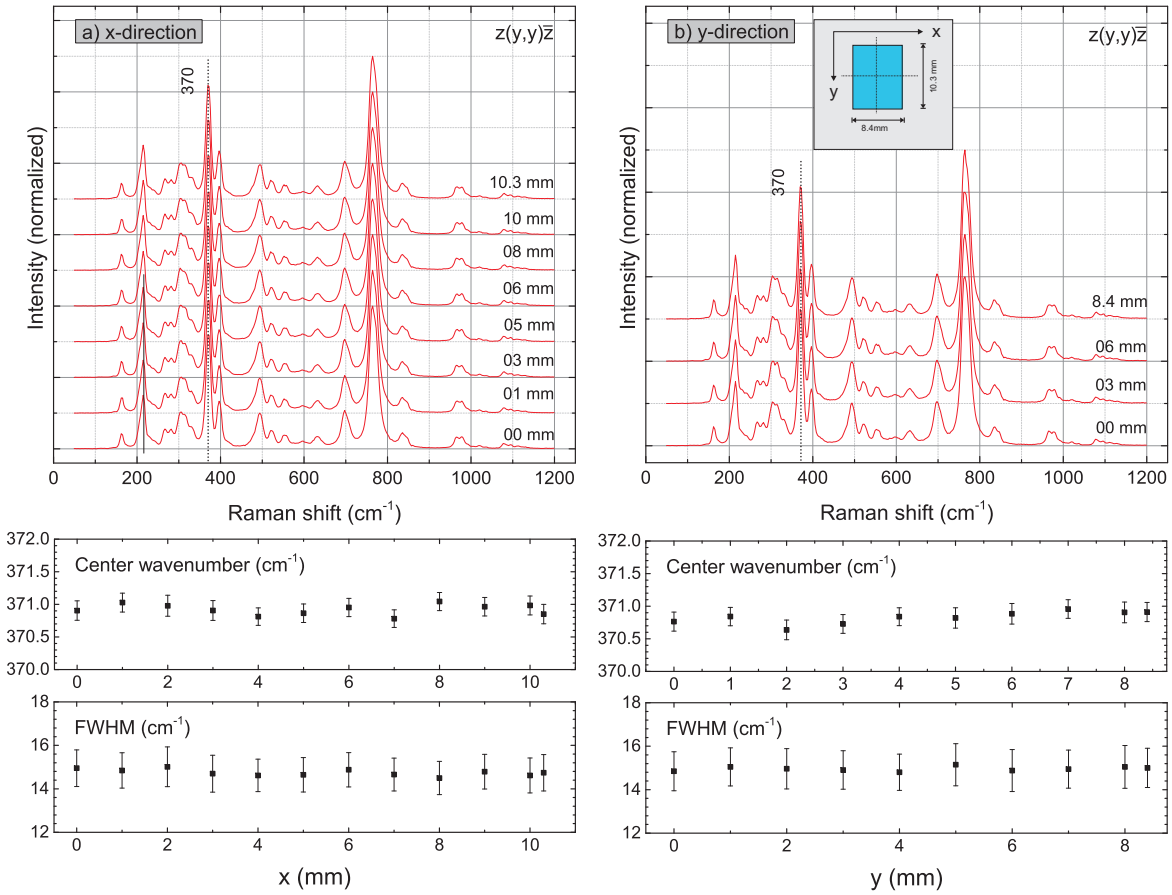

Fig. A.2 Z-cut Raman spectra of a $RbTiOPO_4$ wafer with the dimensions of 8.4 mm (x) by 10.3 mm (y) have been taken at a line parallel to the x-direction (a) and y-direction (b), as indicated by the dotted lines in the inset in b). Here, no significant variations in the spectrum, i.e. spectral positions and FWHM of modes have been detected. As a representative, the determined peak positions and FWHM for the 216 cm^{-1} is plotted below for each plot.

significant positional dependence or variation over the wafers. This result is a strong hint, that the used wafers have a homogeneous structure atleast with respect to Raman spectroscopy, which fits the previous observations on the ionic conductivity, which appears similar over the complete wafers. For further Raman measurements this enables a comparability of spectra taken on different places of the wafer.

Appendix B

Investigation of y-cut PPKTP

As demonstrated in Sec. 5.1 domain walls in $KTiOPO_4$ can also be visualized for y-cut. This is a particular achievement, because the usual standard method for visualization - selective chemical etching - is not applicable for x- and y-face. The so far only practical methods has been piezo-response force microscopy, an AFM derivative [340]. As a AFM method it offers a very high spatial resolution ($<<$ 100 nm) - limited only by the AFM tip size and shape. However, as an AFM derived method it is only surface sensitive. In this regard confocal Raman spectroscopy and Second harmonic microscopy offer an alternative due to their three dimensional resolution, while both methods also offer a sensitivity to structural changes, e.g. defects or waveguides as demonstrated in the sections above. Studies of domains on y-face or x-face of any uniaxial ferroelectric materials are of particular interest, as this allows to investigate the domain growth process including properties, such as nucleation sites, growth directions and velocities or shape of growing domains.

In this analysis we have investigated a sample, which was fabricated by contact poling (stamper technique). Here, the electrode is not directly deposited on the sample or has direct contact via an liquid electrode, but is deposited on a separate substrate. The stamp for this sample consisted of lithographically patterned titanium strips on a glass substrate (SiO_2). For poling this stamper is pressed against the sample and serves as the front electrode. The back electrode is provided by a deposited Chromium layer deposited on the complete back side. Details regarding sample fabrication can be found in literature [294, 343]. The period length of the analyzed samples was $\Lambda = 16.7$ μm with a duty cycle of 10/6.7, where the 10 μm region are inverted.

Figure B.1 now shows several measurements performed from z-cut on this sample. While a) displays a Raman image based on the intensity variation of the 693 cm^{-1} line, subfigure b) shows a different area of the same sample investigated by nonlinear microscopy. For both images one can see two general regions. One is a fairly homogeneous domain of 4-5 μm width, and a large region of 10-12 μm, which further shows small inclusions of domains. Here, apparently the large regions are the inverted ones, while the smaller represent the pre-poling domain orientation. As it is sometimes observed for contact poling small domain fragments in the otherwise inverted domains have not been inverted, which may be, because of an uneven contact [294, 343]. It also can be seen that the obtained duty cycle of $\approx 12/4.7$ slightly differs from the targeted duty cycle, which may be due to field enhancements at the edges of the contact electrodes. This has been also observed in literature [343]. Figure B.1c) shows an xz-scan obtained with confocal Raman spectroscopy also from the z-direction through two domain pairs. Here, one can see that the domain pattern is also reproduced well in depth. Here, it should be noted that the z-scale only shows the z-actuator movement. The approximately 16 μm positioner movement represents actually a range of $16 \cdot 1.78 \approx 28.5$ μm due to refraction. Here, 1.78 is the refractive index of $KTiOPO_4$ and the correction was performed according to Ref. [235].

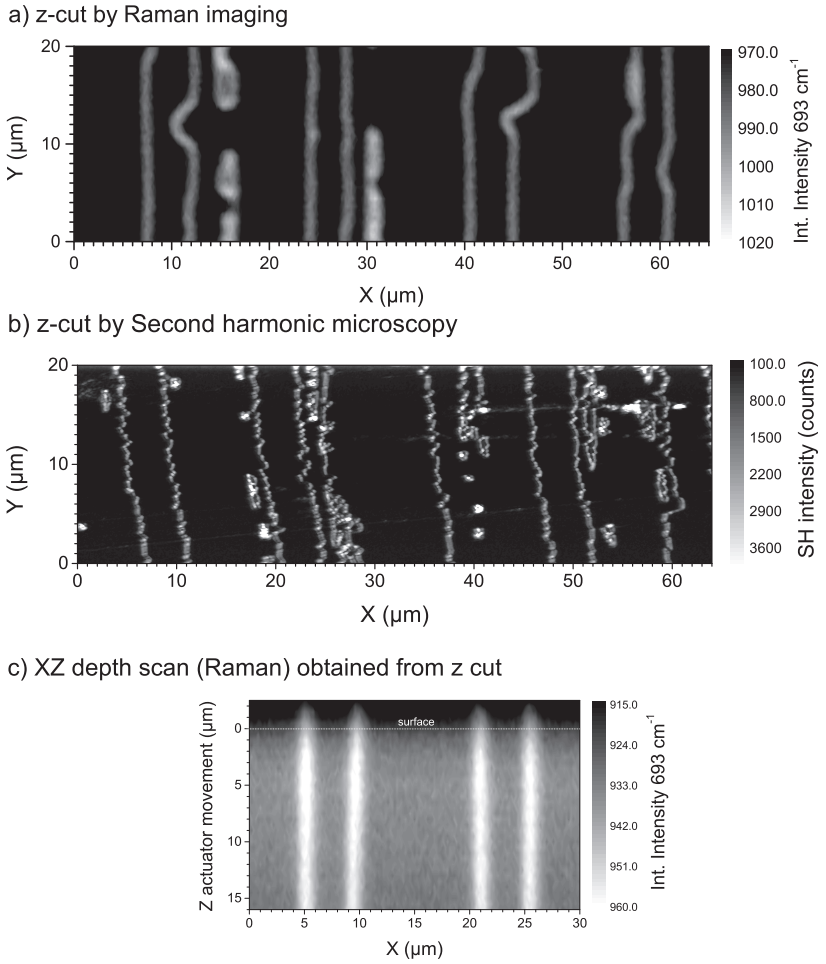

Fig. B.1 Images of ferroelectric domain walls obtained in z-cut on a sample fabricated by stemper technique [294, 343]. Here, Fig. a) shows a result obtained by Raman imaging, Fig. b) shows a different area analyzed in the Second harmonic microscopy setup and c) a depth (XZ) scan performed with Raman microscopy.

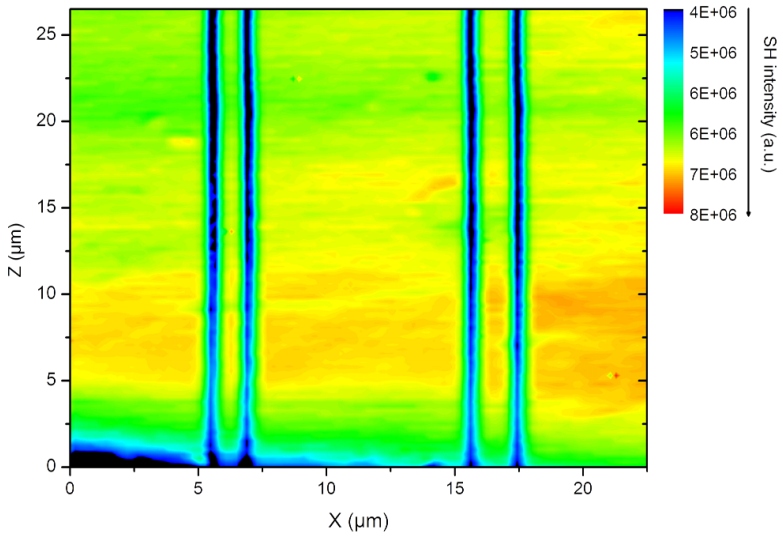

Fig. B.2 Second harmonic image of the y-face of a periodically poled crystal close to the surface, where the electrode was applied. The air/crystal interface is visible in the lower side of the image. Here, the domain walls appear as dark lines. The domain pattern clearly followed the electrode structure duty cycle.

For the analysis of domains in y-direction a similar sample was fabricated, which was cut along x-direction and directly through the suspected poled area. In this context Fig. B.2 shows a second harmonic microscopy scan performed from y-direction of the edge of the sample surface. Here, two domain wall pairs appear as regions of decreased intensity. The results are very similar to the observation made with the z-cut Raman scan presented in Fig. B.1c) and shows that the domain structure close to the surface reproduces the electrode structure very well. Further analysis have now been performed with Raman microscopy.

We have demonstrated previously that domains also on y-cut can be visualized with Raman spectroscopy. This was apparently only possible for y(x,z)$\overline{\text{y}}$ geometry with Raman spectroscopy. Here, it was found that it is most convenient to use the peak frequency of the 783 cm^{-1} to visualize domain walls, as shown in Fig. B.3. This figure shows a spectrum obtained at a domain wall versus the spectrum of bulk KTP. The strong shift of the 783 cm^{-1} is clearly seen. That this mode offers a contrast to domain walls can be understood by a breaking of selection rules at the domain walls. The up-shift of this mode can be explained by the directional dispersion, which is only prominent in the crossed polarization geometries in $KTiOPO_4$ as discussed in Sec. 5.1.2. Figure B.4 shows the result of such an investigation. Here, according the subfigure d), which shows the measurement geometry, three measurements have been performed. First, a line scan approximately 50 μm below the top surface has been performed and is shown in Fig. B.4a). Here, the domain walls are visible and reproduce the period length of 16.7 μm well. However, also domain incursion in the inverted range are seen, which fit with the observations made from z-cut. The results are different, when the measurements somewhere in the middle of the sample and close to the back side. Figure B.4b) shows a 2D plot (xz) scan. Here, the domains, which are visible, show no relation to the period length anymore. At $x = 45$ μm even a domain is seen, which appears to vanish. Here, we may have observed the end of a domain fragment, which is not grown through the complete sample. Close to the back side (subfigure c) no clear period length can be identified and an almost chaotic domain structure is observed.

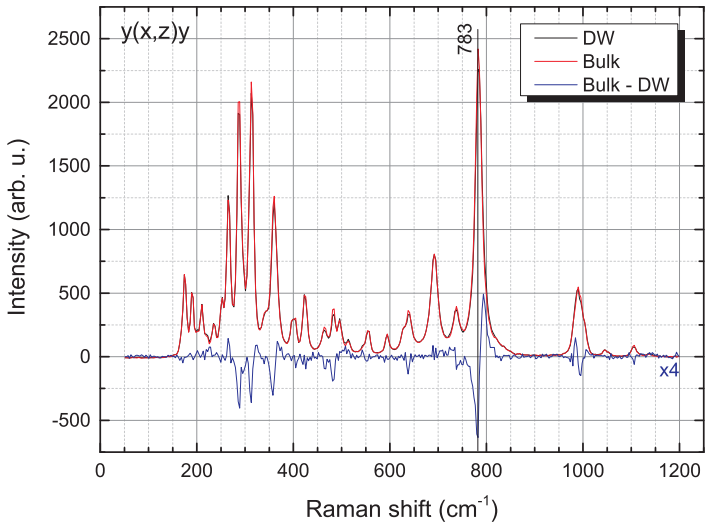

Fig. B.3 This figure shows two as-measured spectra obtained at a domain wall versus the spectrum of bulk KTP. To easily spot the differences, a difference spectrum is given (blue).

In conclusion we have demonstrated that domain walls on y-cut $KTiOPO_4$ can be visualized with Raman spectroscopy, as well as nonlinear microscopy. This is a particular achievement, because the usual standard method of selective etching can not be applied to y or x-faces in $KTiOPO_4$ [340] and AFM based methods have been the only practical alternative so far. Our measurements indicate that the domain pattern in $KTiOPO_4$ closely follows the electrode at the surface ($> 50\ \mu$m), while towards the back only an irregular pattern is achieved, where no short range periodicity is observed. Towards the center of the crystal slab we observed signs for v-shaped domains (v-shaped), which do not reach the back side.

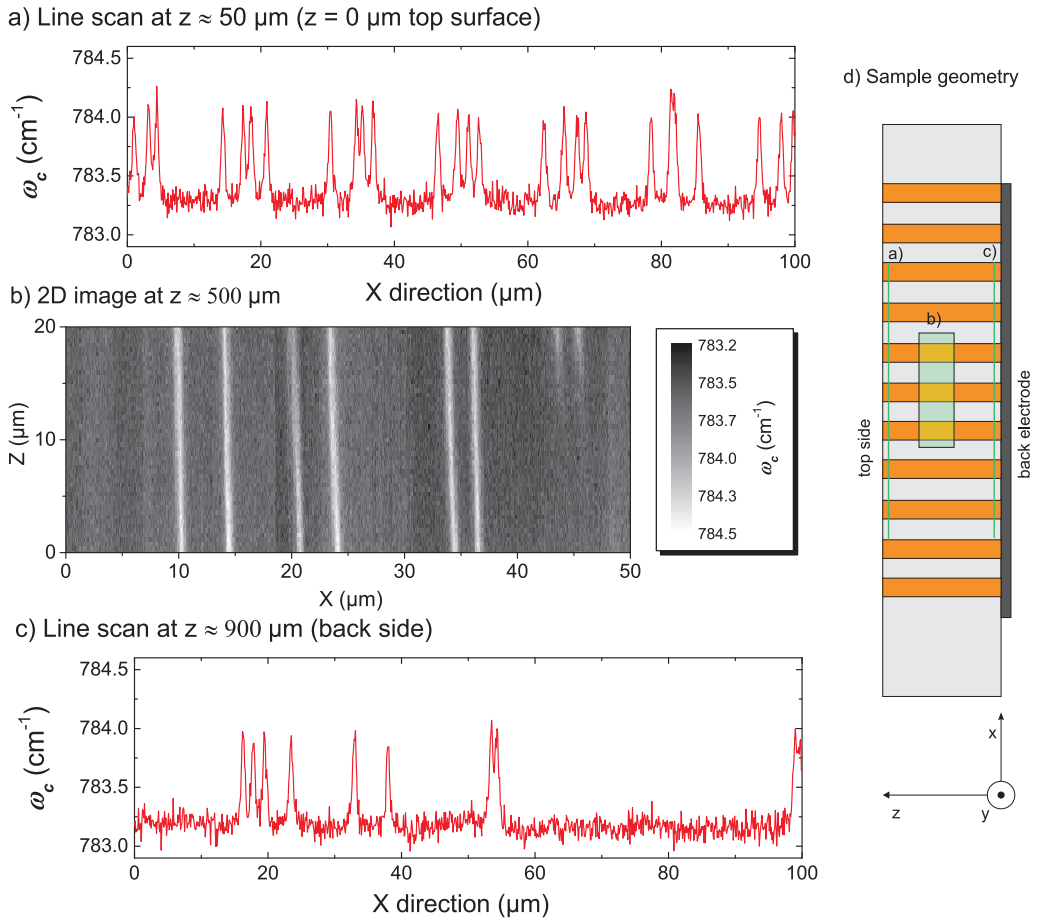

Fig. B.4 Subfigure d) shows the sample and measurement geometry. Three measurements are performed to investigate the domain structure along the z-direction: A line scan close to the front face approximately 50 μm below the surface, a 2D image in the center of the sample (b) and a line scan close to the back side (c). While close to the surface, the period of ≈ 16.7 μm is conserved, no short range periodicity is visible towards the back side anymore.

Appendix C

Publication list

1. ***M. Rüsing***, S. Neufeld, J. Brockmeier, P. Mackwitz, K. J. Spychala, S. Sanna, W.G. Schmidt, S. Sanna, G. Berth, and A. Zrenner, Imaging of 180° ferroelectric domain walls in uniaxial ferroelectrics by Confocal Raman spectroscopy: Unraveling the contrast mechanism, In submission (2018).

2. K. J. Spychala, G. Berth, A. Widhalm, ***M. Rüsing***, L. Wang, S. Sanna, and A. Zrenner, Impact of carbon-ion implantation on the nonlinear optical susceptibility of $LiNbO_3$, *Optics Express* **25**, 21444 (2017).

3. ***M. Rüsing***, S. Sanna, S. Neufeld, G. Berth, W. G. Schmidt, A. Zrenner, H. Yu, Y. Wang, and H. Zhang, Vibrational properties of $LiNb_{1-x}Ta_xO_3$ mixed crystals, *Phys. Rev. B.* **93**, 184305 (2016).

4. P. Mackwitz, ***M. Rüsing***, G. Berth, A. Widhalm, K. Müller, and A. Zrenner, Periodic domain inversion in x-cut single-crystal lithium niobate thin film, *Appl. Phys. Lett.* **108**, 152902 (2016).

5. ***M. Rüsing***, T. Wecker, G. Berth, D.-J. As, and A. Zrenner, Joint Raman spectroscopy and HRXRD investigation of cubic gallium nitride layers grown on 3C-SiC, *Phys. Stat. Solidi* **253**, 778 (2016).

6. ***M. Rüsing***, C. Eigner, P. Mackwitz, G. Berth, C. Silberhorn, and A. Zrenner, Identification of ferroelectric domain structure sensitive phonon modes in potassium titanyl phosphate: A fundamental study, *J. Appl. Phys.* **119**, 44103 (2016).

7. S. Sanna, S. Neufeld, ***M. Rüsing***, G. Berth, A. Widhalm, A. Zrenner, and W. G. Schmidt, Raman scattering efficiency in $LiTaO_3$ and $LiNbO_3$ crystals, *Phys. Rev. B* **91**, 22 (2015)

8. S. Sanna, A. Riefer, S. Neufeld, W. G. Schmidt, G. Berth, ***M. Rüsing***, A. Widhalm, and A. Zrenner, Vibrational Fingerprints of $LiNbO_3$-$LiTaO_3$ Mixed Crystals, *Ferroelectrics* **447**, 63 (2013).

9. M. Rashad, ***M. Rüsing***, G. Berth, K. Lischka, and A. Pawlis, CuO and Co_3O_4 Nanoparticles: Synthesis, Characterizations and Raman Spectroscopy, *J. Nano. Mat.* **2013**, 714853 (2013).

Acknowledgements

Many people have contributed to the success of this work - be it with personal or with professional advice. The following list is probably far from comprehensive.

- I am deeply grateful to Prof. A. Zrenner for taking me as a PhD student in his group providing me with guidance, but also freedom to pursue my own path.
- I thank J.-Prof. Tim Bartley, Prof. Schmidt and XX, who kindly agreed to join the thesis committee. Throughout my time as a PhD student they always had an open ear and provided .
- My deepest gratitude I would like to express to Gerhard Berth, who has become my mentor and friend from my very first semesters in Paderborn. Your guidance and advice has always been an inspiration to me.
- For the fruitful cooperation I want to thank the group of Prof. Silberhorn and in particular C. Eigner for many helpful discussions and advices.
- From the theory department I want to thank in particular Sergej Neufeld and Simone Sanna for the rewarding cooperation, many interesting discussions and helpful feedback throughout all the years.
- Special thanks go to all the other cooperation partners, who provided samples and interesting questions beyond the usual work. In particular this is Tobias Wecker and Sarah Blumenthal from the group of Prof. As, who allowed me to broaden my horizon with work on semiconductors. This was a welcomed change in my usual work.

  I also want to thank Thomas Hett from the Electrical Engineering department for the cooperation, friendship and helpful advice throughout the years.

  Further, I want to thank Prof. H. Hu for the possibility to gain experience with thin film lithium niobate. For the growth of $LiNb_{1-x}Ta_xO_3$ mixed crystals and the cooperation I thank Prof. Zhang and H. Yu from the Shandong University in China.
- Next I want to thank all the colleagues and friends from the group of Prof. Zrenner. In particular I want to express my deepest gratitude to all my current and former office mates.

  Special thanks go to Peter Mackwitz, Julian Brockmeier, TheKani™ and Kai Spychala for many interesting, not always work relating, discussions. Peter I want to thank for PeterTours™ (5/5 ★).
- During the time of my studies I made many new friends, who always had an open ear and advice. Especially I want to thank Thomas Nitsche, Sergej Neufeld, Anna Bauer and Franziska Zeuner.
- Further, I want to thank all the other people in the university who provided a fun and nice environment to work and live in, in particular the "Fachschaft", the "Porquerolles/GRK" group and all the students, whose work I was allowed to supervise.
- Die Sekte. You are the best, craziest and funniest bunch of friends I can think of. M. Sacrificamus.
- Last but not least I owe my deepest gratitude to my whole family, my girlfriend Katharina and in particular my parents, who always supported during all the years. I love you.